Neue Messtechniken und Simulationen für die Strömungsvorgänge und den örtlichen Stoffübergang in nicht-Newtonschen Fluiden

Dissertation zur Erlangung des Doktorgrades
der Naturwissenschaften (Dr. rer. nat.)

Fakultät Naturwissenschaften
Universität Hohenheim

Institut für Lebensmittelwissenschaft und Biotechnologie

vorgelegt von
Gongyuan Zheng

aus China
2010

Dekan: Prof. Dr. rer. nat. Heinz Breer
1. berichtende Person: Prof. Dr.-Ing. habil. Dr. h. c. Volker Kottke
2. berichtende Person: Prof. Dr.-Ing. Reinhard Kohlus
3. berichtende Person: Prof. Dr.-Ing. habil. Jörg Hinrichs

Mündliche Prüfung am: 25. November 2010

Die vorliegende Arbeit wurde am 14. Oktober 2010 von der Fakultät Naturwissenschaften der Universität Hohenheim als „Dissertation zur Erlangung des Doktorgrades der Naturwissenschaften“ angenommen.

To

Prof. Dr.-Ing. habil. Dr. h. c. Volker Kottke
Prof. Dr. Heinz Hesselfeld
my family

Acknowledgements

I would like to express my deep gratitude to my Doktorvater, Prof. Dr.-Ing. habil. Dr. h. c. Volker Kottke, who has motivated and constantly supported me to carry out this present work. He is the one person most responsible in these years in helping me; without his irreplaceable encouragement and help, I would never have been able to reach the goal. I would also like to thank him for giving me a free space to widen and deepen my horizons in this field. I clearly knew in these years, that behind the challenging research, I would always get support from him. With this strong confidence, I was initiated, guided and encouraged by my professor and have been able to make ahead without any hesitations.

The help from Prof. Dr. Heinz Hesselfeld, who always cares about me and is excited with my every progress, is highly acknowledged. He introduced me to Prof. Dr. Kottke and has given me and my family loving help for many years. The work experience with him in Jiangxi - OAI is a treasure in my life. Love lightens life; Hope helps the heart. Now he dedicates most of his efforts helping Chinese children in education. I wish him a peaceful and healthy future ahead.

I am really grateful to the help from Dr.-Ing. Peter Gschwind, for his guidance at all the places, where I got stuck and at all the times, when I felt in difficulties. I am also thankful to my other colleagues, Mrs. Steffi Pavlov, Dr. rer. nat. Svetlana Jesinger, Dr.-Ing. Jörg Meyer, Dipl.-Ing. Thomas Jesinger, Dr.-Ing. Christoph Schill, whose perpetual contributions helped me a lot towards achieving my goals. Without their help, this work could not have been done in such a reasonable period of time. I was fortunate to have had a wonderful work experience in such a helpful group. The homogeneous team atmosphere indeed makes the results of mass transfer in my dissertation more homogeneous.

I was fortunate to have the opportunity to share some of my period of employment in the institute of Food Science and Biotechnology of the University of Hohenheim. I am highly obliged to my present and former colleagues, from whom I learnt so many things. Special thanks to Mr. Lang in the Technikum for his great assistance in building the experimental plant and Ms. Lasta in the Department of Meat Technology for the guidance in spectrophotometry.

I extend my sincere thanks to Dr. Zick of Brucker for helping to enlighten my knowledge in the field of PFG-NMR and for his support in the measurement of the diffusion coefficient.

A word of gratitude goes to Jiangxi-OAI Joint Research Institute and the University of Nanchang in China. I am indeed very grateful to Prof. Shaohua Huang, Prof. Dr. Huadong Li and his family, Prof. Dr. Hongbin Chen, Prof. Jingyan Gao and other colleagues, who have offered me lots of valuable help, during the time I worked and studied there.

I deeply appreciate all kinds of help from my parents, who always stand behind my decisions to further bolster my confidence. And many thanks to my brothers and their families for the constant support and understanding and their long term care for our parents.

I thank my wife Hong and my son Jitao for their patience, constant support and understanding during my long work hours. It is due to her loving care and encouragement, that I could always be in a good state of mind and focus completely on this work. I wish my wife a speedy recovery from her accident.

Table of Contents

List of symbols and abbreviations

Latin letters

A	area	[m^2]
a	radius of grid rods	[m]
b	color density of Acidol-Blue	[mg/m^2]
b'	spanwise dimension of a single characteristic diamond defined by **Eqn. 2-2**	[m]
B	width of the test section	[m]
c	concentration	[%]
C_A	concentration of Acidol-Blue	[mg/kg]
C_b	bulk concentration of Acidol-Blue	[mg/m^3]
C_w	wall concentration of Acidol-Blue	[mg/m^3]
D	diffusion coefficient	[m/s^2]
d_h	hydraulic diameter of the whole test section defined by **Eqn. 2-1**	[m]
$d_{h,d}$	hydraulic diameter of a single characteristic diamond defined by **Eqn. 2-2**	[m]
H	height of the test section	[m]
K	fluid consistency	[kg/ (m s^{2-n})]
K_B	Boltzmann constant	[J/K]
l	streamwise dimension of a single characteristic diamond defined by **Eqn. 2-2**	[m]
L	length of the test section	[m]
m	transferred mass	[mg]
$\dot{m}$	mass flux	[mg/ (m^2 s)]
M_n	number average molecular weight	[g/mol]
M_w	weight average molecular weight	[g/mol]
r_h	hydraulic radius	[m]
S_c	surface of the test section	[m^2]
S_{cs}	surface covered by the spacer at the left/right wall of the test section	[m^2]
S_f	surface, rectangular to flow direction	[m^2]

S_{fs}	surface covered by the spacer at the top/bottom edges of the test section	$[m^2]$
S_g	surface of grid rods in a single characteristic diamond	$[m^2]$
S_{gg}	surface covered by intersection points of the grid rods	$[m^2]$
$S_{m,d}$	surface of membranes in a single characteristic diamond	$[m^2]$
S_M	momentum source	$[kg/(m^2 s^2)]$
S_s	surface of spacer	$[m^2]$
S_w	wetted surface of a single characteristic diamond	$[m^2]$
T	temperature	[K]
t	time	[s]
U	the three-dimensional velocity vector	[m/s]
u	velocity vector in x-direction	[m/s]
v	velocity vector in y-direction	[m/s]
V_c	volume of the test section	$[m^3]$
V_d	volume of a single characteristic diamond with grid rods	$[m^3]$
V_f	volume of fluid domain for a single characteristic diamond	$[m^3]$
V_g	volume of grid rods in a single characteristic diamond	$[m^3]$
V_s	volume of spacer	$[m^3]$
$\dot{V}$	volume flow	$[m^3/s]$
w	velocity vector in z-direction	[m/s]
$\overline{w}$	mean velocity in flow direction	[m/s]
X	coordinate in horizontal direction	[m]
Y	coordinate in vertical direction	[m]
Z	coordinate in flow direction	[m]

Greek letters

η_M	apparent viscosity of modified power law non-Newtonian fluid	[Pa·s]
η_P	apparent viscosity of power law non-Newtonian fluid	[Pa·s]
η_a	apparent viscosity	[Pa·s]
$\bar{\tau}_w$	average wall shear stress	[Pa]
μ	dynamic viscosity	[Pa·s]
η_e	effective viscosity	[Pa·s]
υ	temperature	[^{o}C]
γ	defined surface contact angle in numerical model	[degree]
$\dot{\gamma}_w$	shear rate at wall	[1/s]
$\dot{\gamma}$	shear rate	[1/s]
τ	shear stress	[Pa]
τ_w	wall shear stress	[Pa]
η_0	zero shear viscosity ($=\eta_{\dot{\gamma}=0}$)	[Pa·s]
$\eta_{\dot{\gamma}=500}$	apparent viscosity at 500 s^{-1}	[Pa·s]
β	mass transfer coefficient	[m/s]
θ	flow separation angle	[degree]
λ	wavelength of grid rods	[m]
ρ	density	[kg/m^3]
φ	inclination angle of grid rods	[degree]
Φ	additional variable	[kg/kg]

Miscellaneous letters

$\frac{dp}{dl}$	local pressure gradient	[Pa/m]
$-\left.\frac{\partial C}{\partial y}\right\|_{y=0}$	Acidol-Blue concentration gradient at wall	[mg/m^4]
ΔP	pressure drop	[Pa]

Dimensionless variables

a^*	geometric correction parameter determined by **Eqn. 5-4**
b^*	geometric correction parameter determined by **Eqn. 5-3**
C_d	drag coefficient
$C_{d,f}$	friction drag coefficient
$C_{d,p}$	form drag coefficient
C_h	homogeneity coefficient defined by **Eqn. 7-3**
e	exponential function
f	Fanning friction factor
n	flow index
Nu	Nusselt number
Pe	Peclet number
Pr	Prandtl number
Re	Reynolds number
Re_0	zero shear Reynolds number determined by **Eqn. 5-8**
Re_M	modified power law Reynolds number determined by **Eqn. 5-10** and **Eqn. 5-12**
Re_P	power law Reynolds number determined by **Eqn. 5-2**
Sc	Schmidt number
Sh	Sherwood number
$\overline{Sh}$	average Sherwood number
St	Stanton number
z^*	dimensionless entrance length in flow direction defined by **Eqn. 3-15**
β^*	Reynolds correction factor determined **Eqn. 5-9**
ζ	Darcy friction factor
λ/a	dimensionless wavelength defined for spacers

Subscripts

0	zero shear rate
a	apparent
b	bulk, spanwise width of a single characteristic diamond
c	channel
d	diamond, drag
e	effective

f	fluid, friction, film
g	grid rod
h	hydraulic
l	streamwise length of a single characteristic diamond
m	membrane
M	modified power law non-Newtonian fluids
max	maximum
N	Newtonian fluids
P	power law non-Newtonian fluid
p	pressure
s	spacer
w	wall, wetted
z	local value in flow direction

Abbreviations

CFD	Computational Fluid Dynamic
CFX	a CFD software by ANSYS®, Inc.
HPMC	Hydroxypropyl Methylcellulose
PA	Polyamide
PVA	Polyviny- alcohol
SWM	Spiral Wound Membrane

Summary

Flow and transport phenomena in non-Newtonian fluids are of significant industrial interest. As a kind of static mixer, spacers play an important role in process engineering concerning problems of mixing, homogenizing and dispersing in connection with residence time behavior up to the enhancement of heat and mass transfer. However, the efficiency of such spacers strongly depends on fluid properties, the characteristic geometry and operating conditions. Additionally, it is very difficult to respond to changed operating conditions for such spacers and ill-designed feed spacers can hinder the realization of a high performance.

Here, experimental and numerical methods were introduced for the investigation of flow phenomena and mass transfer for non-Newtonian fluids in spacer-filled channels.

Based on a coupled chemisorption reaction between the sulfonic acid group of Acidol-Blue and the -NH_2- group of Polyamide, an experimental mass transfer method was used to visualize the flow phenomena, determine the local mass transfer, quantify the mixing behavior and determine the homogeneity of mass transfer for Newtonian fluid flow. This method is extended to the case of non-Newtonian fluids in spacer-filled channels in this study.

Numerical methods were also introduced in this study. Three-dimensional computations based on a commercial computational fluid dynamics (CFD) code have been conducted to study the flow phenomena and local mass transfer for non-Newtonian fluids in spacer-filled channels. The simulations focus on a single characteristic diamond of the spacer, which plays an important role in saving computer resources as well as computing time and provides immediate information on the effect of the spacer geometry. Due to the existence of a high viscosity in the non-Newtonian fluids, the laminar flow for low Reynolds number is of the most interest. Equations for the laminar boundary layer with periodic interfaces for steady state were solved three-dimensionally in this study. The equations were coupled with a diffusive transport equation, Acidol-Blue was added as a specific additional variable into computations, when mass transfer was taken into account. Diffusion coefficients for different concentrations of METHOCEL® K15M, determined by PFG-NMR, were used in these calculations.

Comparisons on flow phenomena, pressure drop and the enhancement of mass transfer have been made in this study, either between experimental and numerical methods or between Newtonian and non-Newtonian fluid. Validation assessments were carried out in order to verify that the results are of high accuracy. Performance assessments, based on two different criteria, were executed to optimize the spacer geometry.

Based on the wall information from creeping flow, two geometric correction parameters a^* and b^* for a variety of spacer geometries were determined in this study.

Rheological characteristics of shear thinning (pseudoplastic) and shear thickening (dilatant) systems were investigated in this study. It is suggested, that the modified power law model is the more reasonable and the preferable more accurate constitutive equation for flow in such low Reynolds number conditions as in this study. A further, so-called Reynolds correction factor β^* was introduced, with which the "power law" intensity for modified power law non-Newtonian fluids in arbitrary geometry channels can be quantified. Therefore, first an adapted definition of the Reynolds- number was introduced in this study. Because the effect of flow channel (geometrical corrected parameters), fluid properties (rheological characteristics) and flow intensity (Reynolds correction factor) were simultaneously taken into consideration in the definition, the introduction of the Reynolds number makes universal sense in prediction, comparison and analogical study of hydrodynamic and heat/mass transport problems.

Compared to the flow in a rectangular duct, a higher resistance is produced by the spacer shape, the scale of which strongly depends on the geometry of spacers, i.e. the configuration of inclination angle φ and wavelength λ/a. Flow visualizations show, that the flow in spacer-filled channels is three-dimensional. Three basic flow types in the main flow were observed in spacer-filled channels, depending on the spacer geometry, the "corkscrew flow" characterized through spacers with smaller inclination angles φ and larger wavelengths λ/a; the "channel flow", on the contrary, through spacers with larger inclination angles φ and smaller wavelengths λ/a; and the "mixing flow" behavior in-between these two flow types, in spacers with an appropriate combination of the geometric parameters. For the flow in spacer-filled channels with a higher Reynolds number, more channel type flow phenomena are observed; these occur earlier in spacers with larger inclination angles and/or smaller wavelengths.

The flow behavior in spacer-filled channels is rheology dependent for non-Newtonian fluids. The development of the flow type from a corkscrew flow to a channel flow occurs earlier for a higher flow index n value then for a lower n value. In an identical spacer geometry, a more peaked velocity profile shape has been observed for non-Newtonian laminar flow with a larger flow index n. It thus shows a characteristic difference in velocity profile comparable to flow in straight ducts for different n values.

With the newly defined Reynolds number for fluids with different flow index n values in different geometry spacers, there is a good correlation between Reynolds number and drag coefficient and a very good agreement between the experimental and numerical analysis results. The conclusion can be drawn, that following a common curve $C_d \cdot \mathrm{Re}_M = 16$ for creeping flow, a slow and gradually cumulative deviation with subsequent transition occurs. Position and scale of the deviation and transition depend on the geometry of the spacer. Spacers with high resistance, which possess a smaller wavelength and/or smaller inclination angle, usually have an earlier and larger deviation and the cumulative deviation will develop at an earlier transition point.

The Sherwood number is proportional to the Schmidt number to the power of 1/3. A simple correlation equation was given as $Sh = \psi \cdot \mathrm{Re}_M{}^{\varepsilon} \cdot Sc^{\left(1/3\right)}$ to predict mass transfer for non-Newtonian fluids in spacer-filled channels. These correlations will not be the most accurate available, but are quite satisfactory for the design and the optimization of spacers in non-Newtonian media with normal flow indices (n = 0.3 - 0.9 in this study). The shear dependency becomes significant for a fluid with an especially small flow index n value; the difference in viscosity between η_b and η_w has to be taken into account. An accurate correspondence has been achieved by addition of a term for the viscosity ratio in the correlation equation. An alternative factor can be used more practically to predict mass transfer in experimental methods, because the local viscosities in the flow field are not easy to determine experimentally. Furthermore, investigations show, that a more accurate correlation equation can be achieved, when the drag coefficient has been taken into consideration for the prediction of mass transfer for non-Newtonian flows in spacer-filled channels.

Two criteria have been applied to investigate the efficiency of mass transfer for non-Newtonian flow in spacer-filled channels. Criterion Sh/C_d describes the mass transfer in relation to the resistance (drag coefficient); Sh/C_h the mass transfer in relation to homogeneity. The results show, that the much higher efficiency is observed in spacer-filled channels, represented by

${}^{Sh}\!/_{C_d} = p \cdot \mathrm{Re}^q$, compared to the mass transfer in empty rectangular channel, where the exponent of Reynolds number q > 1, and the factor p shows values between 2.4 to 21. The results of criterion Sh/C_h show that spacers with smaller inclination angle and/or larger wavelength have a higher homogeneity performance.

Zusammenfassung

Strömungs- und Transportvorgänge in nicht-Newton'schen Flüssigkeiten sind von besonderem industriellen Interesse. In der Verfahrenstechnik werden Spacer eingesetzt zur Lösung von Problemen beim Mischen, Homogenisieren und Dispergieren, zur Erzielung eines günstigen Verweilzeitverhaltens sowie zur Steigerung des Stoff- und Wärmetransports. Die Effizienz solcher Spacer hängt stark ab von den Fluideigenschaften, von der Spacer-Geometrie und von den Betriebsbedingungen. Deswegen kommt einer Optimierung dieser Spacer für die jeweiligen Randbedingungen eine wesentliche Rolle zu. Die vorliegende Arbeit befasst sich deswegen mit experimentellen und numerischen Methoden zur Untersuchung der Strömungs- und Transportvorgänge in Kanälen mit Spacern für nicht-Newton'sche Flüssigkeiten.

In einer vorausgegangenen Dissertation wurde ein neues Verfahren zur Sichtbarmachung und Bestimmung örtlicher Stoffübertragung in Newton'schen wässrigen Fluiden eingeführt, das auf einer gekoppelten Chemisorptionsreaktion zwischen der Sulfonsäure-Gruppe von Acidol-Blau und der -NH_2-Gruppe von Polyamid basiert. Mit diesem Verfahren lassen sich nicht nur der örtliche und integrale Stoff- und Wärmeübergang bestimmen. Es eignet sich zugleich zur Sichtbarmachung der Strömungsvorgänge sowie zur Bestimmung des Mischverhaltens und der Stoff- und Wärmeübertragung in Newton'schen Fluiden. Ausgehend von diesem Verfahren werden in dieser Arbeit neue Verfahren entwickelt für nicht-Newton'sche transparente Flüssigkeiten als Modellfluide, wie sie für Lebensmittel von besonderem Interesse sind. Die vorliegende Arbeit beschränkt sich auf die Analyse der Strömungsvorgänge, des Druckverlustes und des örtlichen und mittleren Stoffübergangs. In nicht-Newton'schen Fluiden lässt sich über die erweiterte Analogie der Wärme- und Stoffübertragung aus dem Stoffübergang nur dann auch der Wärmeübergang bestimmen, wenn die Temperaturgradienten sehr klein sind. Für reale Temperaturgradienten sind die Aussagen auf den Stoffübergang begrenzt, da sich dann die Viskosität nicht-Newtonscher Fluide mit der Temperatur sehr stark ändern kann.

Zur Lösung dieser Probleme werden numerische Methoden eingesetzt, die auf dreidimensionalen Berechnungen basieren. Es wird ein kommerzieller CFD-Code verwendet, um die Strömungsvorgänge und den lokalen Stoffübergang für nicht-Newton'sche Flüssigkeiten in Spacer-gefüllten Kanälen zu untersuchen. Die Simulationen können auf eine charakteristische

Einzelraute eines Spacers reduziert werden. Damit lassen sich die Rechenzeit und die Anforderungen an die Computerressourcen sehr stark reduzieren, wie es für die Analyse der zahlreichen Parametern erster Ordnung bei der vorliegenden Problemstellung wesentlich ist. Wegen der z. T. sehr hohen Viskosität nicht-Newton'scher Flüssigkeiten stellt sich bei den dann niedrigen Reynolds-Zahlen eine laminare Strömung ein. Die laminaren Strömungsvorgänge werden für die stationäre Strömung dreidimensional berechnet. Zur Berücksichtigung des Stoffübergangs wird die diffusive Transportgleichung für Acidol-Blau als spezifische zusätzliche Variable eingeführt. Für die Berechnungen mussten die Diffusionskoeffizienten für Acidol-Blau für unterschiedliche Konzentrationen von METHOCEL® K15M bestimmt werden. Dies wurde zum einen mittels PFG-NMR durchgeführt, zum anderen wurde der Diffusionskoeffizient über den bekannten Stoffübergang in einer ebenen Spaltströmung bestimmt, wie es von Kühnel in einer vorausgegangenen Arbeit eingeführt worden war.

Die Ergebnisse der sehr umfangreichen experimentellen und numerischen Untersuchungen zu Strömungsvorgängen, Druckverlust und örtlichem und integralen Stoffübergang wurden zur Validierung der numerischen Ergebnisse miteinander verglichen um nachzuweisen, dass die Resultate eine hohe Genauigkeit aufweisen. Zur Beurteilung der Leistung der Spacer wurden zwei Kriterien verwendet, um die Spacergeometrie zu optimieren.

Basierend auf den Wandinformationen der schleichenden Strömung wurden zwei geometrisch Parameter a^* und b^* eingeführt, mit denen sich die Vielfalt der untersuchten Spacer für die industrielle Auslegung mittels einer einzigen Gleichung auslegen lassen.

Die rheologischen Charakteristiken scherverdünnender (pseudoplastischer) und scherverdickender (dilatanter) Fluide wurden in dieser Arbeit untersucht. Die Ergebnisse zeigen, dass ein modifiziertes Ostwald-de Waele Modell eine genaue Beschreibung der Strömung für die untersuchten niedrigen Reynolds-Zahlen ermöglicht. Des Weiteren wird ein neuer Faktor β^* eingeführt, mit dem die "power law" -Intensität für das modifizierte Ostwald-de Waele Modell in nicht-Newton'schen Flüssigkeiten in beliebigen Geometriekanälen quantitativ bestimmt werden kann. Für eine Zusammenfassung der experimentellen und theoretischen Ergebnisse mittels dimensionsloser Kennzahlen ergibt sich in nicht Newtonschen Fluiden und Spacer-gefüllten Kanälen das Problem, dass in der Re-Zahl die mittlere Geschwindigkeit, die geometrische Bezugsgröße und die Viskosität zuerst für eine zusammenfassende Darstellung in dieser Arbeit definiert werden müssen.

Verglichen mit der Strömung in einem freien Rechteckspalt führt ein Spacer zu einem höheren Widerstand, der stark von der Geometrie des Spacers beeinflusst wird, d.h. von dem Anströmwinkel φ und der Wellenlänge λ/a. Die Strömungsvorgänge in Spacer-gefüllten Kanälen sind bei nicht-Newton'schen Flüssigkeiten in starkem Ausmaß von der Rheologie abhängig. Dabei können die charakteristischen Strömungsformen, die bei hohen Reynolds-Zahlen und turbulenten Fluiden gültig sind, nur in ihren Grundelementen übernommen werden. Die Strömung kann in einen Talströmungsanteil und in einen Längsströmungsanteil aufgespalten werden, wobei in laminaren Strömungen zu kleineren Re-Zahlen der Längsströmungsanteil immer dominanter wird und der Talströmungsannteil immer stärker zurückgedrängt wird. Bemerkenswert ist, dass der Bereich sehr niedrigen Stoffübergangs im Auflagebereich der Spacerstrukturen auf der ebenen Wand umso größer wird, je kleiner die Re-Zahl ist. Deswegen dürfen Spacer bei sehr kleinen Re-Zahlen nicht mehr eingesetzt werden, da sonst der mittlere Stoffübergang sehr klein wird und der Vorteil einer Spacerstruktur in das Gegenteil verkehrt wird.

Mit den neu definierten Bezugsgrößen in der Reynoldszahl für Fluide mit unterschiedlichem Strömungsindex n und unterschiedlichen Spacergeometrien ergibt sich eine gute Korrelation zwischen Reynoldszahl und Reibungskoeffizient und eine sehr gut Übereinstimmung zwischen den Resultaten der experimentellen und numerischen Analyse.

Die Sherwood-Zahl ist proportional zur Schmidt-Zahl zum Exponent 1/3. Eine einfache Bezugsgleichung wurde mit $Sh = \psi \cdot \mathrm{Re}_M{}^{\varepsilon} \cdot Sc^{\left(1/3\right)}$ angegeben, um den Stoffübergang für nicht-Newton'sche Flüssigkeiten in Spacer-gefüllten Kanälen mittels dimensionsloser Kennzahlen zu berechnen. Diese Beziehung ist zufriedenstellend für das industrielle Design und für die Auswahl optimaler Spacer in nicht-Newton'schen Medien mit gemeinsamen Strömungsindices (n = 0,3 ~ 0,9 in dieser Arbeit). Für eine genaue Auslegung stehen die zahlreichen Ergebnisse der Berechnungen und Messungen in dieser Arbeit zur Verfügung.

Die Scherabhängigkeit nicht Newtonscher Fluide wird besonders bedeutsam für Fluide mit einem besonders kleinen Strömungsindexwert n. Hier muss der Viskositätsunterschied zwischen η_b und η_w berücksichtigt werden. Eine genauere Übereinstimmung konnte durch das Hinzufügen eines Terms für das Viskositätsverhältnis in der Korrelationsgleichung erreicht werden. Weiterhin zeigen die Untersuchungen, dass eine genauere Korrelation erreicht werden kann, wenn der Reibungskoeffizient bei der Vorhersage des Stoffübergangs bei nicht-Newton'scher Strömung in Spacer-gefüllten Kanälen berücksichtigt wird.

Zwei Kriterien wurden angewandt, um die Effizienz des Stoffübergangs für nicht-Newton'sche Strömungen in Spacer-gefüllten Kanälen zu analysieren. Das Kriterium Sh/C_d beschreibt den Stoffübergang relativ zum Widerstand (Reibungskoeffizienten), das Kriterium Sh/C_h dagegen beschreibt den Stoffübergang relativ zur Homogenität der Stoffübergangsverteilungen. Die Resultate zeigen, dass die Beziehung $Sh/C_d = p \cdot \mathrm{Re}^q$ eine wesentlich höhere Effizienz eines Spacer-gefüllten Rechteckspalts ergibt gegenüber einem leeren Spalt, wenn der Exponent der Reynoldszahl $q > 1$ ist und der Faktor p Werte zwischen 2,4 und 21 aufweist. Die Resultate des Kriteriums Sh/C_h zeigen, dass Spacer mit kleinerem Anströmwinkel und/oder größerer Wellenlänge eine höhere Homogenität des Stoffübergangs ergeben.

1 Introduction

1.1 Spacer-filled channel flow

A spacer is a net-type structure, which is used in a channel to enhance the heat and mass transfer, to promote turbulence and to stabilize and support membranes. As a kind of static mixer, spacers play an important role in process engineering referring to problems of mixing, homogenizing and dispersing in connection with residence time behavior.

In membrane modules, e.g. ultrafiltration and electrodialysis, and also in plate heat exchangers, spacers have several functions: on one hand they are used as stabilisators (supporting nets) between the membrane sheets, respectively the heat exchanger surfaces; on the other hand, they serve as turbulence promoters to homogenize and increase the heat and mass transfer rates. Furthermore, in spiral-wound membrane modules, spacers aid to enhance wall shear stress and to promote eddy mixing, thereby reducing wall concentration polarization and fouling.

It has been reported in literature that the spacers can significantly alter the hydrodynamic conditions and mass transfer patterns in a membrane channel [1]-[9]. Computational and experimental studies have demonstrated complex hydrodynamics that vary, depending on the spacer geometry, thickness and membrane packing density. Tian and Gill [10] demonstrated that the alternatively placed impermeable sections and membrane sections could reduce concentration polarization and therefore increase membrane productivity noticeably. Kang and Chang [11] and Kim et al. [12] showed that a recirculation flow induced by spacers enhanced mass transfer in electrodialysis systems. Schwinge et al. [13][14] studied mass transfer enhancement under constant wall concentrations and impermeable walls boundary conditions for different filament configurations with commercial CFD software. Geraldes et al. [15][16] simulated concentration polarization in nanofiltration (NF) spiral wound modules with fixed permeate velocity. Apparently, one important aspect of concentration polarization, the interaction between solute transport (concentration polarization) and momentum transfer (permeate velocity), could not be addressed. As indicated by Brian [17] the constant flux assumption would lead to significant errors in concentration polarization simulations, especially when wall concentration profiles are concerned. Analyzing fouling deposits on RO membranes, removed from spiral wound elements, some authors have also revealed, that channel spacers strongly influence foulant deposition patterns. Ill-designed feed spacers can create stagnant zones with elevated concentration polarization. These stagnant regions adversely affect membrane performance by promoting fouling and scaling locally, thus reducing flux, limiting water recovery, and lowering permeate quality.

Most of these studies focused on the process and the performance enhancement of mass transfer from the feed side to the permeate side of a membrane. Another important step for cross flow membrane filtration is that mass should first be transferred from bulk solution to the surface of membrane. The effect of geometry, solution properties and operation parameters on boundary layers and performance analysis on this process is, however, seldom found in literatures. Studies [18][19] on flow and mass transfer in channels with ladder-type spacers showed, that membrane permeation velocity has no significant effect on the flow structure, due to the dense membranes used in most NF and RO applications. The flow structure is determined mainly by the transverse filaments and the presence of longitudinal filaments in the channel was shown to not significantly affect the flow structure for Newtonian fluids in a range of Reynolds number between 50 and 600. Study on flow through channels filled with spacers in different configurations (cavity, zigzag and submerged) under permeable/impermeable boundary conditions [20] also showed, that the configuration of a spacer plays a dominant role in the increase of pressure drop, on the enhancement of wall shear rate, which induces the enhancement of mass transfer, and on the formation of stagnant zones, where the filaments contact the membranes, which leads to the unsatisfactory concentration polarization.

Due to the highly viscous nature of non-Newtonian fluids, fluid dynamic behavior in low Reynolds number laminar flow becomes more interesting. Often, the scalar diffusivity is small, compared with the viscosity of the fluid, so that the so-called Schmidt number Sc is large. For sufficiently high Schmidt number Sc, it can be shown that the mass boundary layer becomes thin in relation to the momentum boundary layer.

Various approximations have been introduced to predict mass transfer in different literatures. Based on the asymptotic analysis [107] $Sc \to \infty$ limit in the case of very large Schmidt number, some of the previous efforts [105][106] have led to a conclusion of $St \sim Sc^{(-2/3)}$.

1.2 Rheology

Rheology, a study of materials deformation and flow, is crucial in many areas of industries. It provides insightful information regarding molecular structure, material morphology as well as material response in industrial processes.

Numerous fluids show non-Newtonian rheological behaviors. Common examples are: yoghurt, butter, applesauce, tomato paste, ketchup, blood, toothpaste, polymers, molten plastics, sediments, petroleum products, drilling mud, sewage sludge, slurries, etc. These fluids are referred to as rheological fluids and exhibit a very broad non-Newtonian nature, characterized by a non-linear relationship between the stress and the rate of strain. Often, the "rheology" arises because the fluid in question builds up a microstructure at the molecular level, which becomes sufficiently extensive to affect the macroscopic properties of the fluid.

Referring to the term of "**rheometry**", a group of experimental techniques was developed to investigate the rheological properties of materials. It is of great importance in determining the constitutive equation of a fluid or in assessing the relevance of any proposed constitutive law [21]-[25]. A large number of constitutive equations have been developed to describe these non-linear rheological behaviors of non-Newtonian fluids. As for the most common type of shear thinning or pseudoplastic non-Newtonian fluid, characterized by an apparent viscosity decrease with increasing shear rate, which becomes more free-flowing and less viscous in response to an applied force, and the so-called dilatant fluid with an opposite behavior, which exhibits a reversible increase in viscosity with the increase of shear rate, a majority of researchers have used the power law (or Ostwald de Waele) model to describe the flow properties [26]-[36]. This model containing two rheological properties, the fluid consistency K and the flow index n, has proved to be quite successful in predicting the behavior of pseudoplastic fluids ($n < 1$), Newtonian fluids ($n = 1$) as well as dilatant fluids ($n > 1$). In this study, two common constitutive equations (power law model and modified power law model) were used to assess the rheological properties of non-Newtonian materials.

The formulation of constitutive equations is an early goal of rheology. From rheometry, the only information we obtain in most cases is the flow curve, i.e., the relation $\tau = f(\dot{\gamma})$, whereas we need more information to model the three-dimensional behavior of fluids. The question is how to express a 3D constitutive equation. Theoreticians such as Coleman, Markovitz, Noll, Oldroyd, Reiner, Toupin, Truesdell, etc. sought to express rheological properties through equations relating suitable variables and parameters representing the deformation and stress states. This gave rise to a large number of studies on the foundations of **continuum mechanics** (Bird et al., 1987). Nowadays the work of these pioneers is pursued through the examination of new problems such as the treatment of multiphase systems or the development of nonlocal field theories. For examples of current developments and applications to geophysics, the reader may consult papers by Hutter and coworkers on the thermodynamically consistent continuum treatment of soil-water systems [37]-[39], the book by Vardoulakis & Sulem [41] on soil mechanics, and the review by Bedford & Dumheller [37] on suspensions.

Computational fluid dynamics (CFD) is one of the branches of fluid mechanics, that uses numerical methods and algorithms to solve and analyze problems that involve fluid flows.

But for many complex fluids of practical importance, bulk behavior is not easily outlined using a continuum approach. It may be useful to first examine, what happens at a microscopic scale and then infer the bulk properties using an appropriate averaging process. Kinetic theories give a common example for gases [42] or polymeric liquids (Bird et al., 1987), which infer the constitutive equations by averaging all the pair interactions between particles. Such an approach is called **microrheology** or **rheophysics**. Recent developments in geophysics are based on using kinetic theories to model bed load transport [43][44], floating broken ice fields [45], rockfall and granular debris flows [46]-[48].

In general, rheology distinguishes different areas and offshoots such as the following: rheometry, formulation of constitutive equation, computational rheometry, microstructural analysis and interpretation of bulk rheological behavior, etc. With other tools, we can make the connection between micro (such as particle size) and macro (bulk) material properties (rheology) and chemical composition (chemical imaging).

A non-Newtonian rheological behavior adds much complexity to fluid flow as well as heat and mass transfer problems, especially in complex geometries such as spacer-filled modules mentioned above. Non-Newtonian fluid mechanics therefore differ from classical Newtonian fluid mechanics in many important respects. The most important difference is, that the complexity of non-Newtonian response essentially results in governing equations that vary from one flow type to another, whereas in the classical situation the Navier-Stokes equations are accepted without question as the governing equations.

Their non-linear characteristics of flow and deformation make the engineering operations very complicated. The complex results from the fact, that the local velocity gradients, from which local viscosity can then be evaluated from constitutive equations in three dimensions, first have to be determined. The velocity profile in a non-Newtonian flow, of course, is strongly dependent on the temperature gradient. Therefore the analysis in this work is limited to mass transfer, where the temperature in the boundary layer is constant. The basic information of the velocity field can be either measured by experimental techniques (e.g. LDA, PDA, PIV) or solved by numerical methods (e.g. CFD). Another complex is to associate the local variables to the engineering bulk variables (e.g. velocity, pressure), with which the common physical function can then be defined.

1.3 Numerical analysis

With the growth of computer performance, numerical analysis to find approximations to difficult problems such as solving differential equations has become a much easier task. The fundamental basis of almost all CFD problems is the Navier–Stokes equations, which are a set of coupled partial differential equations. The idea is that the spatial domain of a continuing fluid is discretized into finite small cells to form a mesh (for a mesh-based method) and then a suitable algorithm is applied to solve the equations. Three major discretization techniques are the Finite Difference Method (FDM), the Finite Element Method (FEM) and the Finite Volume Method (FVM).

ANSYS CFX, a finite volume method based commercial CFD code, was used as the solver in this work. For FVM numerical analysis, the process of mesh generation is used to decompose computational domains into finite volumes and the boundaries are replaced by a number of simple patches. Then for every volume, the governing equations (e.g. conservation of mass, momentum or energy) are solved based upon an integral form of the partial differential equations. As a mesh generator, ICEM CFD was used to generate mesh. For complex computational domains, it is very difficult to generate quality mesh with a good distribution of nodes. Especially in complex boundary layers, for non-Newtonian flow and mass transfer in this study, good quality mesh plays a most important role in capturing the characteristics of the velocity and concentration gradients. The structured mesh is useful when a high spatial resolution is required. Additional advantage is the small computational time required for one iteration on the structured mesh in comparison with the unstructured mesh. The stability of the fluid flow solution algorithm for the structured mesh is essentially higher than for the unstructured mesh. The preprocessing for the structured mesh is generally more elaborate than for the unstructured mesh. Therefore, a block-structured meshing method was applied to generate hexahedral elements in the whole fluid domain in this study.

Previous studies on membrane hydrodynamics and concentration polarization have resorted to simplified analytical models, or numerical models that are fundamentally inaccurate due to uncoupling of the equations of motion, which describe channel hydrodynamics, from the mass conservation equations, which describe rejected solute transport. As a consequence, only limited information is known regarding the complex hydrodynamic and concentration polarization fields that develop around feed spacers of spiral wound membrane elements. The highly oversimplified past models were incapable of handling complex geometries and flow patterns, in which flow instabilities may arise. However, with recent development in finite volume simulations of fluid flow and solute transport, it is now feasible to develop accurate models of the hydrodynamic and concentration fields in spiral-wound membrane elements employing any spacer geometry. In order to simulate the mass transfer, an equation describing the concentration of the added species was solved simultaneously with the Navier–Stokes equations. Accordingly, a comprehensive computational approach, with fully-coupled equations of motion and species convection-diffusion equations, will be undertaken to evaluate and optimize module hydrodynamics. The impact of spacer design (i.e., size, geometry, inclination) and element packing density will be analyzed to aid development and design of new spacer geometries designed to promote intense vortex shedding and eliminate stagnant zones. Results of these simulations will provide detailed three-dimensional views of concentration polarization, thereby enabling complete optimization of spacer geometry and arrangement so as to achieve maximum reduction in concentration polarization, scaling and fouling.

A spacer-filled rectangular channel was designed to simulate the sandwich-like structure of spiral wound membrane (SWM), similar to those used in electrodialysis stacks and in plate heat exchangers as stabilisator and as turbulence promoters to increase the heat and mass transfer rates and to reduce the concentration polarization and fouling behavior.

1.4 Experimental analysis

For the verification of the numerical analysis of local mass transfer and local flow processes in non-Newtonian flows up to now no experimental techniques are known. The present study is based on the previous work of Zimmerer [77] and Kühnel [84]. The flow phenomena and local heat/mass transfer of Newtonian fluids in spacer-filled channels were studied in their PhD thesis. Now, the new techniques are developed for the visualization and the determination of local mass transfer in spacer-filled channels in non-Newtonian fluids.

For non-Newtonian flow, new fluid systems have to be developed, which allow the local flow visualization as well as the determination of local mass transfer, based on the compatibility with the measuring techniques of Kühnel. Therefore, the materials as well as most of the methods have to be newly developed. In the next chapters, the new development of this work based on the previous dissertations on Newtonian flows is presented.

1.5 Aim of the work

1.5.1 The correlation between Reynolds number and friction factor is complex for non-Newtonian fluids in spacer filled channels, because it not only depends on the geometric parameters **λ/a** and **φ**, but also on the flow behavior index **n**, even when the flow is laminar (Fig. 5-1). This complex relationship makes predictions difficult. Besides, other correlations in heat/mass transfer problems also need reasonable definitions for variables. In this case, we want to find information about the influence of the geometric parameters of the spacers, with which the estimation of Reynolds number and other variables becomes more reasonable and easier for further comparison and analogical analysis.

1.5.2 Because of the high viscous characteristics of non-Newtonian fluids (usually 2-3 order magnitude higher than the viscosity of water), especially for the shear thickening case, where the viscosity of a dilatant fluid usually increases strongly with increasing shear rate (even at low shear rate range), low Reynolds number flow becomes interesting in non-Newtonian fluids. So our investigation is focused on laminar flows with Reynolds numbers from a very low level to several tens.

1.5.3 On the other hand, when the velocity (Reynolds number) is very low, a non-Newtonian fluid could be Newtonian in behavior; i.e. there is no decrease in viscosity at low shear rate range for many shear thinning (pseudoplastic) fluids, because there is a Newtonian plateau at the onset of the flow curves. A transition region will then appear with increased shear rate, before power law behavior occurs. A more universal constitutive equation, the modified power law model, that completely describes the rheological properties over the entire shear rate range, therefore needs to be considered. Experimental and numerical methods based on modified power law model are tried to be introduced into the investigation of the momentum and mass transfer problem in this study.

1.5.4 Flow inside the spacer-filled channel is complex. Different flow patterns, secondary flow, flow separation and reattachment, vortex formation as well as recirculation zones, can occur in the flow and can vary with changing Reynolds numbers. These complex phenomena will surely affect the mass transfer. This study tries to obtain information on mass transfer corresponding to the flow behavior in different spacers.

1.5.5 The method developed by W. Kühnel and V. Kottke to investigate the flow phenomena and to determine the mass transfer on the membrane surface in Newtonian fluids, will be extended to the case of non-Newtonian fluids in this study and the experimental results compared with simulations using a commercial computational fluid dynamics (CFD) code.

2 Geometry of spacers and experimental setup

2.1 Geometric parameters of the spacers

In preceding work a comprehensive overview of geometric parameters of regular structures can be found [49]. The cross-section in the case of spiral wound modules can be approximated by a rectangular geometry, since the effect of the channel curvature is practically negligible, due to the small channel height [108]. Spacers, in this study, are built with parallel arrayed and crosswise overlaid round grids, and are then installed inside a narrow rectangular channel (L = 0.4 m, B = 0.15 m, H = 4a = 0.01 m). The rectangular channel is therefore transformed into many diamonds with streamwise length *l* and spanwise width b' (**Fig. 2-1**). Their structures are characterized by the wavelength or grid distance (λ), the inclination angle (φ), the amplitude or grid diameter (2a). All spacers in this study were built by circular grids with the same radius a, the characteristics of the spacer geometry being described by the dimensionless wavelength (λ/a) and the inclination angle (φ). The values of the geometric parameters are listed in **Tab. 2-1**.

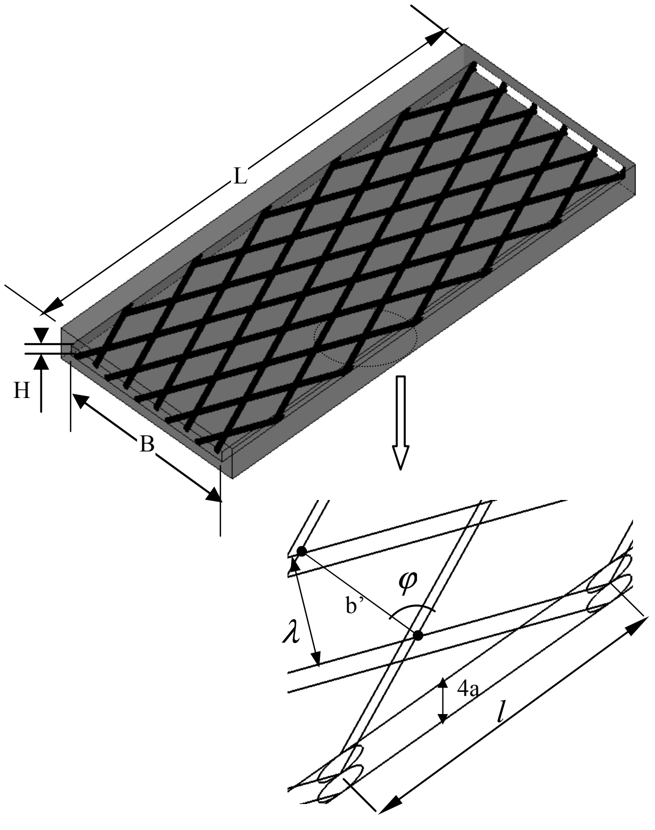

Fig. 2-1 Schematic geometric parameters for a spacer-filled channel

Tab. 2-1 Geometric parameters of the spacers

Spacer Type	λ/a [-]	φ [°]
A15	4	15.5
A30	4	30.0
A45	4	44.4
A60	4	60.1
A75	4	75.2
A90	4	90.0
B15	5.5	16.0
B30	5.5	30.3
B45	5.5	43.4
B60	5.5	60.6
B75	5.5	74.3
C15	7.45	14.4
C30	7.45	29.8
C45	7.45	43.1
C60	7.45	60.4
D15	11	16.0
D30	11	27.3
D45	11	47.2
D60	11	66.4

Several definitions of hydraulic diameter can also be found in [50]-[52]. A definition of the volumetric hydraulic diameter d_h of spacers was introduced by Zimmerer and Kottke [53]:

$$d_h = \frac{4 \cdot (V_c - V_s)}{S_c + S_s + S_f - S_{cs} - S_{fs} - S_{gg}} = \frac{8 - 4 \cdot \pi \cdot \frac{a}{\lambda}}{\frac{4}{B} + \frac{1}{a} + 2 \cdot \pi \cdot (1 - \frac{a}{B}) \cdot \frac{1}{\lambda}}$$

Eqn. 2-1

where V_c = volume of the test section [m^3];

V_s = volume of spacer [m^3];

S_c = surface of the test section [m^2];

S_s = surface of spacer [m^2];

S_f = surface of rectangular to flow direction [m^2];

S_{cs} = surface covered by the spacer at the left/right side walls of the test section [m^2];

S_{fs} = surface covered by the spacer on the top/bottom walls of the test section [m^2];

S_{gg} = surface covered by intersection points of the grid rods [m^2];

a = radius of grid rods [m];

B = width of the test section [m];

λ = wavelength of grid rods [m].

Numerical methods were also used to investigate the flow phenomena and mass transfer in such spacer-filled channels for non-Newtonian fluids. Design and simplification of the physical models becomes necessary in order to meet the limitations of the computer source and to save computing time. Therefore simulation was focused on single diamonds of the spacer-filled channels. For the single diamond of different spacers, we introduce a specific hydraulic diameter $d_{h,d}$ based on:

$$d_{h,d} = \frac{4 \cdot V_f}{S_w} = \frac{4 \cdot (V_d - V_g)}{S_{m,d} + S_g} = \frac{4 \cdot (2 \cdot a \cdot b' \cdot l - \frac{\pi \cdot a^2 \cdot b'}{\cos(\varphi)})}{b' \cdot l + \frac{2 \cdot \pi \cdot a \cdot b'}{\cos(\varphi)}} = \frac{8 - \frac{4 \cdot \pi \cdot a}{\lambda}}{\frac{1}{a} + \frac{2 \cdot \pi}{\lambda}}$$

Eqn. 2-2

where V_d = volume of a single characteristic diamond with grid rods [m^3];

V_f = volume of fluid domain for a single characteristic diamond [m^3];

V_g = volume of grid rods in a single characteristic diamond [m^3];

S_g = surface of grid rods in a single characteristic diamond [m^2];

$S_{m,d}$ = surface of membranes in a single characteristic diamond [m^2];

S_w = wetted surface of a single characteristic diamond [m^2];

a = radius of grid rods [m];

b′ = spanwise dimension of a single characteristic diamond [m];

l = streamwise dimension of a single characteristic diamond [m];

λ = wavelength of grid rods [m];

φ = oriention angle of grid rods [degree].

The hydraulic diameter in **Eqn. 2-2** is not exactly the same as in **Eqn. 2-1** which represents the whole test section, because in the calculation of d_h, the right and left sides of the test section are taken into account as side walls. Comparing both definitions above, we can easily get the relationship as:

$$d_h = \frac{1}{\frac{1}{d_{h,d}} + \frac{1}{2 \cdot B}}$$

Eqn. 2-3

Eqn. 2-3 states the relationship between these two hydraulic diameters. The difference between these two definitions (in **Eqn. 2-1** and **Eqn. 2-2**) is negligible because width B, in practice, is much greater than the foreseen hydraulic diameters. A comparison between these two hydraulic diameters is shown by **Fig. 10-11** in the Appendix. Less than 5% difference is indicated in **Fig. 10-11** for all spacers in the test section with width B = 150 mm used in this study.

2.2 Experimental setup

The experiments are carried out in a fluid channel, as shown in **Fig. 2-2**. Two gear pumps are used to transport the test fluids according to the demanded volume flows. In front of the test section, a flat diffuser and a composite honeycomb are placed to make sure that the entrance velocity is uniform. Volume flow rate is measured by a flow meter and the velocity ($\overline{w}$) is then determined from the measured volume flow rate. The temperature of the fluid inside the channel is controlled by a thermo controller (Unistat® 160W, Peter Huber Kältemaschinenbau GmbH, Germany). On the other side, the pressure drop (Δp) between the both sides of the test section is measured. An anionic azo dye (Acidol-Blue 3 GX, BASF, Germany) as transferable reacting mass component is added homogeneously into the flow in very small concentration. The top/bottom plates of the test section are covered with polyamide-6 coated membranes. The transferred dye is adsorbed and chemically bound in the surface layer of the polyamide. This technique gives the local mass transfer distribution directly as color density distribution. It is possible to analyze flat surfaces by coating them with polyamide chromatography sheets, with polyamide membranes or to build the surface to be analyzed by polyamide. Therefore also highly complex technical surfaces can be analyzed. A partial experimental setup is shown in **Fig. 2-3**.

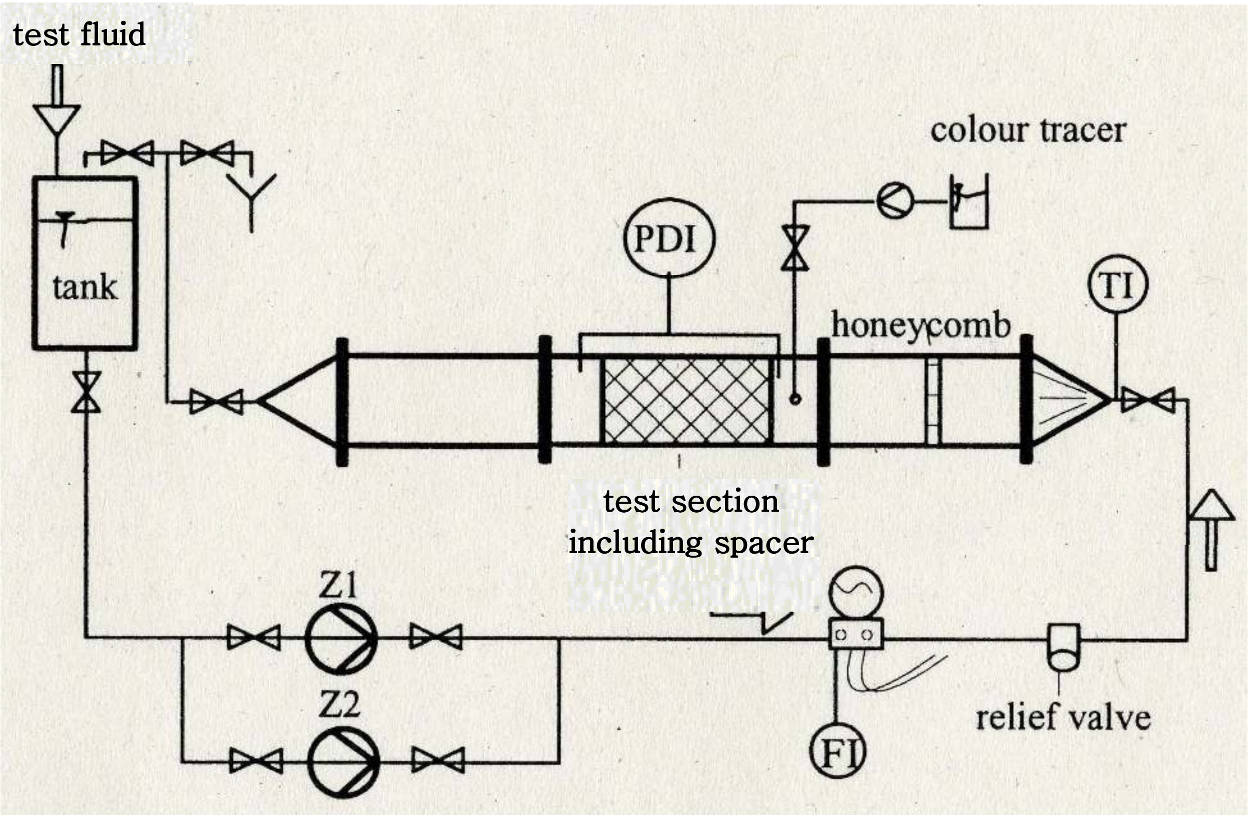

Fig. 2-2 Scheme of experimental setup

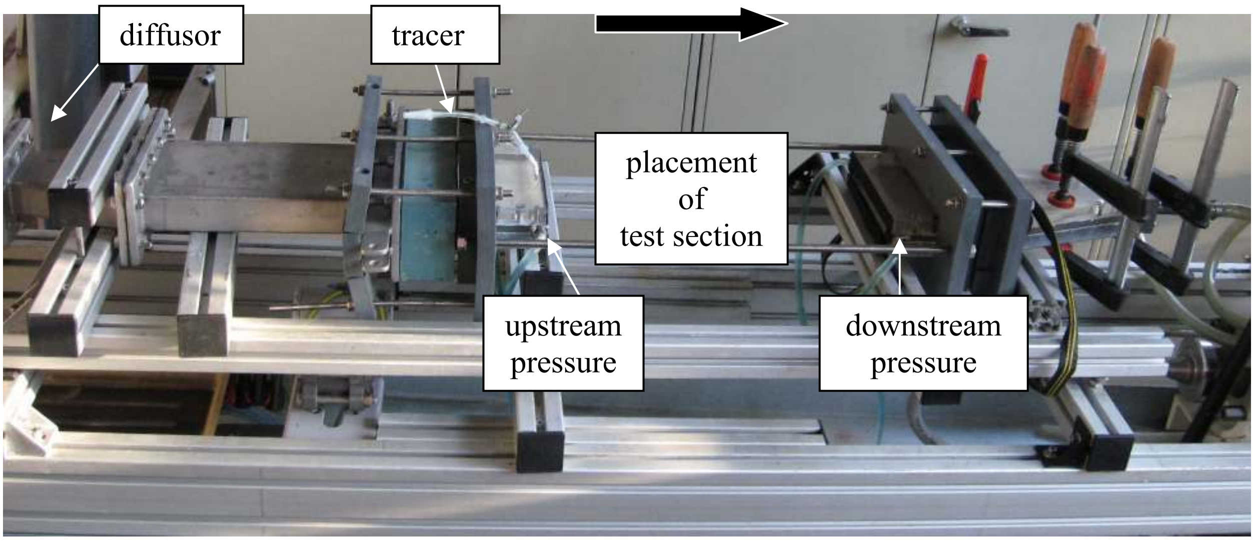

Fig. 2-3 Partial flow channel

3 New measuring techniques and numerical method

Based on a coupled chemisorption reaction between the sulfonic acid group and the -NH_2- group, an experimental method was first introduced [73][74][75] and developed[76]-[83] to quantify the mixing behavior and homogeneity of mass transfer for Newtonian fluid flows in spacer-filled channels. The sulfonic acid group is provided by one reactant, an anionic azo dye (Acidol-Blue 3 GX, BASF, Germany) and the -NH_2- group is provided by the other reactant, a Polyamide-coated membrane (POLYGRAM® polyamid-6 Macherey-Nagel, Germany). The mass transfer distribution is visualized as a color intensity distribution using Acidol-Blue in combination with polyamide-coated chromatographic membranes; thus, even complex flow phenomena at a wall can be visualized and quantified.

This method for measuring conductive mass transfer at a wall was used in Newtonian flows in previous work. Mass transfer process, for non-Newtonian fluid flows, is also critical in process engineering. Extending this measuring technique into the field of non-Newtonian flows is of great interest. Therefore Acidol-Blue and the chemisorption reaction based on polyamide membrane were used to experimentally investigate mass transfer for non-Newtonian fluids in spacer-filled channels in this study.

Viscosity is a critical variable for the determination of many physical quantities; however a non-Newtonian fluid is characterized by its viscosity being shear-rate dependent. A non-Newtonian fluid is complex in its rheological behavior and usually needs to be modified to fit a certain engineering process. How to evaluate the shear rate dependent viscosity in a complex geometry and how to assess the effect of a varied viscosity on the other physical quantities therefore becomes important. Besides, because the visualization and quantification of local mass transfer is based on the color density of Acidol-Blue at the surface of the polyamide membrane, the effect of the non-Newtonian systems on the determination of the color density of Acidol-Blue has to be investigated. The correlation equations achieved from spectrophotometer and remission photometer for Newtonian fluids can likewise not be used for the case of non-Newtonian fluids anymore.

Therefore new measuring techniques have to be developed for non-Newtonian fluids in spacer-filled channels in this study. To verify the results from these newly developed new measuring techniques, a numerical method based on a commercial computational fluid dynamics (CFD) code were conducted in parallel and simulated results were compared with the experimental results.

3.1 New measuring techniques

For the experimental study in non-Newtonian fluids, in general the following requirements should be met:

- The media should be transparent and inert, avoiding an influence on the determination of Acidol-Blue mass transfer;
- The media, especially its rheological characteristics, should have a good storage stability; with middle or low viscosity; should be non-toxic to humans and the environment; with low cost and easy to obtain;
- To be valid for different spacers, non-Newtonian behavior should be present in a relative broad range of shear rate;
- Correlations between photometric extinction and concentration of Acidol-Blue, and between photometric remission and the color density of Acidol-Blue should be able to be established, based on which mass transfer can then be determined;
- The diffusion coefficient of Acidol-Blue in non-Newtonian fluids can be determined.

Suitable polymers from a series of commercial products were screened. METHOCEL® K15M for shear thinning and Polyvinylalcohol-borax-NaCl system for shear thickening were used in this study.

3.1.1 Shear thinning behavior of METHOCEL® K15M aqueous solutions

Hydroxypropyl methylcellulose (HPMC) is a type of cellulose ether, which has the polymeric backbone of cellulose, a natural carbohydrate that contains a basic repeating structure of anhydroglucose units. Besides, propylene oxide is used in addition to methyl chloride to obtain hydroxypropyl substitution on the anhydroglucose units. This substituent group -$OCH_2CH(OH)CH_3$- contains a secondary hydroxyl group on the number two carbon and may also be considered to form a propylene glycol ether of cellulose. These products possess varying ratios of hydroxypropyl and methyl substitution, a factor which influences organic solubility and the thermal gelation temperature of aqueous solutions.

METHOCEL® K15M (Dow Chemical Company) is a brand product of HPMC, which is characterized by a medium viscosity, a desirable combination of easy dispersion in cold water and rapid hydration (viscosity build), its shear thinning behavior appears at relative low shear rate range. Some of the chemical parameters are listed in **Tab. 3-1** and **Tab. 3-2**. Rheological characteristics of METHOCEL® K15M were measured with a rotational cylinder type rheometer (RHEOLAB MC1, Z1 DIN, Rheoplus /32 v2.65, Anton Paar GmbH, Germany)

Tab. 3-1 Degree of Substitution for METHOCEL® K

Methoxyl degree of substitution	Methoxyl [%]	Hydroxypropyl molar substitution	Hydroxypropyl [%]
1.4	22	0.21	8.1

Tab. 3-2 Parameters of METHOCEL® K15M

Viscosity grade [2%, 20℃, mPa·s]	Intrinsic viscosity [dL/g]	Number average degree of polymerization	Number average molecular weight [M_n]
15,000	11.0	650	120,000

3.1.1.1 Description in the power law model

A large number of constitutive equations, which relate the shear stress or apparent viscosity in a fluid to the shear rate through the rheological properties of the fluid, have been developed to describe the properties of non-Newtonian fluids [54]. The power law model is the one most frequently used and has also proved to be quite successful in predicting the behavior of non-Newtonian fluid mechanics and heat transfer. The two forms of power law model used to describe a shear thinning non-Newtonian fluid, with the definition of apparent viscosity in $\eta_a = \frac{\tau}{\dot{\gamma}}$ as shown in **Eqn. 3-1**, are equivalent.

$$\tau = K \cdot \dot{\gamma}^n , \qquad \eta_a = K \cdot \dot{\gamma}^{n-1}$$

Eqn. 3-1

Fig. 3-1 shows the flow curve of METHOCEL® K15M at different concentrations in logarithmic form, where the slope is the flow index n and the consistency K comes from the ordinate intercept at the shear stress axis.

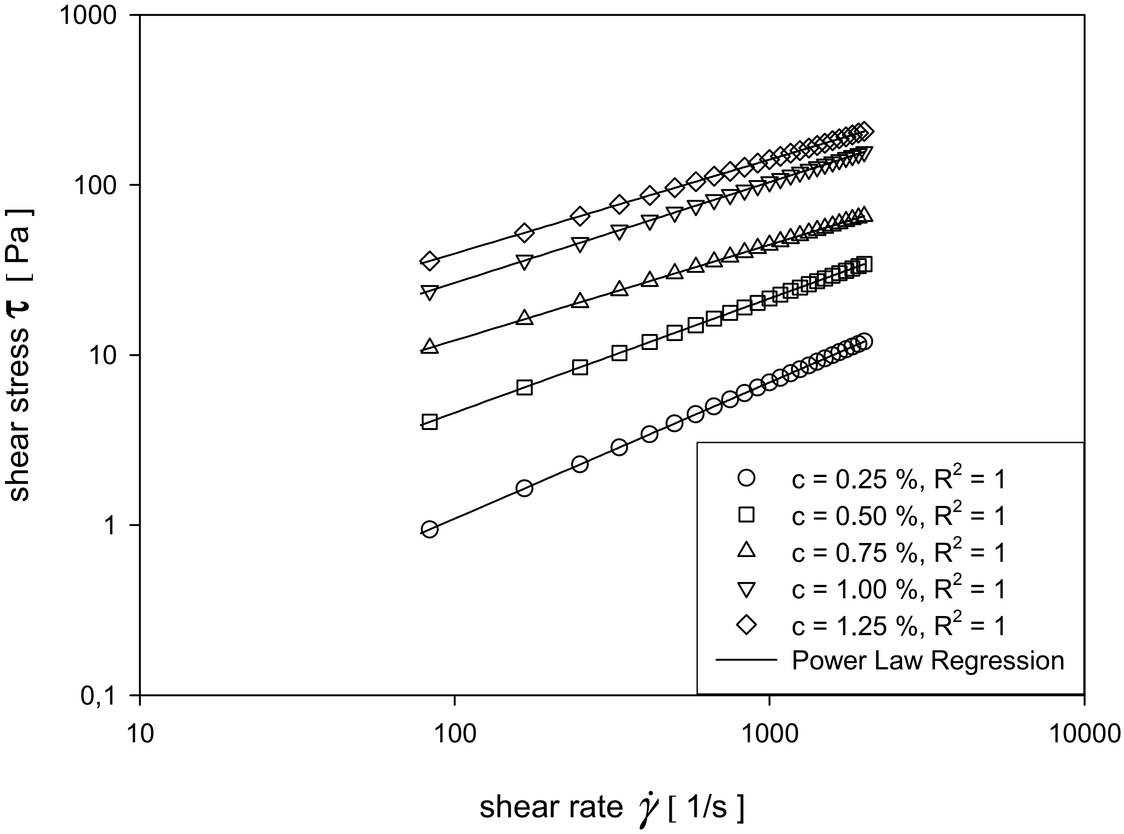

Fig. 3-1 Dependency of shear stress τ on shear rate $\dot{\gamma}$ and concentration c for METHOCEL® K15M aqueous solutions in power law (υ = 25 °C)

3.1.1.2 Description in the modified power law model

If we consider the flow of a power law model non-Newtonian fluid through a circular tube (the simplest case), the shear rate (velocity gradient for the flow profile) at the center of the tube becomes zero and thus the apparent viscosity defined by **Eqn. 3-1** is infinite. In addition, the constitutive equation of power law model cannot correctly represent the rheological property of the flow field considering the low-shear-rate Newtonian region and the following transition region. By introducing an additional parameter of zero shear viscosity, a generalized constitutive equation of modified power law model expands the represented shear rate to these two regions.

The description of shear thinning non-Newtonian fluids in the modified power law model [121] is shown in **Eqn. 3-2**.

$$\eta_M = \frac{\eta_0}{1 + (\frac{\eta_0}{K}) \cdot (\dot{\gamma})^{1-n}}$$

Eqn. 3-2

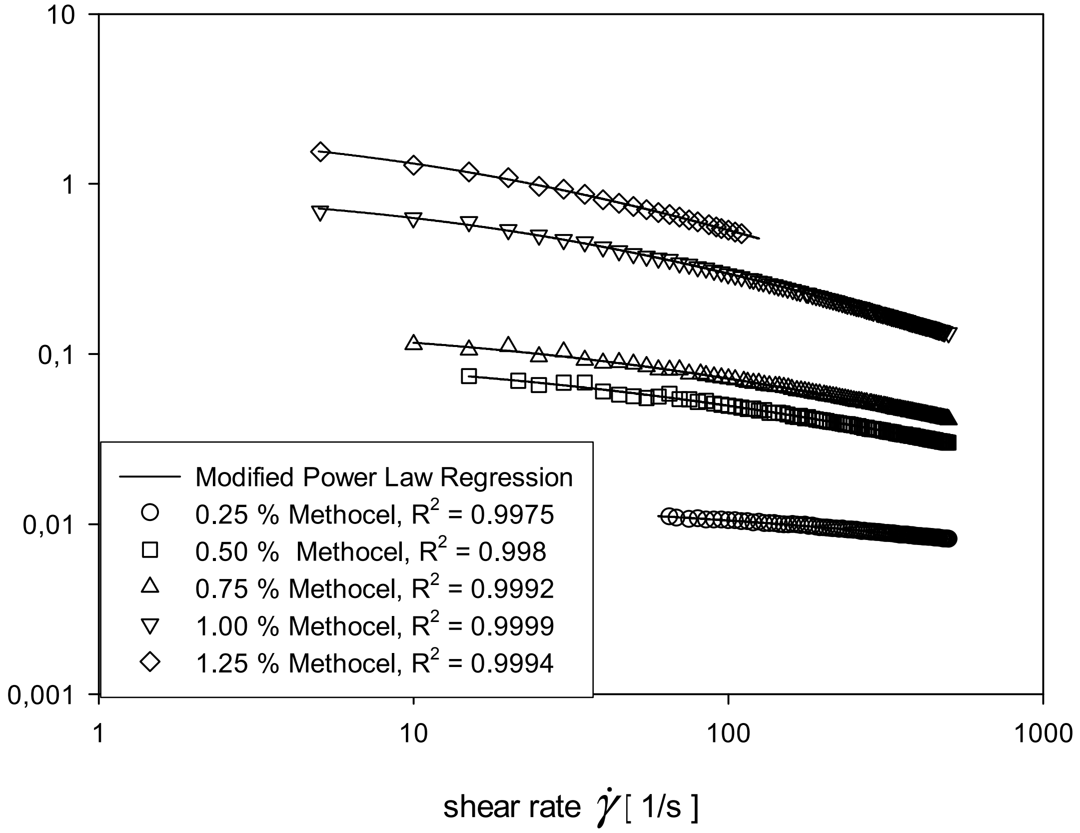

Fig. 3-2 Dependency of the measured apparent viscosity η_M on shear rate $\dot{\gamma}$ and concentration c for METHOCEL® K15M aqueous solutions in modified power law (υ = 25 °C)

An important advantage of modified power law model is that it can correctly and precise represent the rheological property over the whole shear rate range in the flow field. **Fig. 3-2** shows that the apparent viscosity is both shear rate and concentration dependent at a constant measuring temperature.

The three rheological properties of METHOCEL® K15M solutions, described the modified power law model, for different concentrations are listed in **Tab. 3-3**.

Tab. 3-3 Modified power law rheological parameters for METHOCEL® K15M in different concentrations

C [wt%]	η_0 [Pa·s]	n [-]	K [$kg/(m \cdot s^{2-n})$]
0	-	1	0.001
0.025	0.0013	0.91	0.02
0.075	0.0023	0.78	0.06
0.125	0.0041	0.69	0.11
0.25	0.015	0.57	0.27
0.50	0.11	0.51	0.87
0.75	0.16	0.47	1.52
1.00	0.95	0.36	8.10
1.25	2.26	0.35	14.29

3.1.1.3 Dependency of the rheological properties on temperature

Another fact to be considered related to hydrodynamic and heat transfer problems in rheological flows is the dependency of rheological properties on temperature. Some author report that for many power law fluids the fluid consistency has a significant variation with temperature, while the flow index is relatively independent on temperature [55][56]. Taking a certain METHOCEL® K15M solution at 0.75% concentration as an example, the flow curve measured at different temperatures shows that the rheological parameters of both n and K are temperature dependent and the fluid consistency K is, especially, a function of temperature, which agree to the results from literature.

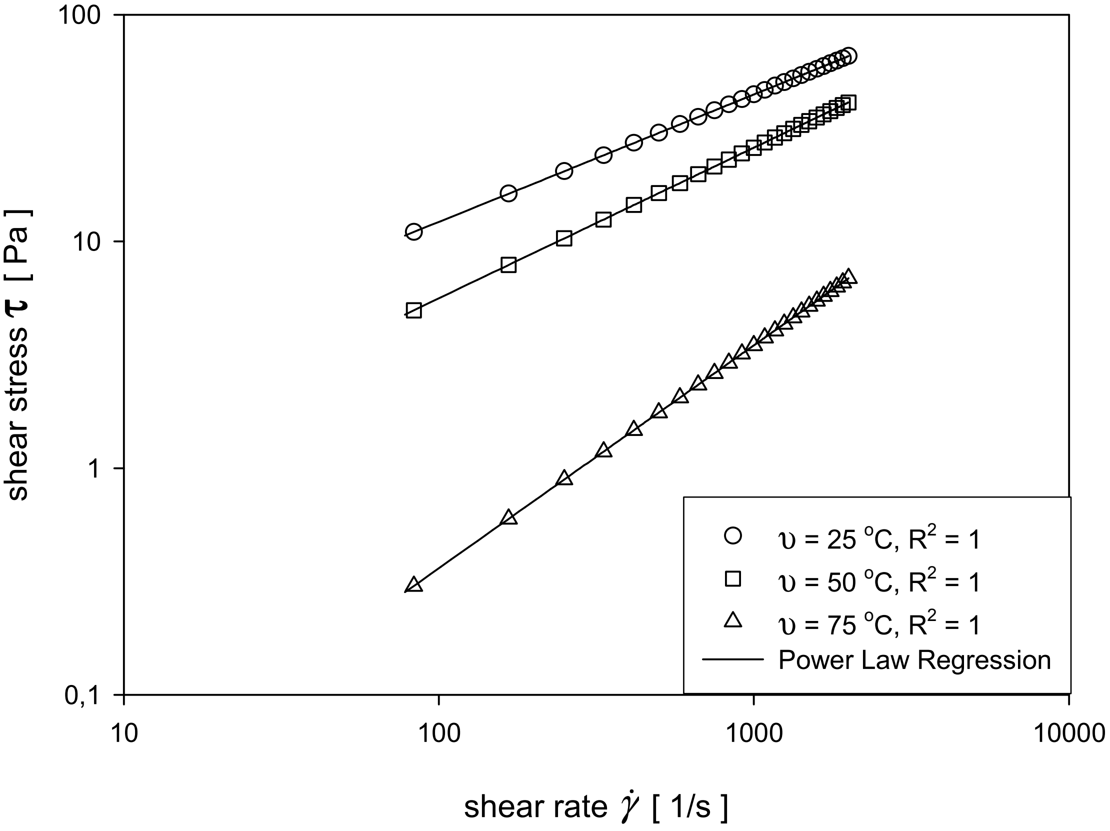

Fig. 3-3 Dependency of shear stress τ on shear rate $\dot{\gamma}$ and temperature T for METHOCEL® K15M aqueous solutions

3.1.1.4 Dependency of the apparent viscosity on temperature and concentration

A common function for concentration and temperature for the apparent viscosity of METHOCEL® K15M is described in **Fig. 3-4**, where the apparent viscosity is determined at shear rate $\dot{\gamma}$ = 500 s^{-1}. The variation in apparent viscosity due to temperature and concentration agrees well with the Arrhenius model:

$$\eta_a = A \cdot \exp\left(\frac{\Delta E}{R \cdot T}\right)$$

Eqn. 3-3

where A is the frequency factor, exp is the exponential function, ΔE is the activation energy, R is the gas constant and T is the absolute temperature. The slopes and intercepts of the regressions of the logarithm of apparent viscosity ($\dot{\gamma}$ = 500 s^{-1}) vs. the inverse of absolute temperature were used to calculate the frequency factors and activation energies at each of the concentrations examined. The examined results for METHOCEL® K15M in this study are then given by the Arrhenius model with A = 0.0001c$^{2.4}$ and ΔE/R = 2221.

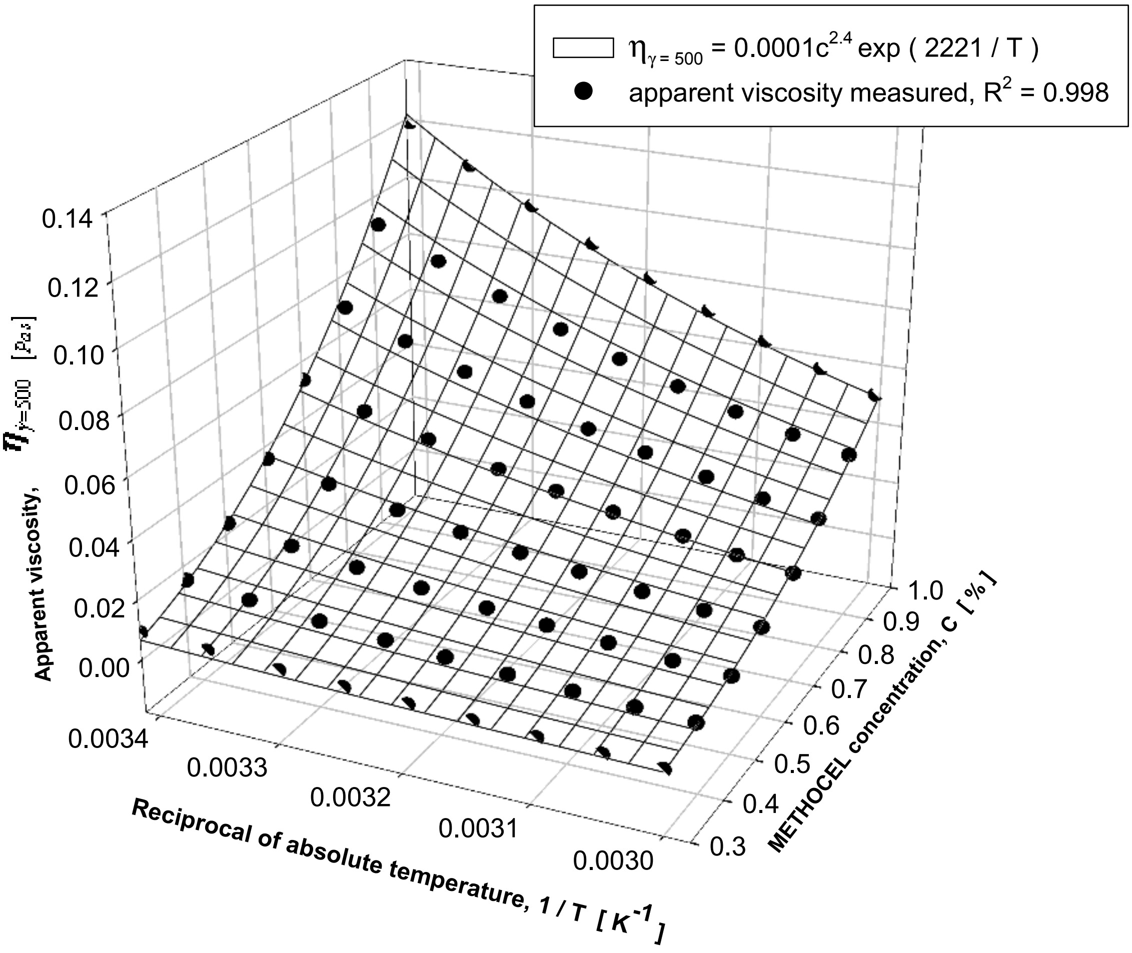

Fig. 3-4 Dependency of apparent viscosity $\eta_{\dot\gamma=500}$ on concentration c and temperature T for METHOCEL® K15M aqueous solutions ($\dot\gamma$ = 500 s^{-1})

3.1.1.5 Dependency of the zero shear viscosity on concentration

Many attemps have been made to determine a relationship between viscosity and solution concentration. Results demonstrated by Pickard [57], Delporte [58], and Prater [59] show that the increase in concentration increases viscosity not linearly, but sharply. The graph of **Fig. 3-5** plotted on an 8th root scale show that the 8th root of the apparent viscosity is a roughly linear function of the concentration, which fits the Philippoff plot [60]. A similar linear function of the 8th root of viscosity on concentration was also found by Aulton et al. in HPMC E5 solution [61].

The equation proposed above, relating the viscosity of METHOCEL® K15M to its concentration, is helpful to estimate the resulting variable in hydrodynamic and thermal problems at zero shear condition and to predict the initial design. Furthermore, a comparison among shear thinning, shear thickening and Newtonian media was carried out based on the fact that they have the same zero shear viscosity.

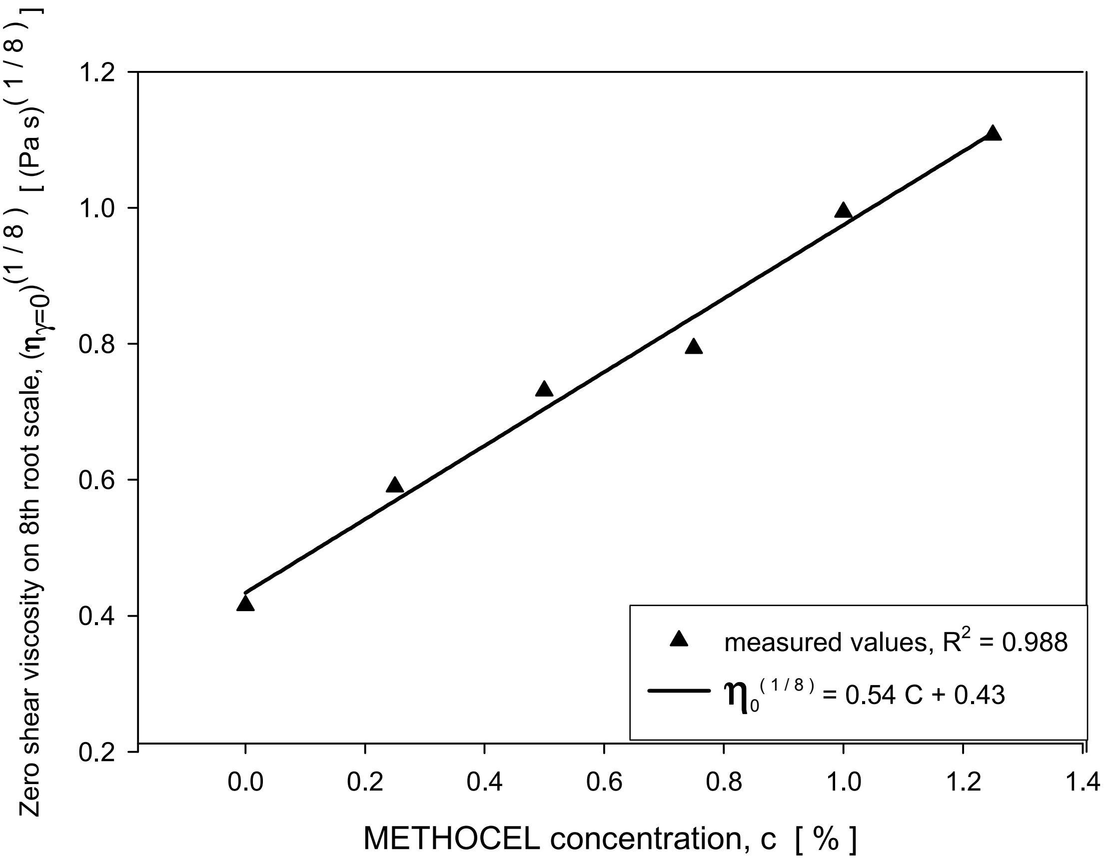

Fig. 3-5 Dependency of zero shear viscosity $\eta_{\dot{\gamma}=0}$ on concentration c for METHOCEL® K15M aqueous solutions ($\upsilon = 25\ ^{o}C$)

3.1.2 Shear thickening behavior of Polyvinylalcohol-borax aqueous solutions

Polyvinylalcohol (PVA) is a synthetic polymer with a large number of hydroxyl groups that can react with many kinds of functional groups to form thermal unstable macromolecules, which exhibit various rheological characteristics. The properties of PVA depend on the molecular weight, the degree of polymerization as well on the degree of hydrolysis [62]. The chemical properties of the PVA samples are listed in **Tab. 3-4**.

Tab. 3-4 Chemical properties of PVA

	d.p.[1]	M_w	d.h.[2] [%]	η [3] [mPa·s]
PVA 8-88	1,400	67,000	86.7-88.7	7-9
PVA 3-96	-	-	96.8-97.6	3.1-3.4
PVA 4-88	630	31,000	86.7-88.7	3-5
PVA 6-98	1,000	47,000	98-98.8	5-7
PVA 18-88	2,700	130,000	86.7-88.7	16-20
PVA 40-88	4,200	205,000	86.7-88.7	38-42
PVA 4-98	600	27,000	98-98.8	4-5
PVA 28-98	3,300	145,000	99-99.8	26-30
PVA 10-98	1,400	61,000	98-98.8	9-11

[1]: degree of polymerization

[2]: degree of hydrolysis

[3]: viscosity measured at 4 % and at 20℃

The following table **Tab. 3-5** shows the affect of the degree of polymerization and degree of hydrolysis on PVA's basic characteristics. The initial choice could be one of a partially hydrolyzed and low degree of polymerization sample, because of its good water solubility, low water resistance and low viscosity.

Tab. 3-5 Effect of chemical properties on the characteristics of PVA aqueous solution

characteristic	degree of polymerization		degree of hydrolysis	
	low	high	partially hydrolyzed	fully hydrolyzed
viscosity of solution	↓↓	↑↑	↓	↑
viscosity at low temperature	↑	↓	↑↑	↓↓
membrane strength	↓↓	↑↑	↓	↑
water solubility	↑	↓	↑↑	↓↓
water resistance	↓	↑	↓↓	↑↑
emulsifying ability	↓	↑	↑↑	↓↓

The higher the number of arrows shown, the greater the effect.

Rheological characteristics of PVAs with different molecular weights, degree of polymerization and degree of hydrolysis were investigated. Based on these basic results, rheological study of the complex of PVA and borax was further carried out, (in Appendix), in order to find a suitable shear thickening system for this study.

Borax is the common name of sodium borate ($Na_2B_4O_7 \cdot 10H_2O$). Due to the formation of a complex between hydroxyl groups and borate anions, which plays a role as a temporary crosslinking among PVA chains [63], a small of amount of borax produces a remarkable increase in viscosity of PVA aqueous solutions.

$$Na_2B_4O_7 + 7 \cdot H_2O \rightarrow 2 \cdot B(OH)_3 + 2 \cdot B(OH)_4^- + 2 \cdot Na^+$$

Eqn. 3-4

Shear thickening (dilatant) behavior demonstrates the formation of complexes between hydroxyl groups of PVA and borate anions of borax [64][65], which plays a role as a temporary crosslinking among PVA chains [63].

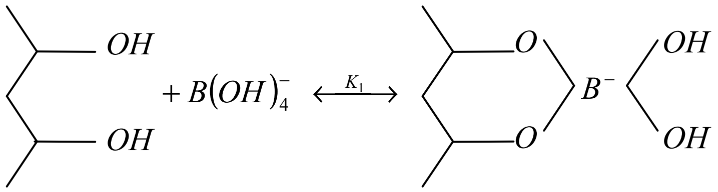

(reaction 1)

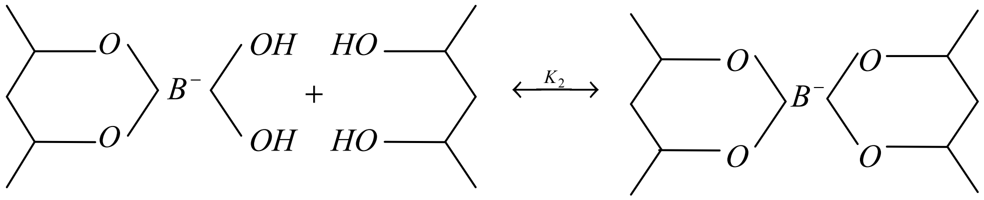

(reaction 2)

Once a borate ion is attached to a PVA chain, monodiol (1:1) complexation (reaction 1) occurs firstly, resulting in an expansion of the individual polymer chains. Furthermore, two types of didiol (1:2) complex formation, characterized with intra- and inter-molecular crosslinkings, result in different degrees of viscosity increasing, such as thickening and gelation, respectively [66].

For a dilute PVA solution, where no gelation develops, even in the presence of excess of borate, only thickening is observed and then it seems reasonable to assume that complex formation occurs only intramolecularly. The PVA/borax system is ruled by electrostatic repulsion and intramolecular crosslinking. A theoretical Flory-type model was presented to describe that the polymer chain size was the consequence of a balance among the elastic energy, the excluded volume effect, and the electrostatic potential [67]. For semi-dilute PVA solutions, both intra- and inter-molecular crosslinkings through reaction 2 may happen, and a gelation of the PVA/borax complex is expected, which would not be appropriate to the interest of this study.

The intrachain crosslinks give rise to a contractive effect and suppress the chain expansion by mutual charge repulsion. Polyelectrolyte behavior can be observed in the dilute PVA/borax systems in the presence of NaCl as an added salt [68][69]. Then a peculiar rheological behavior observed for the PVA/borax/NaCl system can be well explained in terms of a favorable balance between expansion due to charges and contraction due to intrachain crosslinks, which are simultaneously incorporated in the PVA chain upon complexation with tetrahedral borate anions [70]. The negative charges of tetrahedral borate ions can be screened due to the addition of NaCl, a further complexation or transformation from monodiol to didiol can then be induced due to the polymer chain contraction. Potentiometric study for the PVA/borate/NaCl systems showed that the formation constant (k_2) of the didiol type complexes increases with the increase in concentration of NaCl and an increase in apparent viscosity was determined in this study (**Fig. 3-6** and **Fig. 3-7**).

During shear flow, a transition from intramolecular association to intermolecular association can occur, which is one of the explanations in terms of shear thickening mechanisms [71][72]. A shear thickening system can be therefore achieved from the combinations of PVA/borax/NaCl aqueous solutions. Where PVA is present in diluted level, appropriate concentrations surely do not form intermolecular complexes in PVA/borax solutions. NaCl is added to screen the mutual repulsion caused by borate anions. The viscosity of PVA/borax/NaCl solutions is adjusted by the concentration of NaCl, and shear thickening (dilatancy) behavior can be found in different shear rate ranges of shear flow. It is therefore possible, to find a suitable combination of PVA/borax/NaCl system fitting to the flow in spacer filled channel for an appropriate Reynolds number.

The PVA/borax/NaCl solutions were kept with their maximum concentration low enough to prevent intermolecular complexation and were stored for at least one day to confirm that no gelification and no precipitation occurs before experiments.

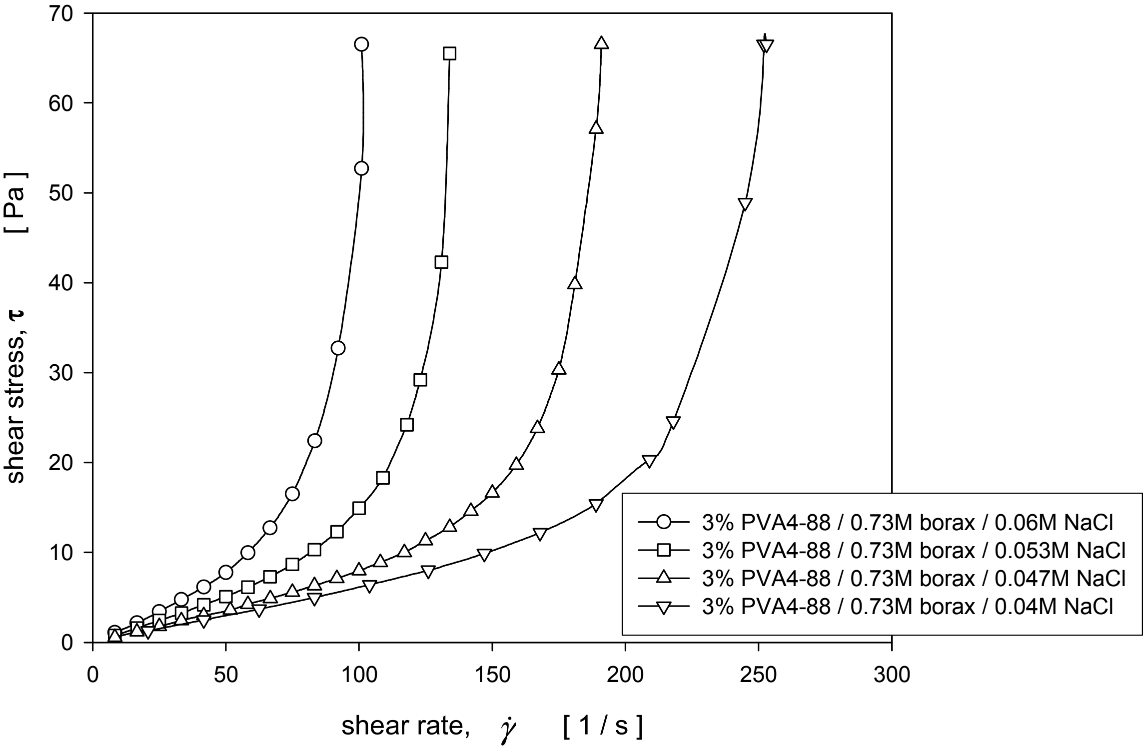

Fig. 3-6 Dependency of shear stress τ on shear rate $\dot{\gamma}$ and on NaCl concentration for PVA/borax/NaCl aqueous solutions (υ = 25 ^{o}C)

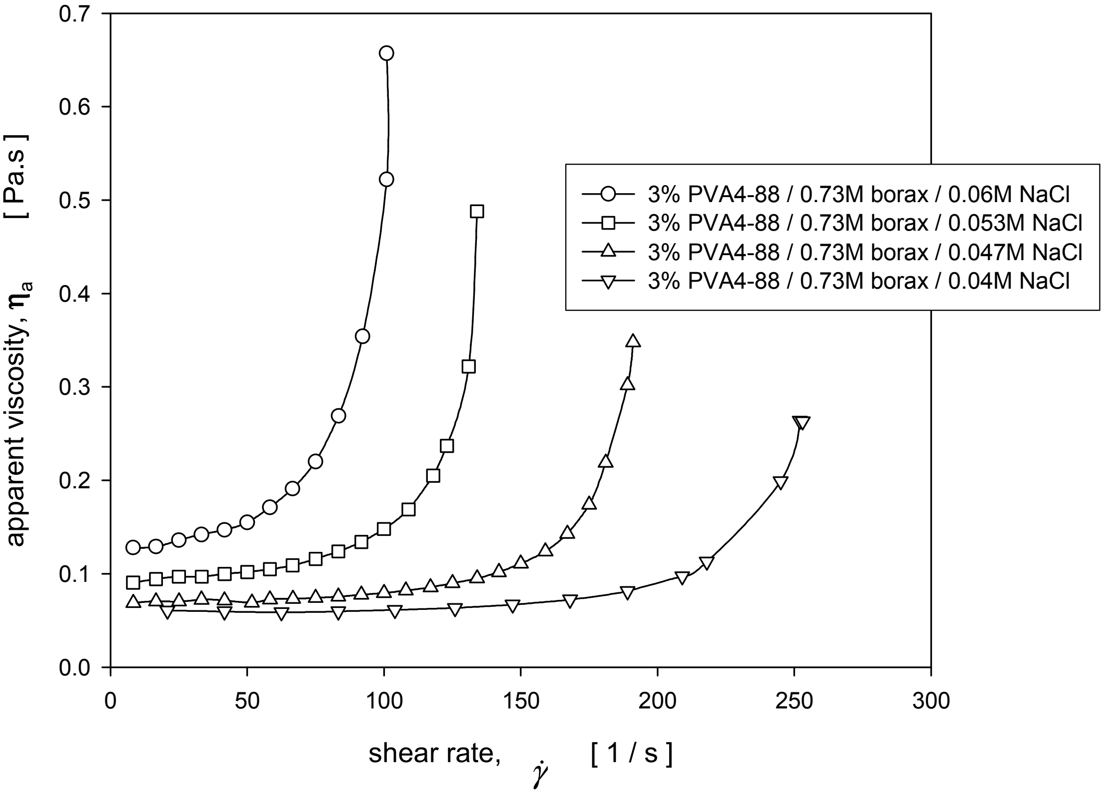

Fig. 3-7 Dependency of apparent viscosity η_a on shear rate $\dot{\gamma}$ and on NaCl concentration for PVA/borax/NaCl aqueous solutions (υ = 25 ^{o}C)

Rheological characteristics of the PVA/borax/NaCl system with 3% PVA4-88, 0.73M borax and 0.04~0.06M NaCl concentration combinations are shown in **Fig. 3-6** and **Fig. 3-7**. A strong shear thickening behavior was observed in these solutions and the behavior is NaCl concentration dependent, while the concentrations of PVA and borax were kept constant. The higher the concentration of NaCl, the higher the viscosity, the stronger shear thickening behavior and earlier shear thickening occurring are demonstrated in these results.

An example plotted in **Fig. 3-8** shows that the apparent viscosity of the three media with roughly the same zero shear viscosity changes as function of shear rate. 82% Glycerin has a Newtonian behavior, 0.5% METHOCEL® K15M has a shear thinning behavior and a PVA/borax/NaCl system presents a significant shear thickening behavior.

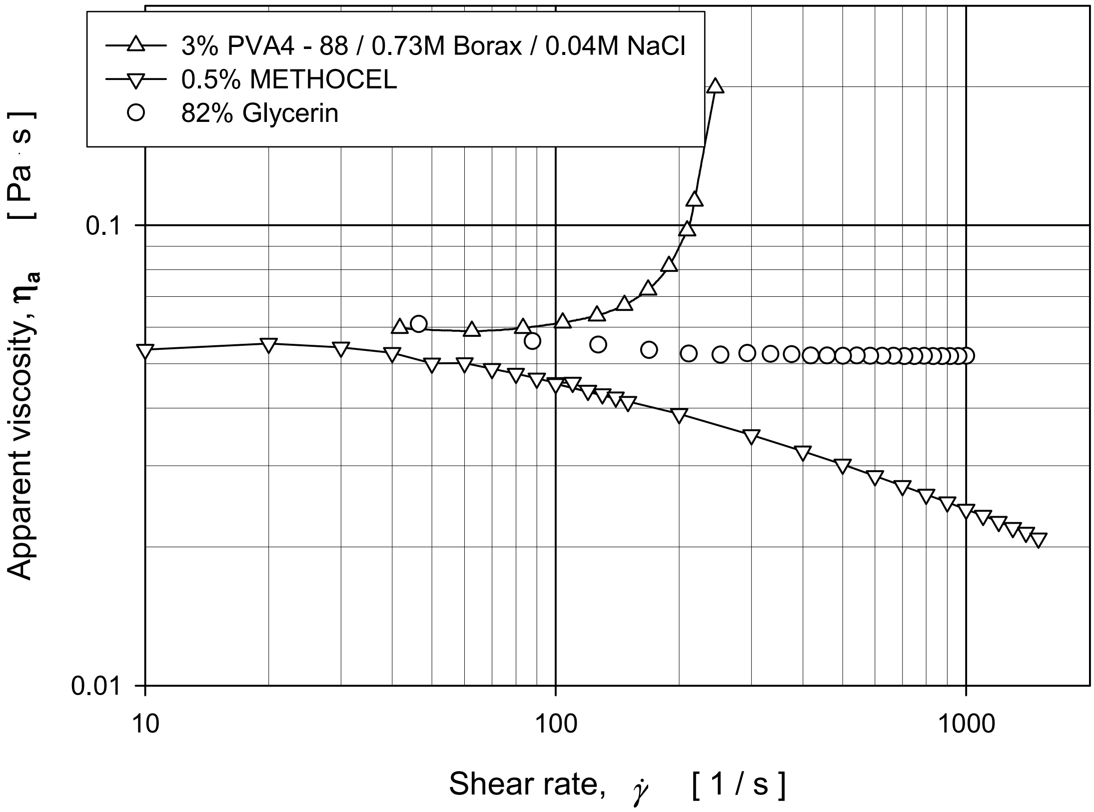

Fig. 3-8 Dependency of apparent viscosity η_a on shear rate $\dot{\gamma}$ for Newtonian, shear thinning and dilatant fluids ($\upsilon = 25\ ^{\circ}C$)

3.1.3 Acidol-Blue and the chemisorption reaction on polyamide membranes

Based on the chemisorption reaction between Acidol-Blue and Polyamide, an experimental method was first introduced and used to quantify the mixing behavior and homogeneity of mass transfer for Newtonian fluid flows in spacer-filled channels. This measurement technique was further developed in this study to investigate the flow phenomena and to determine the local mass transfer for non-Newtonian fluids in spacer-filled channels.

The physiochemical principle is based on mass transfer of a tracer (Acidol-Blue) and its fixation by absorption and subsequent chemical reaction on a polyamide-coated membrane sheet at the solid channel wall. The membrane sheets are pre-coated with a ready-to-use layer of polyamide 6, i. e. perlon (= e-aminopolycaprolactam). Due to the amide groups of the polymer matrix this phase can form hydrogen bonds with numerous classes of compounds (**Fig. 3-9**).

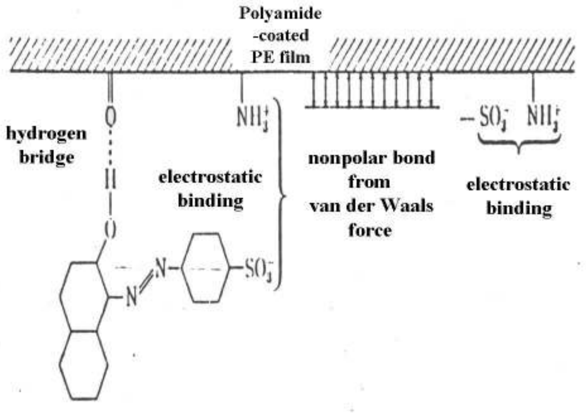

Fig. 3-9 Scheme of chemisorption between Acidol-Blue and PA [81]

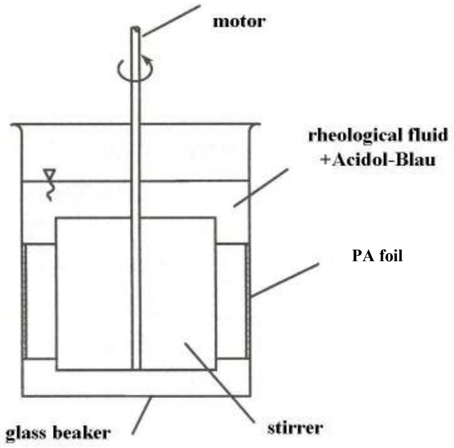

Fig. 3-10 Acidol-Blue transfers from bulk solution to the surface of PA foil in a beaker [81]

The resulting color distribution corresponds directly to the local transferred mass and visualizes the flow phenomena in the channel filled with spacers. The quantification of the local mass transfer is obtained by photometric measurements, which is described in detail in [84].

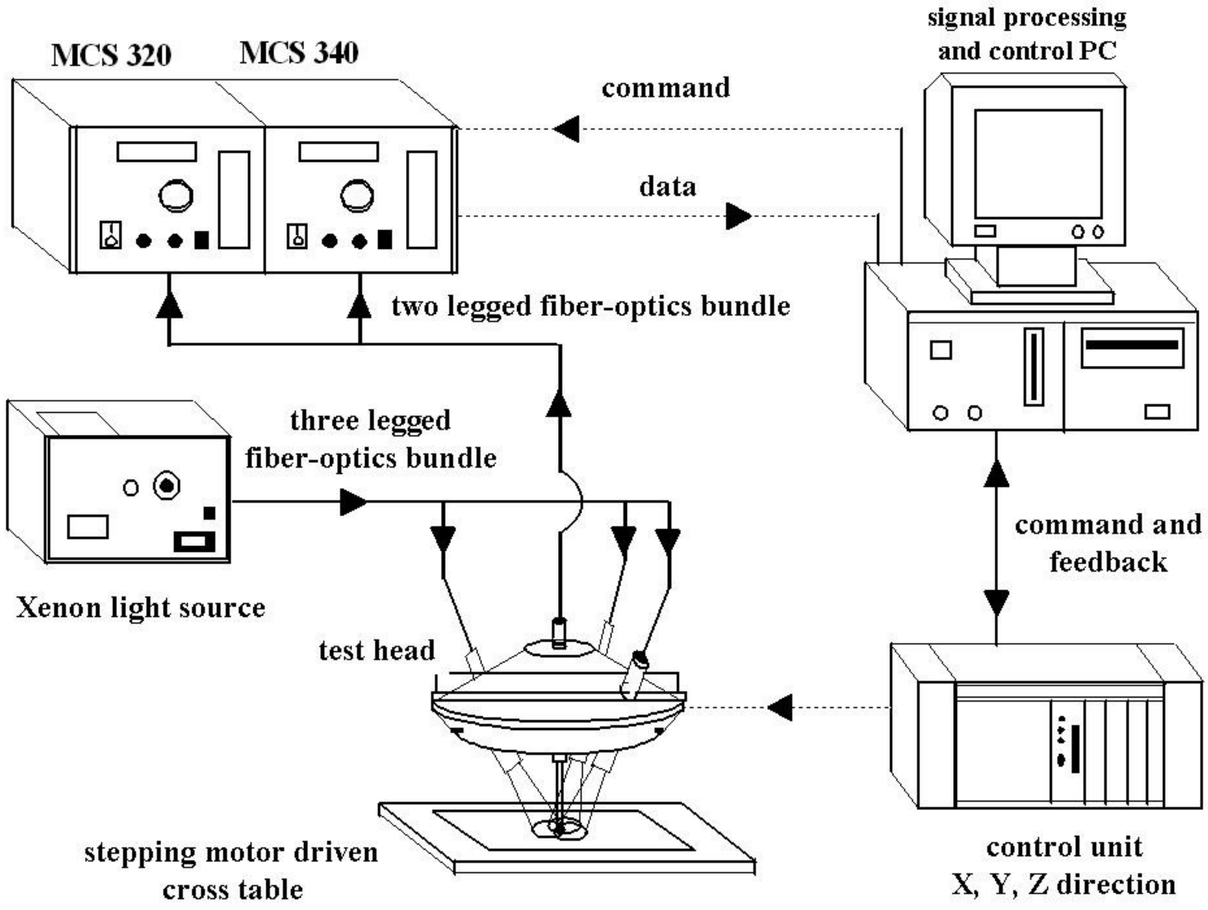

Fig. 3-11 Remission photometer [77]

3.1.4 Flow visualization

By adding a color tracer in the middle of the entrance of the test section, the flow phenomena and the mixing behavior in the fluid channel filled with spacer can be observed. The tracer reacts chemisorptively and is fixed on a polyamide precoated membrane. A mass transfer measuring method was used to analyze and determine the intensity of color. The resulting two-dimensional distribution of the tracer over the membrane corresponds directly to the local transferred mass based on the local flow phenomena allowing a quantification of the homogeneity of mass transfer in the spacer-filled channel. The results for Newtonian fluids in high Reynolds number flows showed three primary flow types (**Fig. 3-12**) characterizing the spacer-filled channels or corrugated wall channels, which strongly depends on the geometries and Reynolds numbers [77].

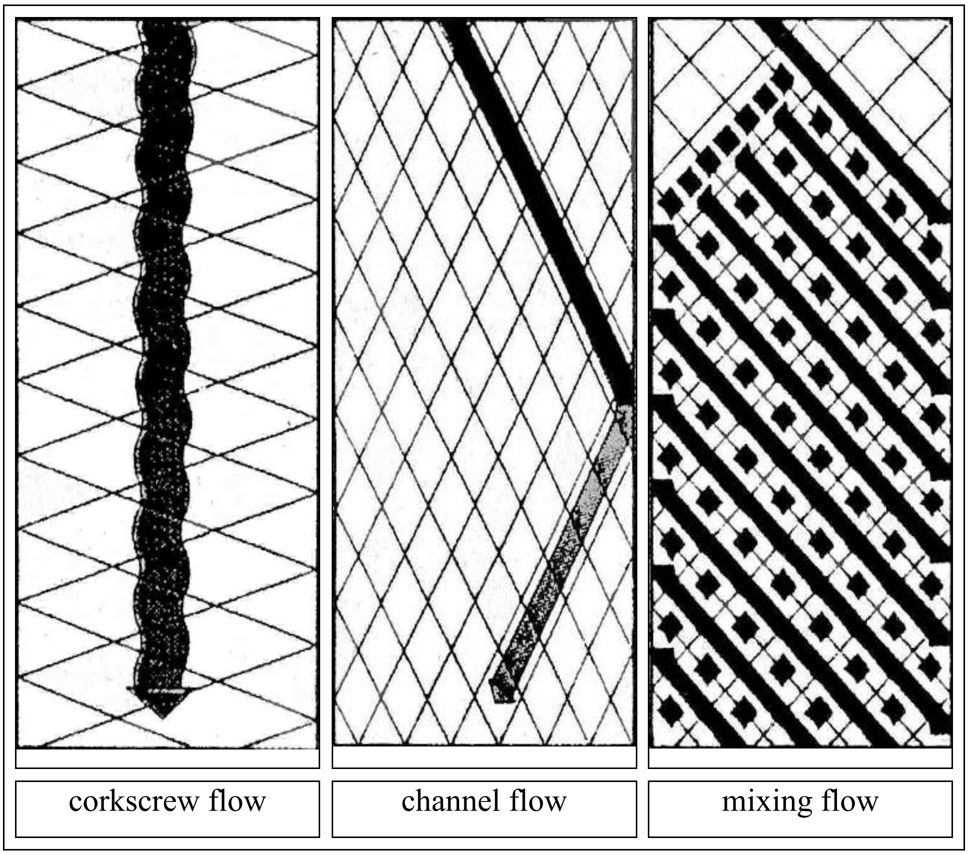

Fig. 3-12 Schematic flow types in spacer-filled channels [109]

For the corkscrew flow, the flow passes through the spacer like a corkscrew. The fluid follows a spiral stream path limited by two rows of neighboring intersection points of the grid rods. For the channel flow, the flow follows the channels formed by two neighboring grid rods. At the side walls, the flow is reflected and then follows then the channels formed by the grid rods at the opposite wall of the duct. The flow moves in zigzag-form through the spacer. These two basic flow types exist only at special combinations of the geometric parameters λ/a and φ. Through an appropriate choice of the dimensionless wavelength λ/a and the inclination angle φ the "channel flow" and "corkscrew flow" can be overlapped, leading to a so-called "mixing flow". Here a perfect mixing behavior can be achieved in an extremely short length of the spacer. The remaining inhomogeneity of the mass transfer is relatively small, so that the surface of the membrane is used very homogeneously. All three flow types are analyzed at relatively high Reynolds numbers. The experiments by Zimmerer [77] show that the "mixing flow" type exists only at higher Reynolds numbers of turbulent flows.

In this study, focusing on the fully developed flow in a periodic characteristic diamond, three-dimensional flow visualization based on CFX was investigated for non-Newtonian fluids, which will be helpful to optimize the spacer configuration.

3.1.5 Pressure drop measurement

At the inlet and outlet of the test section pressure transducers are installed to determine the pressure drop over the spacer. The pressure drop corresponds to the resistance of the spacer and is expressed by a dimensionless friction factor,

$$f = \frac{\Delta p}{\frac{1}{2} \cdot \rho \cdot \overline{w}^2} \cdot \frac{d_h}{4 \cdot L}$$

Eqn. 3-5

which is named fanning friction factor. Another common definition is the Darcy friction factor ζ ,

$$\varsigma = 4 \cdot f = \frac{\Delta p}{\frac{1}{2} \cdot \rho \cdot \overline{w}^2} \cdot \frac{d_h}{L}$$

Eqn. 3-6

3.1.6 Mass transfer determination

3.1.6.1 Correlation between photometric extinction and concentration of Acidol-Blue in METHOCEL® K15M aqueous solutions

For the determination of the local mass transfer coefficient β, it is necessary to determine the concentration of Acidol-Blue in the METHOCEL® K15M aqueous solutions as precisely as possible. Through measurement of the absorption, with aqueous solutions with the same concentration of METHOCEL® K15M used as references respectively, a linear correlation between the Acidol-Blue concentration and the extinction in the photometric measurement (HEWLETT PACKARD 8453, 845X UV-Visible system) was found, **Fig. 3-13**, corresponding to Lambert-Beer law.

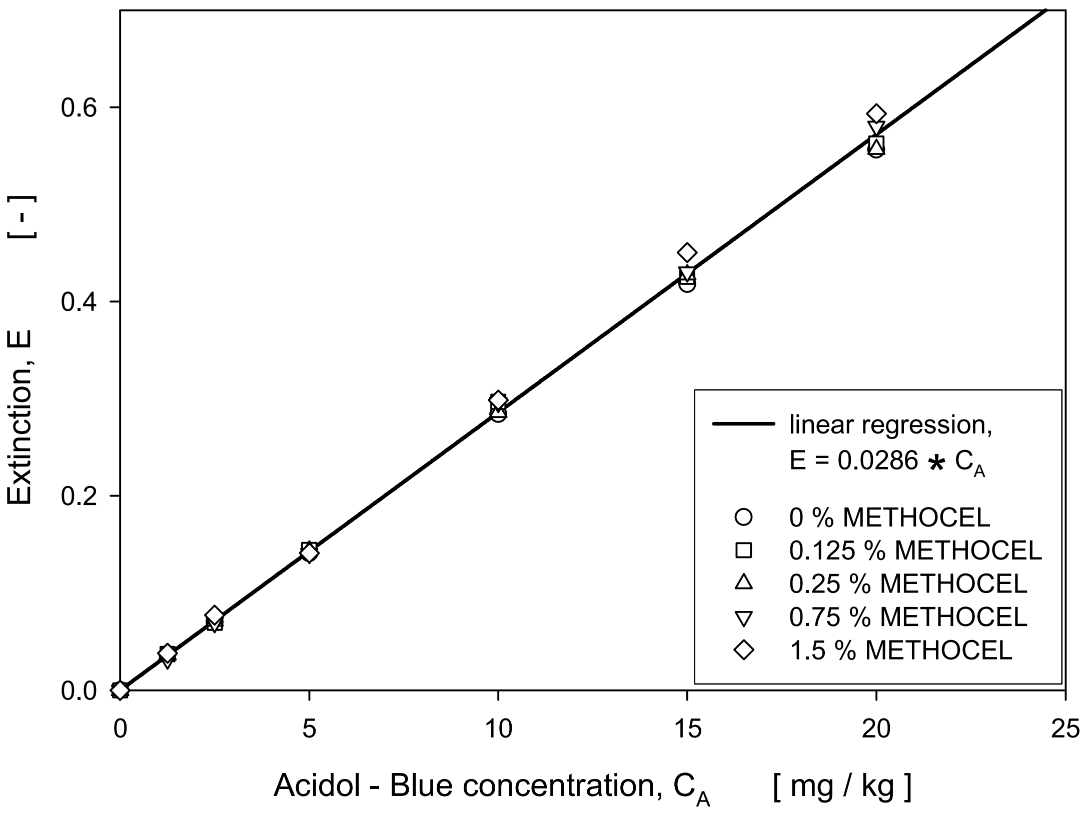

Fig. 3-13 Correlation between extinction E and dissolved concentration c of Acidol-Blue in non-Newtonian case, $\lambda = 645$ nm, $\upsilon = 25\ ^{o}C$

3.1.6.2 Correlation between photometric remission and mass density of Acidol-Blue transferred to the surface of the membranes

A piece of PA membrane was glued onto the inner surface of a glass (see **Fig. 3-10**). METHOCEL®-Acidol-Blue solution was added into the beaker and the membrane was completely merged in this Acidol-Blue-concentration-determined solution. Under a mild stirring (80 rpm) with an appropriate anchor-type stirrer, Acidol-Blue is transferred from the bulk solution to the wall and furthermore homogeneously fixed onto the surface of the membrane through the chemisorption reaction. The Acidol-Blue concentration in solution at the end point of the trial run was determined. The reduced concentration in bulk solution corresponds to the transferred mass on the surface of PA membrane.

The mass transferred per surface area unit, -visible as color intensity and measured as transferred mass density b [mg/m^2] - has to be determined. The evaluation of the measurements was carried out with remission photometric measurements, image processing with a scanner or with a CCD-camera. In this study, taking a blank PA membrane as the reference, the quantification of the local mass transfer was obtained by photometric measurements with a remission photometer (Zeiss MCS 320 (λ = 200-610 nm), 340 (λ = 600-1010 nm), Step MCS), which is described in detail in [84].

The more mass of Acidol-Blue is transferred to the surface of PA pre-coated membrane, the darker the color caused by the chemisorption is observed. The correlation between transferred mass density b and the optically measured value (Remission R, resp. remission value of the scanner or the CCD-camera) was determined by a calibration curve, analog to Kühnel [84],

Fig. 3-14 shows that a quantitative correlation between mass transfer and remission made by an inverse 5th-order polynomial regression was achieved as

$$b = -28.5475 + 35.327R^{-1} - 8.3346R^{-2} + 1.70028R^{-3} - 0.150879R^{-4} + 0.005699R^{-5}$$

Eqn. 3-7

where R stands for the remission value determined by the remission photometer at 645 nm and b is the color density of Acidol-Blue stained on the surface of PA membrane in mg/m^2. The local mass transfer can then be quantitatively determined.

With these two curves, the concentration of Acidol-Blue in the METHOCEL® aqueous solutions was determined by measuring the extinction value and the transferred mass of Acidol-Blue from bulk solutions to the surface of membranes is determined by the remission value. Both parameters, concentration c and color density b, were used to calculate local mass transfer coefficients.

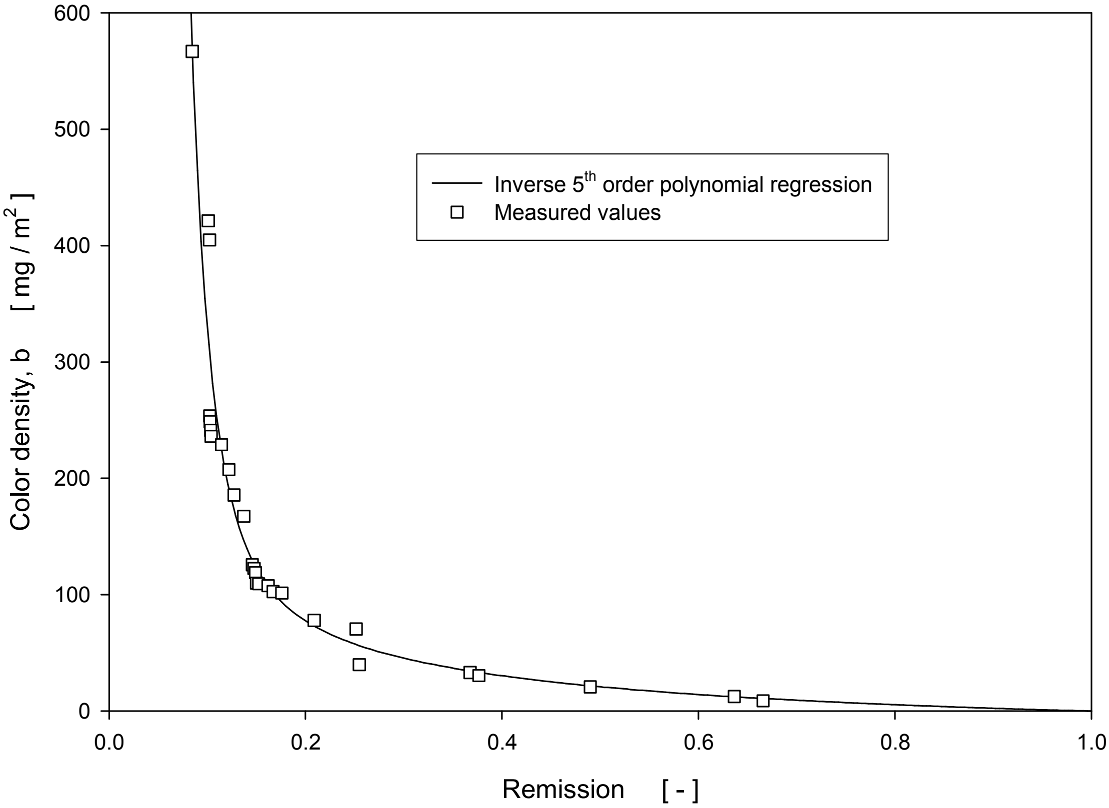

Fig. 3-14 Correlation between photometric remission and color density on the surface of the polyamide membrane for Acidol-Blue in the non-Newtonian case, λ = 645 nm

3.1.7 Diffusion coefficient determination

3.1.7.1 Diffusion coefficient determined by PFG-NMR

A molecule in solution undergoing constant random motion can be characterized by a diffusion coefficient (*D*), which is an important parameter for modeling hydrodynamics and is a measurement of the net displacement of molecules caused by thermal energy (Brownian motion). In an isotropic solution, the self-diffusion coefficient is related to the inverse of the friction opposing the motion of the molecular. The representation of this behavior is:

$$D = \frac{K_B \cdot T}{f_D}$$

Eqn. 3-8

where K_B is the Boltzmann constant ([J/K]), T is the temperature in Kelvin, and f_D is the frictional coefficient ([kg/s]) of the particle undergoing motion.

The friction coefficient f_D is at infinite dilution and is given by:

$$f_D = 6 \cdot \pi \cdot \eta_0 \cdot r_h$$

Eqn. 3-9

where η_0 is the zero shear viscosity and r_h is the hydrodynamic radius of a spherical particle (time-averaged hydrodynamic radius for a macromolecule). A combination of **Eqn. 3-8** and **Eqn. 3-9** yields the well-known Stokes-Einstein equation [86]:

$$D = \frac{K_B \cdot T}{6 \cdot \pi \cdot \eta_0 \cdot r_h}$$

Eqn. 3-10

The probability of finding a molecule originally at point X_0 at position X_i some time later can be measured by the root-mean-squared (RMS) displacement, $\left\langle X^2 \right\rangle$

$$\left\langle X^2 \right\rangle = \left\langle (X_i - X_0)^2 \right\rangle = 2 \cdot D \cdot t$$

Eqn. 3-11

which is known as Einstein's relation (in one dimension). For diffusion in more than one dimension, Einstein's relation is given by

$$\left\langle X^2 \right\rangle = 2 \cdot n \cdot D \cdot t$$

Eqn. 3-12

where n is the number of degrees of freedom (number of dimensions) in which the spin can move. For isotropic, nonrestricted diffusion, a plot of the root-mean-squared displacement $\left\langle X^2 \right\rangle$ versus t is linear, while for anisotropic or restricted diffusion, the plot would deviate from its linear behavior.

Pulsed Field Gradient-Nuclear Magnetic Resonance (PFG-NMR) is a powerful tool for studying self diffusion [87]. This method determines simultaneously the diffusion coefficients of several compounds in one single experiment and one sample can be used for several measurements since the method is noninvasive.

The measured quantity in PFG-NMR, the spin echo attenuation (the ratio of the amplitude of the spin echo in the presence of an applied gradient field to the amplitude of the spin echo in the absence of a gradient), is given by the well known Stejskal-Tanner Equation [88]:

$$\ln\left[{S(t)}/{S(0)}\right] = -\gamma^2 \cdot \delta^2 \cdot g^2 \cdot \left(\Delta - \frac{1}{3} \cdot \delta\right) \cdot D$$

Eqn. 3-13

Where S(t) is the amplitude of the spin echo in the presence of pulsed field gradient, S(0) is the amplitude of the spin echo in the absence of pulsed field gradient, γ is the gyromagnetic ration of the proton, δ is the width of the gradient pulse, g is the magnitude of the applied field gradient, Δ is the total diffusion time, and D is the diffusion coefficient.

The self diffusion coefficient of Acidol-Blue in METHOCEL® K15M solutions at different concentrations was measured using PFG-NMR. A stimulated echo sequence (PSTE) [89] was used at different diffusion times (20 ms, 100 ms, 500 ms) in order to find possible restriction of the diffusion. Results show the expected dependency of the diffusion coefficient on the concentration of the METHOCEL® K15M in the following **Tab. 3-6**. Restricted diffusion can be assumed, but the effect is not very significant.

Tab. 3-6 Diffusion coefficient of Acidol-Blue in METHOCEL® K15M D_2O solutions determined by PFG - NMR ($\dot{\gamma}$ = 0 s^{-1}, υ = 20 °C)

C [wt%]	D [10^{-10}, m^2/s]
0	3
0.25	1.350
0.50	0.714
0.75	0.506
1.00	0.316

Diffusion coefficient determined by PFG-NMR and zero shear viscosity measured by rheometry for METHOCEL® K15M aqueous solutions are shown in **Fig. 3-15** with an exponent of the power -0.33. It seems that the classical Stokes-Einstein correlation cannot be applied, similar results can also be found in [90].

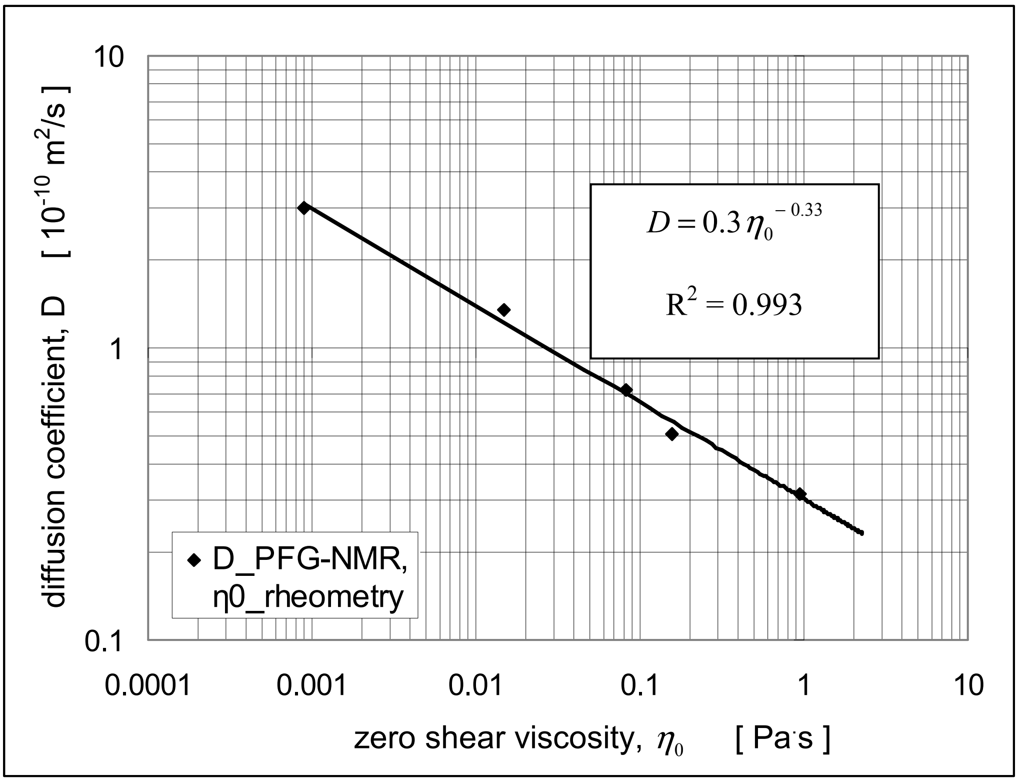

Fig. 3-15 Dependency of diffusion coefficient D of METHOCEL® K15M aqueous solutions on zero shear viscosity η_0, υ = 20 °C

3.1.7.2 Diffusion coefficient determined by mass transfer

For laminar flow in a defined structured channel, mass transfer, represented by the Sherwood number (Sh), is a function of a dimensionless entrance length (z*) and Schmidt number (Sc) along the developing region,

$$Sh = f(z^*, Sc)$$

Eqn. 3-14

where z* is the defined by

$$z^* = \frac{Z}{d_h \cdot \mathrm{Re} \cdot Sc}$$

Eqn. 3-15

For several Schmidt numbers in a range of near magnitude orders, we can find the curves for Sh join in a common part and continually develop to a constant, till the flow is fully developed. Therefore the Sherwood number Sh becomes independent of the Schmidt number Sc in these defined conditions of Schmidt number Sc and dimensionless entrance length z*.

Based on this principle, study on the Sherwood number of Acidol-Blue in Newtonian fluids was conducted in a precious work by Kühnel [84]. Using the CFD-program FIDAP, computations were carried out for simultaneous hydrodynamic and concentration entry flows with Sc = 500, 1200 and 2000 in a rectangular channel (B/H = 15). The dependency of local Sherwood number Sh on the dimensionless entrance length z* for Newtonian flows in rectangular channel (B/H = 15) is demonstrated in Fig. 3-16. The results show, that after a certain entrance length (z* = 1.6e-5), a common part was found among the three curves. That indicates, that after the point of z* = 1.6e-5, the Sherwood number Sh is not the function of Schmidt number Sc, but only the function of the dimensionless entrance length z*.

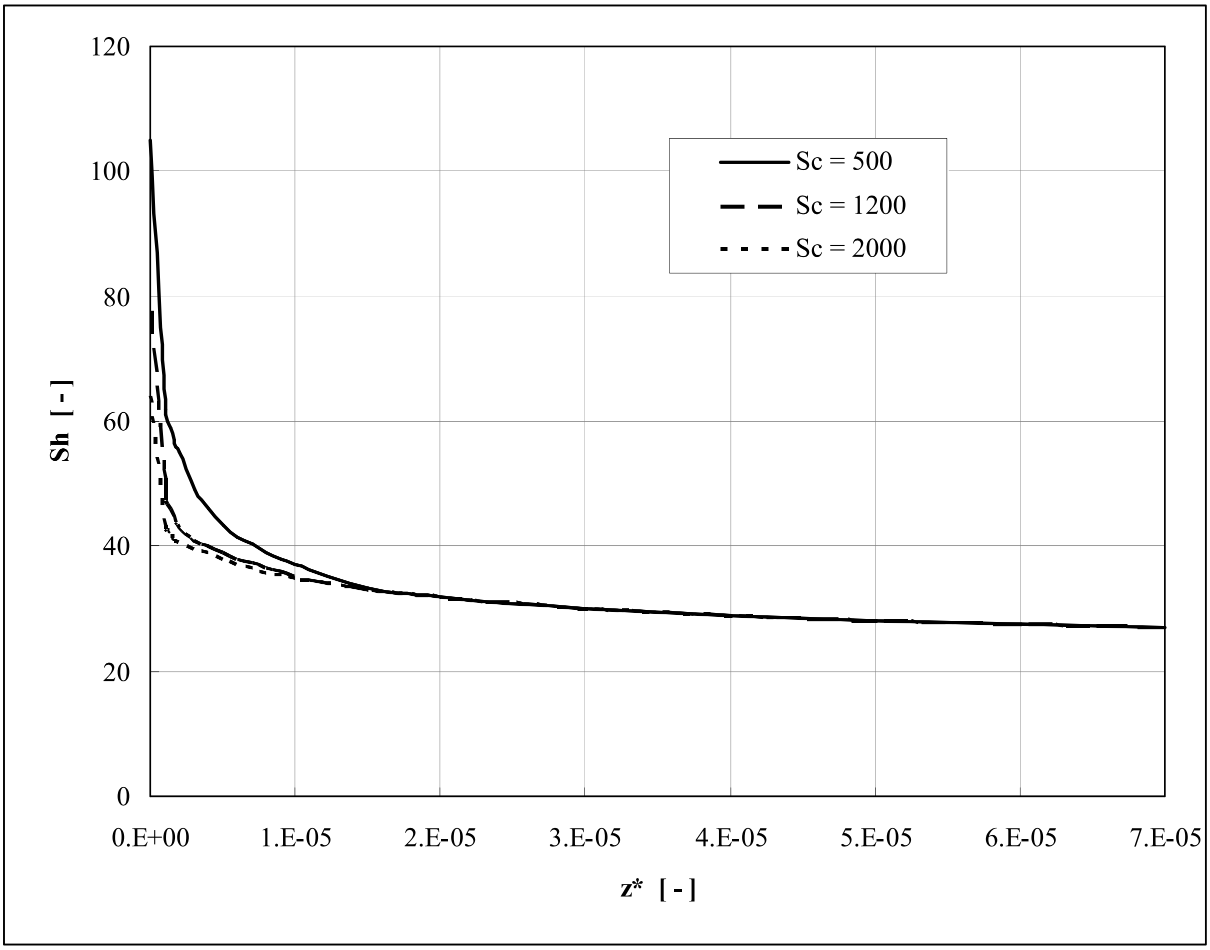

Fig. 3-16 Dependency of local Sherwood number Sh on the dimensionless length z* for Newtonian entry flows in a rectangular channel (B/H = 15) [84]

As mentioned above by **section 3.1.6**, the mass transfer can be experimentally determined by the color density of Acidol-Blue having chemisorptively reacted with the surface of a PA membrane. On the other hand, the concentration gradient of Acidol-Blue can simultaneously be calculated for different Schmidt numbers by numerical methods for the same conditions. Then from the Sherwood number, as a function of z* from numerical results, and as a function of Sc from experimental results, a concrete Schmidt number for laminar flow in a certain structure can be won as intersection. From this Schmidt number the diffusion coefficient D can be calculated. The investigations were based on laminar flow in a rectangular channel (B/H = 15).

Taking a solution of 0.5% METHOCEL$^{®}$ K15M as an example, with a range of assumed Schmidt numbers for the calculations, the correlation between Sherwood number and dimensionless z* for 0.5 % METHOCEL$^{®}$ K15M in a rectangular channel (B/H = 15) is presented in **Fig. 3-17**. The Sherwood number fits the dimensionless z* as a power law regression of

$$Sh_z = 1.39 \cdot z^{*-0.33}$$

Eqn. 3-16

with boundary conditions of Sc = [6.07e+5 ~ 1.98e+6] and z* = [1.53e-7 ~ 2.98e-6].

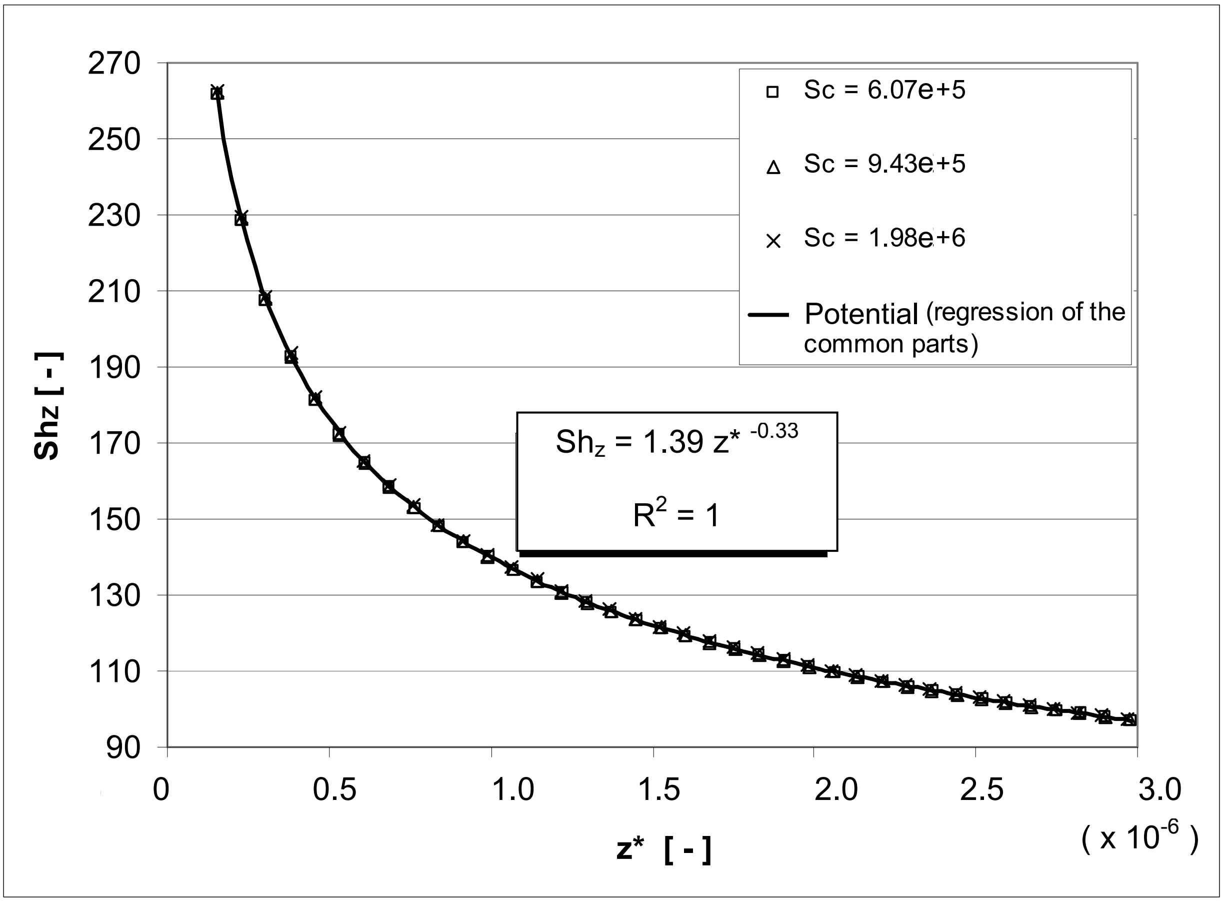

Fig. 3-17 Correlation between Sherwood number Sh$_z$ and dimensionless z* for 0.5 % METHOCEL in rectangular channel (B/H = 15)

On the other hand, the transferred mass was determined experimentally by flow in a fluid channel under the same conditions. According to,

$$Sh = St \cdot \mathrm{Re} \cdot Sc = \frac{\beta}{\overline{w}} \cdot \mathrm{Re} \cdot Sc = \frac{\beta \cdot A \cdot \mathrm{Re}}{\dot{V}} \cdot Sc$$

Eqn. 3-17

Where $St = \frac{\beta}{\overline{w}}$ is the Stanton number.

The Sherwood number over Schmidt number can be evaluated by the slope ($\frac{\beta \cdot A \cdot \mathrm{Re}}{\dot{V}}$) at the corresponding flow length.

The two correlating curves, presented by **Eqn. 3-16** and **Eqn. 3-17,** for a certain flow length Z in **Fig. 3-18** intersect at a common Schmidt number, which can be used to estimate the diffusion coefficient according to,

$$D = \frac{\eta_M}{\rho \cdot Sc}$$

Eqn. 3-18

if the Schmidt number (at the intersection point) falls between the boundaries of the regression.

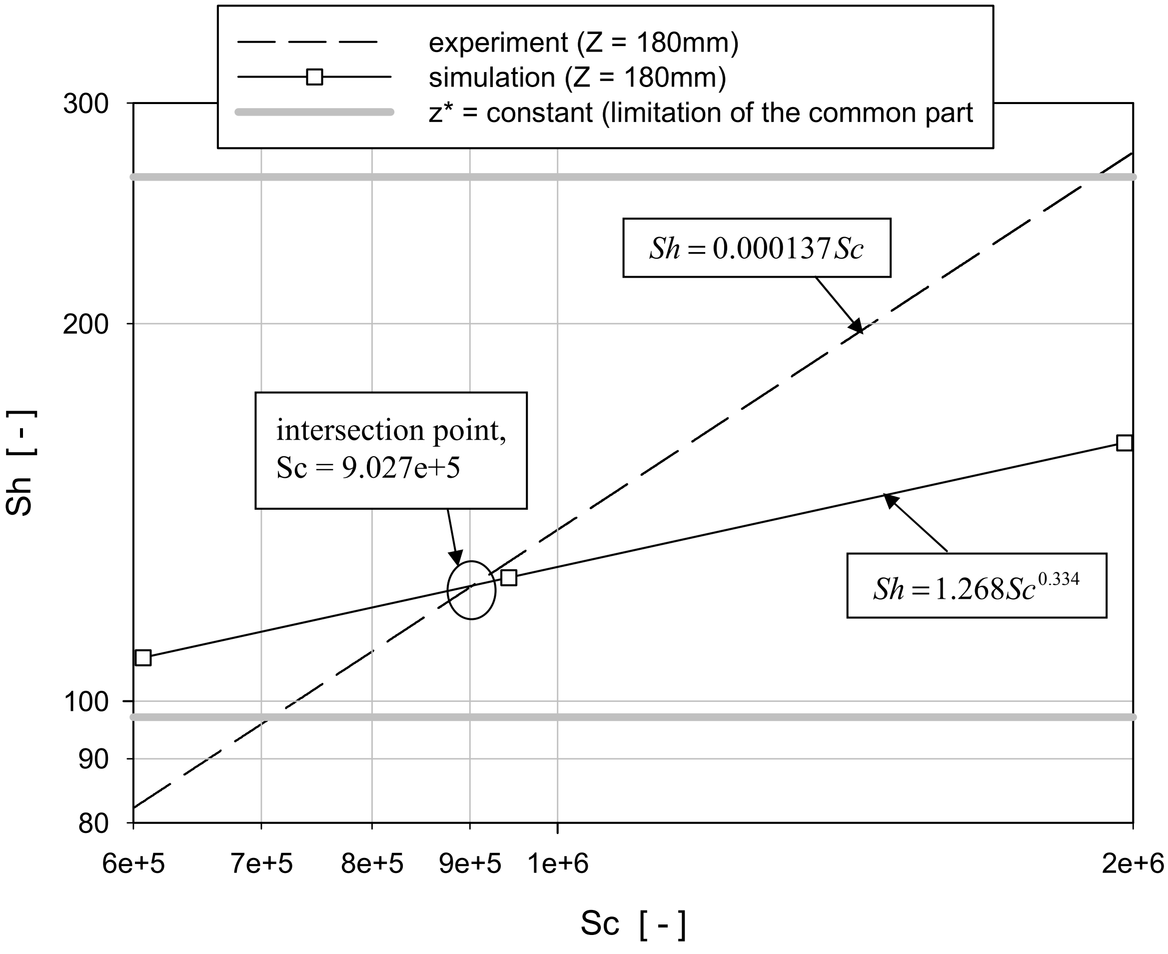

Fig. 3-18 Diffusion coefficient of Acidol-Blue in 0.5 % METHOCEL® determined by the mass transferred on the membrane surfaces

The correlations between Sherwood number and Schmidt number from numerical and experimental results at flow length Z = 180mm are shown in **Tab. 3-7**.

The accuracy of the determination of the Schmidt number Sc by this procedure is the accuracy of the experimental determination of local mass transfer and possible deviation of the real mass transfer from the theoretical mass transfer prediction, depending on the real in- and out-flow deviation from the theoritical ideal interaction, especially at the outflow. Analog to the study of Kühnel for Newtonian fluid flows, only the position of Z = 180mm was taken into consideration. As shown in **Fig. 3-18**, where only the position of Z = 180mm was used, the locally transferred mass from simulated and experimental results meet at a common point. This point located at Z = 180mm exactly fits the boundary conditions of Sc and z* simultaneously. The corresponding value of Sc number was taken to determine the diffusion coefficient. Based on **Eqn. 3-18**, the diffusion coefficient D = 7.49e-11 m^2/s for Acidol Blue in 0.5 % METHOCEL® K15M solution was achieved from the mass transfer method, which is comparable to the result determined by PFG-NMR in **Tab. 3-6**.

Tab. 3-7 Diffusion coefficient of Acidol-Blue
in 0.5 % METHOCEL® K15M determined by the mass transfer method

flow length [mm]	correlation of simulated results	correlation of experimental results	intersection point	D [m^2/s]
180	Sh = 1.268 Sc ^0.334	Sh = 1.37e-4 Sc	9.027e+5	7.49e-11

3.2 Numerical method

3.2.1 Geometry designing and simplification

The spacer-filled channel in the test section, used as plate heat exchanger or spiral wound membrane module, is characterized by two parts: A solid part, which includes the top/bottom plates, two side walls as well as the filled spacer geometry and the corresponding vacant part of the fluid flow region. Of interest are the flow phenomena and heat/mass transport inside the enclosed vacant part, the solid parts simply are solid walls in the numerical study.

Flow in a spacer filled channel develops comparable to the flow development in an empty channel. The length of the flow developing zone till reaching the fully developed state depends on the geometric parameters and Reynolds number. For the larger dimension scales of spacer-filled channels in industrial practices, it is reasonable to assume that after several rhombs the flow is fully developed. If it is fully developed, flow inside a single diamond becomes independent of flow length and characteristic information can be won. The simulations therefore focus on a characteristic single diamond of the spacer, which plays an important role in saving computer resources as well as computing time and provides immediate information on the effect of the spacer geometry.

The individual spacer rod touches the top and bottom plate along a line and forms a tangential surface angle with wall. Likewise upper and lower spacer rods of the spacer grid touch each other at singular contact points. Near these regions (with asymptotic 0° surface angles) a so-called non-manifold structure is created, which causes serious numerical errors in CFX. A modification was made therefore in this study, i.e. a minimum surface contact angle of $\gamma = 10°$ was defined for simulations.

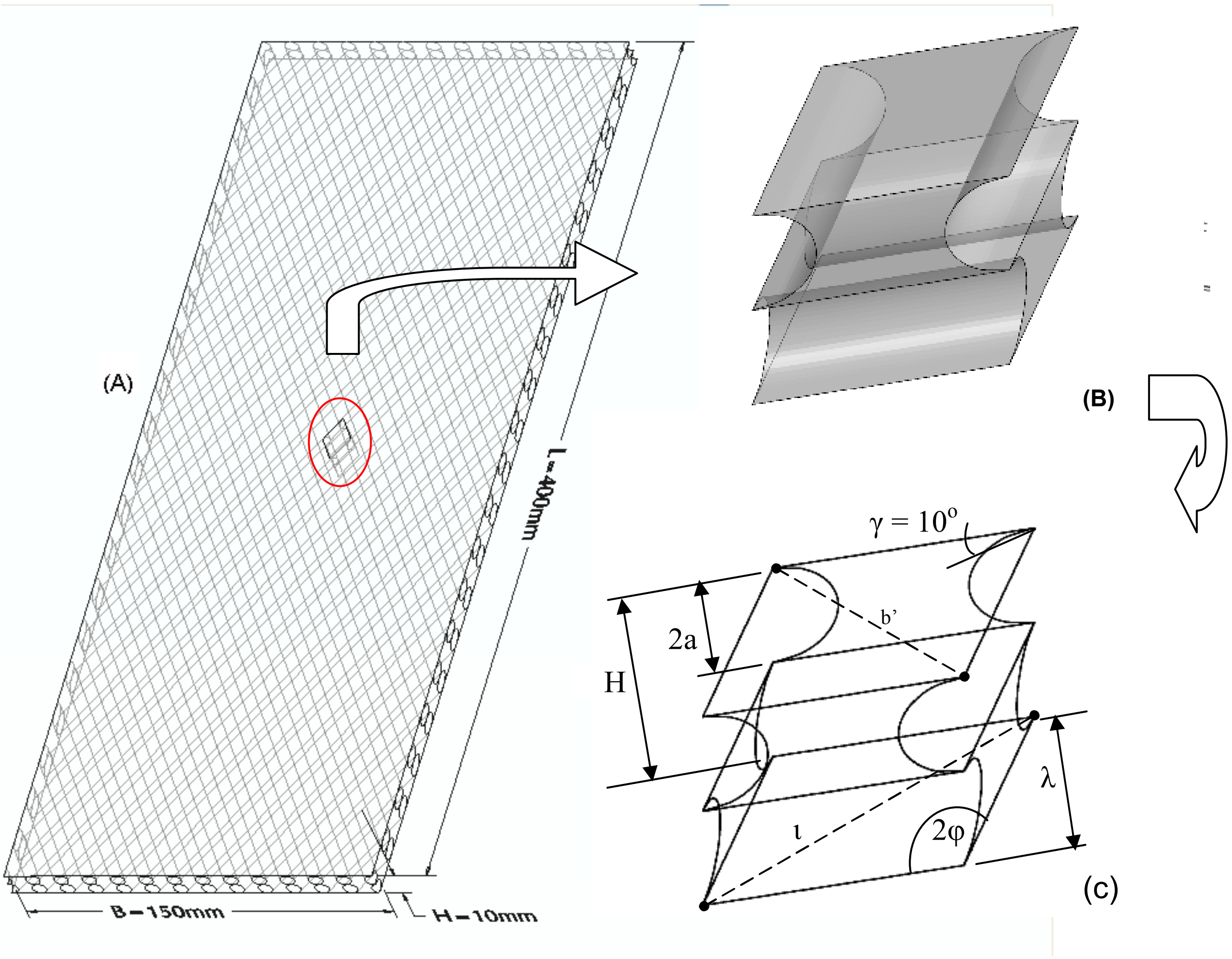

Fig. 3-19 Schematic representation of geometry designing and simplification (A) spacer-filled channel in test section; (B) single characteristic diamond; (C) single characteristic diamond with defined surface angles ɣ = 10°

3.2.2 Mesh generation

The mesh quality is where the CFD analyst has the largest impact on the solution quality. A high quality mesh increases the accuracy of the CFD solution and improves convergence, relative to a poor quality mesh. The demands of mesh quality based on CFX are mainly determined by face angle, edge length ratio and element volume ratio. As mentioned above, in order to achieve a satisfying mesh quality, an appropriate surface contact angle of ɣ = 10° between the touched top/bottom plates and the touching spacer, and between the contact points of the grids themselves was defined during the numericial model design. Mesh quality is then determined by the mesh density and its distribution.

In CFD simulations, a finer mesh typically results in a more accurate solution. Therefore mesh density is extremely important. The mesh should be fine enough to capture the flow gradients and also to reduce the numerical errors. If the mesh is too coarse, results can contain serious errors. However, a too fine mesh will waste computer resources, experience excessively long run times and may be too large to run on the computer system. To avoid such problems, always address the issue of mesh density before beginning model generation.

A question that frequently arises in a numerical analysis is, "how fine should the element mesh be in order to obtain reasonably good results?" Unfortunately, no one can give a definitive answer to this question. Some of the techniques that might be employed to resolve this question include:

- Use adaptive meshing technique to generate a mesh that meets acceptable error estimate criteria.
- Compare the results of a preliminary analysis with independently derived experimental or known accurate analytical results.
- Refine the mesh in regions where the discrepancy between known and calculated results is too great.
- If mesh-refinement testing reveals that only a portion of your model requires a finer mesh, use submodeling to "zoom in" on critical regions.

Mesh density distribution also plays an important role in CFD simulations. If mesh-refinement testing reveals that a portion of the model requires a finer mesh, then an increased mesh density should be zoomed into this critical region; e.g. near the walls, a much finer mesh becomes necessary due to the greater gradients (velocity, concentration, temperature).

Trying to get a mesh that satisfactorily balances accuracy and computing resources, a mesh convergence study was performed in this study as follows:

- Perform an initial analysis using the fewest but still reasonable number of elements and mesh density distribution.
- Recreate the mesh with a more element mesh, especially with a denser element distribution in critical regions, re-analyze it and compare the results to those of the previous mesh.
- Keep increasing the mesh element, improving density distribution and re-analyzing the model until the results are identical and converge satisfactorily.

Besides, two factors were defined to determine the mesh characteristic. One is the first layer height ratio, d_h/h_{1st}, which characterizes the mesh density distribution near the walls; the other is element density, number of nodes/volume of the domain, which characterizes the mesh density over the whole simulated domain. This type of mesh convergence study enables us to obtain an accurate solution with a mesh that is sufficiently dense and not overly demanding of computing resources.

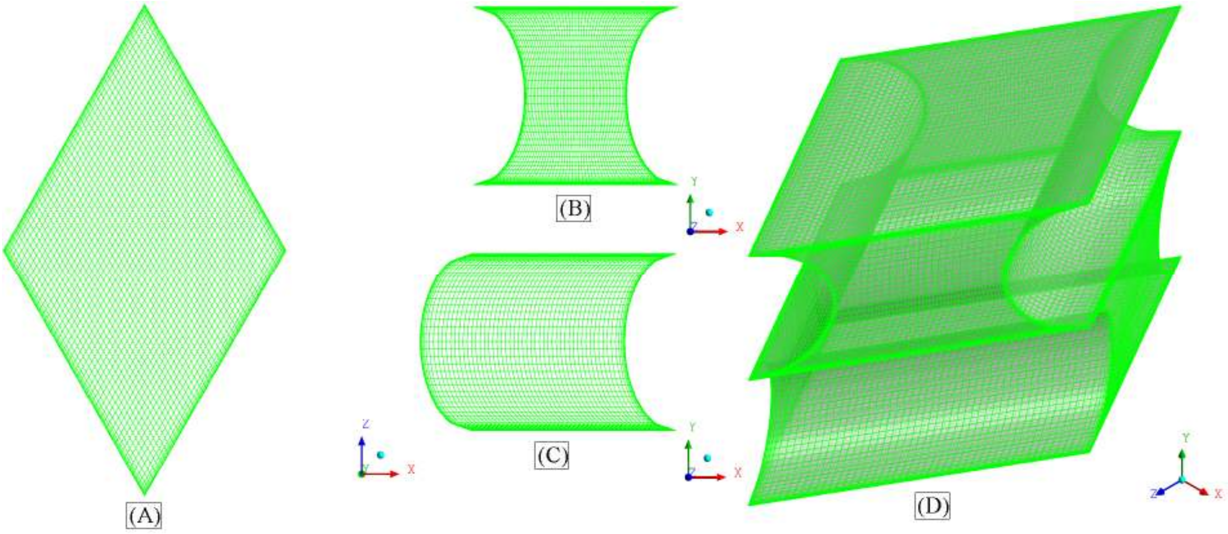

Fig. 3-20 Surface mesh of top/bottom plate (A), periodic interface (B), grid (C); volume mesh of a single diamond (D)

3.2.3 Numerical simulation

The governing equations are the continuity and momentum equations which are solved using ANSYS® CFX (Version 11.0).

Owing to the assumption of the incompressibility of the non-Newtonian fluids used in this study, the continuity equation is given by:

$$\nabla \bullet U = 0$$

Eqn. 3-19

The momentum equations:

$$\frac{\partial \rho U}{\partial t}+\nabla \bullet (\rho U \otimes U)=\nabla \bullet \left(-p\delta+\eta_a\left(\nabla U+(\nabla U)^T\right)\right)+S_M$$

Eqn. 3-20

Where ρ is the density, ∇ is the gradient operator, $\nabla\bullet$ is the divergence operator, δ is the identity matrix or Kronecker delta function, U is velocity, p is pressure, T is the transpose operator of a matrix, S_M is the body force and η_a is the apparent viscosity of non-Newtonian fluids.

The function of $\eta_a = f(\dot{\gamma})$ is determined by **Eqn. 5-5** for shear thinning fluids and **Eqn. 5-11** for shear thickening fluids. Shear rate is defined by:

$$\dot{\gamma}=\left\{2\cdot\left[\left(\frac{\partial u}{\partial x}\right)^2+\left(\frac{\partial v}{\partial y}\right)^2+\left(\frac{\partial w}{\partial z}\right)^2\right]+\left(\frac{\partial u}{\partial y}+\frac{\partial v}{\partial x}\right)^2+\left(\frac{\partial u}{\partial z}+\frac{\partial w}{\partial x}\right)^2+\left(\frac{\partial v}{\partial z}+\frac{\partial w}{\partial y}\right)^2\right\}^{1/2}$$

Eqn. 3-21

In order to simulate concentration boundary layer in spacer-filled channels, Acidol-Blue as a specific scalar additional variable was solved by a transport equation given by:

$$\left(\frac{\partial \Phi}{\partial t}+\nabla \bullet (U\Phi)\right)=\nabla \bullet\left(\left(\rho D+\frac{\eta_a}{Sc}\right)\nabla \bullet\left(\frac{\Phi}{\rho}\right)\right)+S_\Phi$$

Eqn. 3-22

where Φ is the additional variable of Acidol-Blue, η_a is the apparent viscosity for non-Newtonian fluids, Sc is Schmidt number and S_Φ is the extra volumetric source term.

The Reynolds number in spacer-filled channels, in most applications, does not exceed 500, even for fluids with normal viscosity similar to water. For non-Newtonian case, a lower level of Reynolds number should be more interesting in practices. The numerical simulation in this study focuses on flows with Reynolds number up to about 100.

Laminar flow with periodic interfaces under steady state was solved three dimensionally in this study. Dynamic viscosity was estimated by modified power law model. Coupling with the diffusive transport equation, Acidol-Blue was added as an additional variable into computations when mass transfer was taken into account. Diffusion coefficients for different concentrations of METHOCEL® K15M determined by PFG-NMR were used to make the calculations. The local Acidol-Blue value at the surfaces of the channel wall was considered as zero.

In order to get a periodic solution, the computational domain was additionally set as a subdomain, in which the momentum source was specified. Another additional variable of Acidol-Blue was also specified as a source, if mass transfer was computed simultaneously. The following boundary conditions were imposed for the computations in this study:

- Periodic interface: the inlets and outlets of single characteristic diamonds were imposed. Because the geometry was transformed into two layers, a pair of periodic interface should be specified in the upper- and lower layer, respectively;
- No slip wall: the curved surfaces (surfaces of the rod-segments) and top- and bottom-flat surfaces (surfaces of the top- and bottom-plate of the test section), were imposed as no lip walls. Additionally, the curved surfaces were imposed as no flux for the additional variable of Acidol-Blue and the top- and bottom-flat surfaces were imposed with $C_w = 0$, if mass transfer was taken into account.

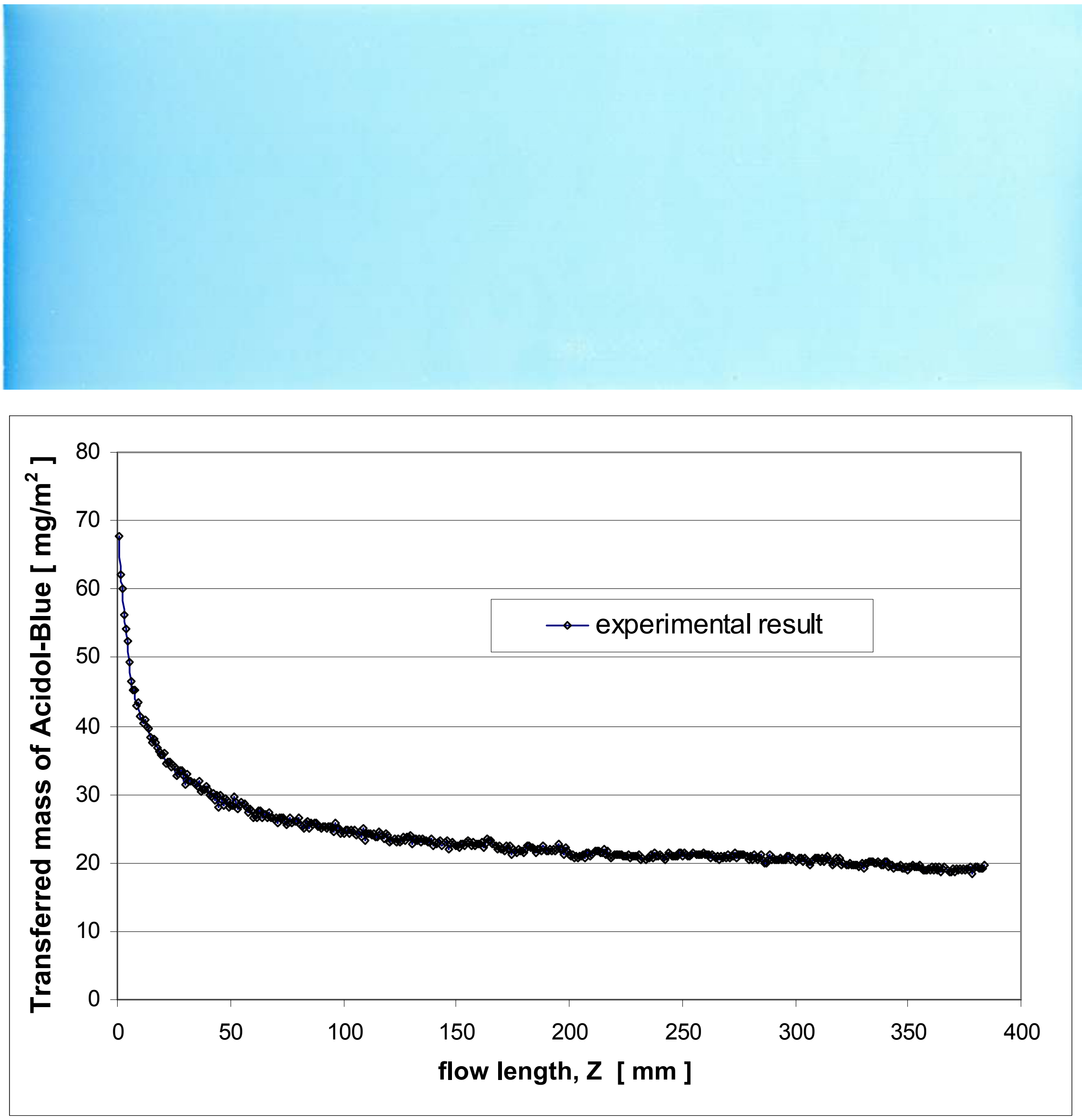

Fig. 3-21 Visualization of the local mass transfer distribution as the blue color density distribution of Acidol-Blue. Local transferred mass over flow length for a rectangular channel (B/H = 15)

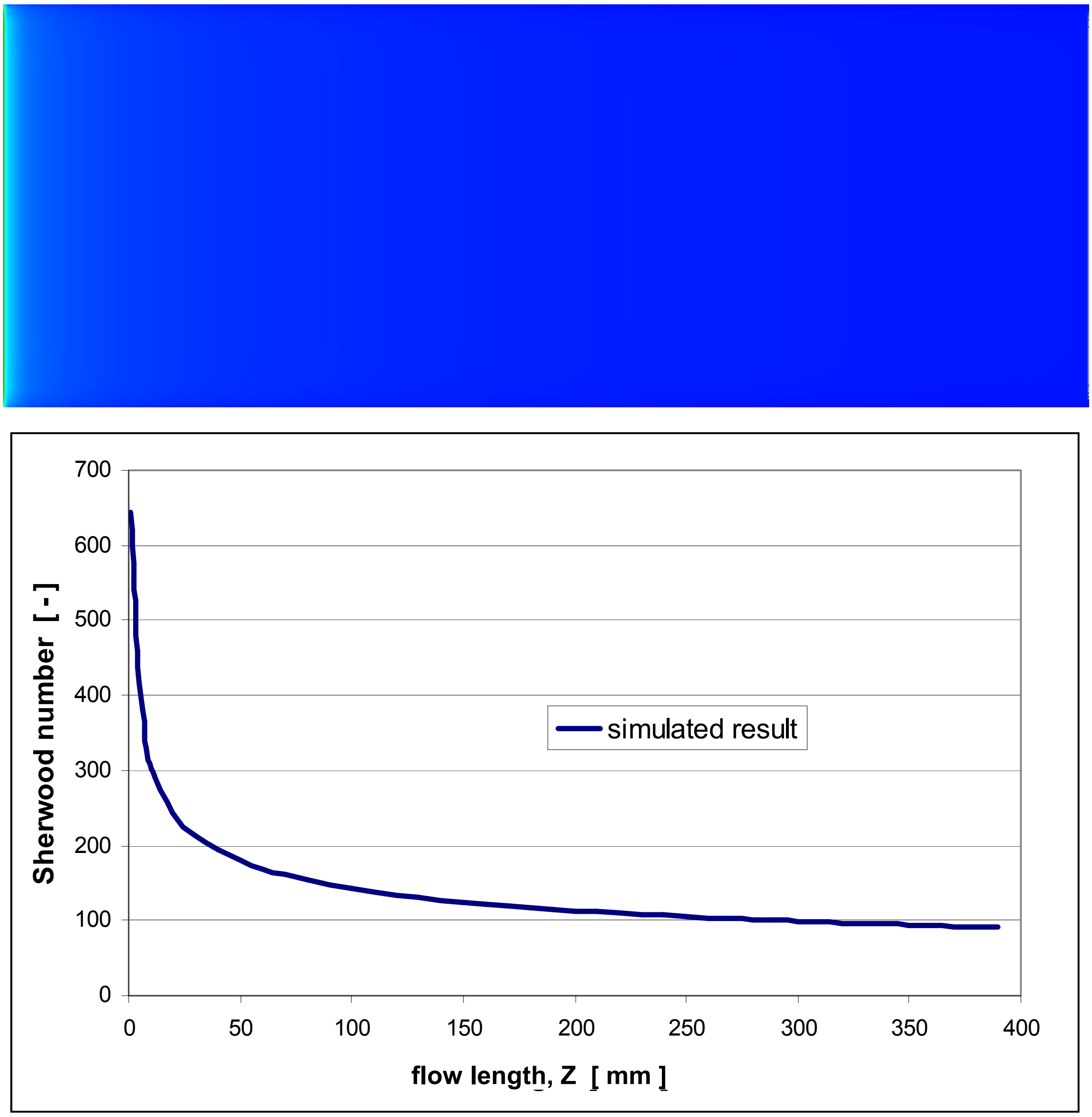

Fig. 3-22 Simulation of the local mass transfer distribution as the concentration gradient of the specific additional variable. The diagram shows the numerical Sherwood number over flow length for a rectangular channel (B/H =15)

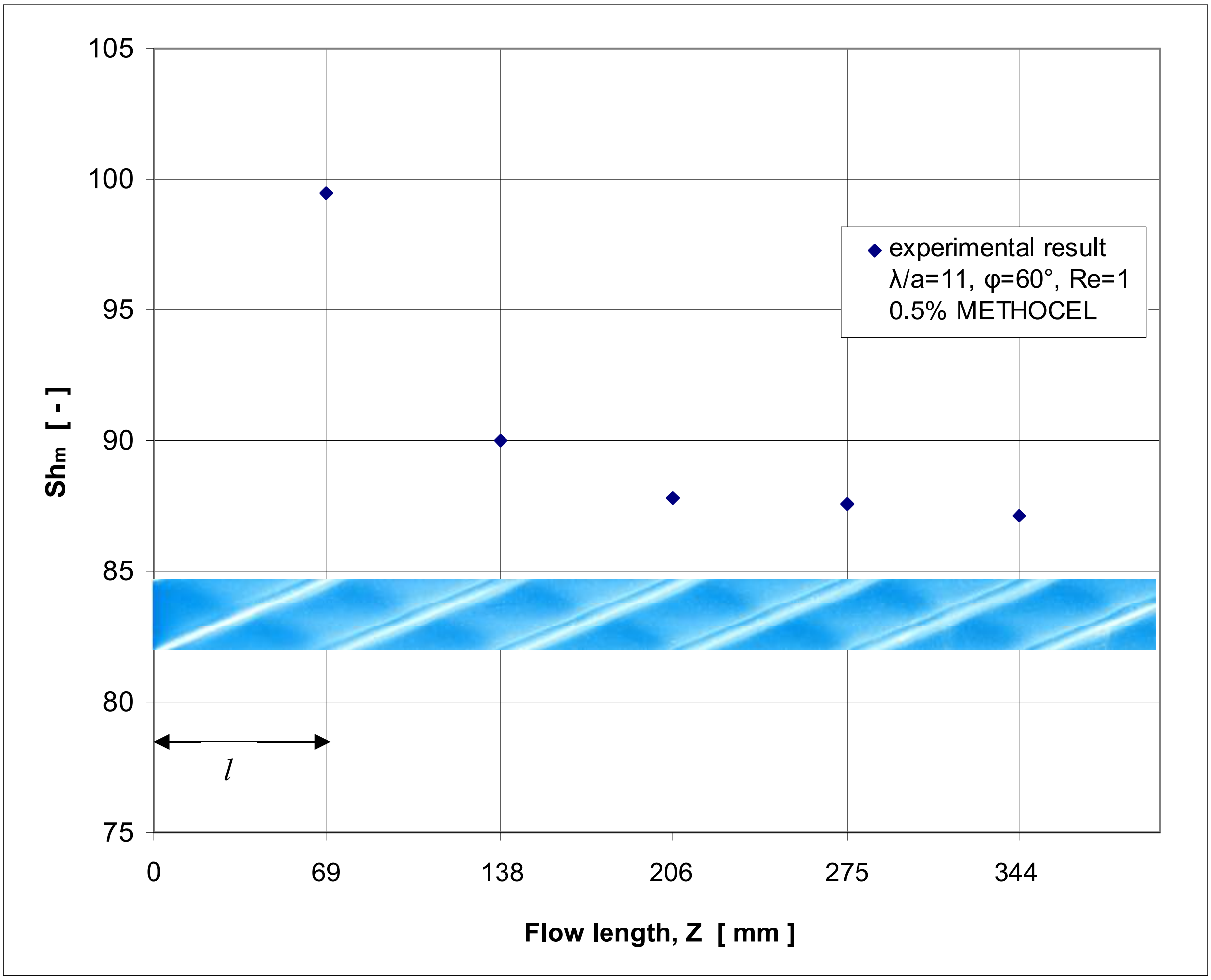

Fig. 3-23 Visualization of the local mass transfer distribution as color density distribution of Acidol-Blue and quantification of the local Sherwood number Sh_M for different flow lengths Z in the spacer-filled channel with spacer D60

3.2.4 Validation

The accuracy of a CFD code has to be demonstrated， so that it may be used with confidence and that the simulation results are considered credible for decision-making in design. CFD simulations require verification assessments, which examine for computer programming errors, and validation assessments, which prove that the computational simulation agrees with physical reality.

Verification and validation are on-going activities due to the complex nature of the CFD codes. Some basic verification should be done prior to release of a code and basic validation studies should be performed on classes of flow features prior to use of the code for similar flows. Some processes, such as examination of iterative convergence, examination of consistency, etc. have been done during computations. Here, taking as examples, we only discuss a mesh refinement study and compare the CFD simulation results to the experimental data and to the results presented in literatures of the two cases of empty ducts and spacer-filled channels.

3.2.4.1 Validation with empty rectangular and square ducts

For the empty rectangular channel (B/H = 15), the integration values of the two geometric correction parameters are $a^* = 0.4395$ (according to **Eqn. 5-4**) and $b^* = 0.9367$ (according to **Eqn. 5-3**). Mesh refinement study shows that the geometric correction parameters from simulation results based on **Eqn. 5-3** and **Eqn. 5-4** agree to the real values very well (error < 1 %), if the first layer height is smaller than 0.005 mm (**Fig. 3-24**).

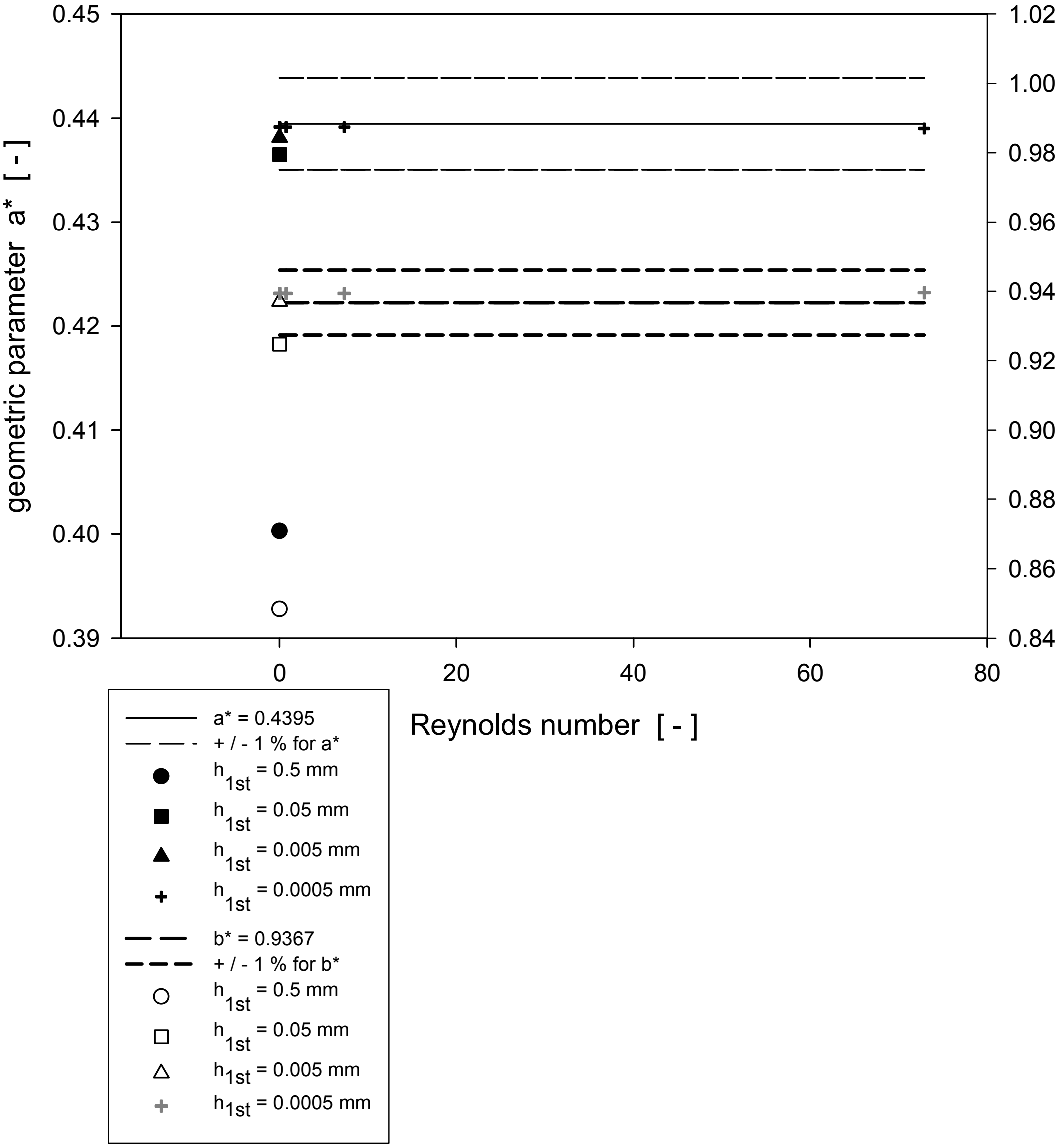

Fig. 3-24 Mesh refinement study on geometric parameters for an empty rectangular channel (B/H = 15)

A comparison of the correlation between friction factor and Reynolds number for an empty square duct was made between the simulation results and theory. **Fig. 3-25** shows that the correlation between friction factor f and Reynolds number Re_M fit the equation of $fRe_M = 16$ quite nice for a variety of flow index n values.

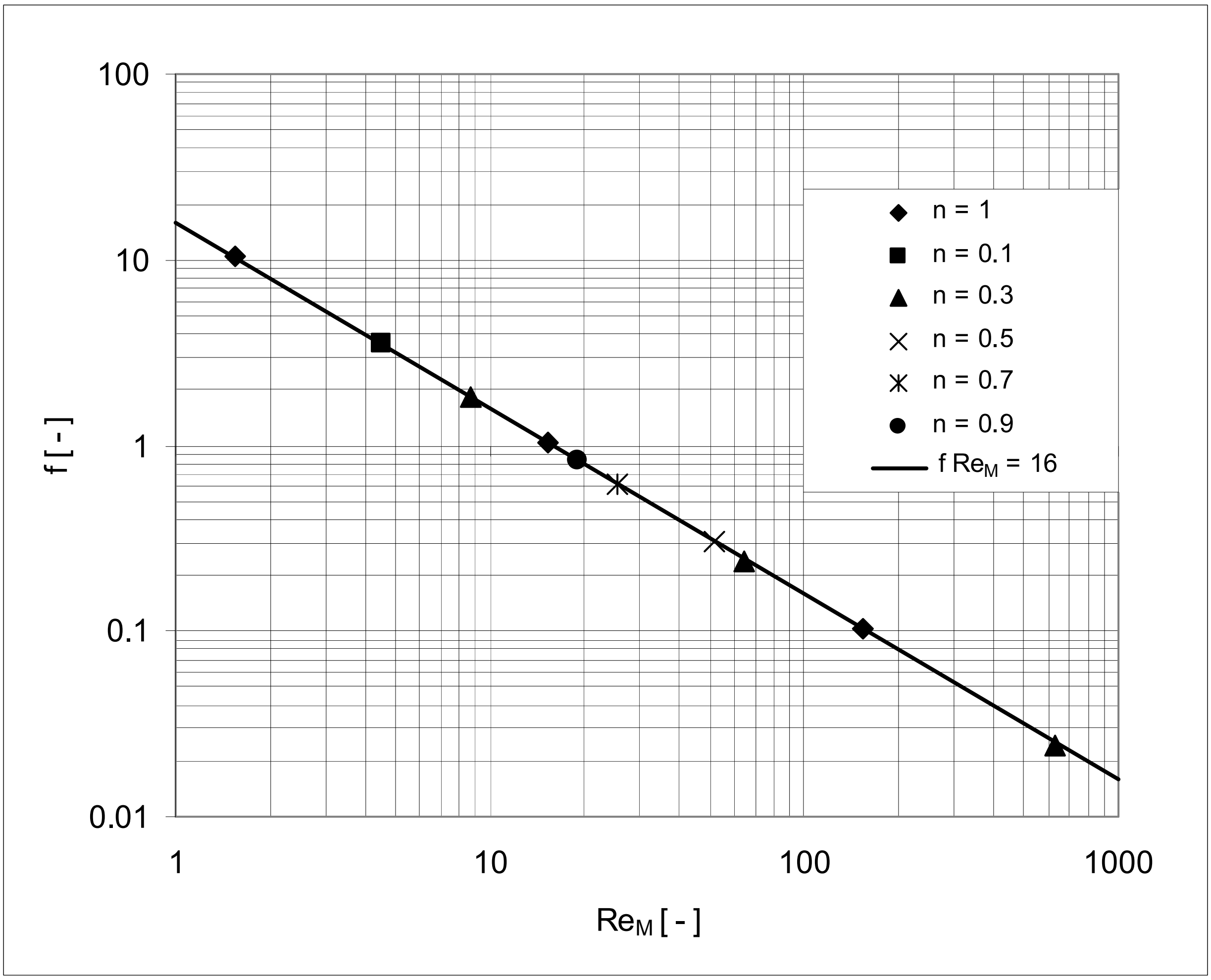

Fig. 3-25 Validation assessment on the correlation between friction factor f and Reynolds number Re$_M$ in an empty square duct

Another validation based on mass transfer was also made in the empty square duct. Simulation results of mass transfer from CFX were compared to the results from literature. An accuracy of 5% relative to Nusselt number with constant wall temperature for non-Newtonian fluids was achieved.

Tab. 3-8 Sherwood number Sh_M in an empty square duct for fully developed laminar flow of non-Newtonian fluids

Flow index n	**Re_M**	**Sh_M (error, %)**			**Nu** /4/
		simulated /1/	**predicted** /2/	**predicted** /3/	
1.0	1.54	2.956 (-0.639)	2.956 (0.000)	2.956 (0.000)	2.975
1.0	15.38	2.956 (-0.639)	2.956 (0.000)	2.956 (0.000)	2.975
1.0	153.75	2.956 (-0.639)	2.956 (0.000)	2.956 (0.000)	2.975
0.9	19.15	2.959 (-1.268)	2.959 (0.000)	2.957 (-0.068)	2.997
0.7	25.43	2.975 (-3.094)	2.972 (-0.101)	2.966 (-0.303)	3.070
0.5	51.74	3.028 (-4.899)	3.018 (-0.330)	2.999 (-0.958)	3.184
0.3	629.13	3.253 -	3.221 (-0.984)	3.119 (-4.119)	-
0.3	64.69	3.142 -	3.117 (-0.796)	3.087 (-1.750)	-
0.3	8.66	3.048 -	3.035 (-0.427)	3.040 (-0.262)	-
0.1	4.53	3.085 -	3.067 (-0.583)	3.232 (4.765)	-

/1/: simulated results, Nu values were considered as reference respectively to determine the error;

/2/: predicted by Eqn. 3-23, simulated results were considered as reference respectively to determine the error;

/3/: predicted by Eqn. 3-24, simulated results were considered as reference respectively to determine the error;

/4/: values from literature [92]

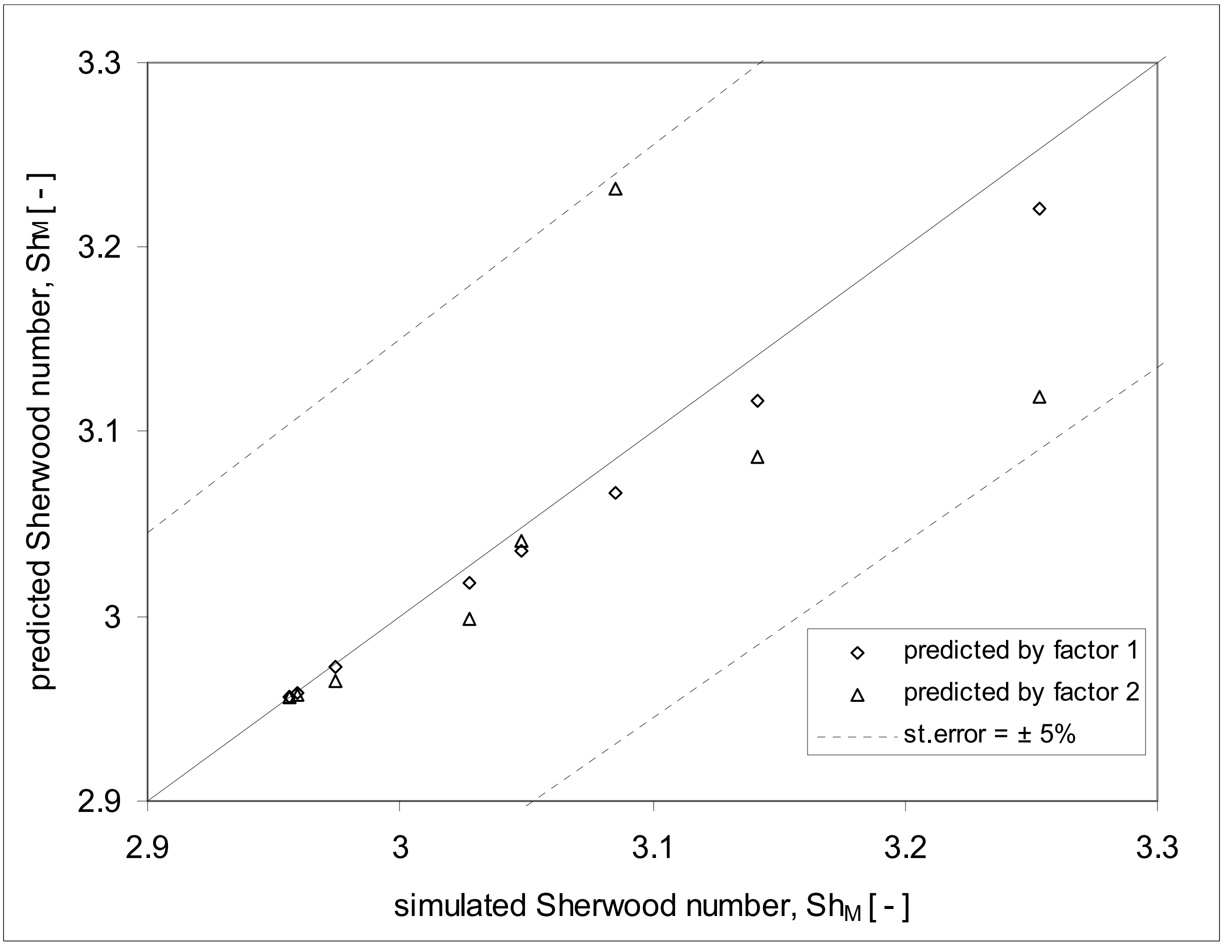

Fig. 3-26 Comparison of the simulated Sherwood number Sh_M by CFX with the predicted Sherwood number in a square duct (Tab. 3-8) according to different correlation factors:

factor 1 = $\left(\dfrac{\eta_b}{\eta_w}\right)^{0.14}$ **from Eqn. 3-23 and factor 2 =** $\left[\dfrac{1+\dfrac{a^*+b^*\cdot n}{(a^*+b^*)\cdot n}\cdot\beta^*}{1+\beta^*}\right]^{\left(1/3\right)}$ **from Eqn. 3-24**

$$Sh_M = Sh_N \cdot \left(\frac{\eta_b}{\eta_w}\right)^{0.14}$$

Eqn. 3-23

$$Sh_M = Sh_N \cdot \left[\frac{1+\dfrac{a^*+b^*\cdot n}{(a^*+b^*)\cdot n}\cdot\beta^*}{1+\beta^*}\right]^{\left(1/3\right)}$$

Eqn. 3-24

for shear thinning non-Newtonian fluids, and

$$Sh_M = Sh_N \cdot \left[\frac{1+\beta^*}{\frac{(a^*+b^*)\cdot n}{a^*+b^*\cdot n}+\beta^*} \right]^{\left(\frac{1}{3}\right)}$$

Eqn. 3-25

for shear thickening non-Newtonian fluids

3.2.4.2 Validation with spacer-filled channels

Taking spacer A15, D15 and D60 as representatives of spacers with different geometric parameters, validation based on mesh refinement for non-Newtonian flow with different flow index n at different Reynolds numbers was studied. Among the investigated range of Reynolds numbers, drag coefficient becomes mesh-independent if the 1st layer mesh height ratio d_h/h_{1st} is larger then about 75. But the Sherwood number here still has a relative large error. That indicates that near the wall, the variable of concentration gradient, which determines Sherwood number is higher than that of velocity gradient, which determines drag coefficient. In another word, a finer mesh becomes necessary when mass transfer is taken into considerations.

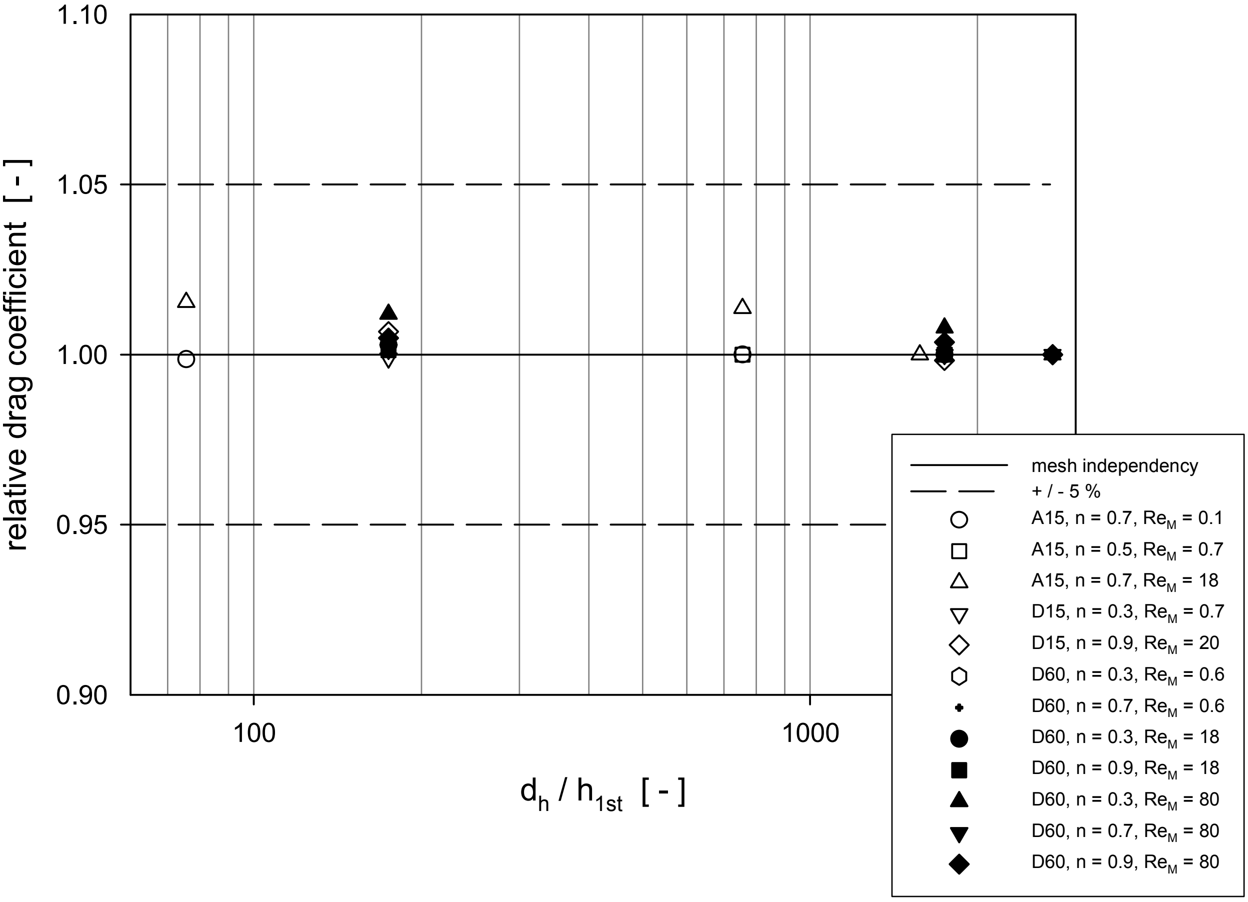

Fig. 3-27 Mesh refinement study on drag coefficient C_d for non-Newtonian fluids in spacer-filled channels

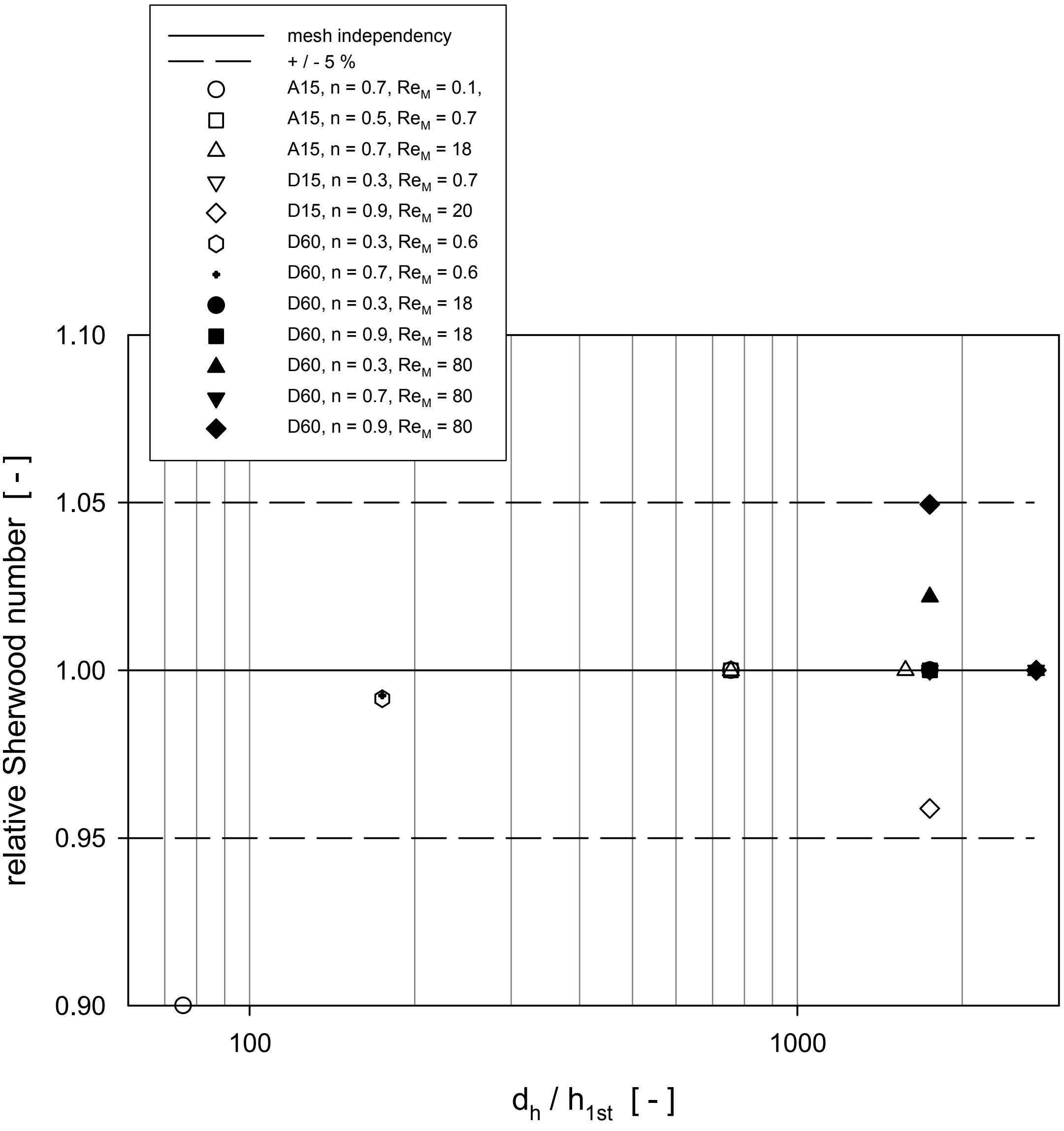

Fig. 3-28 Mesh refinement study on mass transfer for non-Newtonian fluids in spacer-filled channels

4 Flow and transport phenomena in spacer-filled channels

4.1 Creeping flow in spacer-filled channels

Creeping flow in spacer-filled channels was simulated by numerical methods. Three-dimensional flow visualization with CFX code was carried out within a single characteristic diamond under periodic interfaces boundary conditions, which corresponds to fully developed laminar flow. Relative high pressure drag is caused by the geometry of the spacers compared to straight empty duct flows; its scale strongly depends on the geometric paratmeters of the spacers. Creeping flow was simulated under very low Reynolds number ($Re_M = 10^{-5}$) in order to avoid flow separation. Creeping flow through spacer-filled channels was first simulated in order to capture the flow characteristics and their dependency on the geometric parameters. In **Fig. 4-1,** the streamlines from the inlet of the top-layer are shown; the situation in the bottom-layer is symmetric. Results show that flow behavior is strongly depends on the geometric parameters of the spacers.

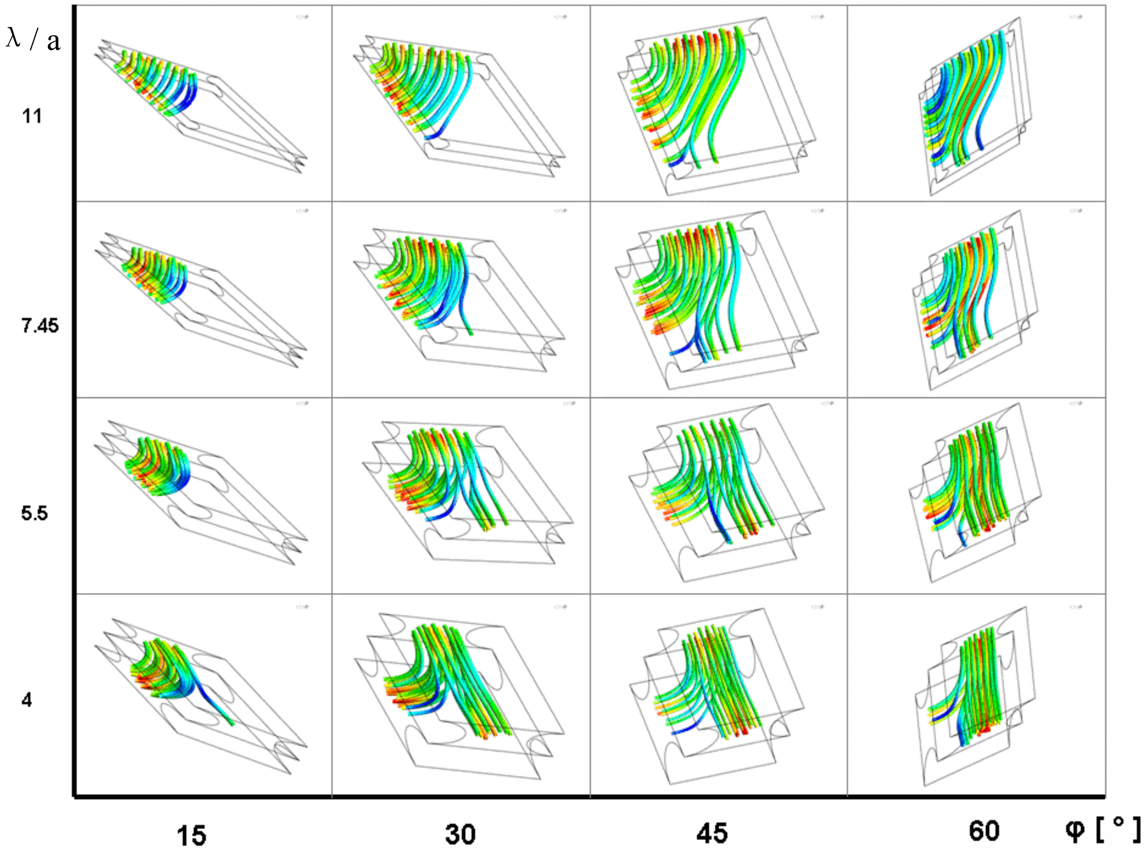

Fig. 4-1 Flow behavior in single diamond of the spacer

$\lambda/a = 4\text{-}11$, $\varphi = 15\text{-}60^{\circ}$, $n = 1$, $Re_M = 10^{-5}$

For flow in spacer-filled channels with smaller inclination angles φ, especially simultaneously with larger wavelength λ/a, there is a low-flow zone between the two streams in the middle of the diamonds. On the other side, for flow in spacer-filled channels with larger inclination angles φ, especially simultaneously with smaller wavelength λ/a, the stream is bifurcated into the top and bottom part of the spacer in different directions. In Fig. 4-1 to Fig. 4-6 red color indicates high velocity and blue indicates low velocity. These phenomena are clearly demonstrated in **Fig. 4-2**.

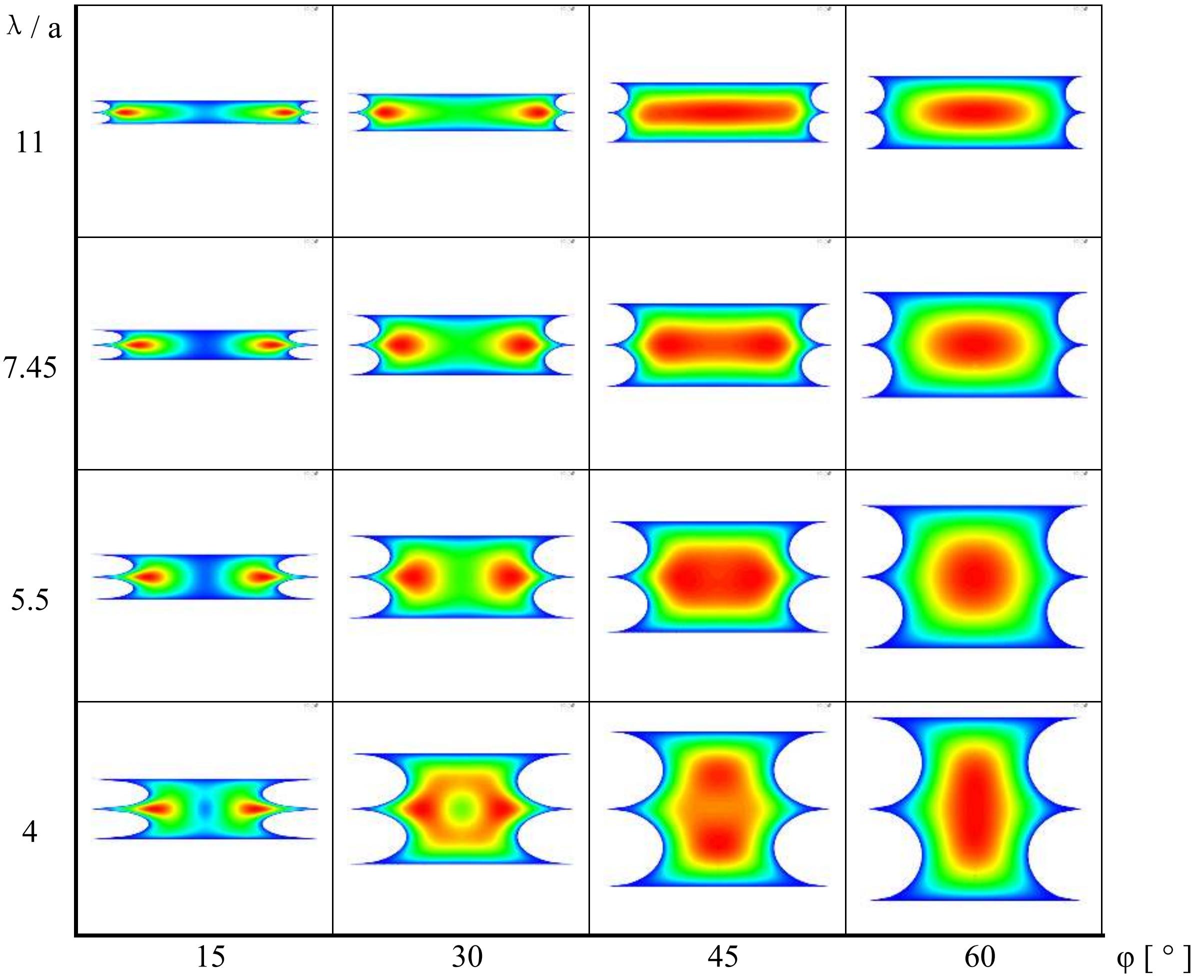

Fig. 4-2 Typical flow profiles in spacer-filled channels

$\lambda/a = 4\text{-}11$, $\varphi = 15\text{-}60°$, $n = 1$, $Re_M = 10^{-5}$

4.2 Flow behavior development with increasing of Reynolds number

Flows in spacer-filled channels with Reynolds number $Re_M = 10$ were simulated in order to investigate the flow behavior developing with an increase of Reynolds number. Taken as an example, flow for spacer A ($\lambda/a = 4$) for a Reynolds number of 10 is shown in **Fig. 4-3**. A comparison with the behavior presented in **Fig. 4-1** and **Fig. 4-2**, shows that more channel flow type phenomena result with higher Reynolds number flow for spacers with the constant wavelength of λ/a = 4.

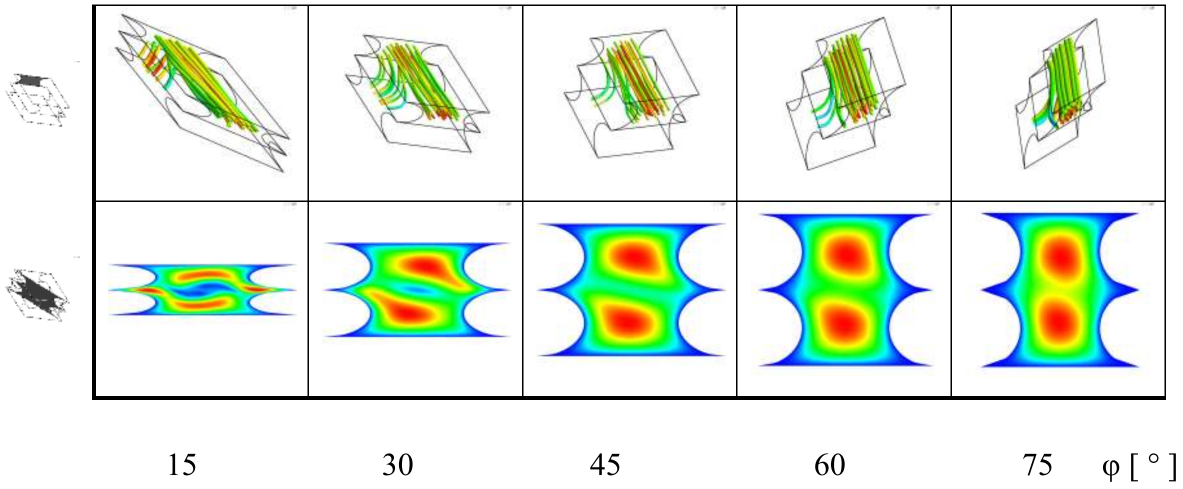

Fig. 4-3 Dependency of flow behavior on inclination angle φ,
λ/a = 4, φ = 15-75°, n = 1, Re_M = 10

Similar phenomena occur for flow in spacer-filled channels with other geometric parameters for a higher Reynolds number. The difference among the spacers is that the channel flow phenomena occur easier (with regard to the increase in Reynolds number) for spacers with larger inclination angles and/or smaller wavelengths. **Fig. 4-4** presents a comparison among spacers with a same inclination angle of φ = 45°, but different wavelengths, for a Reynolds number Re_M of 10. Spacer A45 has already been more dominant in channel flow, but spacer D45 is still characterized by a low-flow zone near the two streams in the middle of the diamond. Spacers B45 and C45 show that more channel flow type has been developed for a Reynolds number Re_M = 10 compared to their creeping flow behavior.

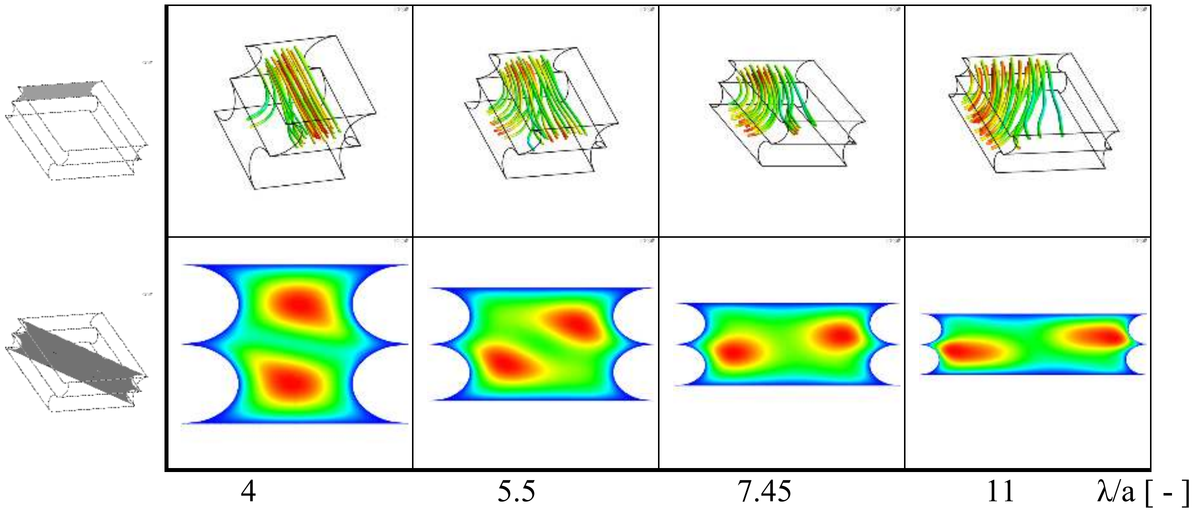

Fig. 4-4 Dependency of flow behavior on wavelength λ/a = 4-11, φ = 45°, n = 1, Re_M = 10

Flow behavior in spacer-filled channels also depends on rheology for non-Newtonian fluids. Its influence is demonstrated by an example of the flow for spacer A15 for a Reynolds number $Re_M = 10$ in **Fig. 4-5**. Channel flow type is more pronounced (as for the increase of Reynolds number) for higher flow index n value than for lower n.

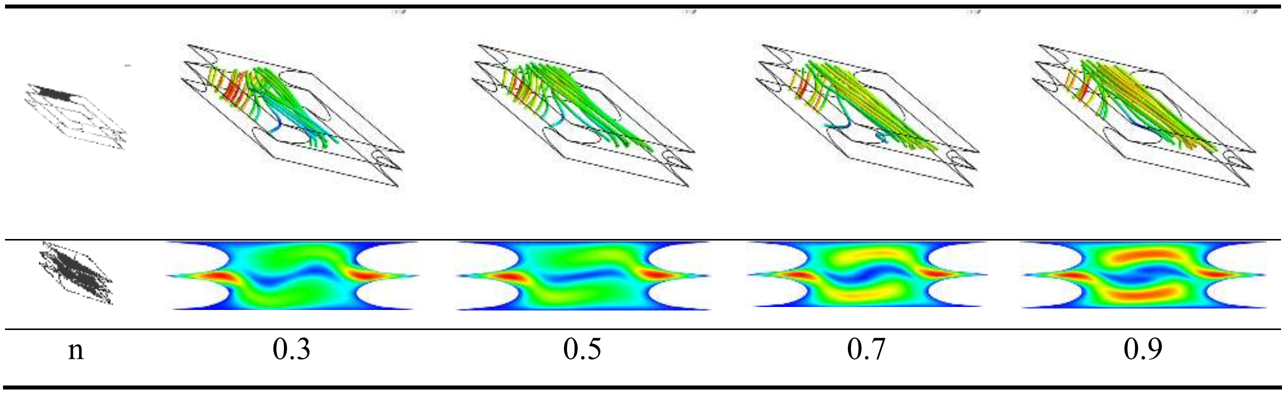

Fig. 4-5 Dependency of flow behavior on the flow index of non-Newtonian fluids

$\lambda/a = 4$, $\varphi = 15°$, $n = 0.3\text{-}0.9$, $Re_M = 10$

For non-Newtonian flow in a straight channel, it is well known, that a more parabolic (peaked) velocity profile can be observed for non-Newtonian laminar flow with a larger flow index n than for a smaller flow index n in the same geometry. **Fig. 4-6** shows non-Newtonian flows with different n values in the spacer-filled channel of D60 for a Reynolds number $Re_M = 80$, which gives an analogous velocity profile effect of the flow, that is, a more peaked flow with increasing n-value.

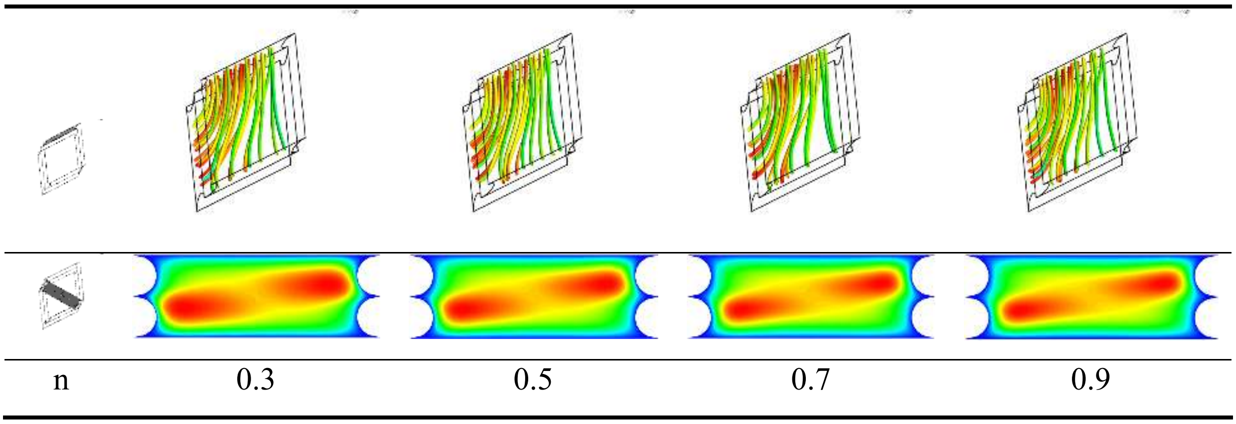

Fig. 4-6 Dependency of flow behavior on the flow index n of non-Newtonian fluids

$\lambda/a = 11$, $\varphi = 60°$, $n = 0.3\text{-}0.9$, $Re_M = 80$

4.3 Velocity profiles in spacer-filled channels

4.3.1 Dependency of velocity profile on the flow index of non-Newtonian fluids in spacer filled channels

The velocity profile plays an important role in hydrodynamic and/or thermal mechanic studies, especially for a non-Newtonian fluid flow, because the viscosity of a non-Newtonian fluid is shear rate dependent, and shear rate is determined by the vector variable of velocity gradient. **Fig. 4-7** presents characteristic velocity profiles for non-Newtonian fluids with different n values for spacer A30. The profile shapes are characterized by a pair of symmetric adjacent parabolic curves. This can be explaned by the bifurcated flow (going into two different directions) for spacers with small wavelengths, especially those simultaneously having large inclination angles. Flow in these spacer-filled channels is dominated by the channel flow type.

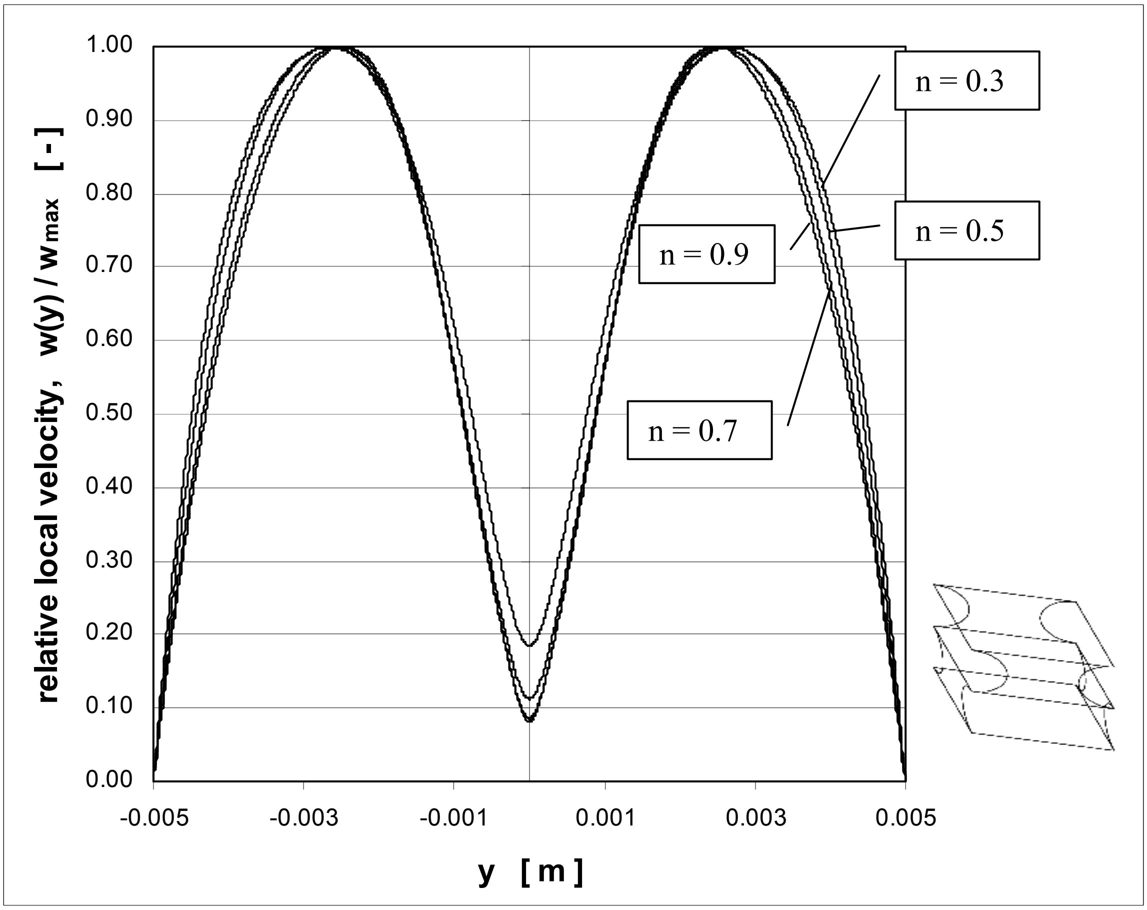

Fig. 4-7 Velocity profiles of non-Newtonian fluids with different flow index in a spacer-filled channel (spacer A30, $Re_M = 1$)

4.3.2 Dependency of velocity profile on the inclination angles of spacer geometry

A similar bifurcated velocity profile can also be found for spacer A with other inclination angles (**Fig. 4-8**). This figure demonstrates that velocity profile in spacer-filled channel is inclination angle dependent.

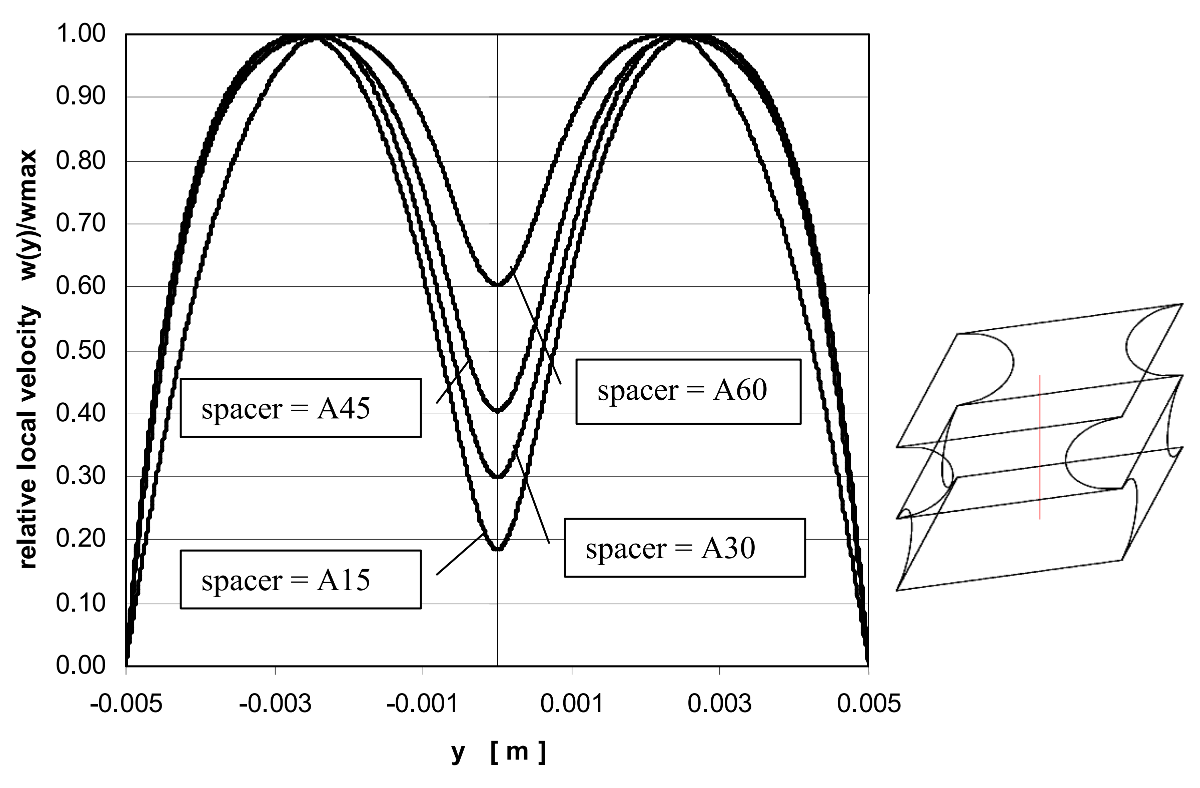

Fig. 4-8 Velocity profiles for different inclination angles for constant wavelength ($\lambda/a = 4$, $n = 0.3$, $Re_M = 1$)

4.3.3 Dependency of velocity profile on the wavelength of spacer geometry

The dependency of the velocity profile on the wavelength of the spacers is shown in **Fig. 4-9**, where the bifurcated velocity profile disappears for spacers with large wavelengths.

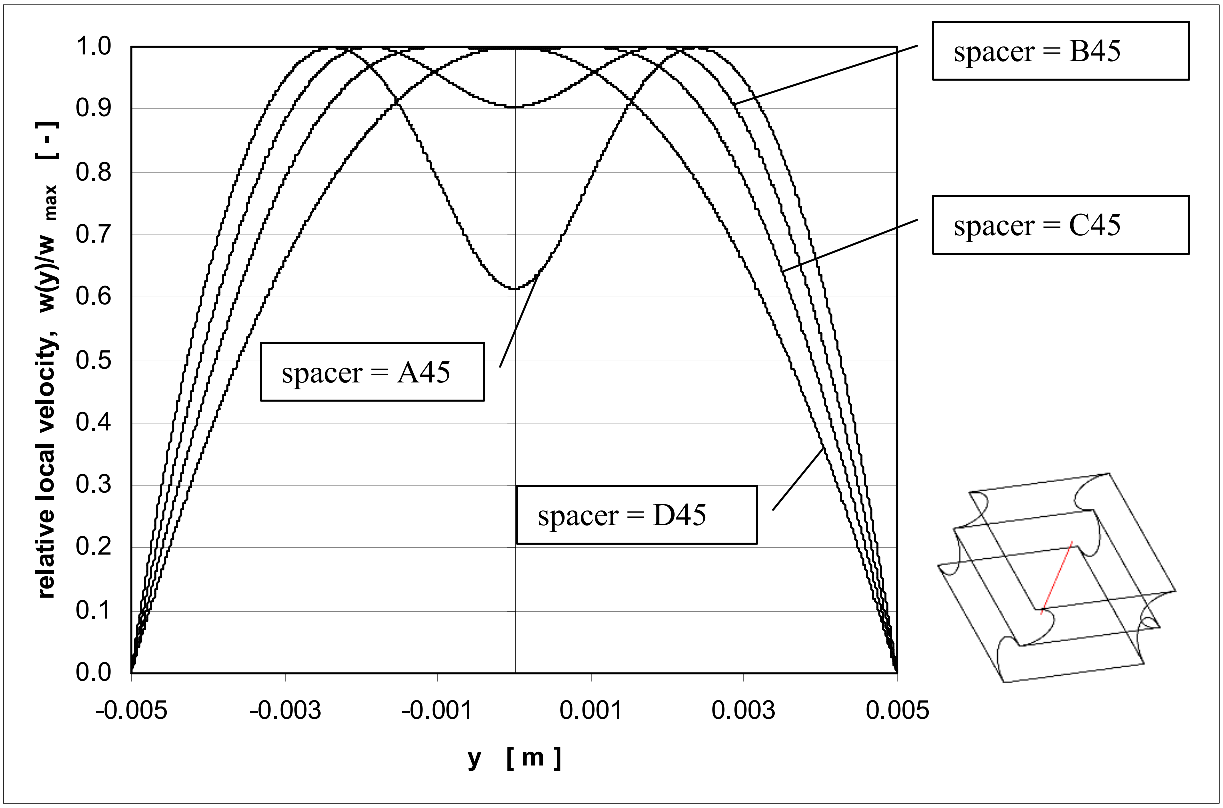

Fig. 4-9 Dependency of velocity profile on the wavelength λ/a of the spacer geometry with constant angle (φ = 45°, n = 1, Re_M = 1)

A typical observation is a valley in the flow profile near the center of the profile except for spacer D45. The minimum of these valleys depends on φ, λ/a and n. This demonstrates the flow phenomena of the bifurcated streams in spacer-filled channels. Spacers D have a relative large wavelength. Here the flow, coming from two different directions, has enough space to meet and merge over flow length.

4.3.4 Dependency of velocity profile on Reynolds number

Velocity profile in a spacer-filled channel, as above shows, depends on the geometric parameters (φ, λ/a) and the non-Newtonian flow index n. Besides this, a dependency of velocity profile on the Reynolds number was investigated. A D-type spacer, with the small angle of 15 degree, was used and a more plug (thicker) shape profile can be observed with an increasing Reynolds number (**Fig. 4-10**).

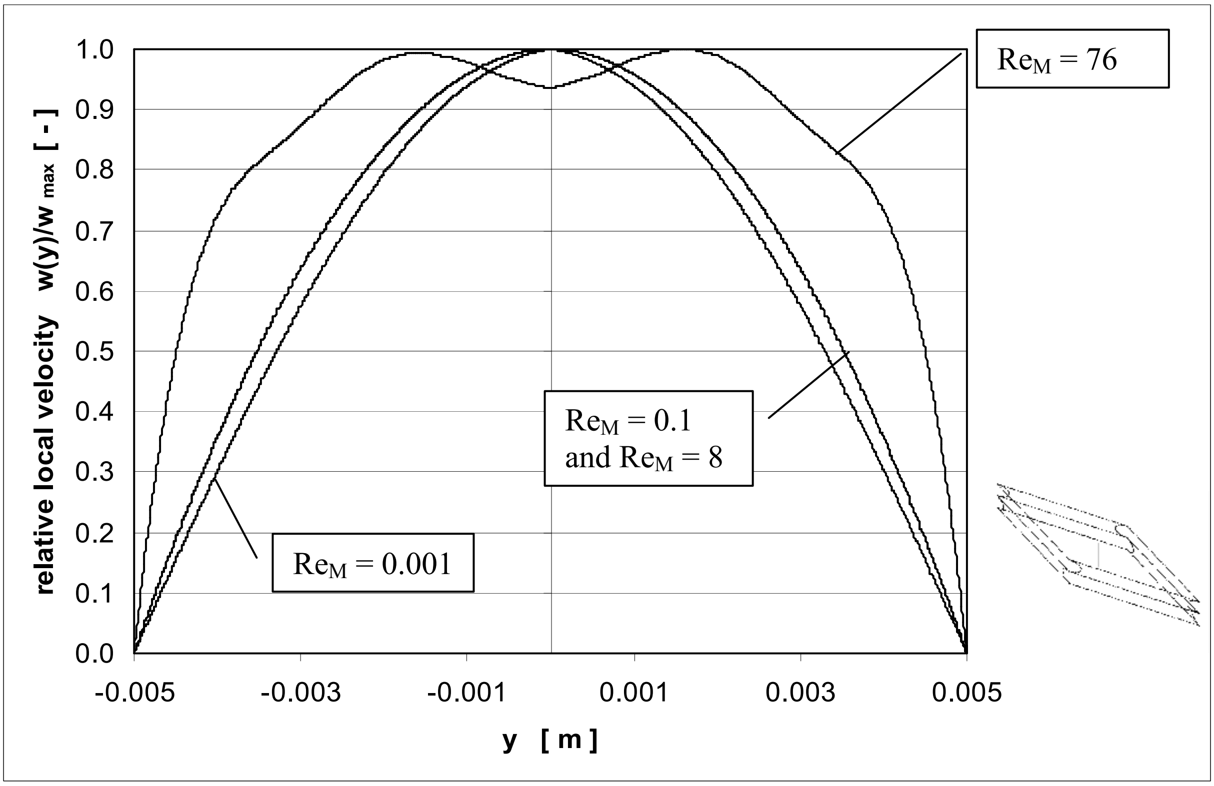

Fig. 4-10 Velocity profiles in spacer-filled channels (spacer D15, n = 1) depending on Reynolds number (The curves for Re$_M$ = 0.1 and Re$_M$ = 8 are overlayed)

4.4 Viscosity profiles in spacer-filled channels

4.4.1 Shear rate profile in spacer-filled channels for non-Newtonian fluids with different flow index n

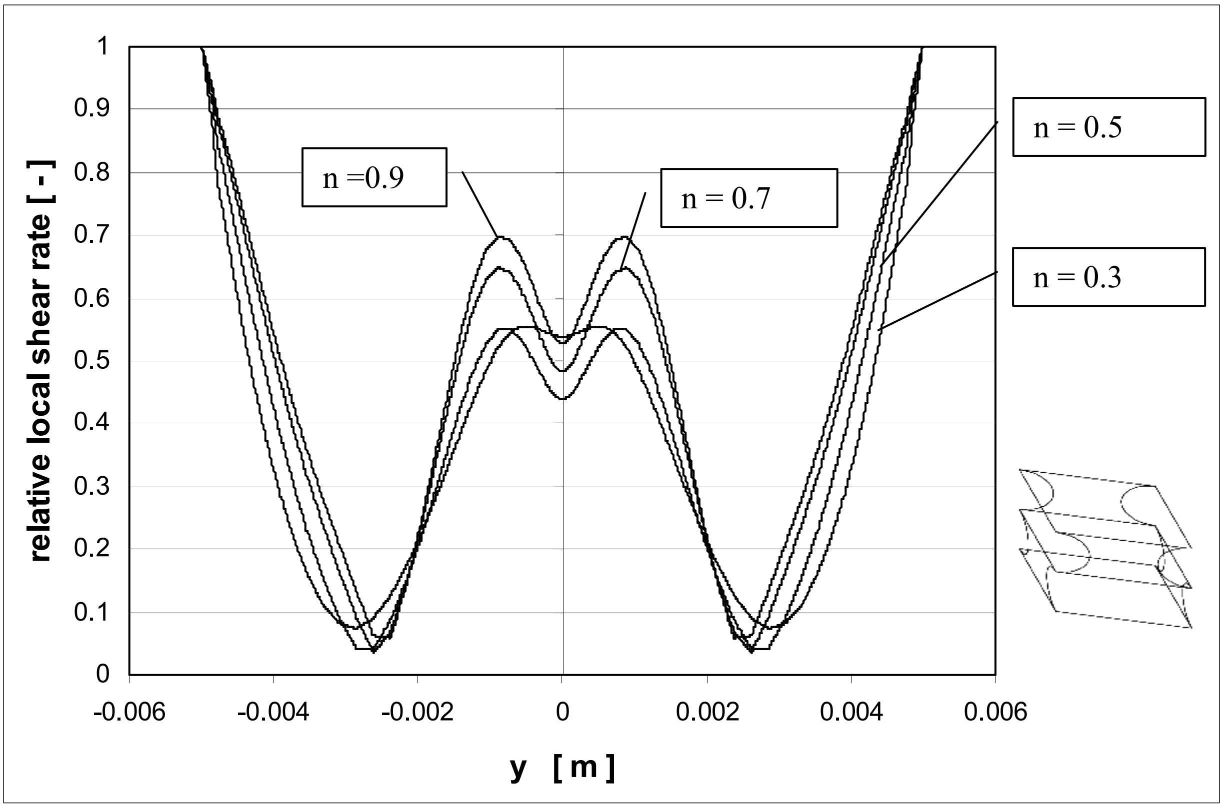

Fig. 4-11 Relative local shear rate profiles of non-Newtonian fluids with different flow index n in a spacer-filled channel (spacer A30, Re_M = 1)

4.4.2 Viscosity profile in spacer-filled channels for non-Newtonian fluids with different flow index n

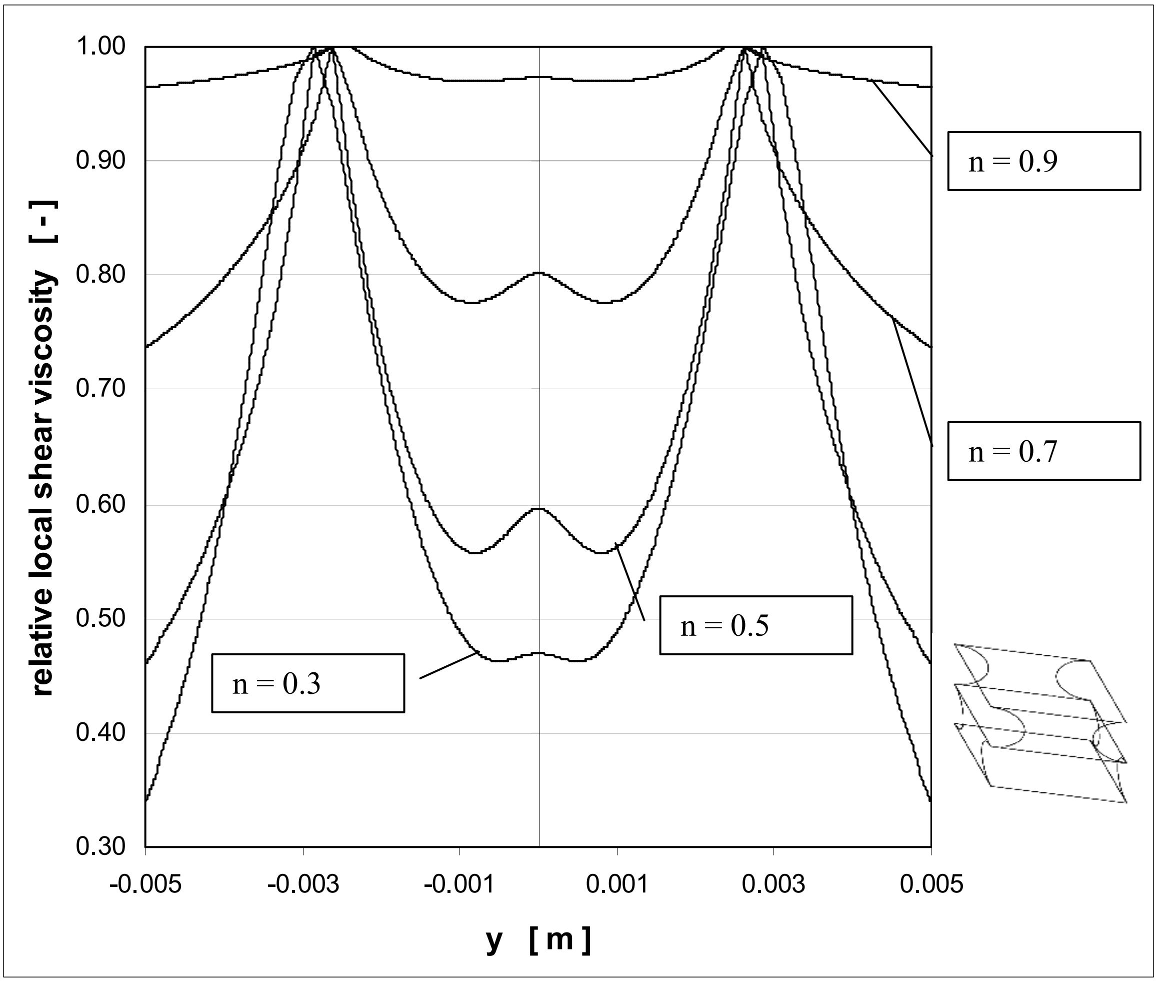

Fig. 4-12 Viscosity profile of non-Newtonian fluids with different flow index in a spacer-filled channel (spacer A30, $Re_M = 1$)

4.5 Dependency of concentration profile on Reynolds number

The concentration profiles are of interest, when mass transfer problems have to be taken into consideration in fully developed laminar flow in spacer-filled channels, shown in **Fig. 4-13** for the same spacer D15 and Reynolds numbers as the velocity profile in **Fig. 4-10**. On one side, the concentration profile for spacer D15 becomes flatter with increasing Reynolds number, which is similar to the velocity profile; on the other side, this transitional changing in the concentration profiles is more dominant than the alteration in velocity profile. A comparison of the two curves of $Re_M = 0.001$ and $Re_M = 0.1$ in both **Fig. 4-10** for the velocity profile and **Fig. 4-13** for the concentration profile shows, that for creeping flow there are no changes in the velocity profile, whereas for the concentration profiles, the profile at $Re_M = 0.1$ is more plug-shaped than that at $Re_M = 0.001$. This trend becomes still more dominant, when the Reynolds number is increased to $Re_M = 8$, where the velocity profile is still parabolic shape and the concentration profile is much stronger plug-shaped. It can be concluded that the Reynolds number affects the concentration boundary layer in spacer D15 much stronger then the velocity profile.

Therefore a finer mesh is needed for the simulation of flow coupled simultaneously with mass transfer in spacer-filled channels.

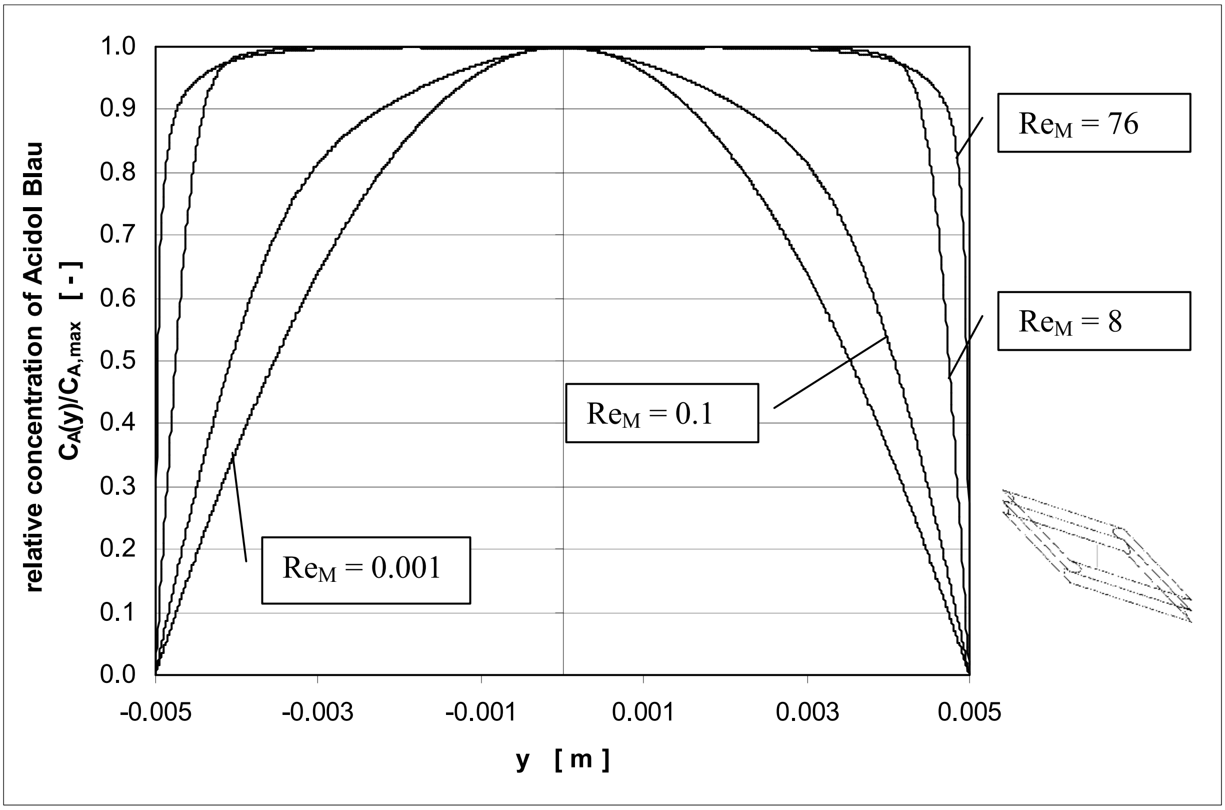

Fig. 4-13 Concentration profiles in a spacer-filled channel (spacer D15) for different Reynolds numbers

5 Pressure drop in spacer-filled channels

5.1 Dimensionless quantities

5.1.1 Geometric correction parameters

The famous Rabinowitsch correction, which is based on the Rabinowitsch-Mooney equation (**Eqn. 5-1**), gives the relationship between wall shear stress and average velocity for flow through circular cross-sections and rectangular channels [119]. The equation contains two geometric correction parameters with a* = 0.25, b* = 0.75 for circular cross-section and a* = 0.5, b* = 1 for parallel plates, respectively.

$$f(\tau_w) = a^* \cdot \tau_w \cdot \frac{d\left[\frac{2 \cdot (\overline{w} - w_w)}{r_h}\right]}{d(\tau_w)} + b^* \cdot \left[\frac{2 \cdot (\overline{w} - w_w)}{r_h}\right]$$

Eqn. 5-1

A generalized Reynolds number is then commonly used for power law non-Newtonian fluids in ducts of arbitrary cross sections.

$$\mathrm{Re}_p = \frac{\rho \cdot \overline{w}^{2-n} \cdot d_h^{\ n}}{K \cdot 2^{3\cdot(n-1)} \cdot (\frac{a^* + b^* \cdot n}{n})^n}$$

Eqn. 5-2

Taking into account the calculation of the Reynolds number with the two geometric correction parameters a* and b*, a common relationship $f \cdot \mathrm{Re}_P = 16$ yields for steady laminar flow, which is very helpful to predict flow of fluids with different properties through different geometries.

For Newtonian fluids, two equations were proposed [93] in terms of these two geometric correction parameters to characterize the flow with mean and maximum flow velocities.

$$\frac{8 \cdot \overline{w}}{d_h} = \frac{1}{a^* + b^*} \left(\frac{1}{\mu} \right) \cdot \left(\frac{dp}{dl} \right) \cdot \left(\frac{d_h}{4} \right)$$

Eqn. 5-3

$$\frac{8 \cdot w_{\max}}{d_h} = \frac{1}{2 \cdot a^*} \left(\frac{1}{\mu} \right) \cdot \left(\frac{dp}{dl} \right) \cdot \left(\frac{d_h}{4} \right)$$

Eqn. 5-4

Then in [94] it was verified that the geometric correction parameters are a function of the flow geometry only and are independent of the fluid properties.

Knowledge of wall shear stress, average as well as maximum velocity was achieved from the simulation results for a Newtonian fluid with CFX, from which the geometric correction parameters a* and b*, characterizing the different spacer geometries respectively, were evaluated. These were used in this work for the prediction of non-Newtonian flow in the same spacers (**Tab. 5-1**).

Tab. 5-1 Geometric correction parameters of different spacers

Spacer	**A15**	**A30**	**A45**	**A60**	**A75**	**A90**
a*	0.550	0.411	0.268	0.186	0.137	0.136
b*	3.925	1.734	0.961	0.620	0.487	1.071
Spacer	**B15**	**B30**	**B45**	**B60**	**B75**	
a*	0.456	0.389	0.302	0.195	0.149	
b*	3.218	1.715	1.051	0.669	0.524	
Spacer	**C15**	**C30**	**C45**	**C60**		
a*	0.364	0.369	0.335	0.226		
b*	2.811	1.740	1.127	0.745		
Spacer	**D15**	**D30**	**D45**	**D60**		
a*	0.354	0.367	0.366	0.242		
b*	2.318	1.822	1.075	0.751		

The geometric correction parameters for different spacers achieved as yet are suitable to predict power law non-Newtonian fluid flows. However, modified power law model is whensoever more precise to describe the rheological behavior over the whole shear rate range, especially under such a low Reynolds number level as we are interested in. Therefore we need another correction factor (here named as Reynolds correction factor) to define the contribution of power law intensity to the whole rheological behavior. This so-called Reynolds correction factor β^* will be interpreted in detail in the followed section.

5.1.2 Reynolds number

When the shear rate is at a relative low level (depending on the characteristic of the polymer and its concentration), the flow curve of a shear thinning fluid usually includes a Newtonian plateau at the beginning. The approximation of this plateau by the power law model is undesirable, because of inherent errors. In this situation, the use of a modified power law model is suggested.

For shear thinning fluids, modified power law is given by

$$\eta_M = \frac{\eta_0}{1+(\frac{\eta_0}{K})\cdot(\dot{\gamma})^{1-n}}$$

Eqn. 5-5

This equation may be rewritten as

$$\frac{1}{\eta_M} = \frac{1}{\eta_0} + \frac{1}{K\cdot(\dot{\gamma})^{n-1}}$$

Eqn. 5-6

Then transferred to this form

$$\frac{\rho\cdot\overline{w}\cdot d_h}{\eta_M} = \frac{\rho\cdot\overline{w}\cdot d_h}{\eta_0} + \frac{\rho\cdot\overline{w}\cdot d_h}{\eta_p}$$

Eqn. 5-7

This means that the Reynolds number, approximated by the modified power law, can be determined by two parts, one Newtonian and another non-Newtonian part.

According to Kozicki [94], using two geometric correction parameters a* and b*, we have the following equation

$$\mathrm{Re}_0 = \frac{\rho \cdot \overline{w} \cdot d_h}{\eta_0 \cdot (a^* + b^*)}$$

Eqn. 5-8

for the determination of Reynolds number at zero shear viscosity, and **Eqn. 5-2** for the determination of Reynolds number in the power law range.

Another parameter can then be defined by a Reynolds correction factor,

$$\beta^* = \frac{\mathrm{Re}_p}{\mathrm{Re}_0} = (\frac{\eta_0}{K}) \cdot (\frac{8 \cdot \overline{w}}{d_h})^{1-n} \cdot \frac{a^* + b^*}{(\frac{a^* + b^* \cdot n}{n})^n}$$

Eqn. 5-9

The Reynolds number defined by modified power law model is therefore simplified to,

$$\mathrm{Re}_M = \frac{\rho \cdot \overline{w} \cdot d_h}{\eta_0 \cdot (a^* + b^*)}(1 + \beta^*)$$

Eqn. 5-10

Similarly, for shear thickening non-Newtonian fluids, defined by modified power law model

$$\eta_M = \eta_0 \cdot \left(1 + \frac{K}{\eta_0} \cdot \dot{\gamma}^{n-1}\right)$$

Eqn. 5-11

the Reynolds number is written as

$$\mathrm{Re}_M = \frac{\rho \cdot \overline{w} \cdot d_h}{\eta_0 \cdot (a^* + b^*)}(\frac{\beta^*}{1 + \beta^*})$$

Eqn. 5-12

According to these two Equations **Eqn. 5-10** and **Eqn. 5-12**, we can easily reach the conclusion of $f \cdot \mathrm{Re}_M = 16$ or $\varsigma \cdot \mathrm{Re}_M = 64$ for modified power law non-Newtonian fluids with different flow index n values in different geometry of spacer-filled channels, if the flow is fully developed laminar.

Then the results among different spacers or between spacer-filled channels and other channels (even tubes) become comparable.

5.1.3 Drag coefficient

Pressure drop between entrance and exit of the test section filled with spacers can be measured for different Reynolds numbers, with which a friction factor can then be defined as **Eqn. 3-4**, the fanning friction factor or as another common definition as **Eqn. 3-5** the Darcy friction factor.

In straight and empty channel, pressure drives the fluid to flow, and keeps in a balance with the wall shear stress over the wetted surface by

$$\bar{\tau}_w = \frac{\Delta p \cdot d_h}{4 \cdot L}$$

Eqn. 5-13

All of the pressure losses contribute to the frictional resistance of the wall, i.e. only a pair of forces work on the fluid and keep a force balance in the fully developed laminar flow.

But the flow in spacer-filled channels is similar to the flow over a bluff body. The contribution of the total force exerted on the whole domain is a combination of the tangential stress at the domain surface, which can be integrated over the area of surface, and of the normal stress, which gives a reverse pressure gradient and causes flow separation. These forces are named, respectively, the friction drag and the pressure drag, since the first one is a consequence of viscosity or friction in the fluid, and the second results from pressure force, which depends strongly on the shape of the body. Therefore besides the wall shear stress, the resistance for the different geometric shapes of spacers becomes more dominant in flow over spacers.

The drag coefficients contributed by friction drag and pressure drag, respectively, are usually named friction drag coefficient and form drag coefficient. These two parts of drags can easily be determined in numerical CFD code with the integration method.

$$\overline{\tau}_w = \frac{\iint\limits_S \tau_w \cdot ds}{S}$$

Eqn. 5-14

$$\overline{\frac{dp}{dl}} = \frac{\iiint\limits_V \frac{dp}{dl} \cdot dv}{V}$$

Eqn. 5-15

$$C_{d,f} = \iint\limits_S \dot{C}_{d,f} \cdot ds = \frac{\overline{\tau}_w}{\frac{1}{2} \cdot \rho \cdot \overline{w}^2}$$

Eqn. 5-16

$$C_{d,p} = \iiint\limits_V \dot{C}_{d,p} \cdot dv = \frac{1}{\frac{1}{2} \cdot \rho \cdot \overline{w}^2} \cdot \left(\overline{\frac{dp}{dl}} \right) \cdot \frac{d_h}{4}$$

Eqn. 5-17

The drag coefficient is then determined by

$$C_d = C_{d,f} + C_{d,p} = F(\mathrm{Re})$$

Eqn. 5-18

Which is identical to the friction factor estimated by **Eqn. 3-4** in experimental results.

The drag coefficient distribution ratio $C_{d,f}/C_d$, friction drag coefficient to (total) drag coefficient, varies with the different geometry of the spacers. From the results in **Tab. 5-2**, the pressure drag caused by the form of the spacers becomes dominant with decreasing inclination angle.

For non-creeping flow, the normal force will result in a flow separation behind the spacer rods. In this situation, a flow separation angle θ has to be taken into the integration as

$$C_{d,f} = \int_0^l \int_0^\theta \dot{C}_{d,f}(l,\theta) \cdot dl \cdot d\theta$$

Eqn. 5-19

The pressure drag is due to the unbalanced pressures which exist between the relatively high pressures on the upstream surfaces and lower pressures on the downstream surfaces of the grids. It can be written as

$$C_{d,p} = \int_0^l \int_0^\theta \dot{C}_{d,p}(l,\theta) \cdot dl \cdot d\theta$$

Eqn. 5-20

Therefore the total drag coefficient is won by the sum of the integration of both drag coefficients

$$C_d = \int_0^l \int_0^\theta \dot{C}_{d,f}(l,\theta) \cdot dl \cdot d\theta + \int_0^l \int_0^\theta \dot{C}_{d,p}(l,\theta) \cdot dl \cdot d\theta$$

Eqn. 5-21

This can be used for the calculation of the total drag force from the local values in **Eqn. 5-16** and **Eqn. 5-17**.

5.2 Non-dimensional correlation between drag coefficient and Reynolds number of creeping flows in spacer-filled channels

As an important dimensionless variable, the Reynolds number plays a role for the judgement of flow velocity, the prediction of the transition from laminar to turbulent flow, and the determination of other dimensionless variables of problems in fluiddynamics as well as heat and mass transfer. For non-Newtonian flows, the rheological characteristics of the fluids must be taken into consideration for the definitions of the Reynolds number. These can differ from each other according to different conservative equations. A famous and commonly used definition is written as **Eqn. 3-1** based on power law model.

We extended the Reynolds number by adding a Reynolds correction factor. The introduced equations, written as **Eqn. 5-10** and **Eqn. 5-12**, are suitable for non-Newtonian fluids, described by a modified power law model in the universal range of shear rate. The estimation takes into account the geometric correction parameters a^*, b^*, the effect of rheology (η_0, n, K) and the shear strain effect (Reynolds correction factor β^*). A common curve can thus be achieved for modified power law non-Newtonian fluids for different spacers in laminar flow.

As **Fig. 5-1** shows, that for every spacer and, even in the same spacer geometry, for every n value, individual correlation constants were necessary, before the new Reynolds number Re_M was introduced.

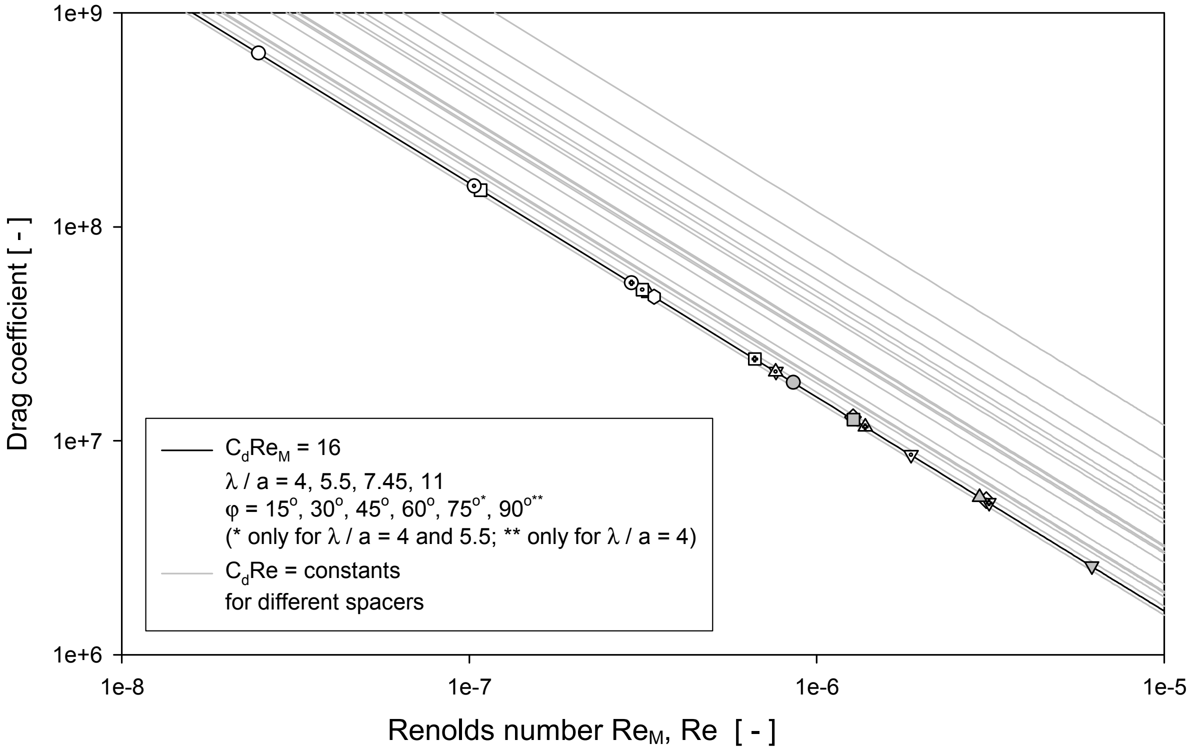

Fig. 5-1 Correlation between Reynolds number and drag coefficient in spacer-filled channels

5.3 Drag coefficient contribution and development

The drag coefficient -as demonstrated in **Fig. 5-1**, also written by **Eqn. 5-18**- includes two parts, the friction drag coefficient from wall shear stress and the form drag coefficient from pressure gradient as explained above in **section 5.1.2**. The quantitative distribution of these two parts in spacer-filled channels for creeping flow is shown in **Tab. 5-2**. **Tab. 5-2** shows that the ratio of

$C_{d,\,f}/C_d$ strongly depends on the geometry of the spacer, and increases with the increase of the inclination angle and the wavelength. This indicates, that smaller inclination angle and/or smaller wavelength of the spacer geometry induces a larger form drag coefficient portion.

Tab. 5-2 Drag coefficient distribution in spacer-filled channels for creeping flow

Spacer	**A15**	**A30**	**A45**	**A60**	**A75**	**A90**
$C_{d,f}/C_d$ [%]	**19**	**31**	**51**	**74**	**93**	**52**
Spacer	**B15**	**B30**	**B45**	**B60**	**B75**	
$C_{d,f}/C_d$ [%]	**22**	**33**	**49**	**74**	**92**	
Spacer	**C15**	**C30**	**C45**	**C60**		
$C_{d,f}/C_d$ [%]	**27**	**38**	**52**	**74**		
Spacer	**D15**	**D30**	**D45**	**D60**		
$C_{d,f}/C_d$ [%]	**37**	**43**	**62**	**84**		

Fig. 5-2 and **Fig. 5-3** show that the drag coefficient depends on the Reynolds number Re_M for non-Newtonian fluids and for the spacers A15 and D15, respectively.

The form drag coefficient for spacer A15 is much larger than for spacer D15. The form drag coefficient becomes dominant, with increase in Reynolds number, while friction drag coefficient decreases linearly with increase in Reynolds number. Therefore the effect of the frictional resistance becomes smaller, when the transition from laminar to turbulence flow occurs. Here the form drag becomes dominant.

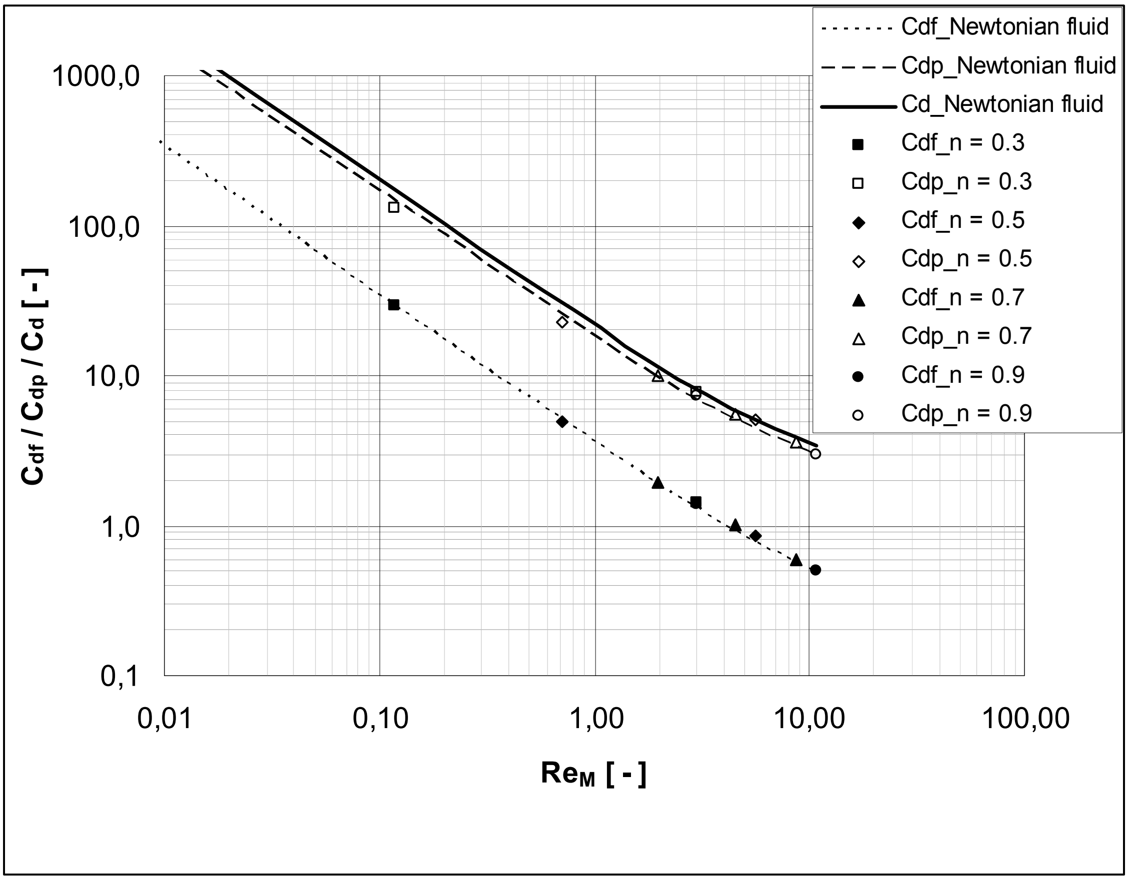

Fig. 5-2 Drag coefficient contribution and development in spacer A15 (λ/a = 4, φ = 15°)

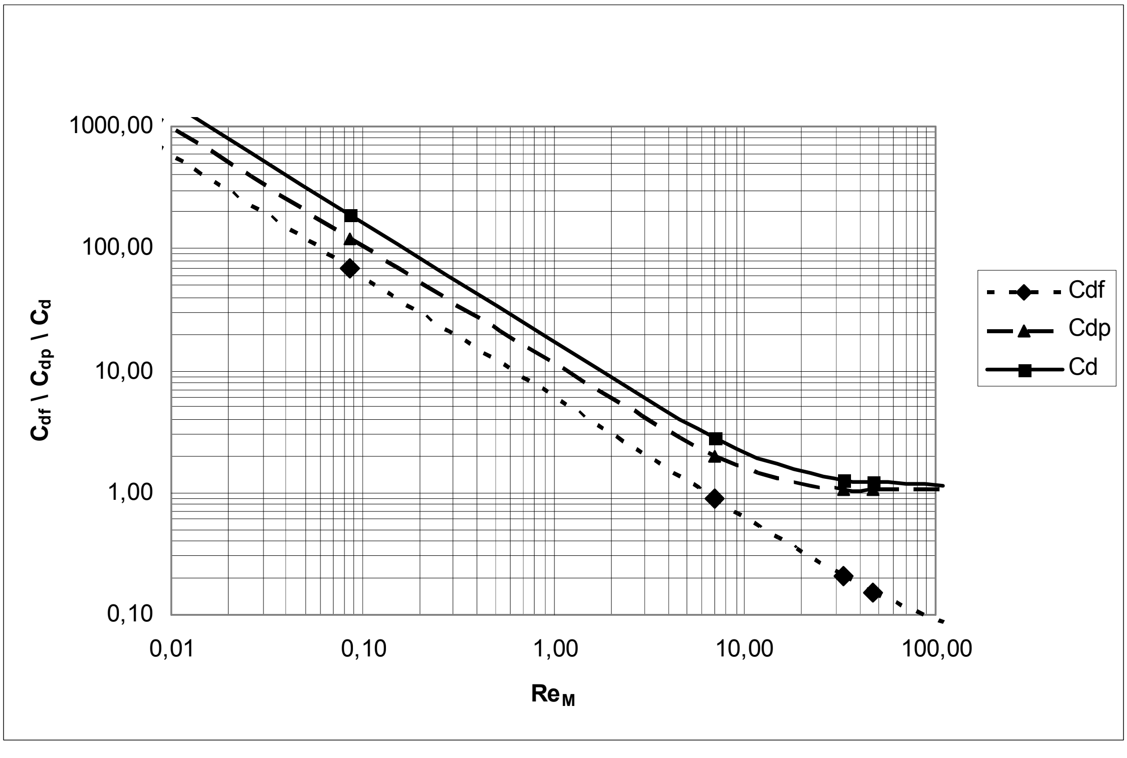

Fig. 5-3 Drag coefficient contribution and development in spacer D15 (λ/a = 11, φ = 15°)

5.4 Effect of the flow index n

Correlation between Reynolds number and drag coefficient (here C_d is identical to the friction factor f) fits the constant = 16 very well, if the flow is laminar fully developed and steady. The results show that this correlation is independent of the spacer geometry, fluid properties and operating parameters, if an adapted definition of Reynolds number Re_M is used.

For spacers with large inclination angle (e.g. spacer A75 in **Fig. 5-4**), in a logarithmus diagram a linear correlation can be maintained, up to a Reynolds number of several hundreds. The correlation between Reynolds number and drag coefficient remains unchanged, even if an extreme value of flow index n = 0.03 is taken into account.

For spacers with smaller angle, a deviation from the linear correlation can be observed for low level Reynolds numbers (e.g. spacer D15 in **Fig. 5-5**).

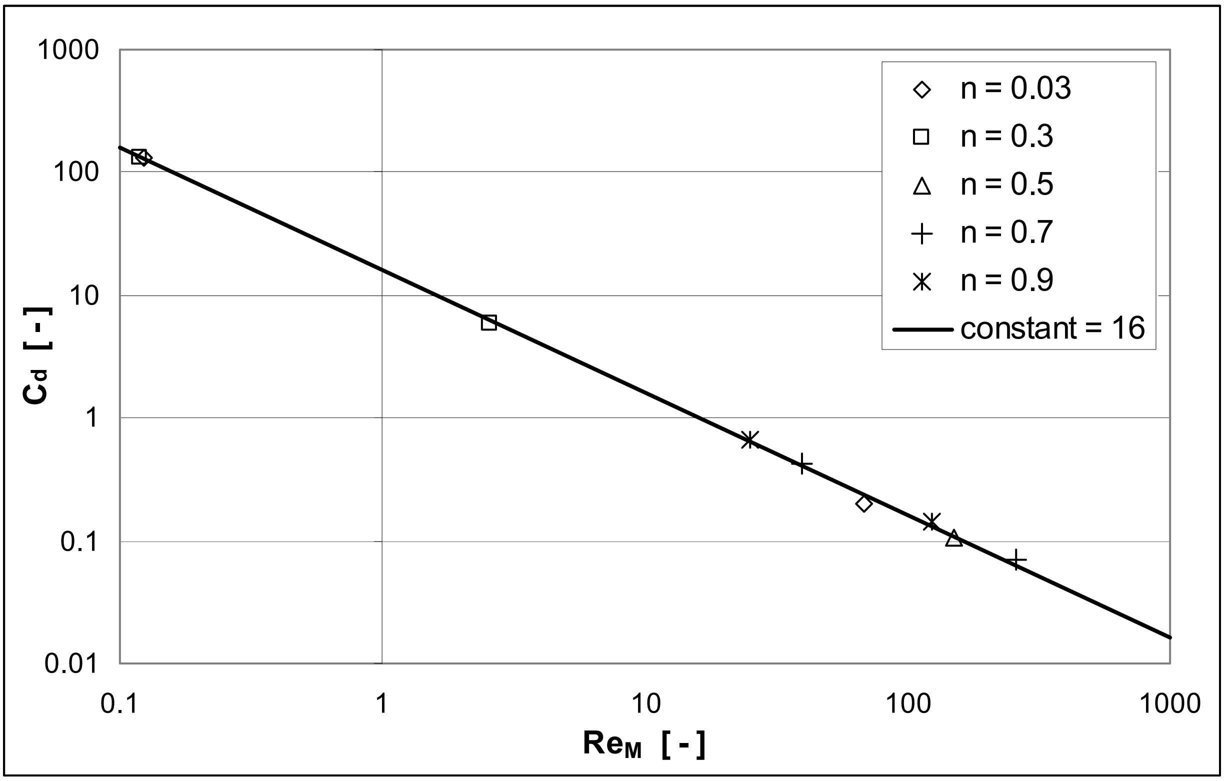

Fig. 5-4 Correlation between Reynolds number and drag coefficient in spacer A75 for non-Newtonian fluids with different flow indexes

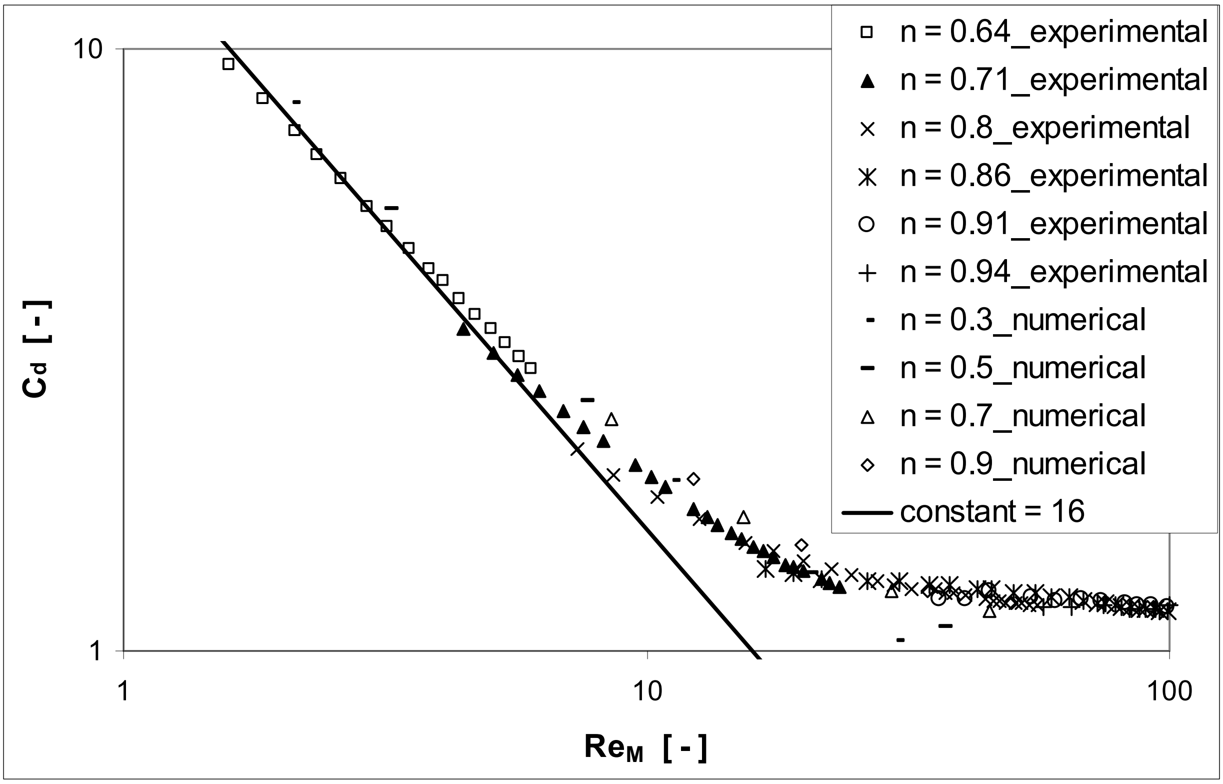

Fig. 5-5 Correlation between Reynolds number and drag coefficient in spacer D15 for non-Newtonian fluids with different flow indices

5.5 Comparison of the experimental results between Newtonian and non-Newtonian fluids

A comparison of the experimental results between Newtonian and non-Newtonian fluids was made for spacer-filled channel flows. The data for the Newtonian case cited here are from the previous work of Zimmerer [77]. A satisfactory agreement of the experimental results between Newtonian and non-Newtonian fluids is shown in **Fig. 5-6** to **Fig. 5-8**.

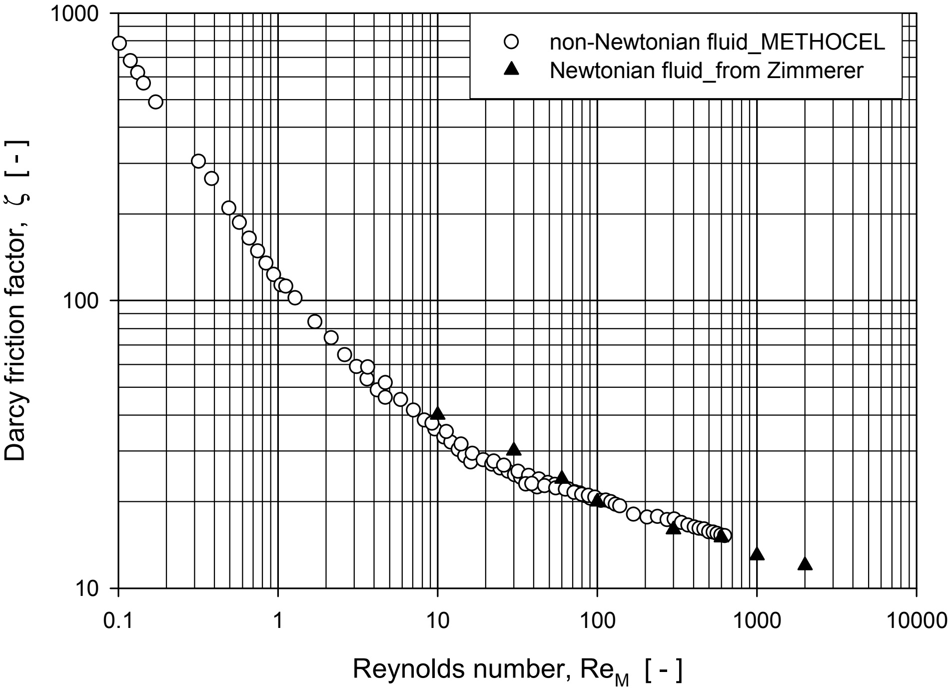

Fig. 5-6 Friction factor of Newtonian and non-Newtonian fluids in spacer-filled channel with λ / a = 5.5, φ = 15°

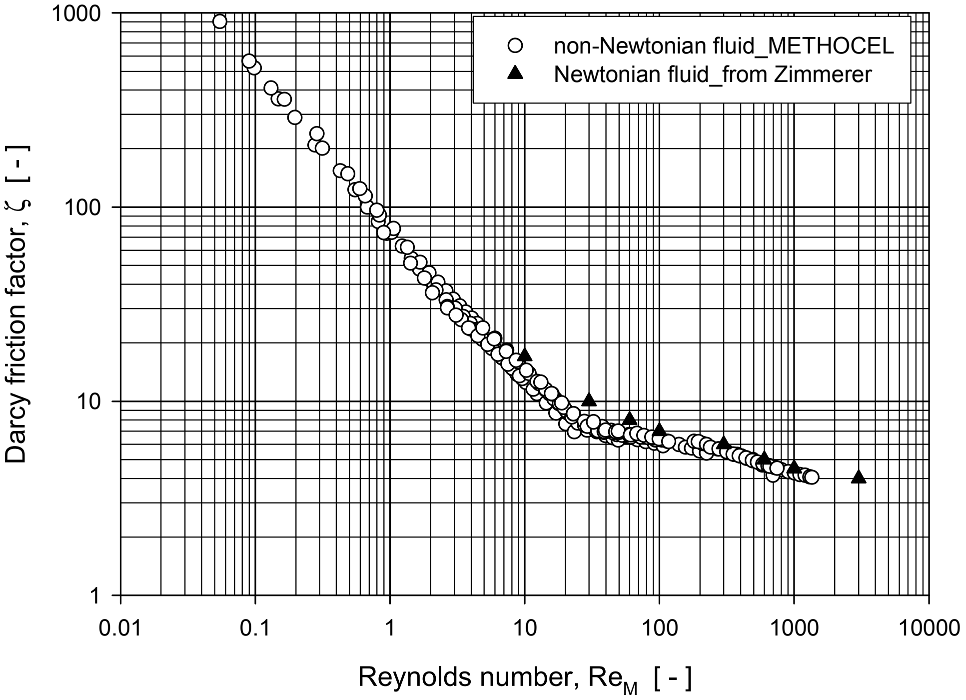

Fig. 5-7 Friction factor of Newtonian and non-Newtonian fluids in spacer-filled channel with λ / a = 5.5, φ = 30°

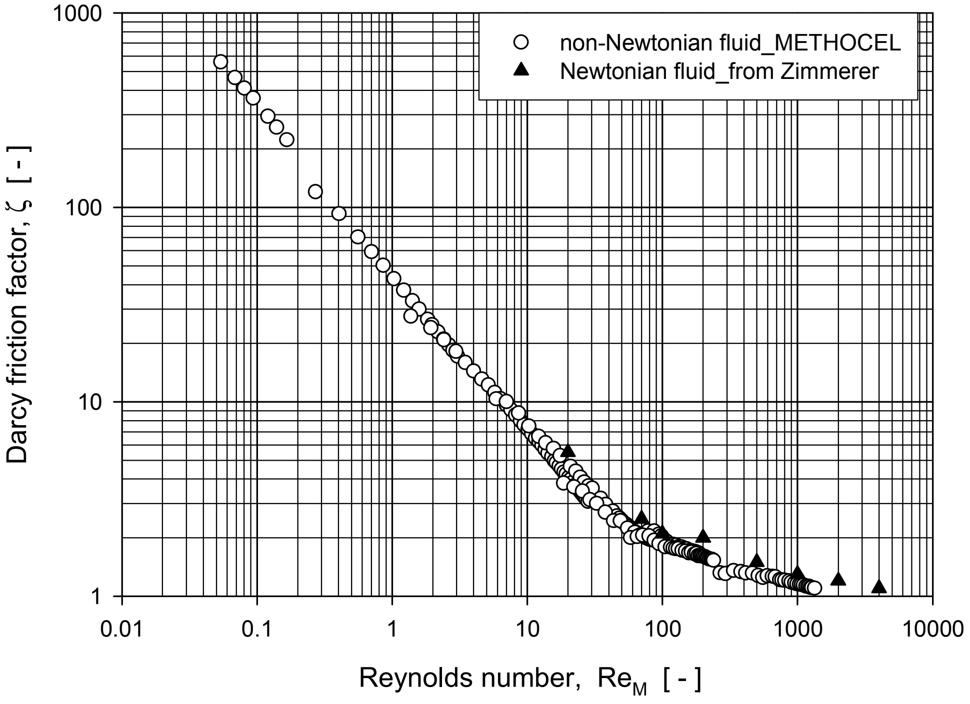

Fig. 5-8 Friction factor of Newtonian and non-Newtonian fluids in spacer-filled channel with λ / a = 5.5, φ = 45°

5.6 Effect of the geometric parameters λ/a and φ

The effect of the geometric parameters λ/a and φ on the drag coefficient Cd over the Reynolds number are presented in **Fig. 5-9** to **Fig. 5-17**. The correlation between C_d and Re_M agrees to the relationship $C_dRe_M = 16$ very well for low Reynolds numbers, but a deviation can be observed when the Reynolds number becomes higher and the transition from laminar to turbulent state occurs. The deviation is cumulative and develops slowly as well as gradually.

The experimental and numerical results are in quite good agreement, as these diagrams prove.

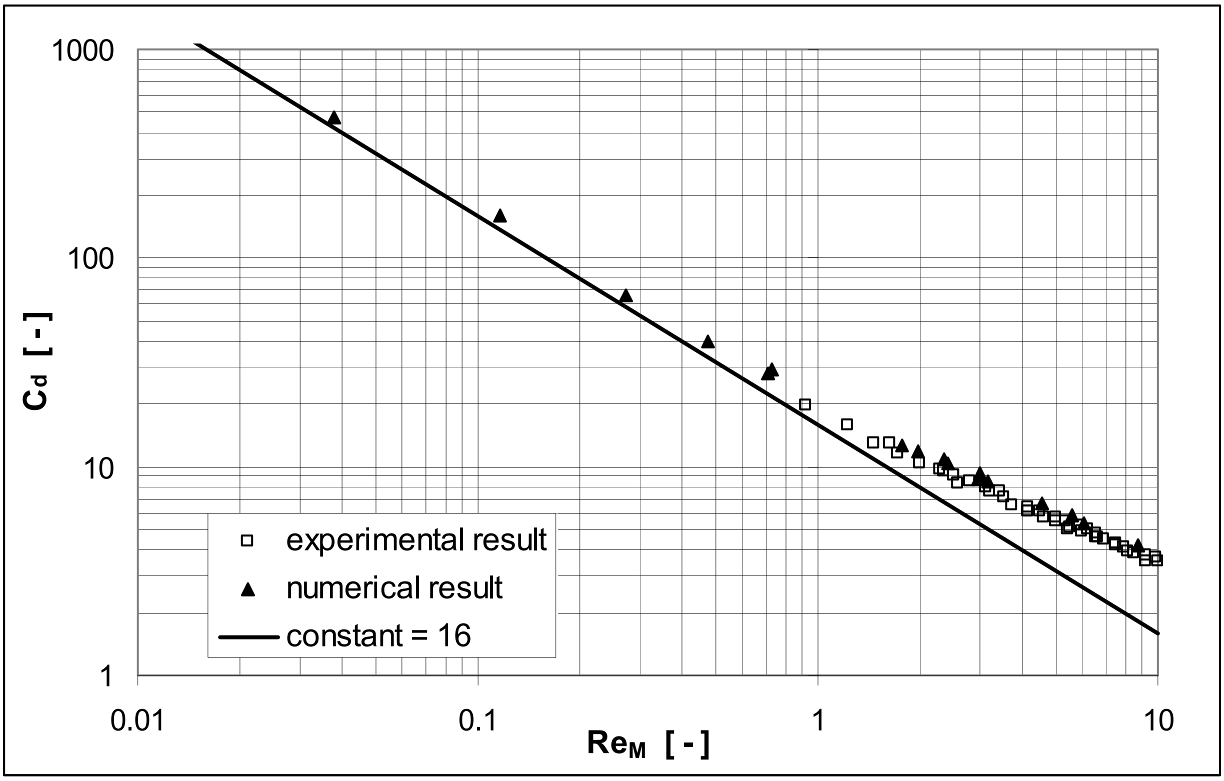

Fig. 5-9 Correlation between Reynolds number and drag coefficient for spacer A15 ($\lambda/a = 4$, $\varphi = 15°$)

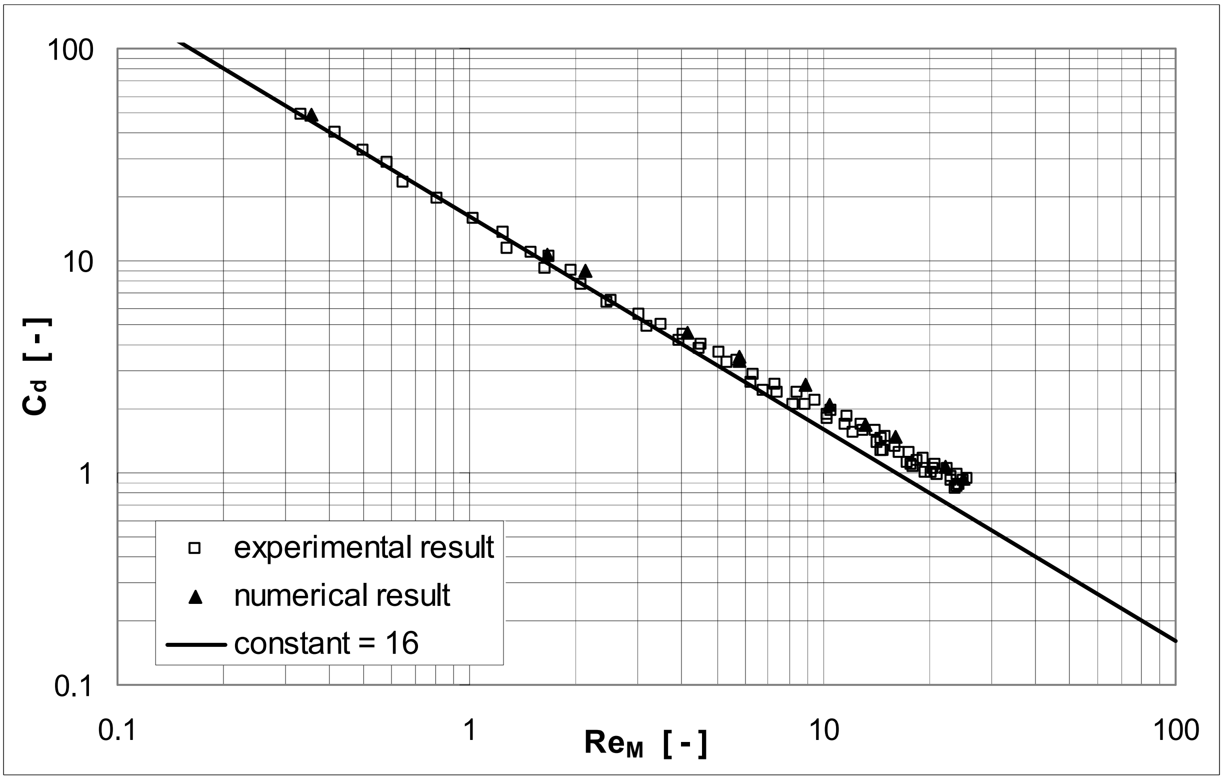

Fig. 5-10 Correlation between Reynolds number and drag coefficient for spacer A30 ($\lambda/a = 4$, $\varphi = 30°$)

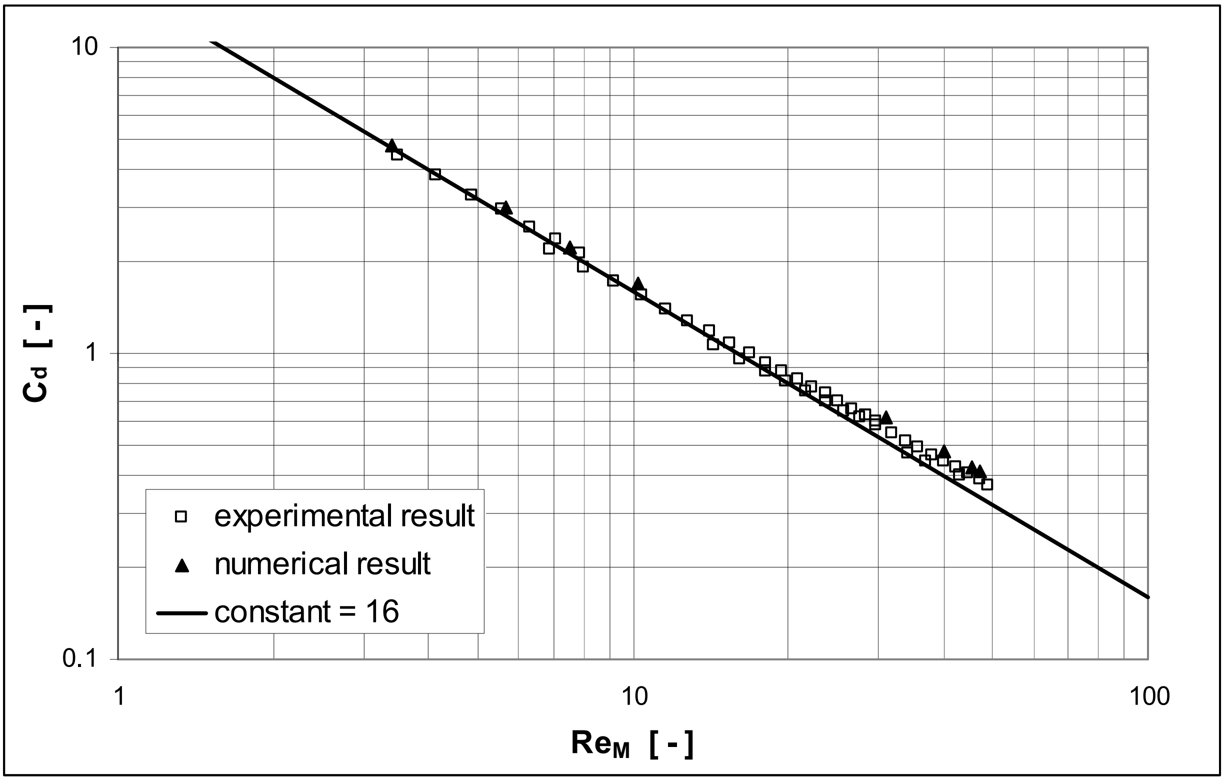

Fig. 5-11 Correlation between Reynolds number and drag coefficient for spacer A45 (λ/a = 4, φ = 45°)

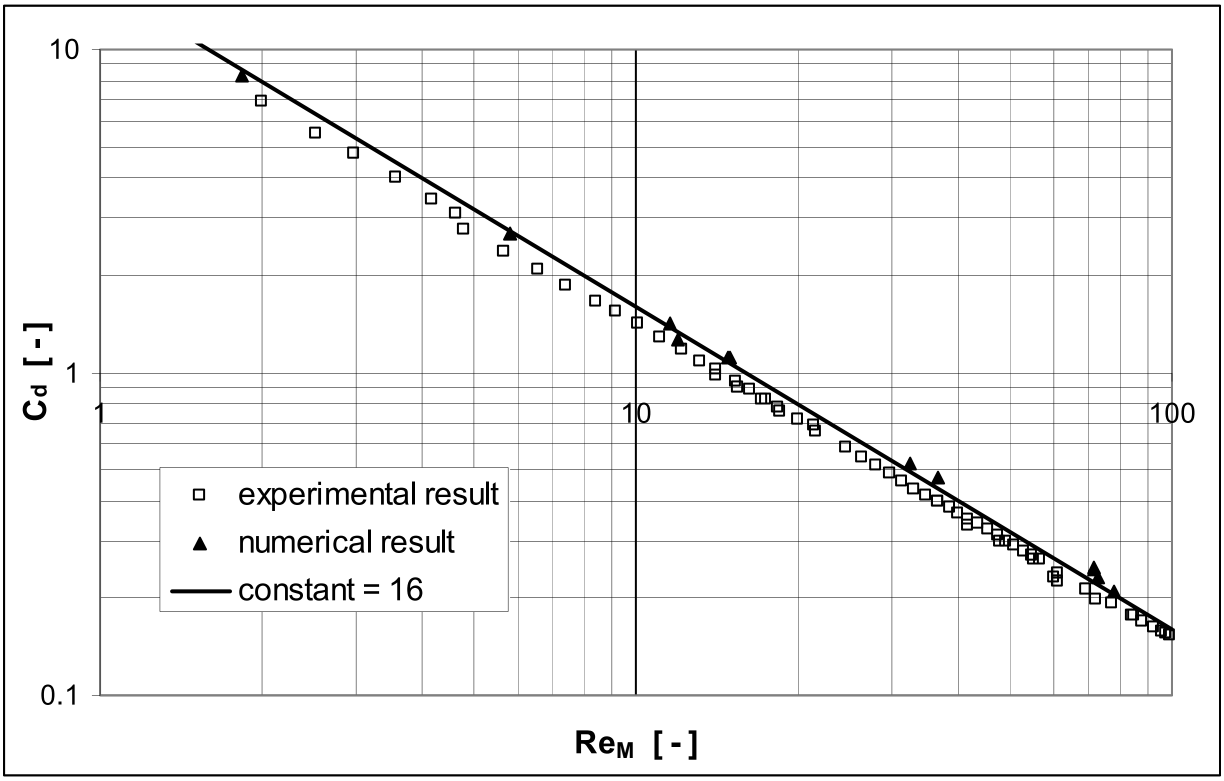

Fig. 5-12 Correlation between Reynolds number and drag coefficient for spacer A60 (λ/a = 4, φ = 60°)

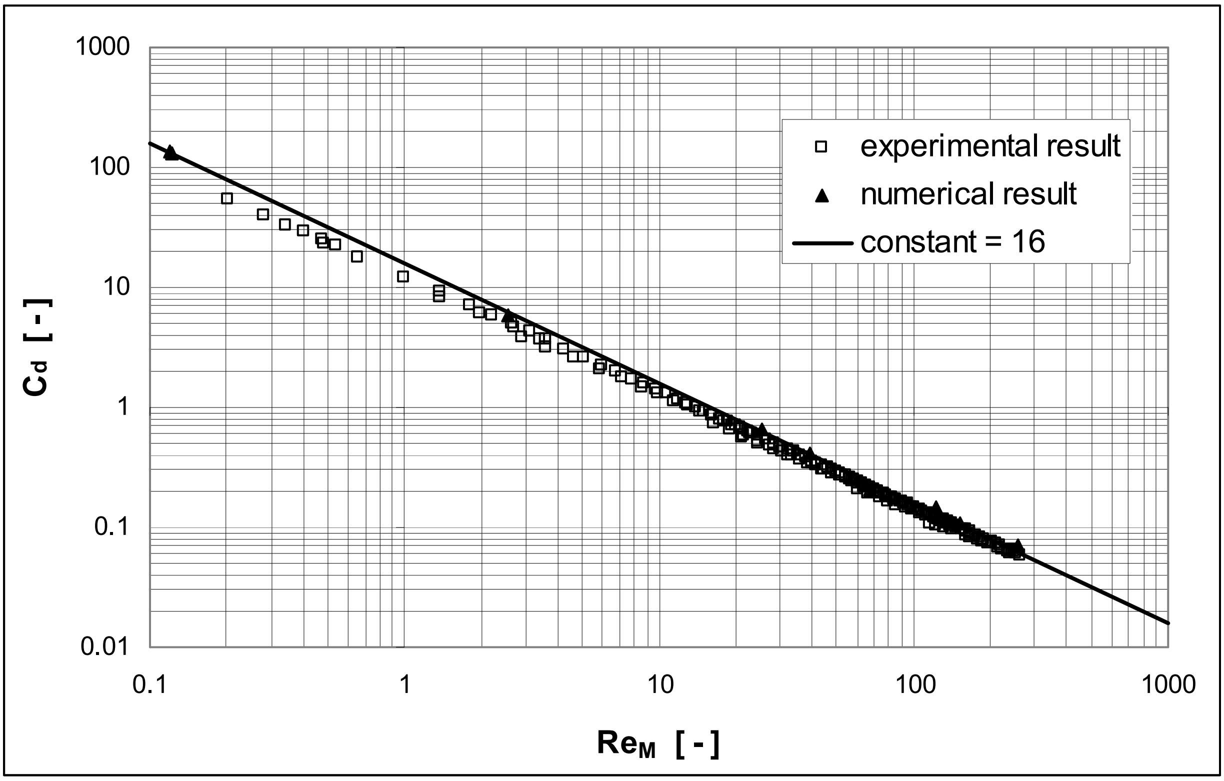

Fig. 5-13 Correlation between Reynolds number and drag coefficient for spacer A75 (λ/a = 4, φ = 75°)

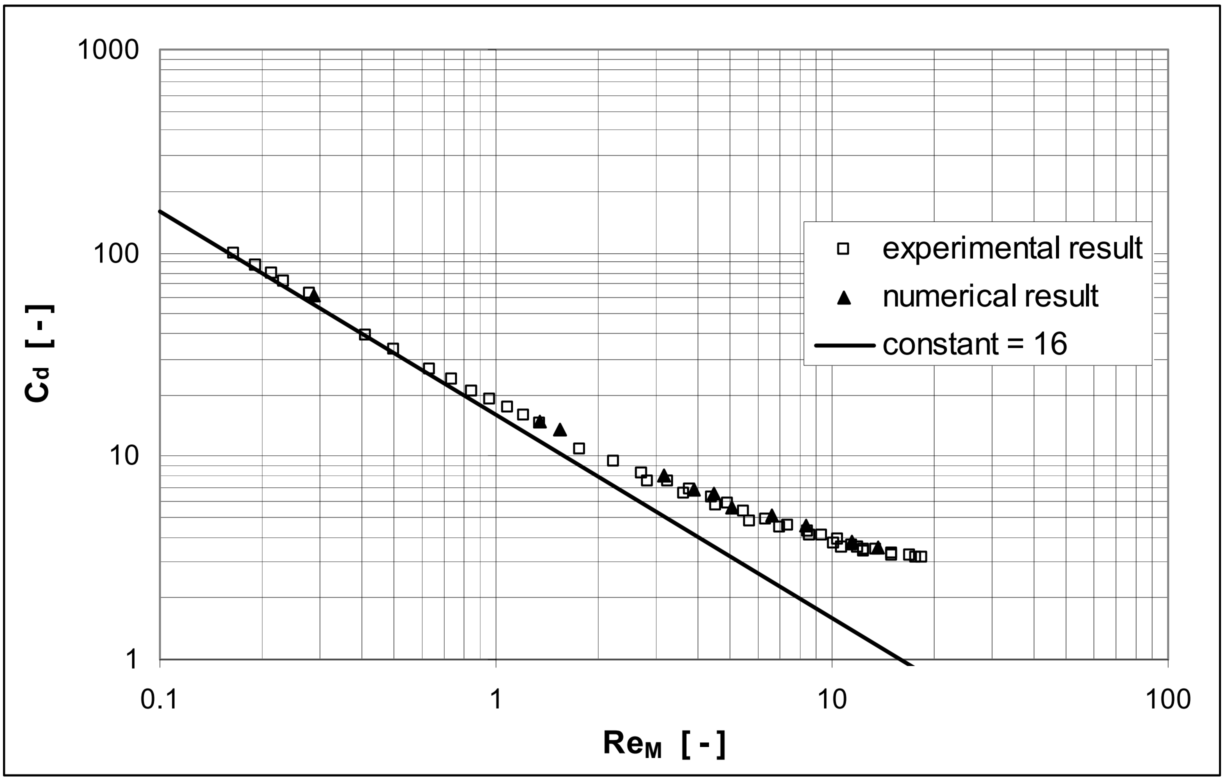

Fig. 5-14 Correlation between Reynolds number and drag coefficient for spacer B15 (λ/a = 5.5, φ = 15°)

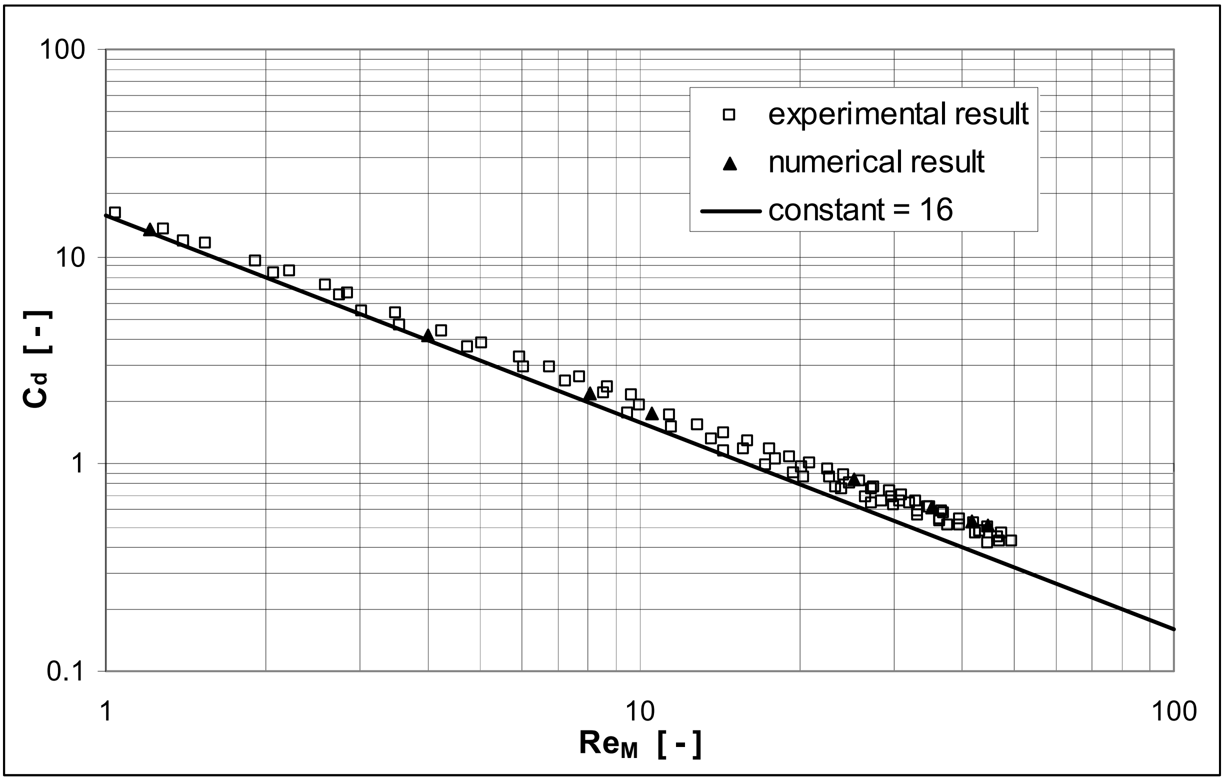

Fig. 5-15 Correlation between Reynolds number and drag coefficient for spacer B45 (λ/a = 5.5, φ = 45°)

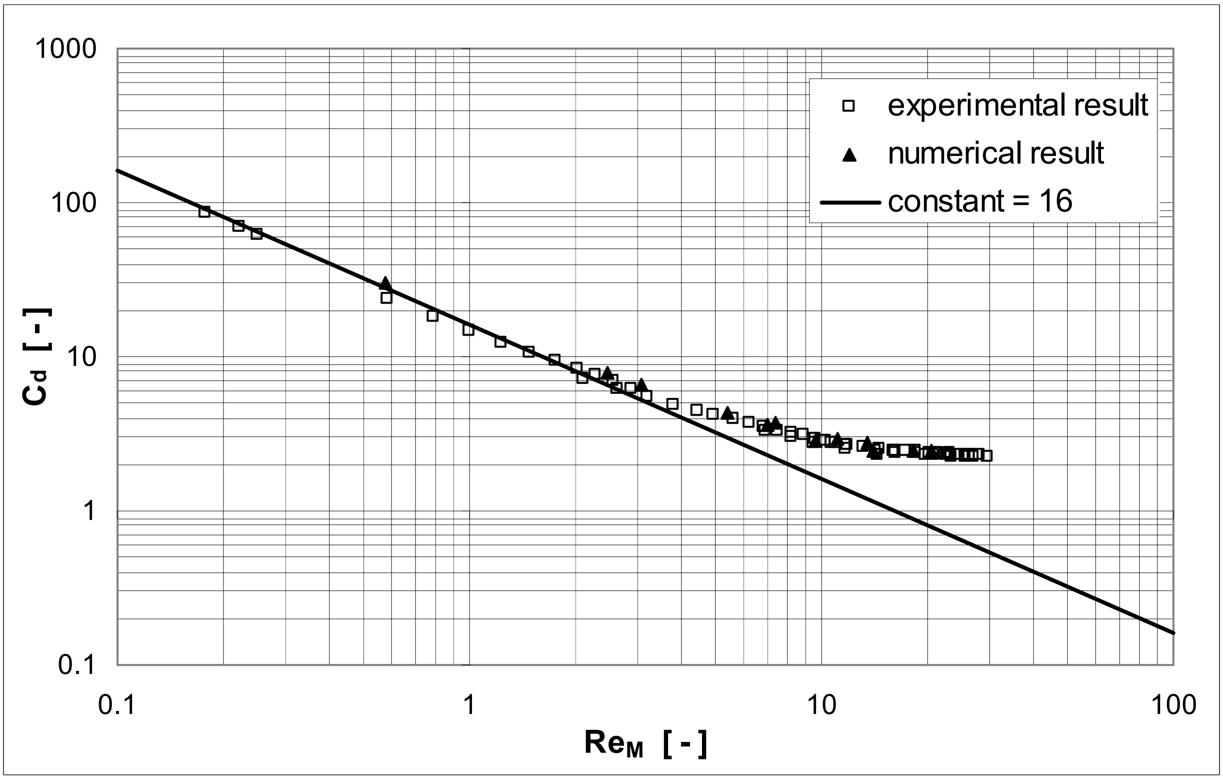

Fig. 5-16 Correlation between Reynolds number and drag coefficient for spacer C15 (λ/a = 7.45, φ = 15°)

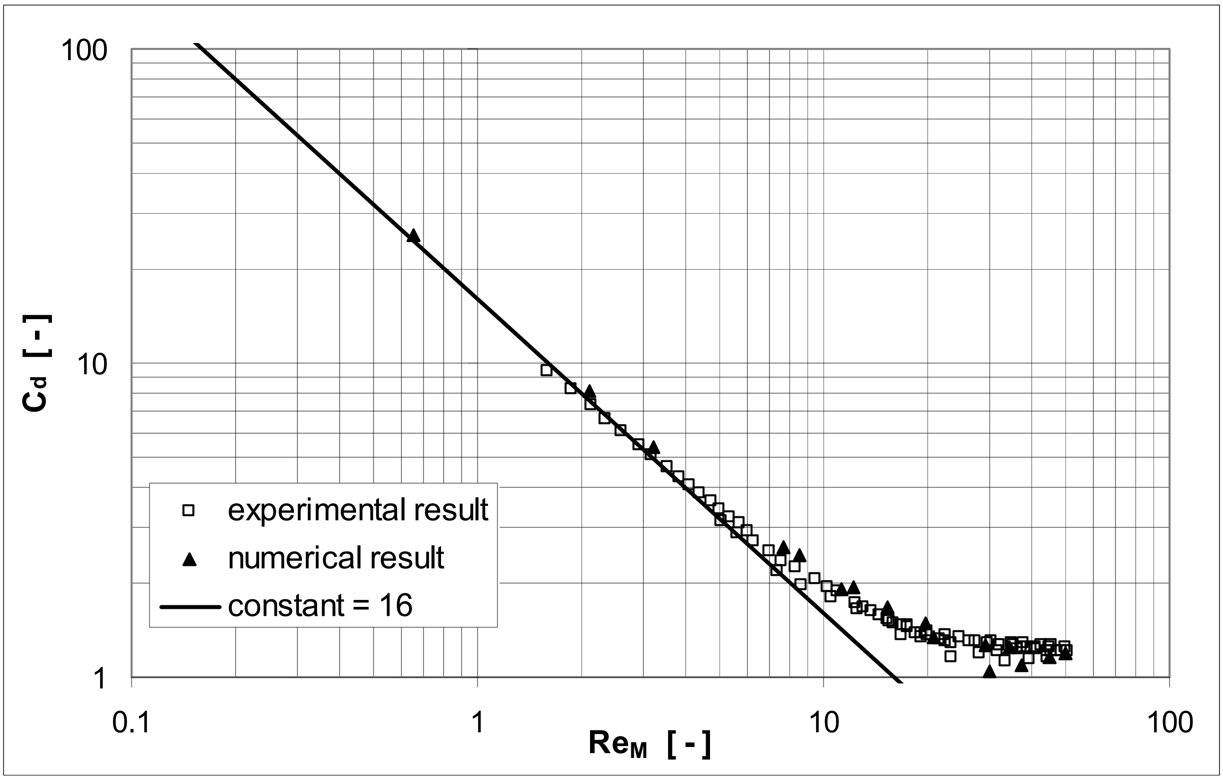

Fig. 5-17 Correlation between Reynolds number and drag coefficient for spacer D15 ($\lambda/a = 11$, $\varphi = 15°$)

5.7 Effect of Reynolds number

The dependency of the drag coefficient on Reynolds number in a higher Re-range was further investigated experimentally. With increasing Reynolds number, the flow in spacer-filled channels can show a very good mixing behavior induced by secondary flows with flow separations and vortices. The form drag increases dominantly as mentioned in **section 5.3**, if a transition from laminar to turbulent flow is observed. The transition for the different spacers strongly depends on the geometric parameters.

For smaller inclination angles, the transition usually occurs for lower Reynolds numbers. For spacers A in **Fig. 5-18**, transition points at the Reynolds number 10, 40, 200, 500 and 1300 can be found for the inclination angle of 15°, 30°, 45°, 60° and 75°, respectively. Similar results can also be found for spacers B (**Fig. 5-19**), C (**Fig. 5-20**) and D (**Fig. 5-21**).

On the other side, for smaller wavelength at a certain inclination angle, the transition usually also occurs earlier, as the comparisons between different wavelengths, but constant inclination angle prove, from **Fig. 5-22** to **Fig. 5-24**.

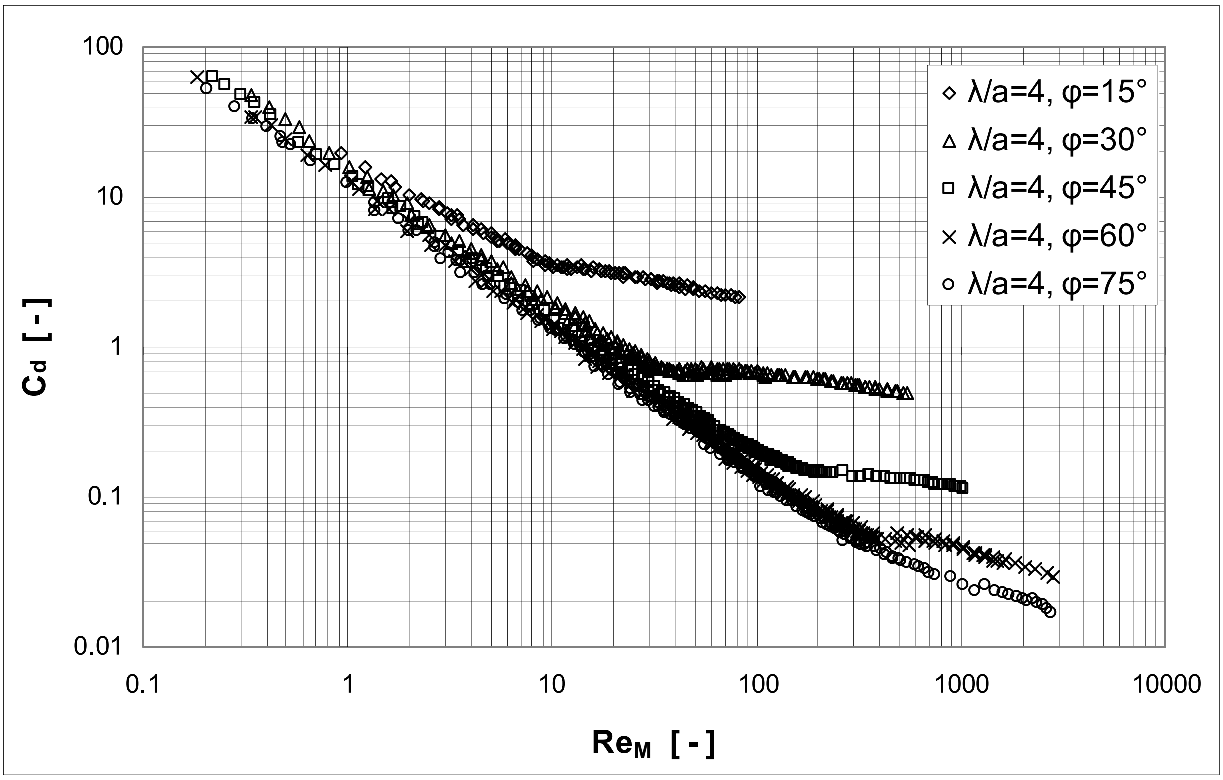

Fig. 5-18 Drag coefficient C_d vs. Reynolds number for non-Newtonian fluids in spacers A with different inclination angles λ = 15-75°

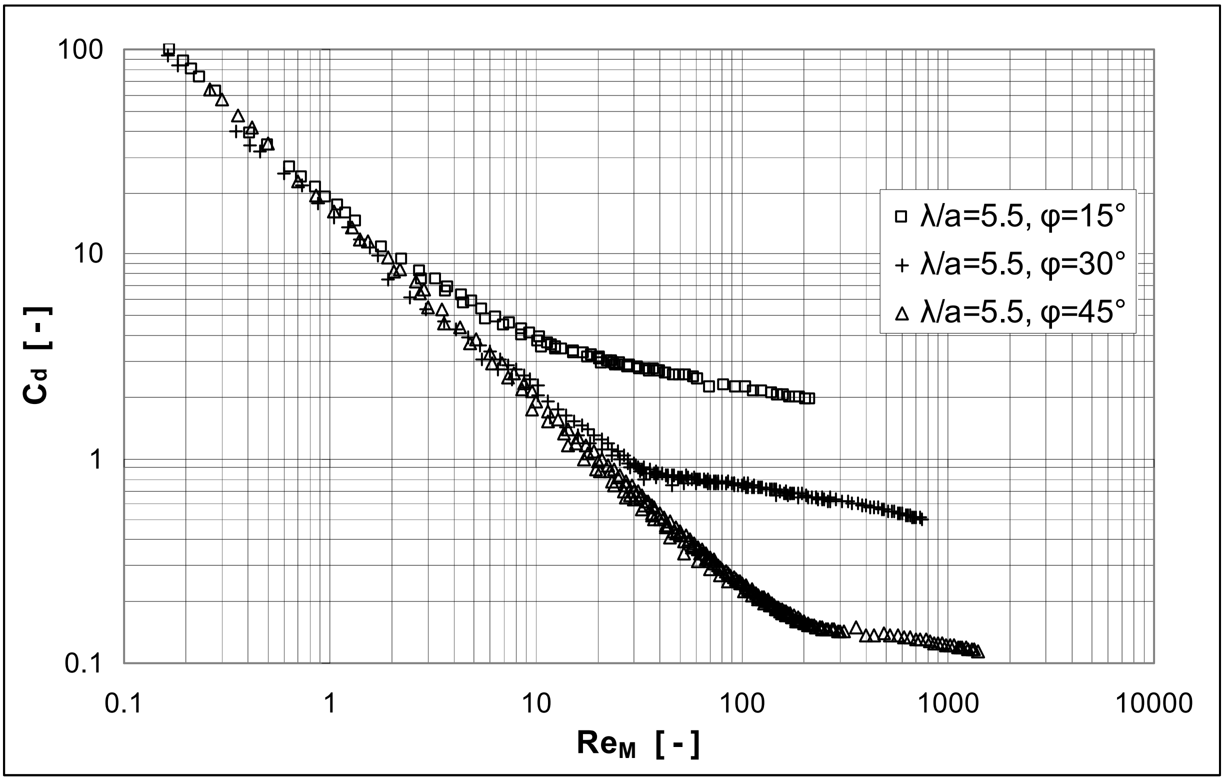

Fig. 5-19 Dependency of drag coefficient on Reynolds number for non-Newtonian fluids in spacers B with different inclination anglesλ = 15-45°

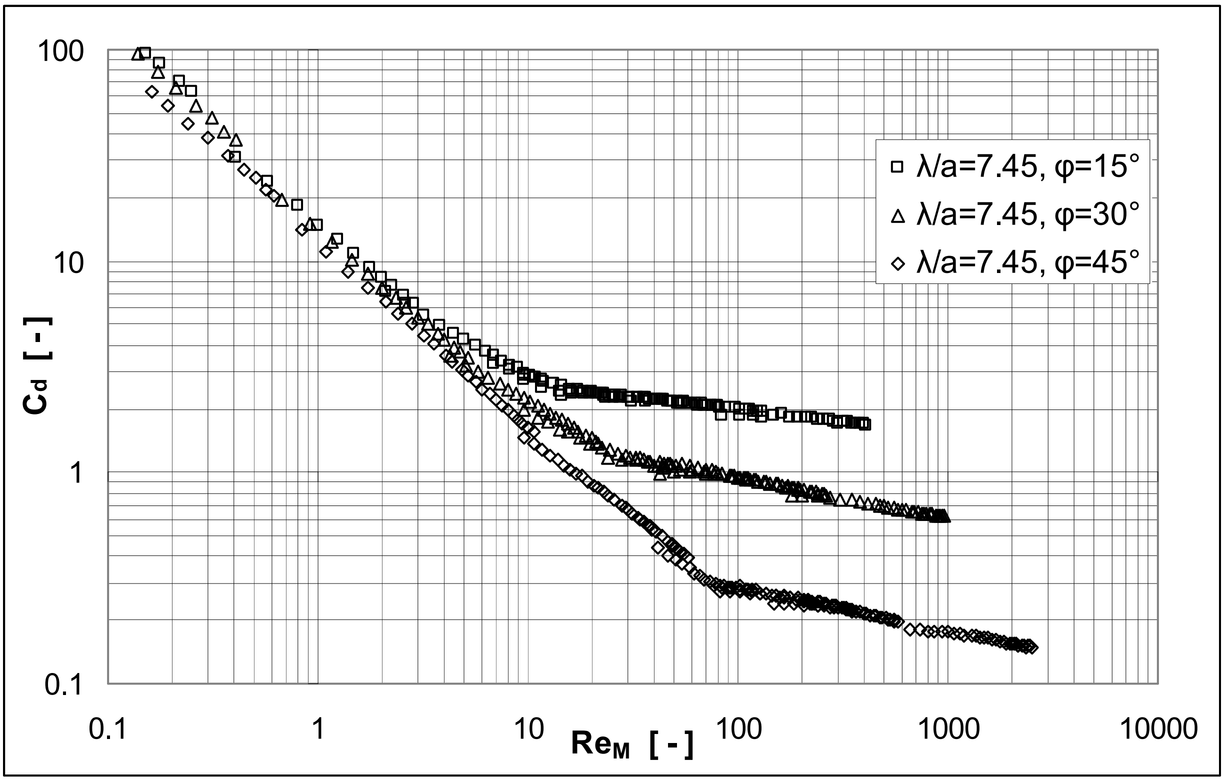

Fig. 5-20 Dependency of drag coefficient on Reynolds number for non-Newtonian fluids in spacers C with different inclination angles λ = 15-45°

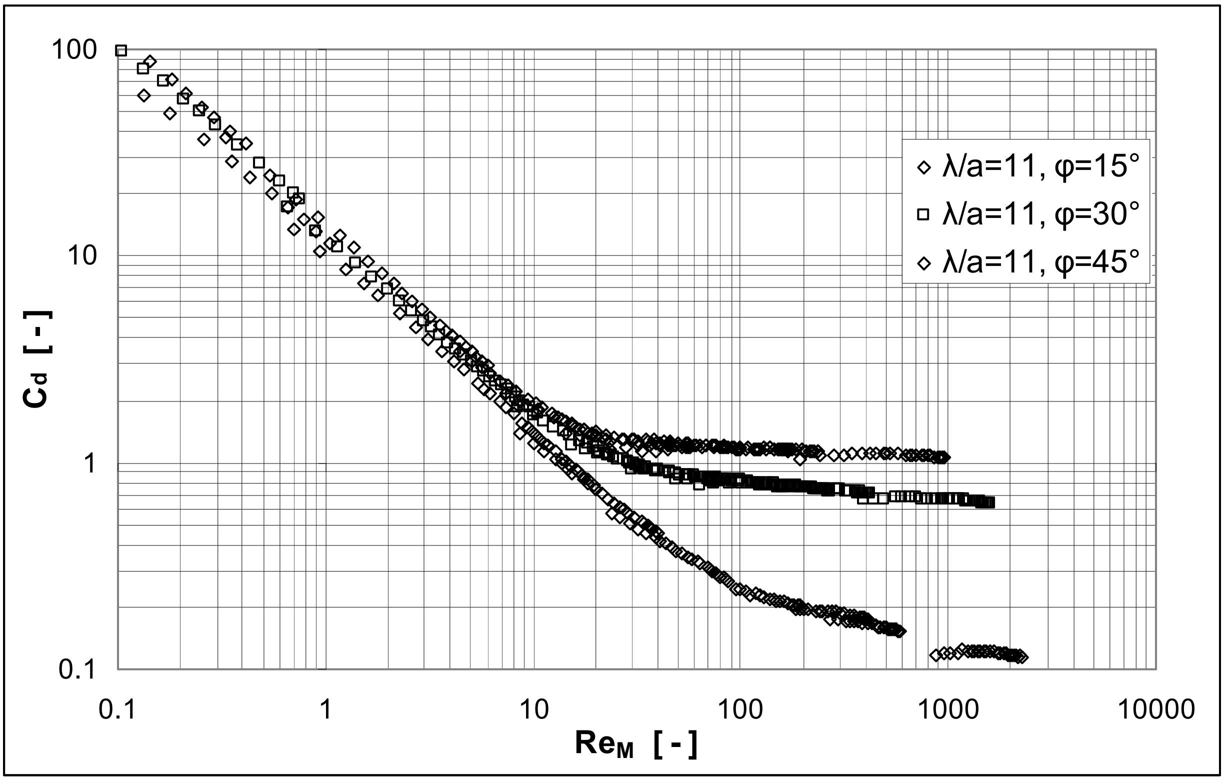

Fig. 5-21 Dependency of drag coefficient on Reynolds number for non-Newtonian fluids in spacers D with different inclination anglesλ = 15-45°

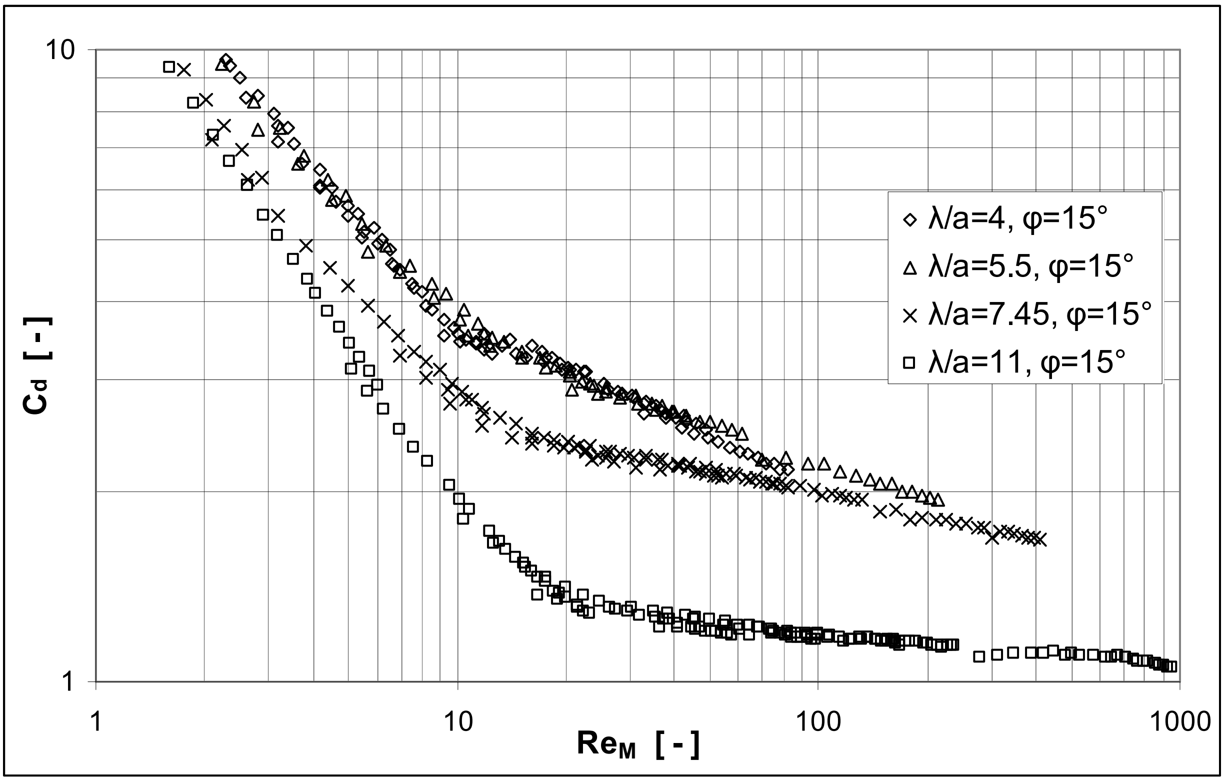

Fig. 5-22 Dependency of drag coefficient on Reynolds number for non-Newtonian fluids in spacers with a same φ= 15° but different λ/a = 4-11

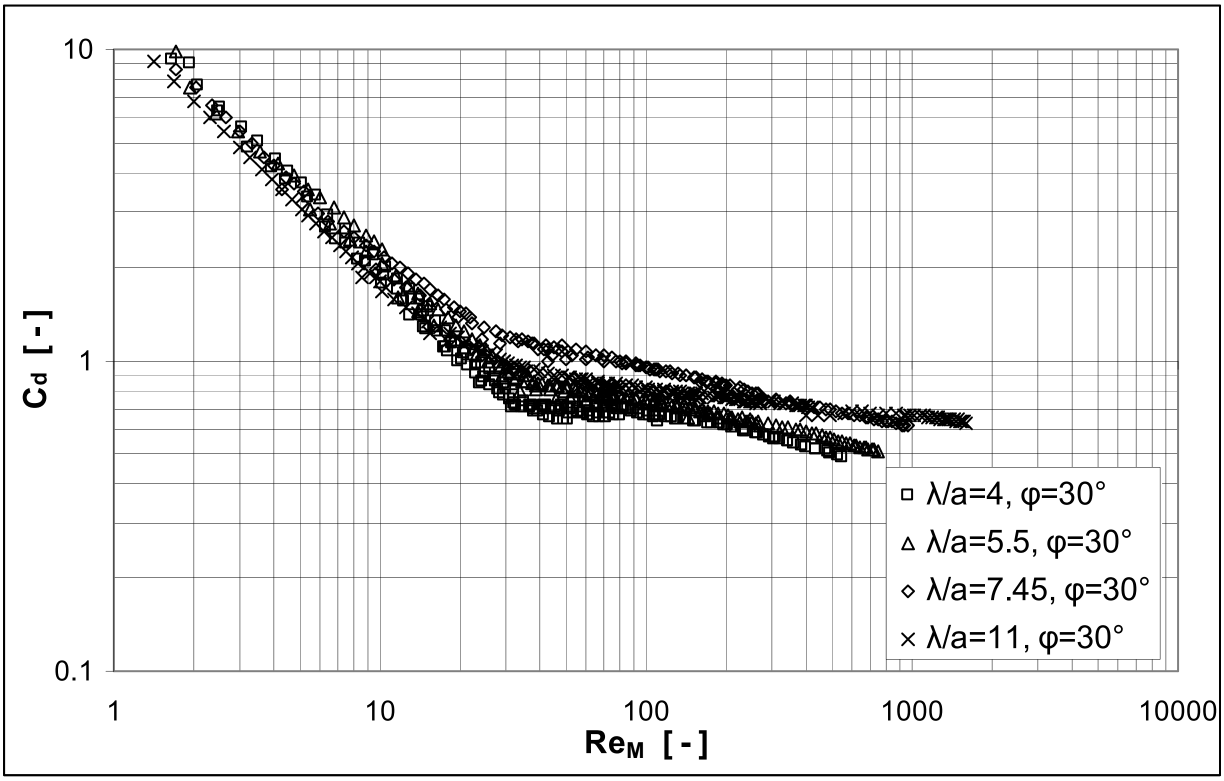

Fig. 5-23 Dependency of drag coefficient on Reynolds number for non-Newtonian fluids in spacers with a same φ= 30° but different λ/a = 4-11

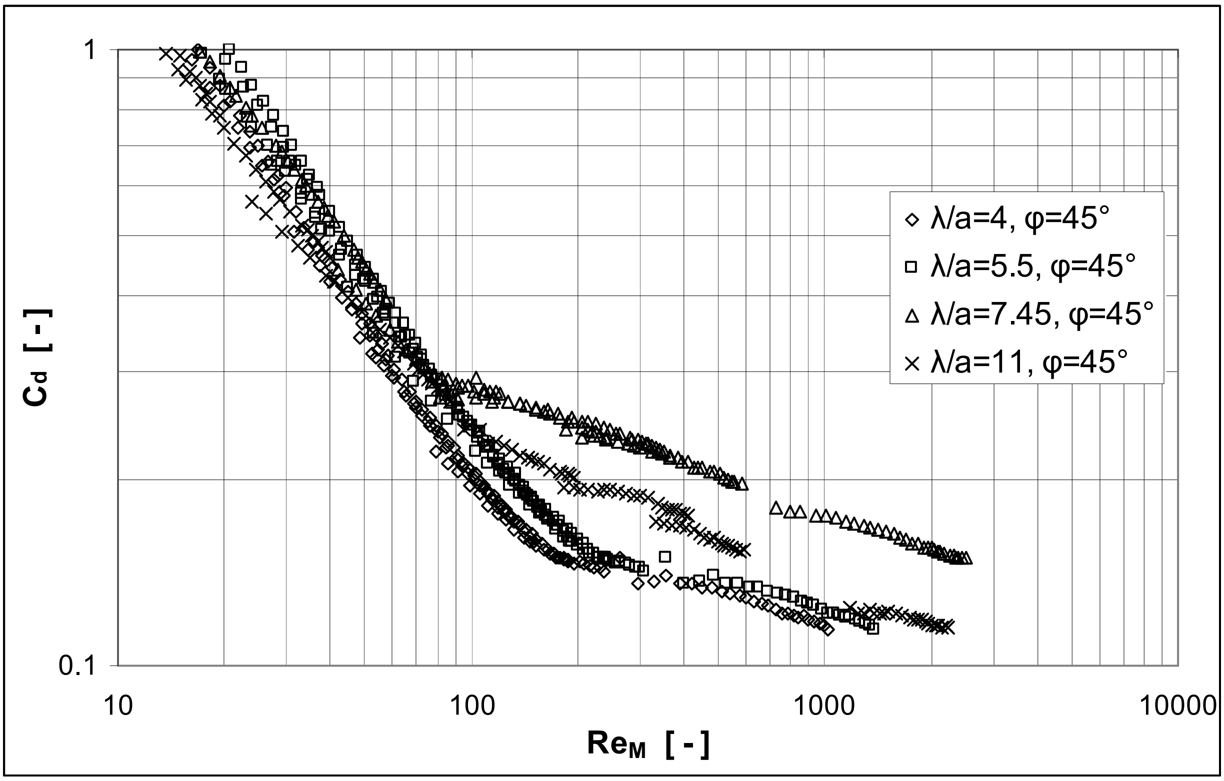

Fig. 5-24 Dependency of drag coefficient on Reynolds number for non-Newtonian fluids in spacers with a same φ= 45° but different λ/a = 4-11

6 Fully developed mass transfer in spacer-filled channels

6.1 Dimensionless quantities

6.1.1 Mass transfer coefficient

The transport law for the transferred mass of the specific Acidol-Blue per surface area can be written as

$$\dot{m} = \beta \cdot (C_b - C_w)$$

Eqn. 6-1

Under the assumption of chemisorption, it can be proved, that the dye reacts fast with the surface A of a polyamide membrane and is fixed quantitatively, so that the wall concentration can be assumed to be $C_w \sim 0$. The mass transfer coefficient is then constant, $\beta = const.$, for small concentrations C_b. The locally transferred mass per area can thus be expressed as

$$b = \frac{m}{A} = \int_0^t \dot{m} \cdot dt = \int_0^t \beta \cdot (C_b - C_w) \cdot dt = \beta \cdot \int_0^t C_b \cdot dt$$

Eqn. 6-2

As the amount of dye in the solution changes only in a very small scale during the experimental run, C_b can be taken as constant

$$b = \beta \cdot C_b \cdot t$$

Eqn. 6-3

where t is the residence time, during which the surface to be investigated is exposed to the Acidol-Blue-METHOCEL®-solution. Based on Eqn. 3-7, the local color density of Acidol-Blue b can be determined by remission photometry. The local mass transfer coefficient then is

$$\beta = \frac{b}{C_b\, t}$$

Eqn. 6-4

Here, taking the spacer C30 as an example, the visualization of transferred mass distribution for a non-Newtonian fluid flow is shown in Fig. 6-1. The visualization of mass transfer distribution for other spacers can be found in the Appendix.

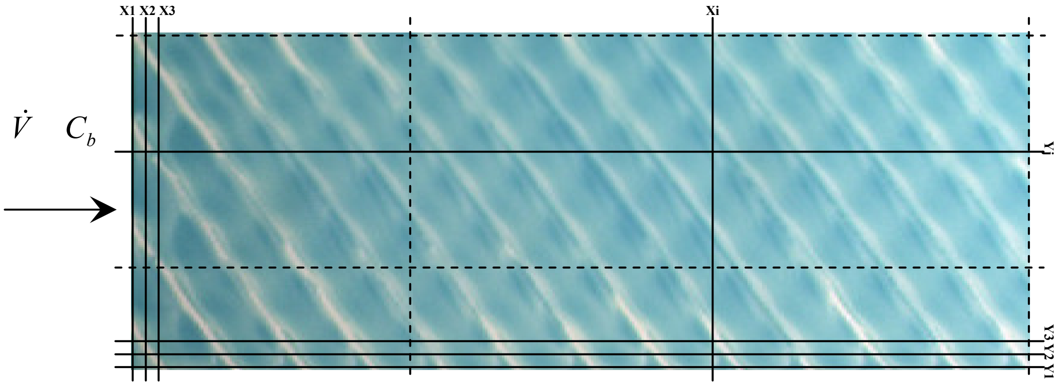

Fig. 6-1 Visualizition of mass transfer distribution for a non-Newtonian fluid flow in a spacer-filled channel, λ/a = 7.45, φ = 30^o, 0.5% METHOCEL® K15M, Re$_M$ = 50.

The local remission R values, at the positions X1, X2, X3 … Xi and Y1, Y2, Y3…Yj for the coordinates in streamwise and spanwise direction, respectively, were measured by remission photometer. The local color density of Acidol-Blue can then be determined. The color density distribution over flow entrance length is presented in **Fig. 6-2**.

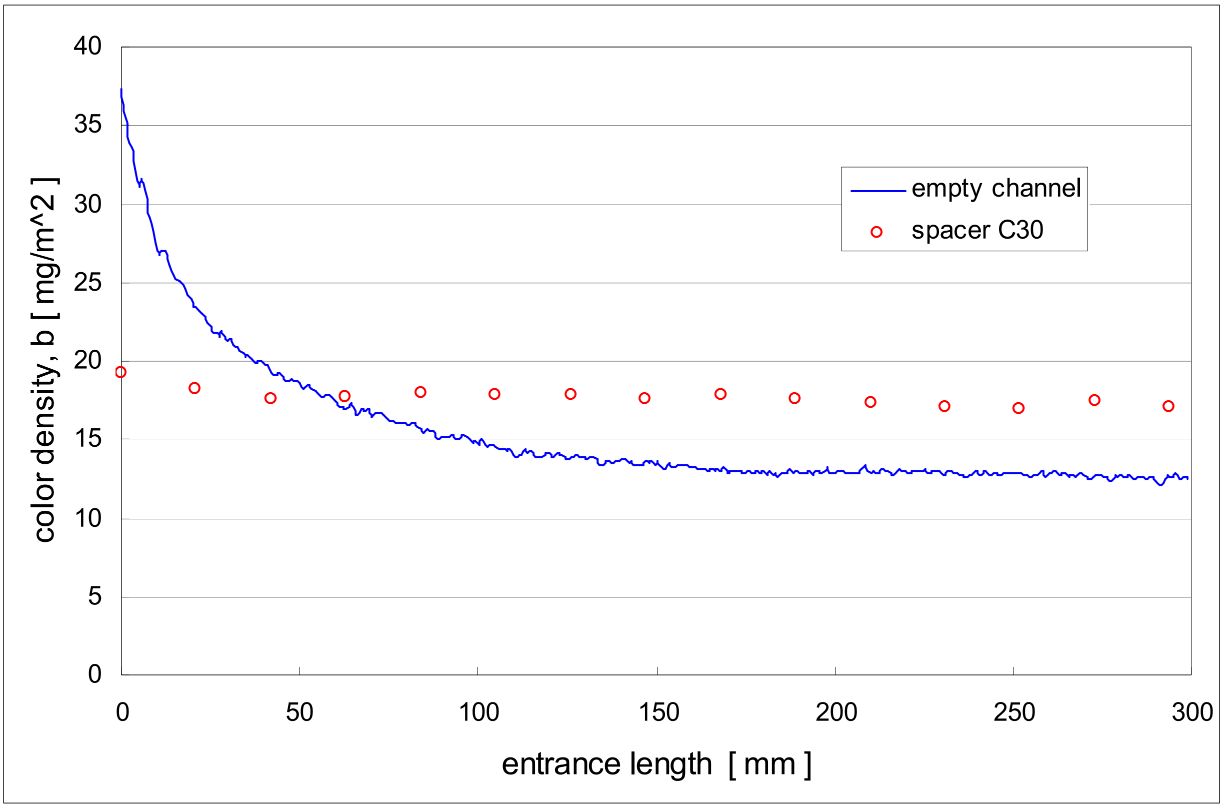

Fig. 6-2 Quantification of the transferred mass for a non-Newtonian fluid flow in a spacer-filled channel at the surface of the PA membrane in Fig. 6-1.

6.1.2 Schmidt number

For non-Newtonian fluids, dynamic viscosity is shear rate (velocity gradient) dependent. Local shear rate is spatially dependent due to the three dimensional complex flow in spacer-filled channels. Although local vector information, such as velocity gradient, can easily be extracted from the solution results of the CFD code, there is no way, however, in industrial practices to obtain such information. A relationship between local (e.g. shear rate or velocity gradient) and bulk (e.g. volume flow) values therefore makes sense for in the prediction of physical variables. In the most simple case of Newtonian fluids in tubes, for example, $\dot{\gamma} = \frac{8 \cdot \overline{w}}{d_h}$. Likewise for modified power law non-Newtonian fluids in spacer-filled channels, after taking the geometric correction parameters a^* and b^*, and the Reynolds correction factor β^* into account, an effective viscosity can be determined:

For shear thinning modified power law non-Newtonian fluids by

$$\eta_M = \frac{\eta_0 \cdot \left(a^* + b^*\right)}{1 + \beta^*}$$

Eqn. 6-5

and for shear thickening modified power law non-Newtonian fluids by

$$\eta_M = \frac{\eta_0 \cdot \left(a^* + b^*\right)}{\dfrac{\beta^*}{1 + \beta^*}}$$

Eqn. 6-6

The Schmidt number is then defined by

$$Sc = \frac{\eta_M}{\rho \cdot D}$$

Eqn. 6-7

Here the diffusion coefficient D, as measured by PFG-NMR method, is taken to estimate the Schmidt number, assuming that D is independent of shear rate. Although the apparent viscosity for non-Newtonian fluids is surely shear rate dependent, this has been accounted for in the variable of η_M. This assumption is based on experimental results of CMC solutions measured by Couette-flow method [95], rotating-disc electrode method [96] and by unsteady diffusion method [97]. In this experimental observation, an explanation was given by [96] that the CMC molecular may be considered as a quasi-static frame and the solution is then the electrolyte without polymer, corresponding to a viscosity similar to the one of water.

6.1.3 Nusselt number

The Nusselt number Nu is an important dimensionless parameter, which represents the dimensionless temperature gradient at an interface, where heat transfer by convection is taking place. It is a function of the Reynolds number Re, the Prandtl number Pr, and if the fluid is still at the thermal entry region, the Nusselt number will also vary as a function of the length of the tube. After both the thermal and hydrodynamic boundary layers become fully developed, the Nusselt number becomes uniform. For non-Newtonian fluids in fully developed laminar heat transfer problem, some solutions for a correlation between the Nusselt number of non- and Newtonian fluids are available from [98]-[103]. For power law non-Newtonian fluids in arbitrary cross-section geometry, an interesting correlation has been suggested by [104]:

$$Nu_P = Nu_N \cdot \left(\frac{a^* + b^* \cdot n}{\left(a^* + b^*\right) \cdot n} \right)^{\left(1/3\right)}$$

Eqn. 6-8

When the flow is turbulent, the momentum and thermal boundary layers develop very fast because of the turbulent mixing. For flow in tubes, the critical Reynolds number is ~2300.

Most correlations between Nusselt number and Reynolds number and Prandtl number are variations on the Dittus-Boelter correlation:

$$Nu = \psi \cdot \mathrm{Re}^{\varepsilon} \cdot \mathrm{Pr}^{\omega}$$

Eqn. 6-9

Differences between the correlations are mainly the values of the fluid properties that are used to evaluate the dimensionless numbers (bulk properties, wall properties or something in between). Taking the reference temperature as an example, bulk or "cup mixing" temperature is the most convenient temperature to use in the macroscopic balances [120], which is given by;

$$T_b = \frac{\iint_A w \cdot T \cdot dA}{\iint_A w \cdot dA}$$

Eqn. 6-10

in many early heat transfer studies the film temperature was taken as the reference temperature, which is defined as

$$T_f = \frac{1}{2}\left(T_b + T_w\right)$$

Eqn. 6-11

Besides, sometimes other factors are added to the correlation. The viscosity as a physical property of the fluid is temperature dependent. The temperature gradient will thus bring a viscosity gradient into the thermal boundary layer. A corrected factor of viscosity ratio $\left(\mu_b/\mu_w\right)^{\vartheta}$, which represents the ratio of the viscosity evaluated at the mean bulk temperature to the viscosity evaluated at the mean wall temperature, was added into the correlations in some studies in order to get more accurate predictions.

6.1.4 Sherwood number

As a variable analogous to the Nusselt number in heat transfer, Sherwood number is a very important number for mass transport problems and is defined by:

$$Sh = \frac{\beta \cdot d_h}{D}$$

Eqn. 6-12

which can be conveniently used to determine the Sherwood number, when the mass transfer coefficient has already evaluated by remission photometer (**section 3.1.6** and **section 6.1.1**).

According to Fick's first law,

$$\dot{m} = -\left.\frac{\partial C}{\partial y}\right|_{y=0} \cdot D = \beta \cdot (C_b - C_w)$$

Eqn. 6-13

Then the local Sherwood number can be evaluated by

$$Sh = \frac{-\left.\frac{\partial C}{\partial y}\right|_{y=0} \cdot d_h}{C_b - C_w}$$

Eqn. 6-14

where y = 0 means the concentration gradient is locally at the membrane surfaces, C_w is the local concentration at the wall and C_b is the bulk or mixing cup concentration based on volume and defined by

$$C_b = \frac{\iiint\limits_V w \cdot C \cdot dv}{\iiint\limits_V w \cdot dv}$$

Eqn. 6-15

From **Eqn. 6-14**, the Sherwood number can also be determined by numerical methods. The conclusion that **Eqn. 6-12** and **Eqn. 6-14** are equivalent has been proven in this study.

When we consider the mass transfer problem: If both the concentration and hydrodynamic laminar boundary layers are fully developed, the Sherwood number becomes uniform, but is, however, still geometry and flow index dependent. Similar to **Eqn. 6-8**, correction factors can also be introduced to predict fully developed laminar mass transfer in modified power law non-Newtonian fluids, which are given by **Eqn. 3-23** to **Eqn. 3-25** and have been validated in **section 3.2.4.1**.

Under mass transfer, analogous to the heat transfer problem, the correlation between Sherwood number and Reynolds number and Schmidt number can assumedly be determined by

$$Sh = \psi \cdot \mathrm{Re}_M{}^{\varepsilon} \cdot Sc^{\omega}$$

Eqn. 6-16

For the experiments as well as for the simulations, the topic of mass transfer was selected for this work. The concentration of the added tracer, Acidol-Blue, is very small and has been proven to have no effect on the viscosity of the fluid. During mass transfer, in opposition to heat transfer, the viscosity of the fluid remains unchanged. Therefore the additional effects of the viscosity changed by the temperature need not be considered.

In the case of non-Newtonian flows, only the changes of the viscosity by the fluid properties and shear rates must be considered. The additional temperature properties of non-Newtonian fluids, which make the non-Newtonian flows much more complicated, were not taken into account in this work.

If the viscosity ratio of the non-Newtonian fluids, caused by the shear rate difference in the concentration boundary layer, are considered, the correlation can then given by

$$Sh = \psi \cdot \mathrm{Re}_M{}^{\varepsilon} \cdot Sc^{\omega} \cdot \left({\eta_b}/{\eta_w} \right)^{\vartheta}$$

Eqn. 6-17

where in the term of viscosity ratio $\left({\eta_b}/{\eta_w} \right)^{\vartheta}$, the viscosities are dependent on shear rate due to non-Newtonian characteristics of the fluids. Additional effects of viscosity change by the heat transfer are avoided here.

For mass transfer in modified power law non-Newtonian fluids, correlations can therefore be given for shear thinning non-Newtonian fluids by

$$Sh = \psi \cdot \mathrm{Re}_M{}^{\varepsilon} \cdot Sc^{\omega} \cdot \left[\frac{1 + \dfrac{a^* + b^* \cdot n}{(a^* + b^*)n} \cdot \beta^*}{1 + \beta^*} \right]^{\left(1/3 \right)}$$

Eqn. 6-18

and for shear thickening non-Newtonian fluids by

$$Sh = \psi \cdot \mathrm{Re}_M{}^{\varepsilon} \cdot Sc^{\omega} \cdot \left[\frac{1 + \beta^*}{\dfrac{(a^* + b^*) \cdot n}{a^* + b^* \cdot n} + \beta^*} \right]^{\left(1/3 \right)}$$

Eqn. 6-19

As for the exponent ω of Sc in the equations above, various approximations have been introduced in different literature. Based on the asymptotic analysis [107] $Sc \to \infty$ limit in the case of very large Schmidt number, some of the previous efforts [105][106] have led to a conclusion of St ~ $\mathrm{Sc}^{(-2/3)}$, which for Newtonian flows gives the most simple correlation as $Sh = \psi \cdot \mathrm{Re}^{\varepsilon} \cdot Sc^{1/3}$. Mass transfer has been predicted for non-Newtonian fluids in spacer-filled channels assuming ω = 1/3 in this study, justified by the relatively high Schmidt number.

6.2 Mass transfer on the surfaces of membranes in spacer-filled channels for Newtonian creeping flow

Numerical results on mass transfer for creeping flow in spacer-filled channels are shown in **Fig. 6-3**. It is interesting, that the mass transfer in spacer-filled channels under very low Reynolds numbers is inclination angle independent. The Sherwood number is only depends on the wavelength of the spacer; the larger the wavelength, the larger the Sherwood number, which is similar to laminar flow in rectangular channels.

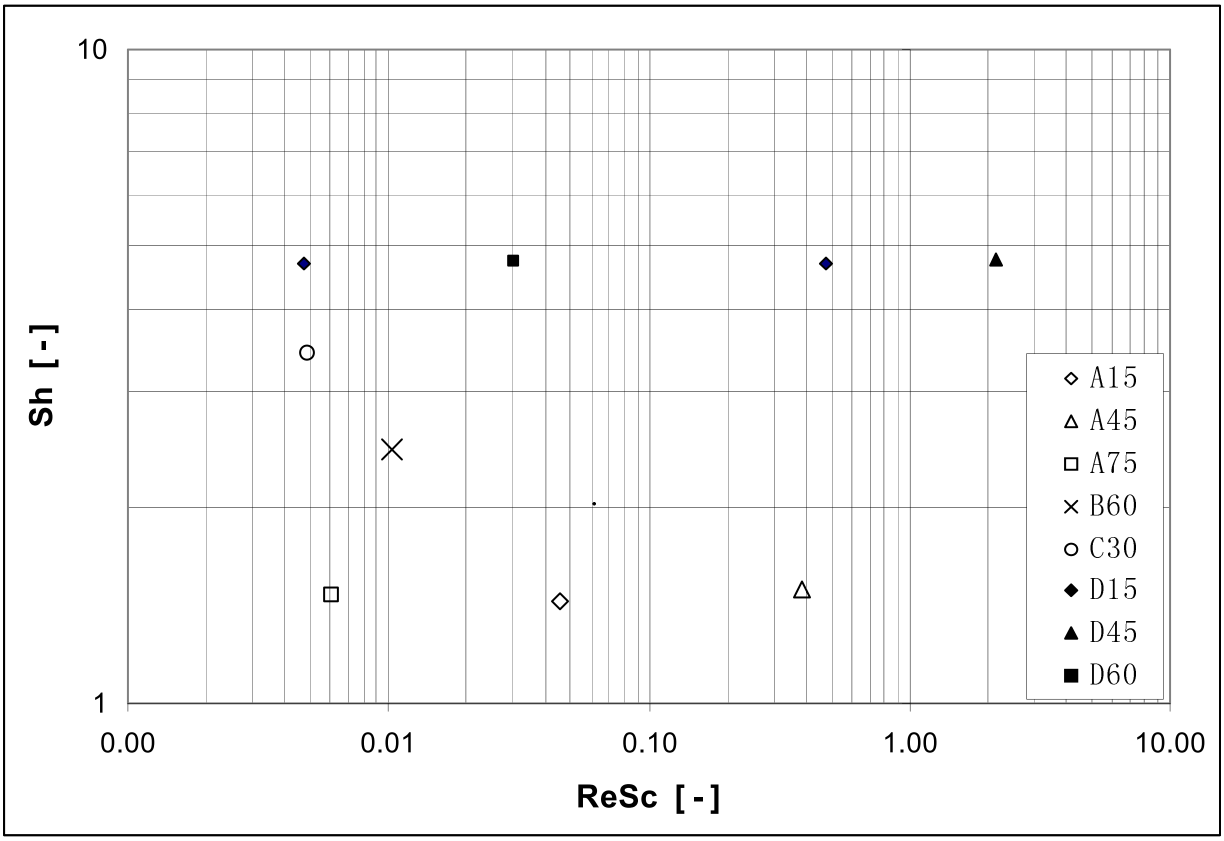

Fig. 6-3 Mass transfer for creeping flow in spacer-filled channels

From the results of flow phenomena presented in **section 4.1**, three types of flow could be characterized for spacers in high Reynolds number flow, which strongly depend on the geometry. These flow types aren't valid anymore for low Reynolds number laminar flow. As an example, mass transfer distribution for creeping flow in a spacer-filled channel with $\lambda/a = 7.45$, $\varphi = 30^{\circ}$ is shown in **Fig. 6-4**. The quantitative values of the Sherwood number in the spacer-filled channels are similar to that of laminar flow in two-layer, empty, but crossed rectangular channels. Mass transfer near the contact lines of the spacer is found to be extremely low (blue area in **Fig. 6-4**). It was found that the ratio of extremely low mass transfer area for creeping flow in different spacers is only a function of λ/a and not a function of inclination angle φ, as shown in **Tab. 6-1**. The results show that in spacers with smaller wavelength the extremely low mass transfer area is larger than in spacers with bigger wavelengths. That means, that at small wavelengths the area with extremely low mass transfer results from areas with extremely low flow velocities, where the convection becomes extremely low.

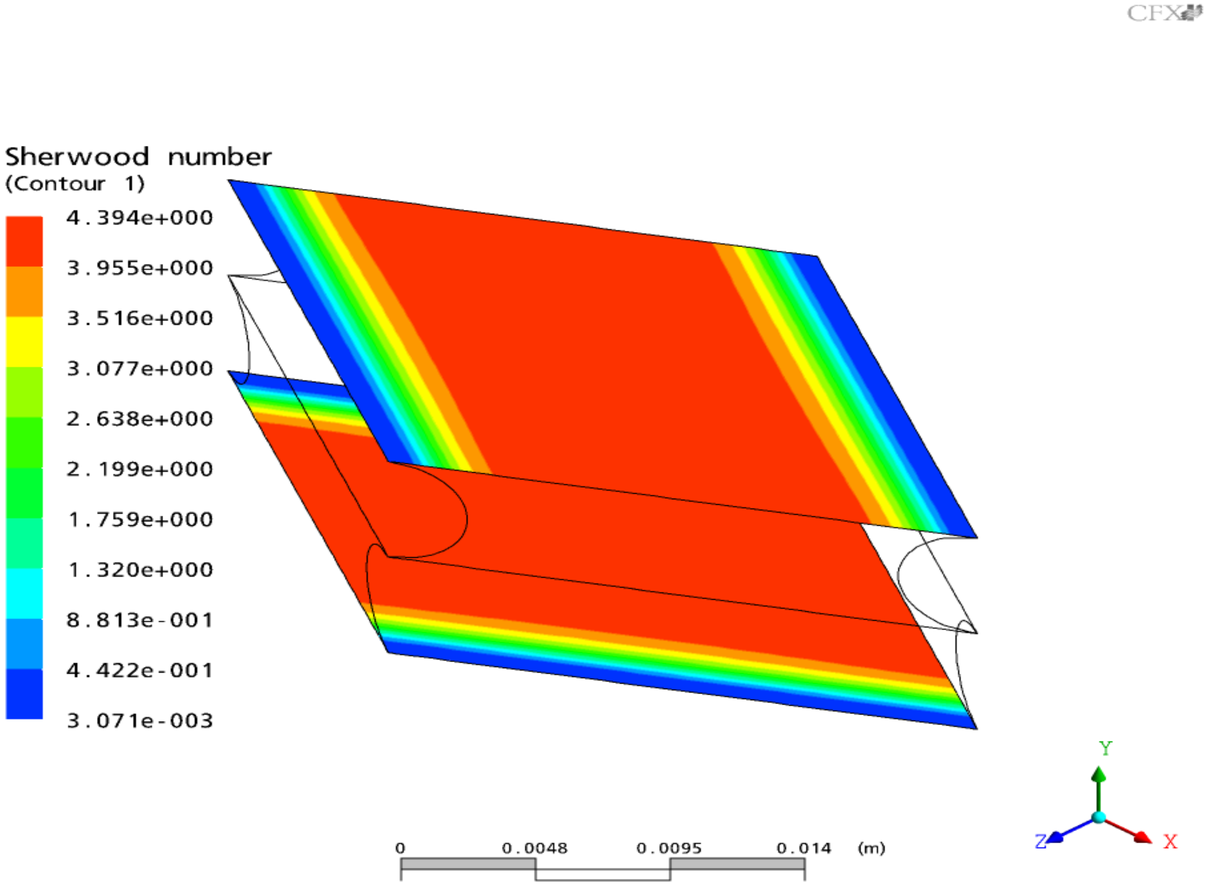

Fig. 6-4 Mass transfer distribution for creeping flow in a spacer-filled channel, λ/a = 7.45, φ = 30°, Re$_M$ = 10^{-5}. Red corresponds to high mass transfer, and blue to low mass transfer.

Tab. 6-1 Area of extremely low mass transfer in spacer-filled channels for creeping flow

Spacer	λ/a = 4	λ/a = 5.5	λ/a = 7.45	λ/a = 11
Ratio* [%]	17.36	12.83	9.05	5.91

$$^{*}:\ Ratio = \frac{area\ of\ \ extremely\ low\ mass\ transfer}{area\ of\ \ polyamide\ membrane}$$

6.3 Effect of flow index n

The goal of this study is to find an appropriate correlation equation to predict the mass transfer for modified power law non-Newtonian fluids in spacer-filled channels. Defined by **Eqn. 5-10** and **Eqn. 5-12**, the determination of Reynolds number has taken λ/a, φ, η_0, n, K, and β^* into account; by **Eqn. 6-7**, the determination of Schmidt number has taken an effective viscosity into consideration. An assumption was made to give the exponent of Schmidt number by (ω = 1/3), and a good agreement was then found for a general correlation equation, which is independent of flow index n values as shown in **Fig. 6-5** to **Fig. 6-9**.

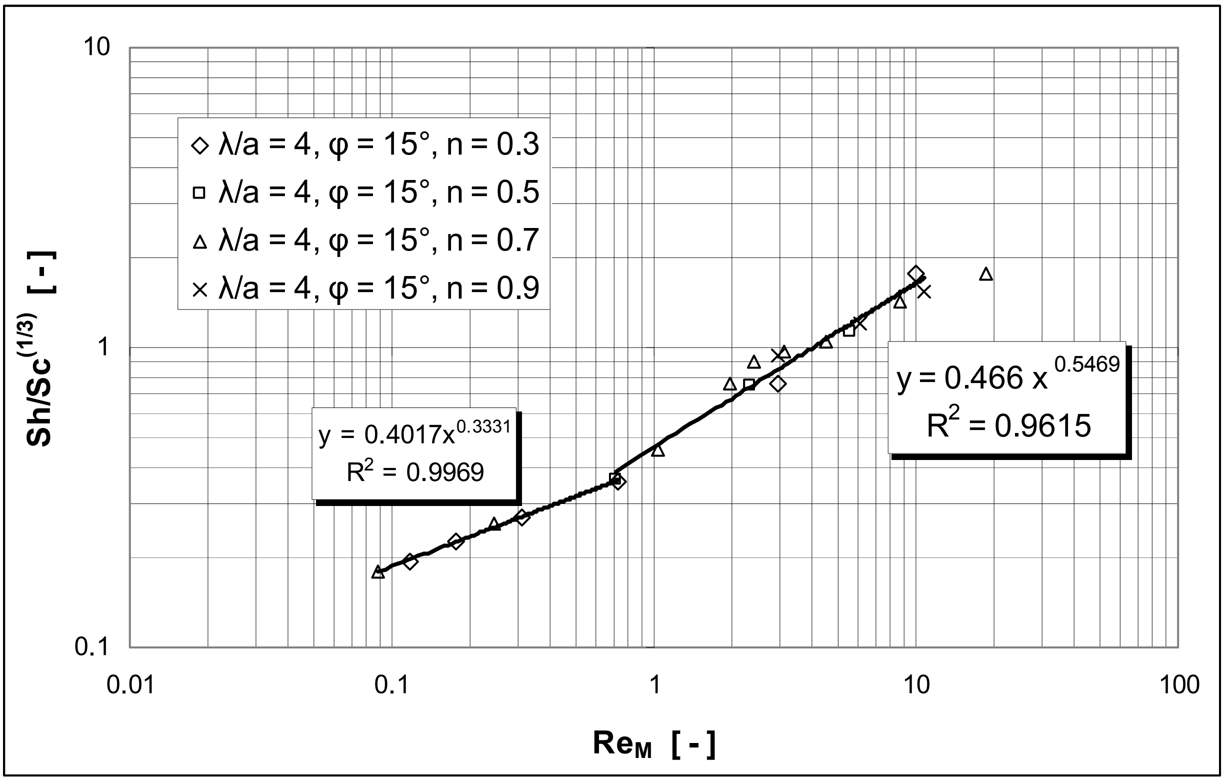

Fig. 6-5 Mass transfer vs. Reynolds number for different flow index in spacer A15

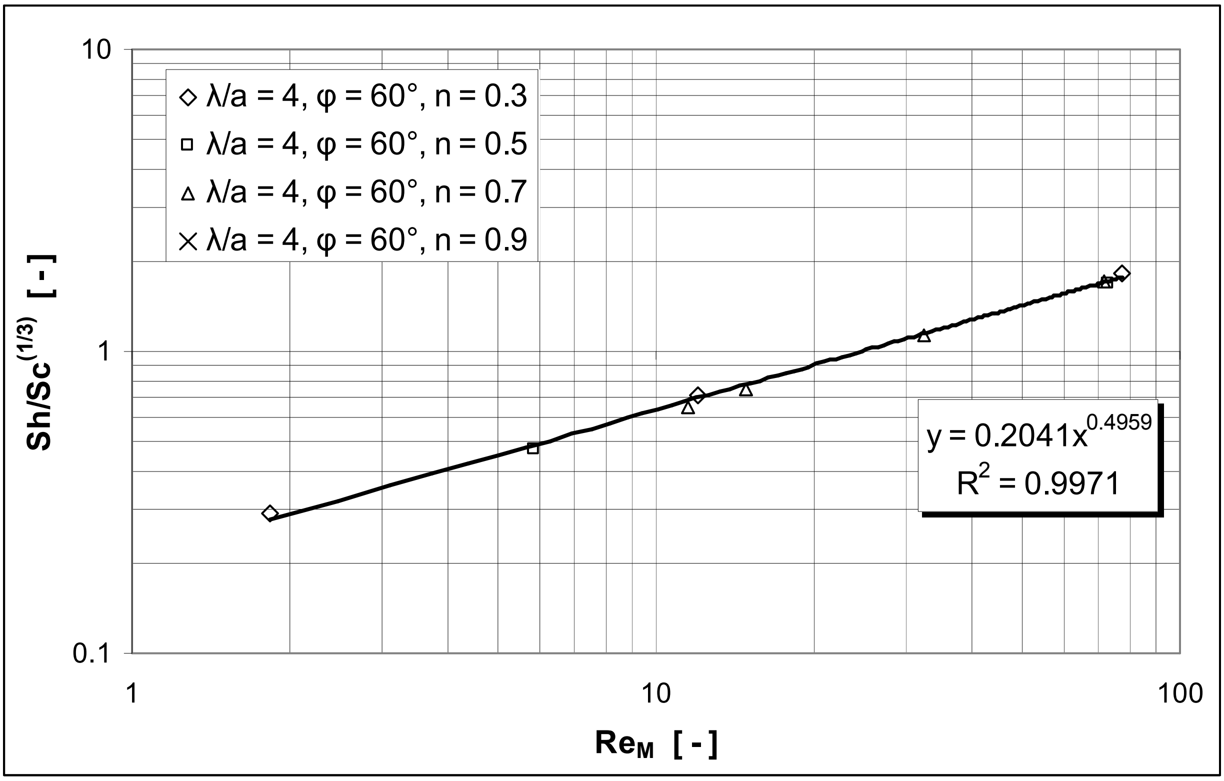

Fig. 6-6 Mass transfer vs. Reynolds number for different flow index in spacer A60

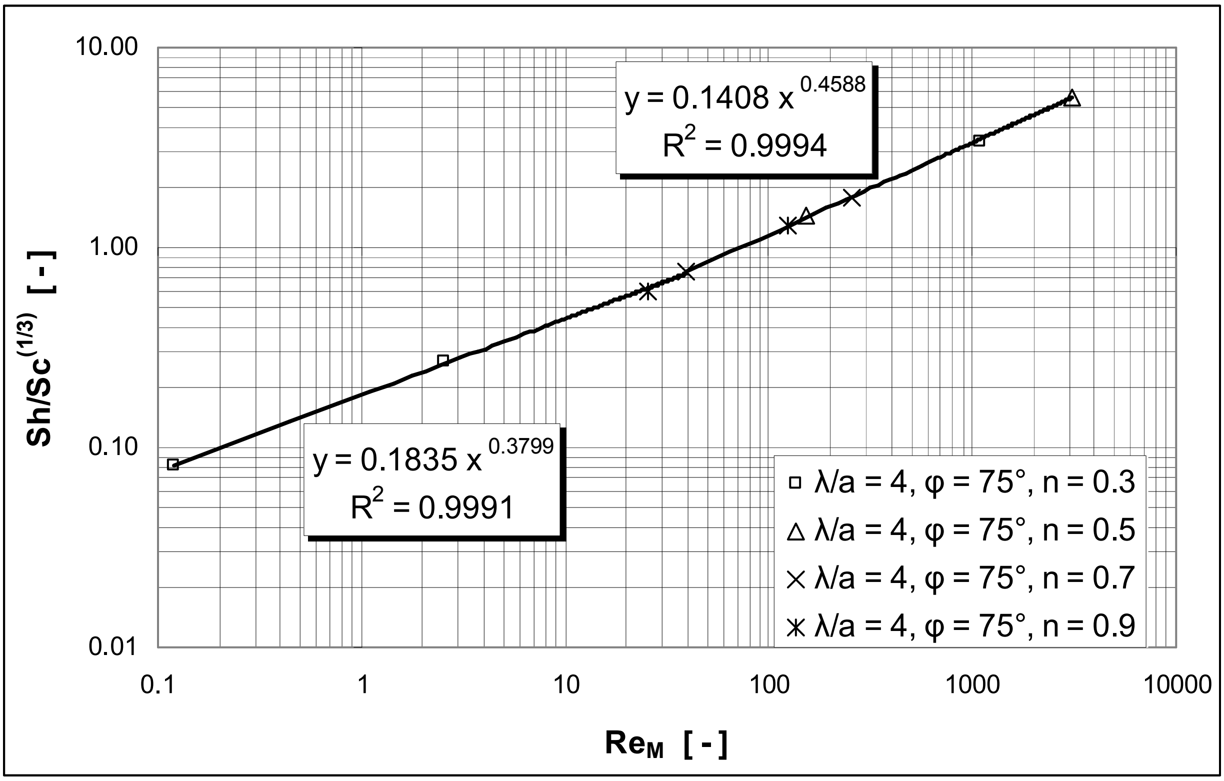

Fig. 6-7 Mass transfer vs. Reynolds number for different flow index in spacer A75

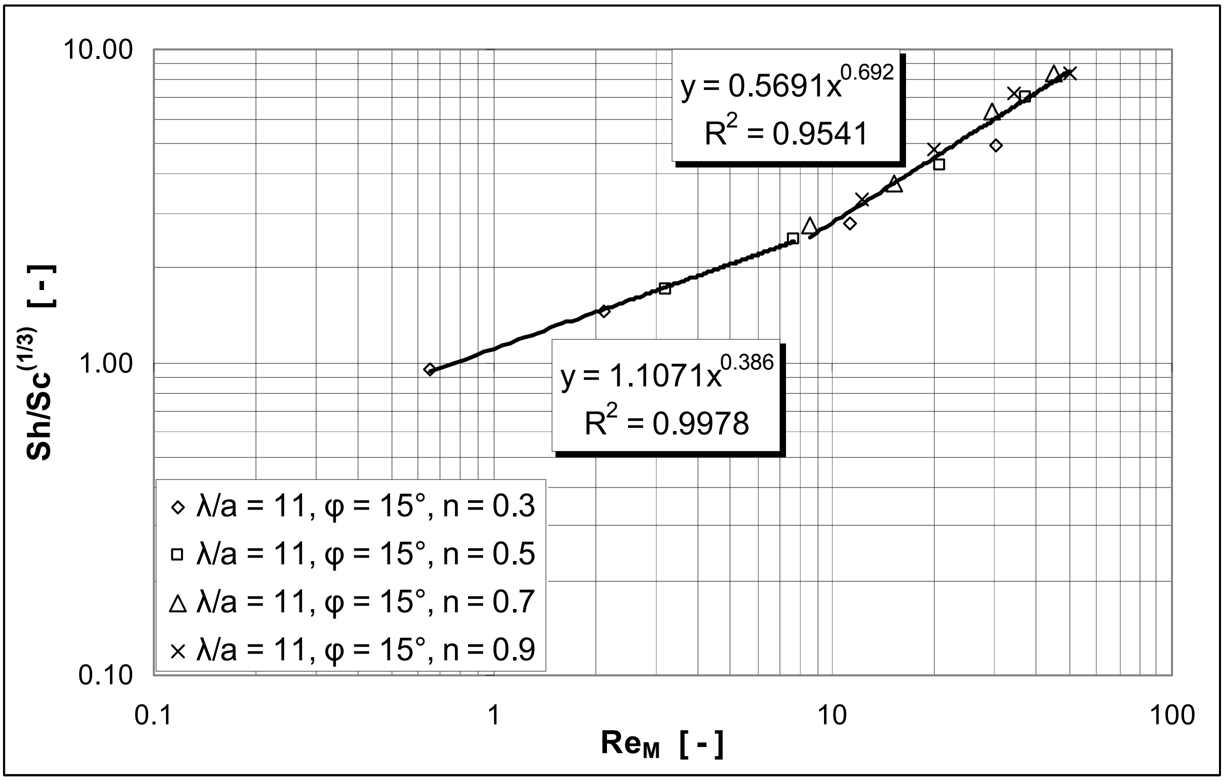

Fig. 6-8 Mass transfer vs. Reynolds number for different flow index in spacer D15

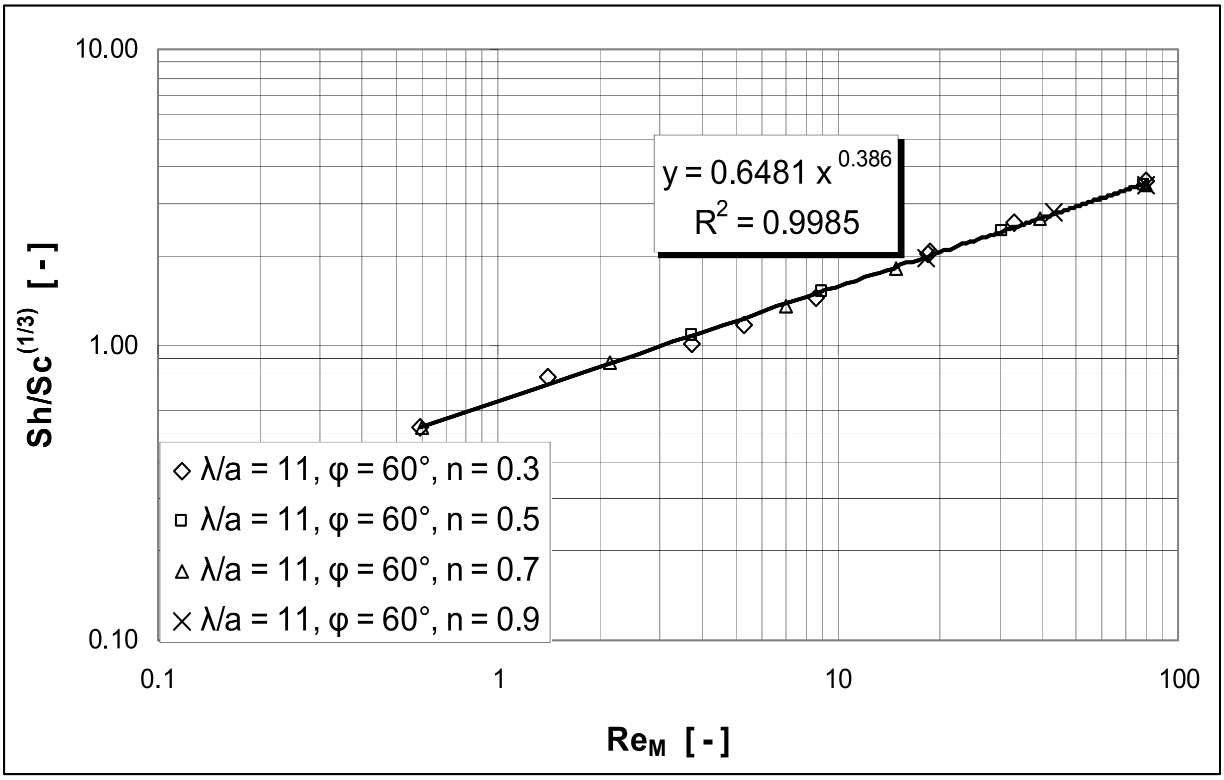

Fig. 6-9 Mass transfer vs. Reynolds number for different flow index in spacer D60

6.4 Comparison between experimental and numerical results

The new experimental methods for the determination of local mass transfer allow a comparison between experimental and numerical results. Based on the method given by **section 3.1.6**, the Sherwood number can be determined experimentally by **Eqn. 6-4** and **Eqn. 6-12** through the measurement with the remission photometer. On the other hand, numerical results on Sherwood number for the same fluid in the same spacer geometry under the same operating parameter can be achieved by **Eqn. 6-14** from CFX solution data.

Fig. 6-10 is an example of 0.5 % METHOCEL® (n = 0.5) in spacer B60 under a Reynolds number $Re_M = 1$. From the experiment, the length averaged Sherwood number from the entrance up to the x – value of the test section is plotted. The simulated value represents the fully developed Sherwood number in the single characteristic diamond. After 350 mm flow length, the experimental value becomes constant, which indicates, that the concentration boundary layer is developed. A little higher Sherwood number from the experiment than for the numerical prediction is the result, because the experiment shows the local, length averaged Sherwood number, whereas the numerical prediction represents only the local fully developed Sherwood number. If the local experiment is compared with the numerical prediction, the results agree very well.

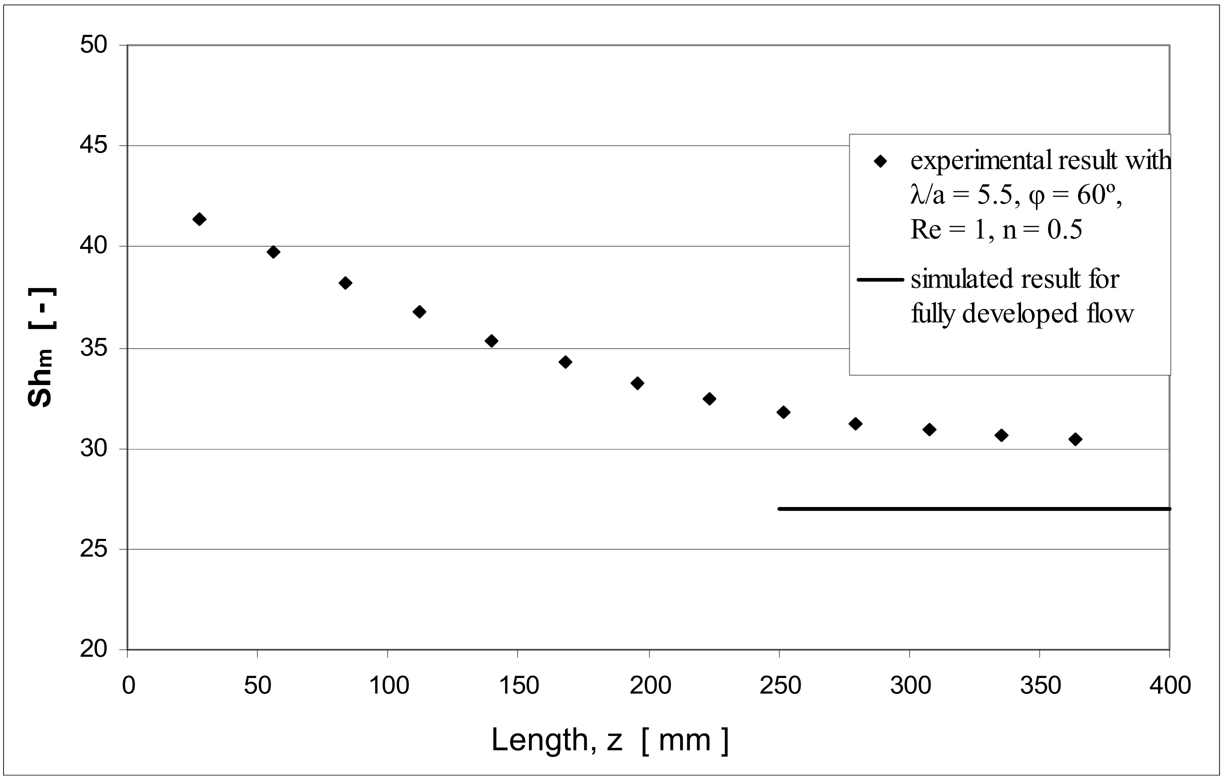

Fig. 6-10 Comparison of mass transfer between experimental and numerical results in spacer B60, $Re_M = 1$

6.5 Effect of the geometric parameters λ/a and φ

The effects of geometric parameters λ/a and φ on the flow phenomena and pressure drop in spacer-filled channels are discussed in **section 4.1** and **section 5.6**, respectively. The mass transfer also strongly depends on spacer geometry, as the following numerical results show.

The spacer A15 with $\lambda/a = 4$ and $\varphi = 15°$ is taken as an example. **Eqn. 6-16** predicts the mass transfer very well (**Fig. 6-5**). A transition point can be seen near Reynolds number $Re_M = 1$, where the transitional flow starts. According to **Fig. 5-9**, a deviation of the drag coefficient at this point can also be observed.

For spacers with a larger inclination angles, a single correlation equation covers a relative large Reynolds number range, e.g. spacer A60 (**Fig. 6-6**) and D60 (**Fig. 6-9**) up to Reynolds number $Re_M = 100$, and A75 (**Fig. 6-7**) even exceeding $Re_M = 1000$.

For spacers with a larger wavelength, but small inclination angle, e.g. D15 (**Fig. 6-8**), the transition point shifts to the higher Reynolds numbers of $Re_M = 8$, corresponding to the starting point of deviation for the drag coefficient in **Fig. 5-17**.

The effects of the inclination angle on mass transfer are shown in **Fig. 6-11** for modified power law non-Newtonian fluid with flow index $n = 0.3$. As the Reynolds number increases, mass transfer in creeping flow does not exhibit angle independency anymore. A smaller inclination angle leads to a higher mass transfer at constant wavelength. More data supplemented with different n values for spacer A (**Fig. 6-12**) and for spacer D (**Fig. 6-13**) are presented.

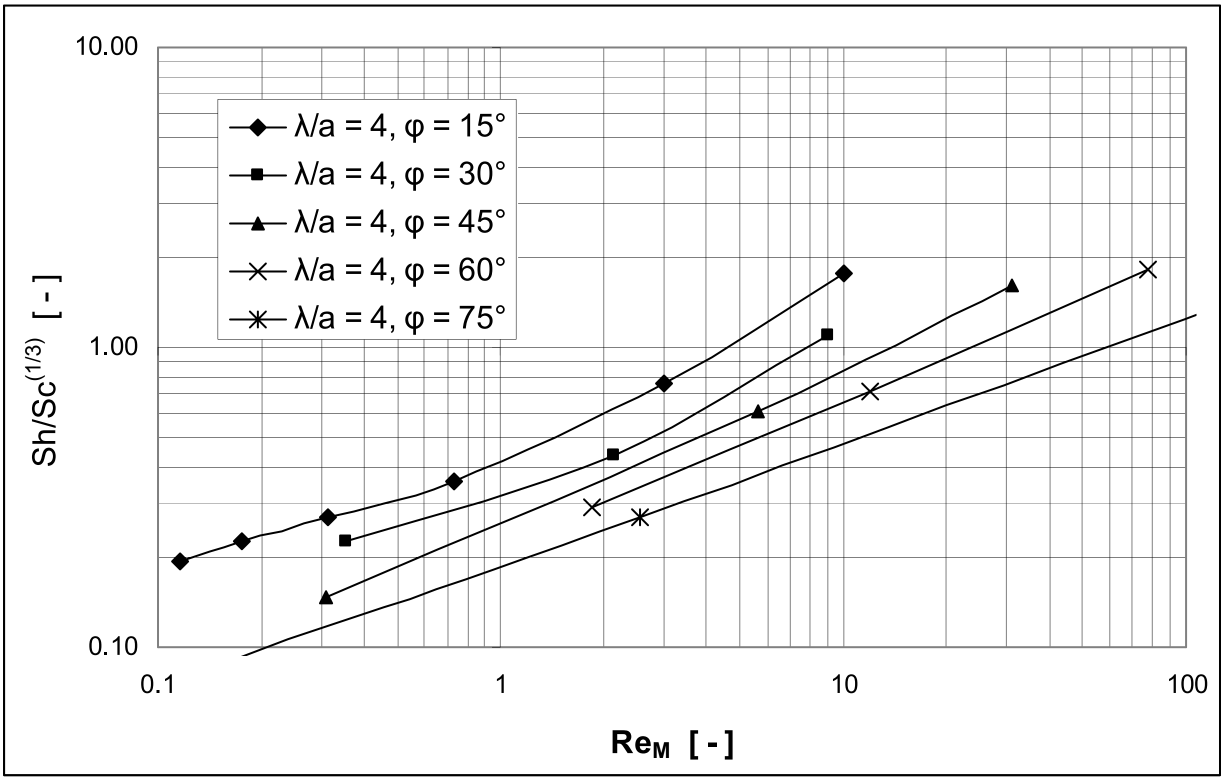

Fig. 6-11 Mass transfer vs. Reynolds number for different inclination angles for spacer A, non-Newtonian fluid with n = 0.3

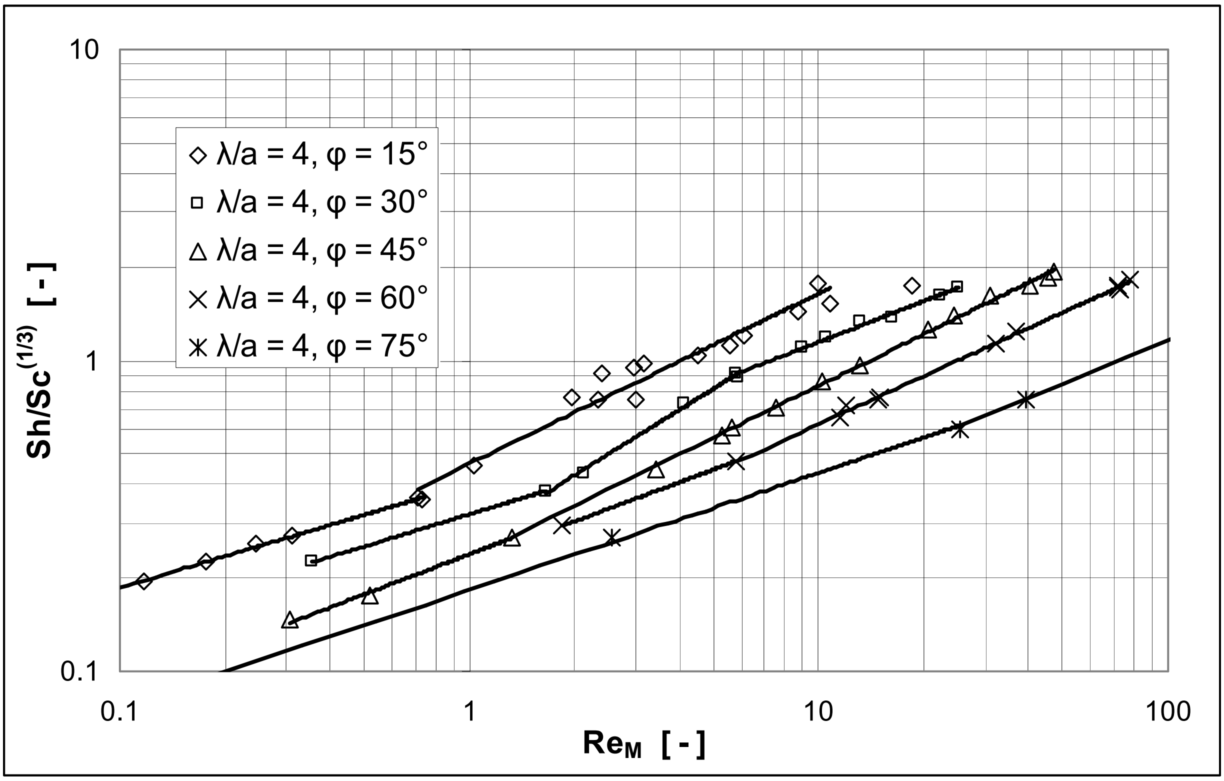

Fig. 6-12 Mass transfer vs. Reynolds number for different inclination angles for spacer A, non-Newtonian fluids with different n values

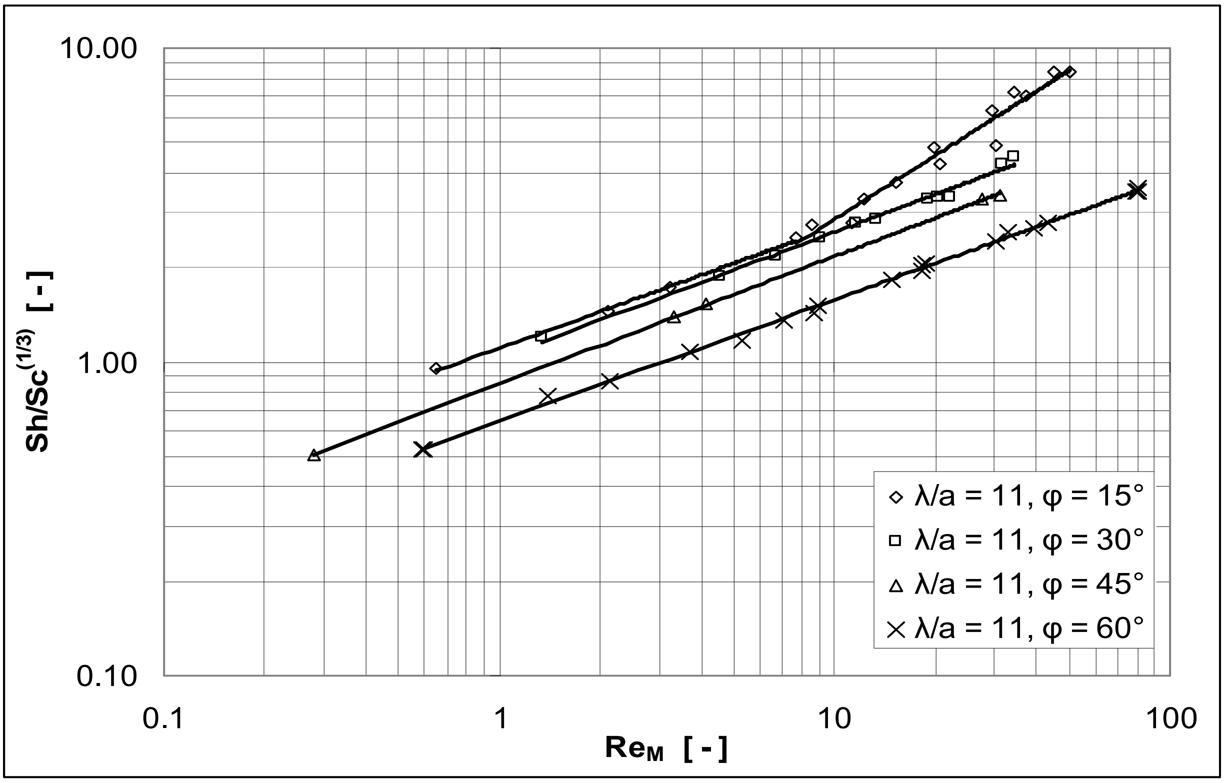

Fig. 6-13 Mass transfer vs. Reynolds number for constant wavelength, different inclination angles for spacer D, non-Newtonian fluids with different n values

The dependency of mass transfer on wavelength for modified power law non-Newtonian fluid with n = 0.3 indicates, that for constant small inclination angle, a larger wavelength gives a higher mass transfer, which agrees to the results in creeping flow. But more considerations have to be taken in this case, as different slopes can be found in **Fig. 6-14**. For higher Re-number, this does not have to remain true, as the curves for the different wavelengths have different slopes, and seem to draw closer to each other.

Fig. 6-15, shows the mass transfer versus Reynolds number and wavelength for non-Newtonian fluid in spacers with constant φ = 60 for a variety of n values.

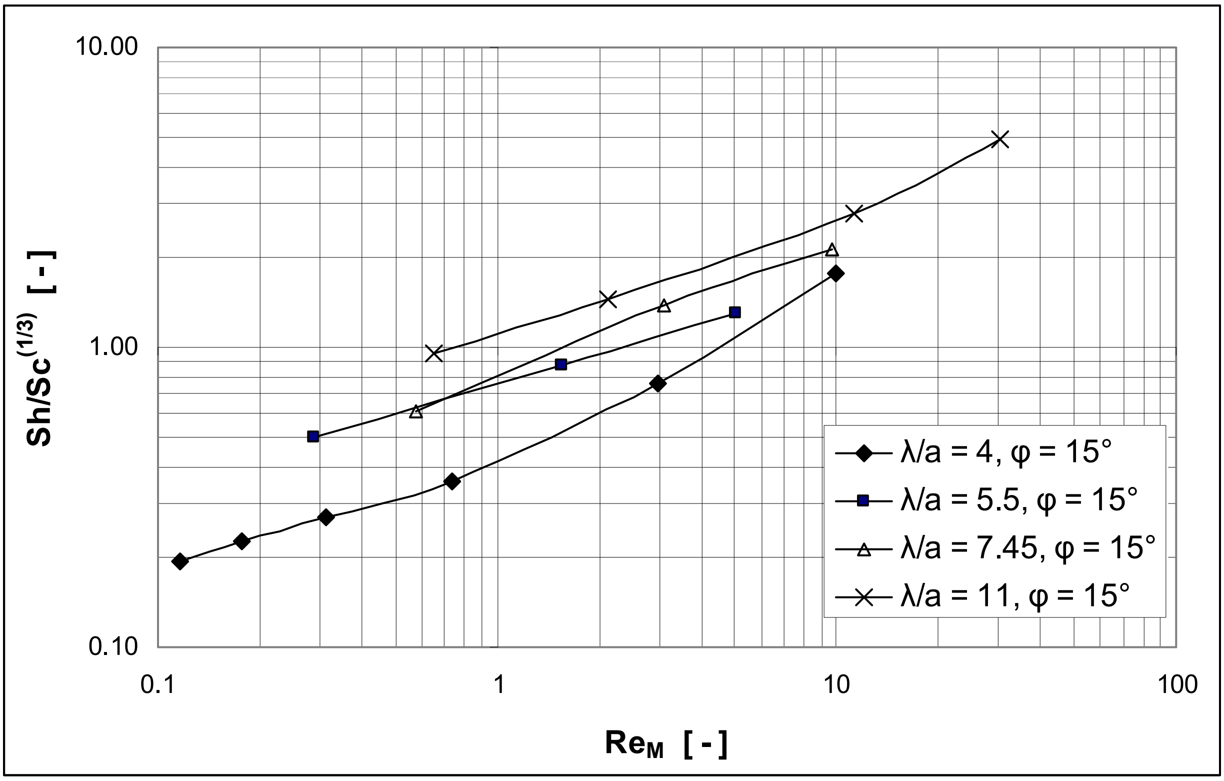

Fig. 6-14 Mass transfer vs. Reynolds number for constant inclination angle, different wavelength, for non-Newtonian fluid with n = 0.3

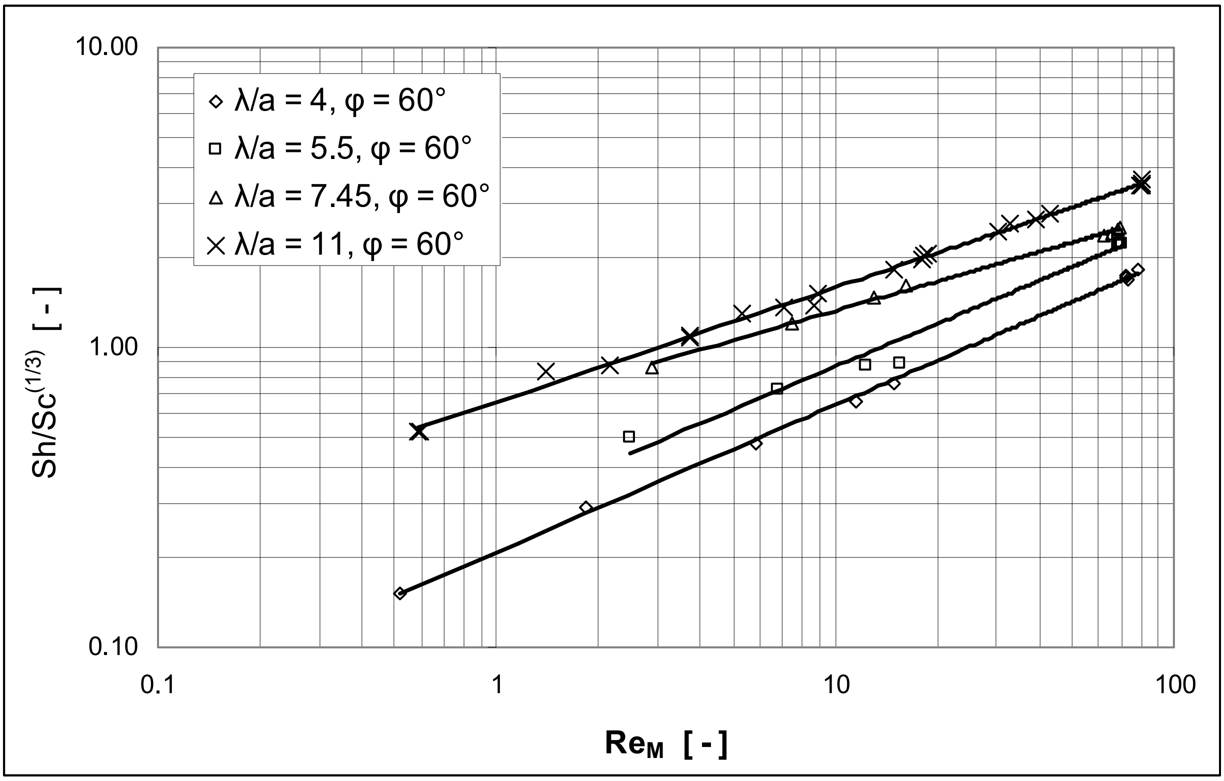

Fig. 6-15 Mass transfer vs. Reynolds number and wavelength for non-Newtonian fluids with different n values for spacers with constant inclination angle φ = 60

6.6 Effect of Reynolds number

Fig. 6-7 shows, that mass transfer versus Reynolds number and flow index for non-Newtonian fluids with n = 0.3, 0.5, 0.7, 0.9 in spacer A75 (λ/a = 4, φ = 75°) can be represented more accurately by two correlation equations with a intersection point at a Reynolds number of about 40. Here in **Fig. 6-16** only one equation is used for the reason of simplification. Additionally, a one magnitude order lower n value was added. The results show, that a larger error is observed for the extremely low flow index n = 0.03. In this case, the common correlation equation $Sh = \psi \cdot \mathrm{Re}_M{}^{\varepsilon} \cdot Sc^{\left(1/3\right)}$ does not fit here so well anymore, if this very strong shear rate dependent non-Newtonian fluid is taken into consideration.

In early studies in literature, the following phenomenon was observed in heat transfer problems in Newtonian fluids when, for example, highly viscous oil was used in investigations: As a temperature dependent physical variable, the oil viscosity became spatially dependent, because it resided in a temperature-gradient field. The functional dependence of Nusselt number $Nu = f(\mathrm{Re}, \mathrm{Pr})$ was not able to correlate the data, before a viscosity ratio (μ_b/μ_w) was added into the correlation equation.

If the fluid in the heat transfer problem additionally becomes non-Newtonain in its rheological behavior, to the viscosity ratio another additional correction factor must be added, to include the effects of the non-Newtonian characteristics.

Here, the analysis of mass transfer has the big advantage, that the fluid viscosity is unchanged by the mass transfer and only the effects of non-Newtonian flow must be involved. Therefore only the effects on the correction factor by the shear flow need to be analysed and can be fully separated from additional heat effects.

However the measurements of the shear rate are not as easy as temperature measurements, which means, that the viscosity ratio for a non-Newtonian fluid in flow field is difficult to determine by experiments.

To include the effects of the shear rate of non-Newtonian fluids, a correction factor was introduced in section 6.1 for modified power law non-Newtonian fluids. A good prediction for the mass transfer could be based on **Eqn. 6-18** (with ω = 1/3) and is demonstrated in **Fig. 6-17**, with $\Omega = \left[\dfrac{1 + \dfrac{a^* + b^* \cdot n}{(a^* + b^*)n} \cdot \beta^*}{1 + \beta^*} \right]$.

Some studies on heat transfer have developed the method of predicting the Nusselt number by adding a term for the friction factor into the correlation equations. As shown in **Fig. 6-18**, a very good agreement can be achieved by adding C_d into the correlation equation in this study for the mass transfer in this study.

The conclusion can then be drawn, that the correlation, given by **Eqn. 6-16** with ω = 1/3, is not necessarily the most accurate available, however, it is easy to use and quite satisfactory for non-Newtonian fluids with normal flow index n values. Based on a more universal correlation equation, $Sh = \psi \cdot \mathrm{Re}_M{}^{\varepsilon} \cdot Sc^{\left(1/3\right)} \cdot \Omega^{\left(1/3\right)} \cdot C_d$, a more precise prediction of mass transfer on non-Newtonian fluids though spacer-filled channels can be made, especially when fluids are very "non-Newtonian".

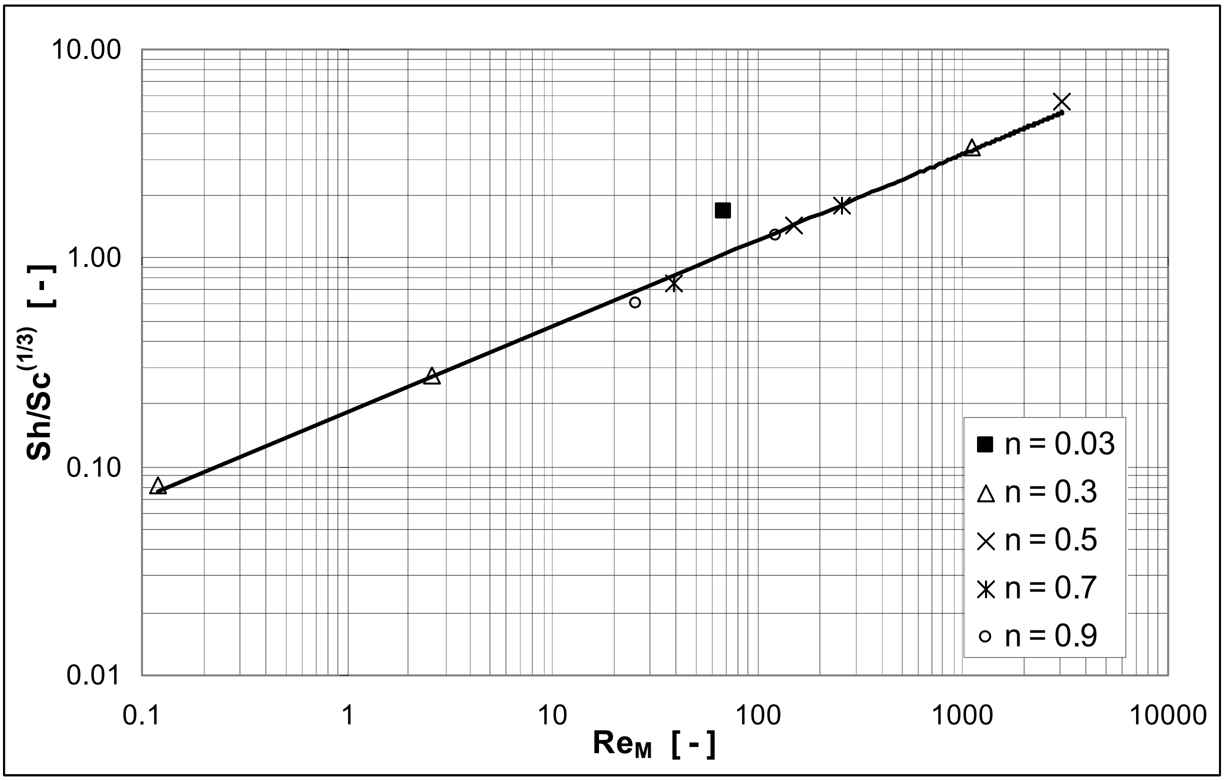

Fig. 6-16 Mass transfer estimated by the correlation equation of $Sh = \psi \cdot \mathrm{Re}_M{}^{\varepsilon} \cdot Sc^{\left(1/3\right)}$

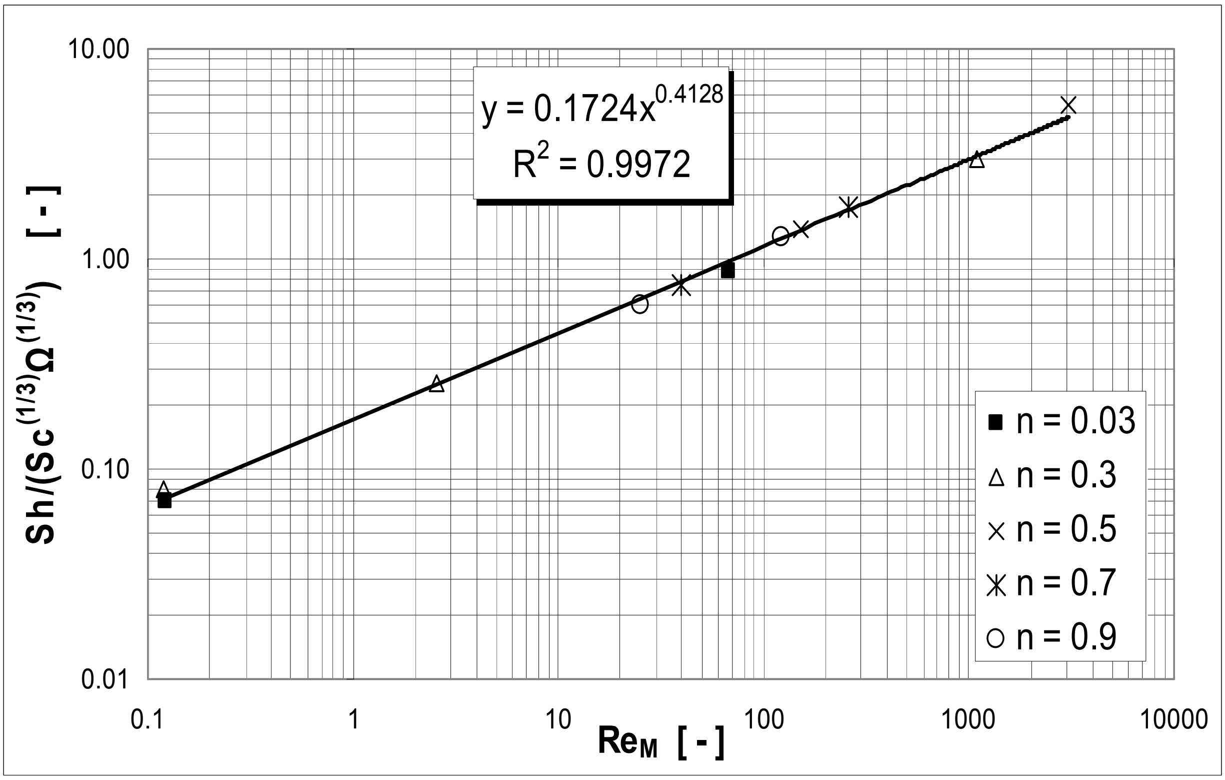

Fig. 6-17 Mass transfer estimated by the correlation equation of $Sh = \psi \cdot \mathrm{Re}_M{}^{\varepsilon} \cdot Sc^{\left(\frac{1}{3}\right)} \cdot \Omega^{\left(\frac{1}{3}\right)}$

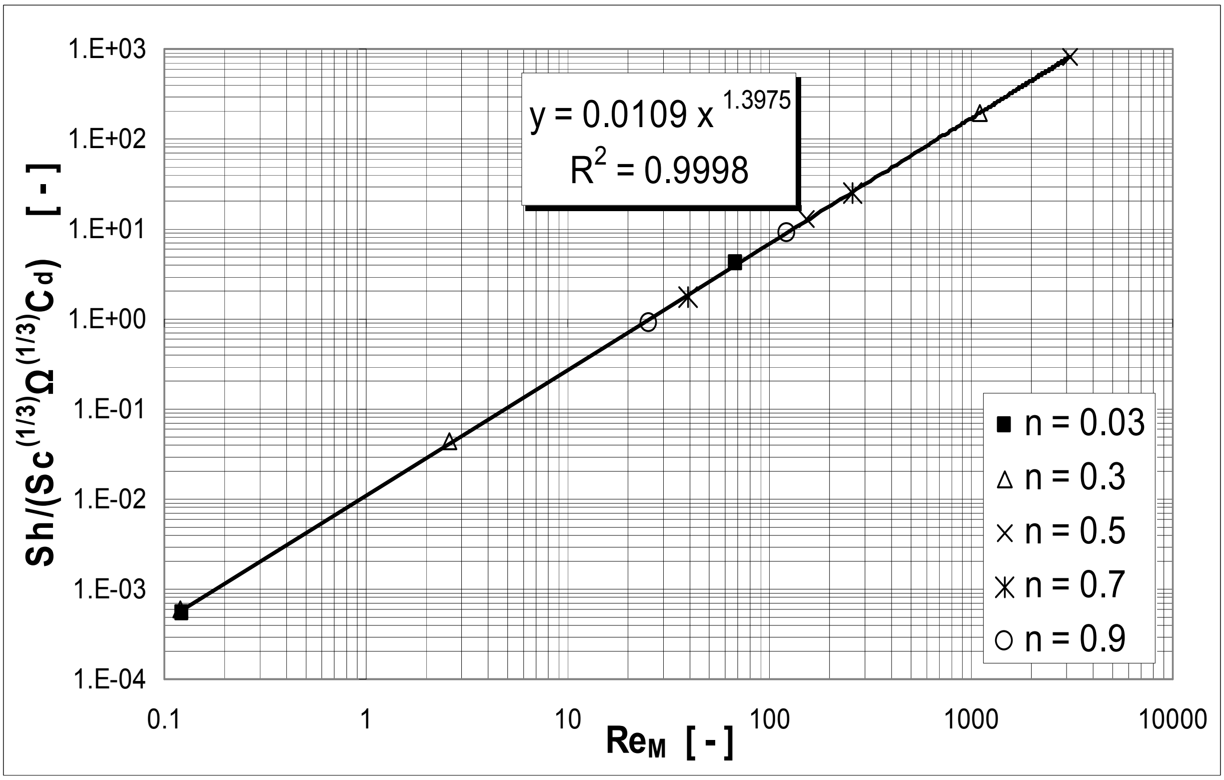

Fig. 6-18 Mass transfer estimated by the correlation equation of

$$Sh = \psi \cdot \mathrm{Re}_M{}^{\varepsilon} \cdot Sc^{\left(\frac{1}{3}\right)} \cdot \Omega^{\left(\frac{1}{3}\right)} \cdot C_d$$

7 Performance

7.1 Performance assessment by the criteria of Sh/C_d

Based on the criterion of Sh/C_d, the results of performance assessment are presented in **Fig. 7-1** to **Fig. 7-7**. A strong improvement in the performance of mass transfer by the spacer, compared to an empty rectangular channel, can be seen.

Comparison was made among spacers with the geometric parameters inclination angle and wavelength. Better performance can be found with smaller inclination angles for all wavelengths and for larger wavelength at constant inclination angle in the range of the Reynolds numbers studied.

Note that the results are only valid in the range of the analysis. For an extrapolationt to lower and higher Renolds numbers, there are no results available up to now.

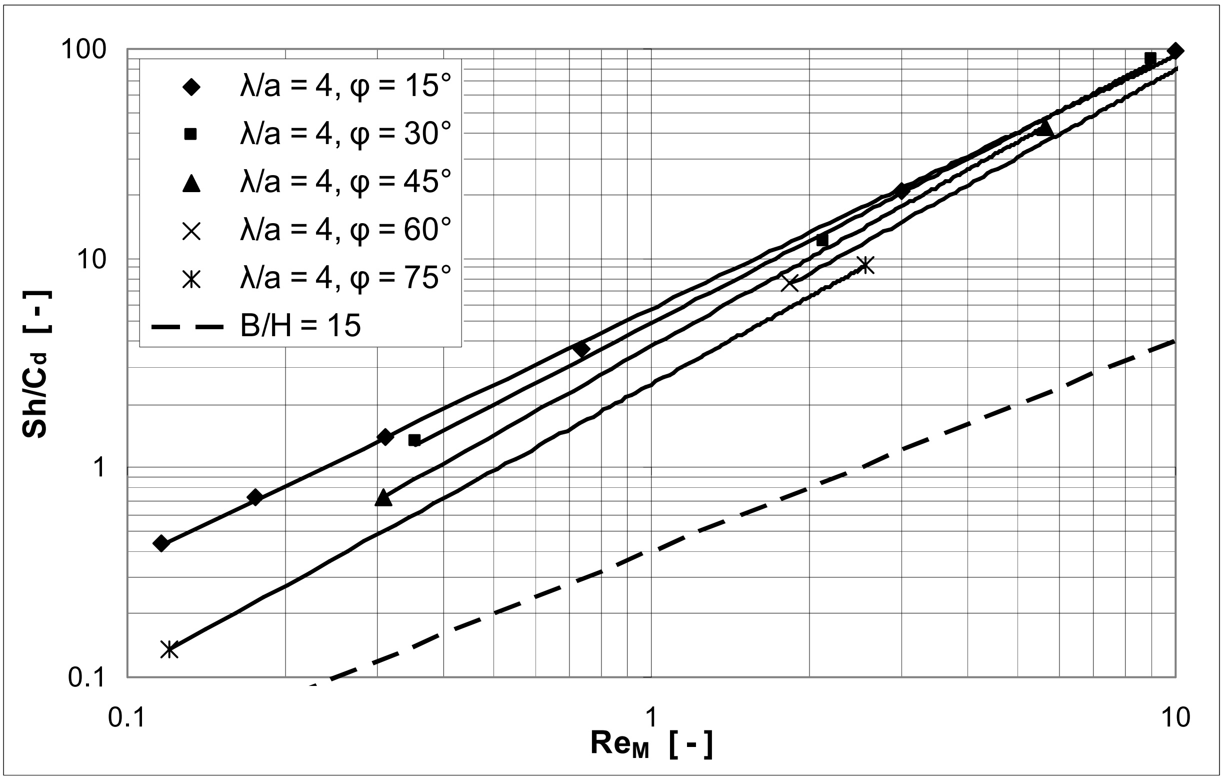

Fig. 7-1 Assessment of mass transfer performance for non-Newtonian fluids in spacer A with constant λ/a = 4, different inclination angles φ

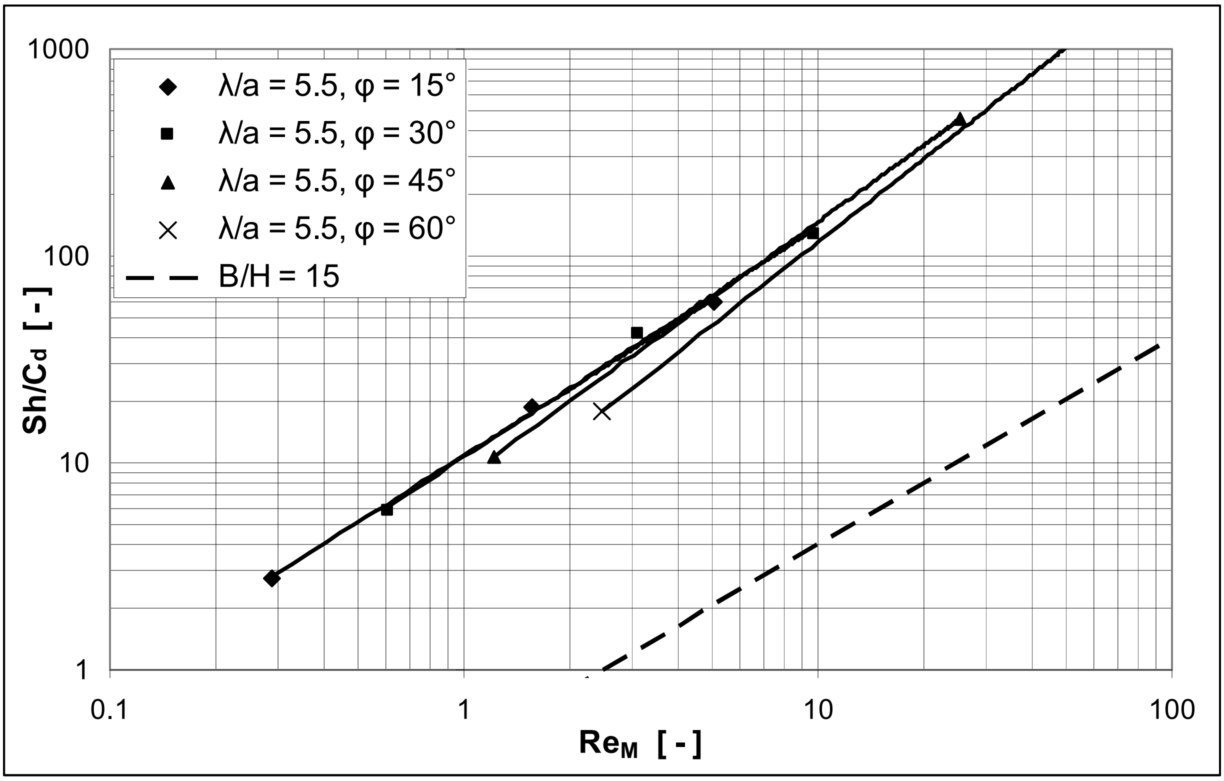

Fig. 7-2 Assessment of mass transfer performance for non-Newtonian fluids in spacer B with constant λ/a = 5.5, different inclination angles φ

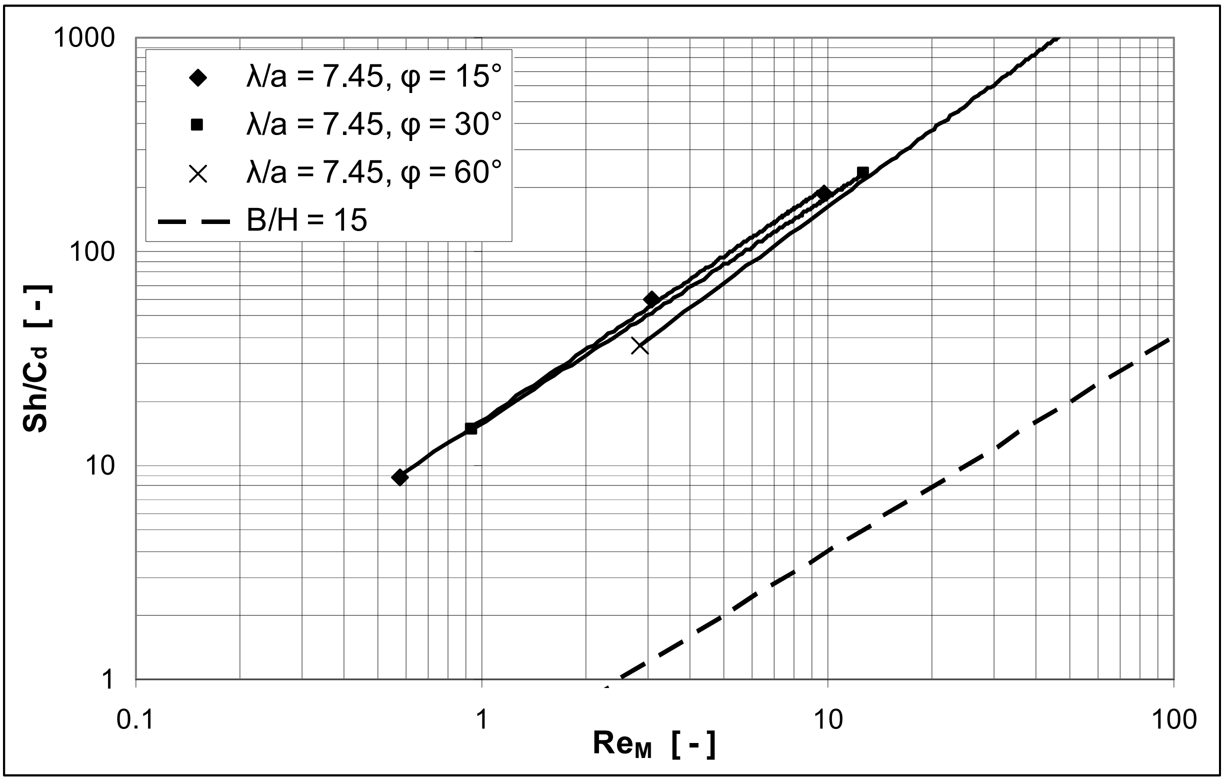

Fig. 7-3 Assessment of mass transfer performance for non-Newtonian fluids in spacer C with constant λ/a = 7.45, different inclination angles φ

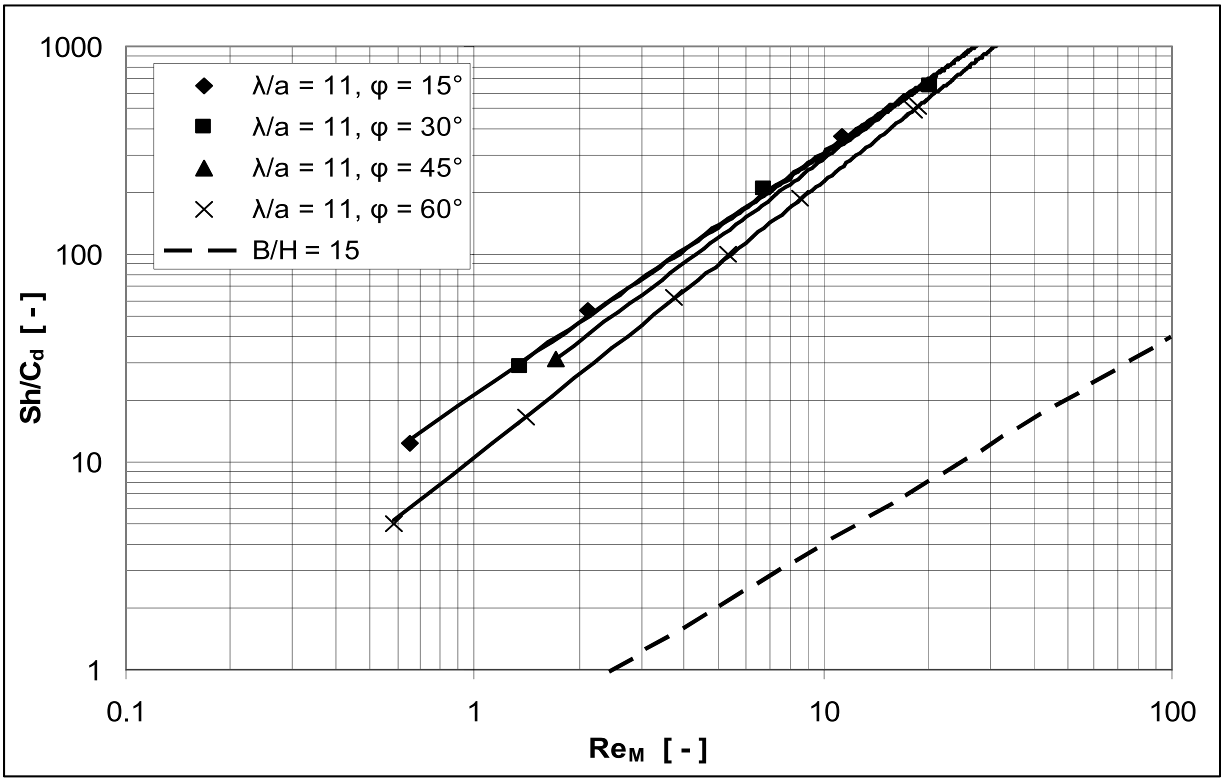

Fig. 7-4 Assessment of mass transfer performance for non-Newtonian fluids in spacer D with constant λ/a = 11, different inclination angles φ

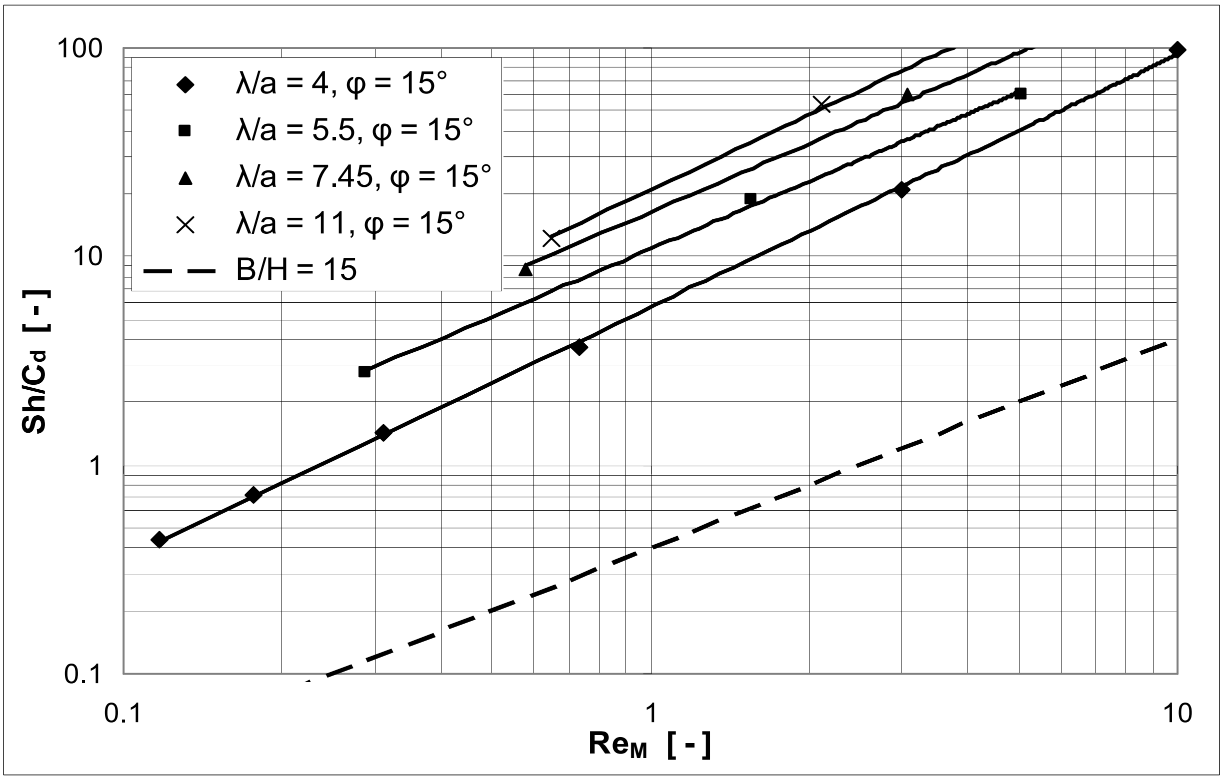

Fig. 7-5 Assessment of mass transfer performance for non-Newtonian fluids in spacers with constant φ = 15°, different wavelengths λ/a

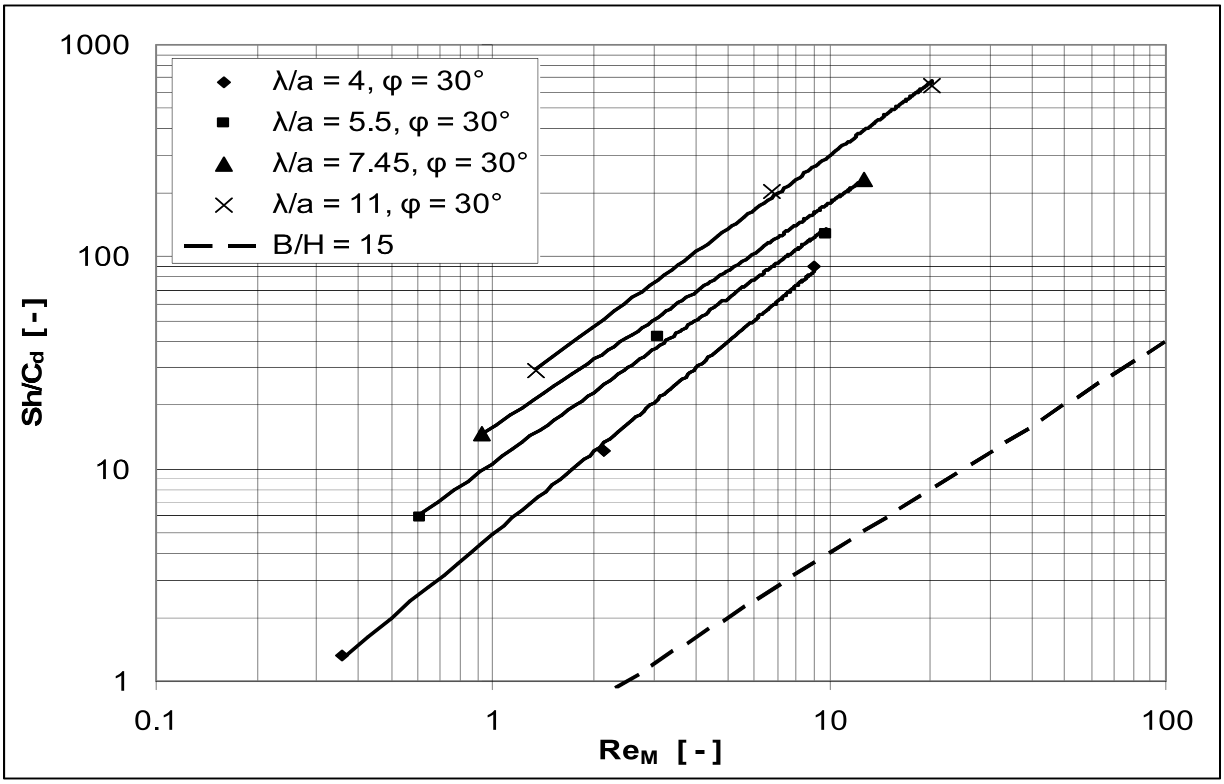

Fig. 7-6 Assessment of mass transfer performance

for non-Newtonian fluids in spacers with constant φ = 30°, different wavelengths λ/a

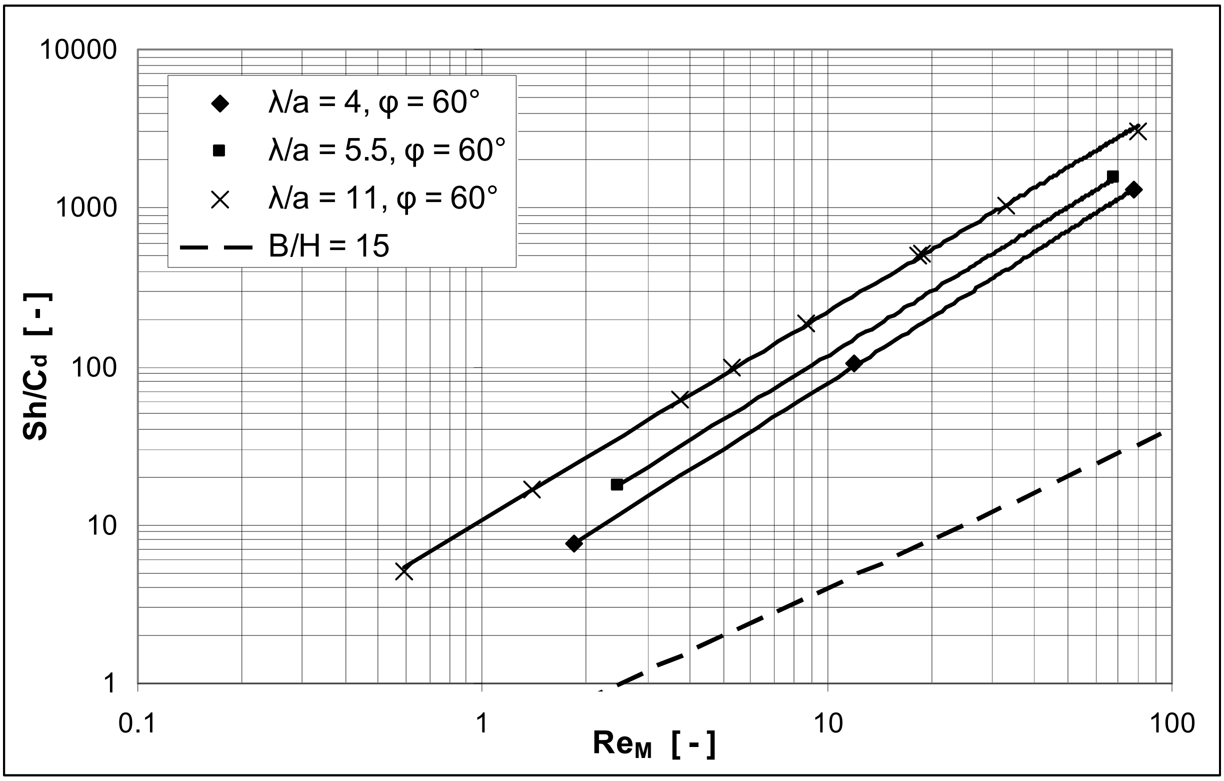

Fig. 7-7 Assessment of mass transfer performance

for non-Newtonian fluids in spacers with constant φ = 60°, different wavelengths λ/a

The results of the mass transfer performance are evaluated by the equation of $Sh/C_d = p \cdot \mathrm{Re}^q$ in the Reynolds number range from $\mathrm{Re}_M = 0.1 - 10$ for non-Newtonian flow in spacer-filled channels (**Tab. 7-1**). An exponent larger than 1 (q > 1) of the Reynolds number was found for various spacers, which denotes that mass transfer efficiency in spacer-filled channel strongly depends on the Reynolds number. The scales of the parameters of p and q depend on geometry; larger wavelengths have higher p values, but smaller q values, and spacers with φ = 45° and 60° have the largest q values among the different inclination angles. A conclusion can then be made that for very low Reynolds number mass transfer in spacer-filled channels: A better efficiency occurs in spacers with larger wavelength and/or smaller inclination angles. However this situation changes in spacers with smaller wavelengths and/or larger inclination angles (e.g. φ = 45° and 60°).

Tab. 7-1 Performance evaluated by $Sh/C_d = p \cdot \mathrm{Re}^q$
for a non-Newtonian fluid (n = 0.3) in spacer-filled channels

Spacer	A15	A30	A45	A60	A75
P	5.74	4.92	3.80	3.23	2.52
Q	1.21	1.30	1.40	1.39	1.38
Spacer	**B15**	**B30**	**B45**	**B60**	**B75**
P	10.86	10.66	8.55	5.32	2.39
Q	1.08	1.11	1.23	1.34	1.32
Spacer	**C15**	**C30**	**C45**	**C60**	
P	16.32	15.76	11.64	10.43	
Q	1.09	1.06	1.24	1.19	
Spacer	**D15**	**D30**	**D45**	**D60**	
P	20.91	21.19	16.08	10.60	
Q	1.19	1.15	1.25	1.32	

7.2 Performance assessment by the criterion of Sh/C_h

The homogeneity of mass transfer can be quantified by statistical means and defined by a variation coefficient [109] as:

$$V(x_j) = \frac{\delta(x_j)}{\overline{\overline{b(x_j)}}} = \frac{\sqrt{\sum_{i=1}^{n}(\overline{b_i(x_j)} - \overline{\overline{b(x_j)}})^2}}{\sqrt{n-1} \cdot \overline{\overline{b(x_j)}}}$$

Eqn. 7-1

$$\overline{\overline{b(x_j)}} = \frac{\sum_{i=1}^{n}\overline{b_i(x_j)}}{n}$$

Eqn. 7-2

Where

$\delta(x_j)$	square root of the variance [mg m^{-2}]
$\overline{b_i(x_j)}$	mean b value over one rhomb [mg m^{-2}]
$\overline{\overline{b(x_j)}}$	mean b value over all rhombs of the width of the spacer [mg m^{-2}]
x_j	longitudinal distance from the entrance of the test section [m]
N	number of rhombs over the width of the duct/spacer

The variation coefficient here was used to assess the homogeneity over the whole spacer-filled test section, taking one rhomb as the statistical unit.

In this study, the local homogeneity within a single characteristic diamond was taken into account. An integral definition of homogeneity coefficient based on local Sherwood number was defined by:

$$C_h = \frac{\sqrt{\iint_A \left(Sh - \overline{Sh}\right)^2 \cdot dA}}{\sqrt{A} \cdot \overline{Sh}}$$

Eqn. 7-3

Where

$$\overline{Sh} = \frac{\iint\limits_A Sh \cdot dA}{A}$$

Eqn. 7-4

A high homogeneity coefficient demonstrates a high inhomogeneity of the local Sherwood number.

Sh/C_h has then been used as a second criterion to judge the mass transfer performance among different spacers. As shown in **Fig. 7-8** to **Fig. 7-10**, identical results have been achieved in the sense, that the smaller the inclination angle, the better the performance is; the larger the wavelength, the better the performance is.

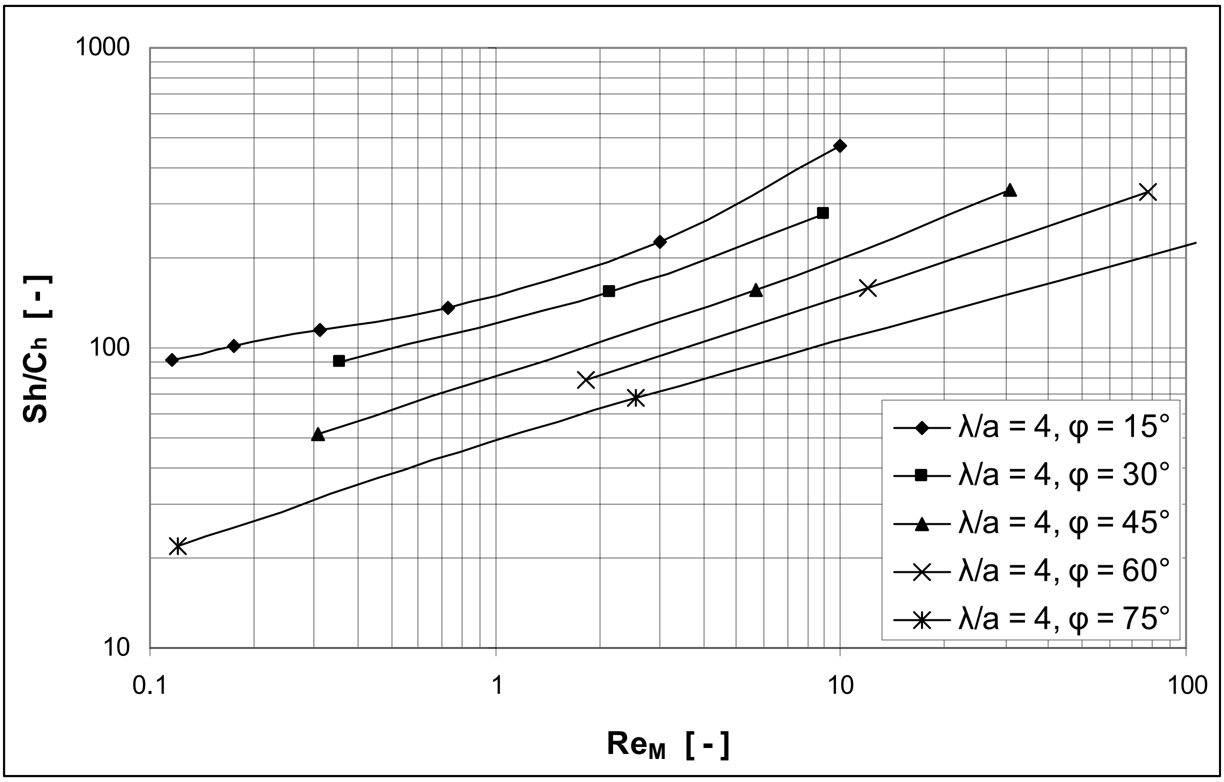

Fig. 7-8 Assessment of mass transfer performance for non-Newtonian fluids in spacer A with constant λ/a = 4, different φ

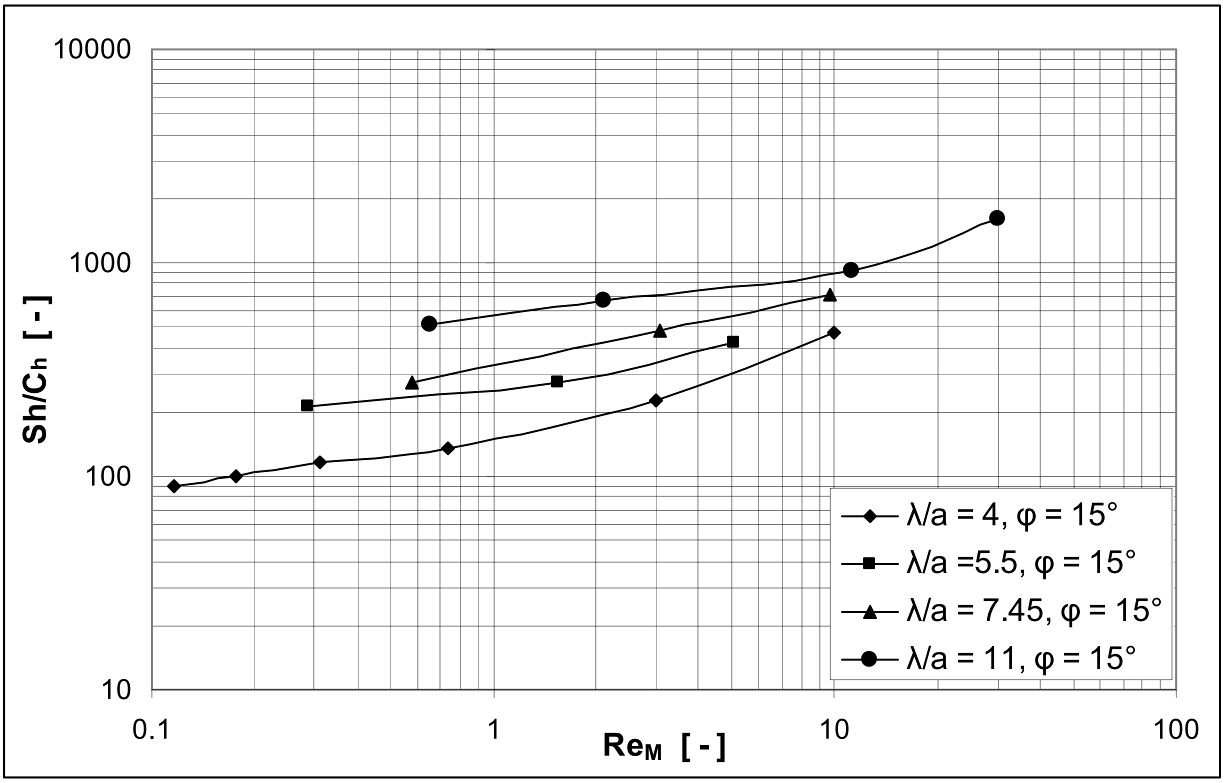

Fig. 7-9 Assessment of mass transfer performance

for non-Newtonian fluids in spacers with constant φ = 15°, different λ/a

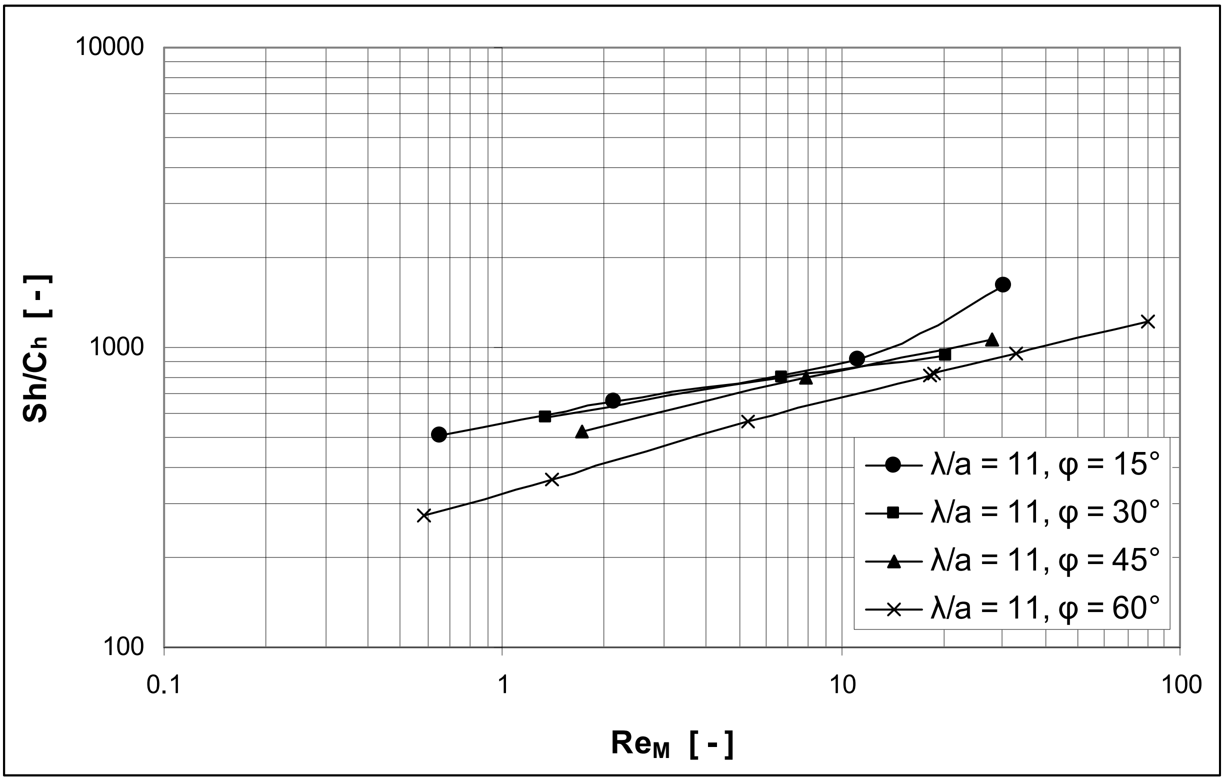

Fig. 7-10 Assessment of mass transfer performance

for non-Newtonian fluids in spacer D with constant λ/a = 11, different φ

8 Conclusions

1 It has been proven that the method introduced for Newtonian fluids in the previous work of Kühnel [84] can be used as a basis to investigate flow and transport phenomena in non-Newtonian fluids, to measure pressure drop and to visualize and determine mass transfer for non-Newtonian flows in spacer-filled channels. However, new fluids had to be developed to be compatible with the method of Kühnel.

2 A commercial CFD code based on finite volume method was used to solve momentum and mass transfer problems in non-Newtonian fluids. Numerical simulation focused on fully developed, laminar, simultaneous hydrodynamic and concentration boundary layer flow with periodic interface condition in single characteristic diamonds of spacer-filled channels. The numerical method included physical model design, mesh generation and refinement. A validation assessment was carried out.

3 Comparison between experimental and numerical methods on flow phenomena, pressure drop and local mass transfer was conducted. A good agreement was achieved in this study. Flow and transport phenomena, pressure drop and mass transfer in spacer-filled channels strongly depend on the geometric parameters of spacers, on the rheological properties of the fluids as well as on Reynolds number itself as well. The results of performance assessment based on two criteria show that spacers with large wavelength λ/a and small inclination angle φ have a better mass transfer performance in the low Reynolds number range.

4 Rheometry studies were conducted on both shear thinning (pseudoplastic) and shear thickening (dilatant) systems. Two common conservative equations were examined to describe the rheological characteristics of METHOCEL® K15M and PVA/borax/NaCl aqueous solutions. It is suggested that the modified power law model is a reasonable and preferable accurate conservative equation, especially for flows in such low Reynolds numbers as in this study.

5 Based on the wall information from creeping flow, two geometric correction parameters a^* and b^* for a variety of spacers were determined in this study. Another, so-called Reynolds correction factor β^* was also developed in this study especially for modified power law non-Newtonian fluids, with which the "power law" intensity for these fluids in arbitrary geometry

channels can be quantified. Therefore, an adapted definition of Reynolds number **Eqn. 5-10** for shear thinning fluids and **Eqn. 5-12** for shear thickening fluids first was introduced in this study. This Reynolds number definition takes the effect of channel (geometric correction parameters), media (rheological characteristics) and flow intensity (Reynolds correction factor) in account and thus has an extended range of validity in prediction, comparison and analogous study of hydrodynamic and heat/mass transport problems.

6 With the newly introduced definition of Reynolds number, correlation between Reynolds number and drag coefficient is well represented. The results between experimental and numerical agree to each other very well. The conclusion can be drawn, that a common curve $C_d \cdot \mathrm{Re}_M = 16$ at creeping flow is followed by slowly and gradually cumulative deviations, and further-on by transitions. Position and scale of the deviation and transition depend on the geometry of the spacer. High resistance spacers with smaller wavelength and/or smaller inclination angle usually have an earlier and larger deviation. The cumulative deviation will developes to an earlier transition point.

A simple correlation equation for mass transfer in non-Newtonian fluids is also given by Eqn. 6-16 with $\omega = 1/3$. For non-Newtonian media with a common flow index (like n = 0.3 ~ 0.9 in this study), the correlations can't be the most accurate available, but they are already quite satisfactory for the optimum design of the spacers.

7 Due to the fact that viscosity is temperature dependent, in heat transfer a correction factor based on a viscosity ratio is usually added to the correlation equation for a more accurate prediction of the Nusselt number. Under the isothermal condition of mass transfer in this study, where the viscosity is shear rate dependent, the simulation results show that an accurate agreement in **Eqn. 6-17** with $\omega = 1/3$ and $\vartheta = 0.14$ can be achieved by adding an apparent viscosity ratio. An alternative factor $\Omega = \left[\dfrac{1 + \dfrac{a^* + b^* \cdot n}{(a^* + b^*)n} \cdot \beta^*}{1 + \beta^*} \right]$ is more practical for the prediction of mass transfer, shown as **Eqn. 6-18** for shear thinning fluids and **Eqn. 6-19** for shear thickening fluids, because the local viscosities in the flow field are not easy to determine in practice. Furthermore, investigations show that a more accurate correlation equation

$$Sh = \psi \cdot \mathrm{Re}_M{}^{\varepsilon} \cdot Sc^{\left(\frac{1}{3}\right)} \cdot \left[\frac{1 + \frac{a^* + b^* \cdot n}{(a^* + b^*)n} \cdot \beta^*}{1 + \beta^*} \right]^{\left(\frac{1}{3}\right)} \cdot C_d \qquad \textbf{Eqn. 8-1}$$

for shear thinning non-Newtonian fluids, and

$$Sh = \psi \cdot \mathrm{Re}_M{}^{\varepsilon} \cdot Sc^{\left(\frac{1}{3}\right)} \cdot \left[\frac{1 + \beta^*}{\frac{(a^* + b^*) \cdot n}{a^* + b^* \cdot n} + \beta^*} \right]^{\left(\frac{1}{3}\right)} \cdot C_d \qquad \textbf{Eqn. 8-2}$$

for shear thickening non-Newtonian fluids, can be achieved when the drag coefficient is taken into consideration for the prediction of mass transfer for non-Newtonian flows in spacer-filled channels.

9 References

[1] Winograd Y., Solan A., Toren M., Mass transfer in narrow channels in the presence of turbulence promoters, Desalination, 13 (1973) 171

[2] Chiolle A., Gianotti G., Gramondo M., Parrini G., Mathematical model of reverse osmosis in parallel wall channels with turbulence promoting nets, Desalination, 26 (1978) 3

[3] Miyoshi H., Fukumoto T., Kataoka T., A consideration of flow distribution in an ion exchange compartment with spacer, Desalination, 42 (1982) 47

[4] Focke W. W., Nuijens P. G., Velocity profile caused by a high porosity spacer between parallel plates (membrane), Desalination, 49 (1984) 243

[5] Schock G., Miquel A., Mass transfer and pressure loss in spiral wound modules, Desalination, 64 (1987) 339

[6] Da Costa A. R., Fane A. G., Net-type spacers: effects of configuration on fluid flow path and ultrafiltration flux, Ind. Eng. Chem. Res., 33 (1994) 1845

[7] Van Gauwbergen D., Baeyens J., Macroscopic fluid flow conditions in spiral-wound membrane elements, Desalination, 110 (1997) 287

[8] Cao Z., Wiley D. E., Fane A. G., CFD simulations of net-type turbulence promoters in a narrow channel, J. Membr. Sci., 185 (2001) 157

[9] Karode S. K., Kumar A., Flow visualization through spacer filled channels by computational fluid dynamics, I. pressure drop and shear rate calculations for flat sheet geometry, J. Membr. Sci., 193 (2001) 69

[10] Tian C., Gill W. N., The relaxation of concentration polarization in a reverse osmosis Desalination system, AIChE J., 12 (1966) 722

[11] Kang I. S., Chang H. N., The effects of turbulence promoters on mass transfer-numerical analysis and flow visualization, Int. J. Heat Mass Transfer, 25 (1982) 1167

[12] Kim D. H., Kim I. H., Chang H. N., Experimental study of mass transfer around a turbulence promoter by the limiting current method, Int. J. Heat Mass Transfer, 26 (1983) 1007

[13] Schwinge J., Wiley D. E., Fletcher D. F., Simulation of the flow around spacer filaments between narrow channel walls, 1. Hydrodynamics, Ind. Eng. Chem. Res., 41 (2002) 2977

[14] Schwinge J., Wiley D. E., Fletcher D. F., Simulation of the flow around spacer filaments between narrow channel walls, 2. Mass transfer enhancement, Ind. Eng. Chem. Res., 41 (2002) 4879

[15] Geraldes V., Semiao V., Pinho M. N., The effect of the ladder-type spacers configurations in NF spiral wound modules on concentration boundary layers disruption, Desalination, 146 (2002) 187

[16] Geraldes V., Semiao V., Pinho M. N., Concentration polarization and flow structure within nanofiltration spiral-wound modules with ladder-type spacers, Comput. Struct., 82 (2004) 1561

[17] Brian P. L. T., Concentration polarization in reverse osmosis desalination with variable flux and incomplete salt rejection, Ind. Eng. Chem. Fundam., 4 (1965) 439

[18] Geraldes V., Semiao V. A., de Pinho M. N., Flow management in nanofiltration spiral wound modules with ladder-type spacers, J. Membr. Sci., 203 (2002) 87-102

[19] Geraldes V., Afonso M. D., Generalized mass transfer correction factor for nanofiltration and reverse osmosis, AIChE J., 52 (2006) 3353-3362

[20] Subramani A., et al., Pressure, flow and concentration profiles in open and spacer-filled membrane channels, J. of Membr. Sci., 277 (2006) 7-17

[21] Coleman B., Markowitz H., Noll W., Viscometric flows of non-Newtonian fluids, Springer Tracts in Natural Philosophy, 5 (1966) Berlin: Springer-Verlag

[22] Bird R., Armstrong R., Hassager O., Dynamics of Polymeric Liquids, (1987) New York: John Wiley & Sons

[23] Coussot P., Ancey C., Rhéophysique des pâtes et des suspensions, (1999) Les Ulis: EDP Sciences

[24] Steffe J., Rheological methods in food process engineering, 2nd edn. (1996) East Langing, USA: Freeman Press

[25] Walters K., Rheometry, (1975) London: Chapman and Hall.

[26] Charm S. E., Viscometry of non-Newtonian food materials, Food Res., 25 (1960) 351-362

[27] Harper J. C., El Sahrigi A. F., Viscometric behavior of tomato concentrates, J. Food Sci., 30 (1965) 470-476.

[28] Saravacos G. D., Moyer J. C., Heating rates of fruit products in an agitated kettle, Food Technol., 21 (1967) 372-376.

[29] Saravacos G. D., Tube viscometry of fruit purees and juices, Food Technol., 22 (1968) 1585-1588.

[30] Rao M. A., Bourne M. C., Cooley H. J., Flow properties of tomato concentrates, J. Text Studies, 12 (1981) 521-538.

[31] Barbosa-Canovas G., Peleg M., Flow parameters of selected commercial semiliquid food products, J. Text Studies, 14 (1983) 213-234.

[32] Dickie A. M., Kokini J. L., An improved method for food thickness from non-Newtonian fluid mechanics in the mouth, J. Food Sci., 48 (1983) 57-61,65.

[33] Dervisoglu M., Kokini J. L., Steady shear rheology and fluid mechanics of four semi-solid foods, J. Food Sci., 51(1986) 541-546,625.

[34] Hassan B. H., Hobani A. I., Flow properties of Roselle (Hibiscus sabdariffa L.) extracts, J. Food Eng., 35 (1998) 459-470.

[35] Hobani A. I., Rheological behavior of date-water concentrates, J. Food Eng., 36 (1998) 349-357.

[36] Ibanoglu S., Ibanoglu E., Rheological characterization of some traditional Turkish soups, J. Food Eng., 35 (1998) 251-256.

[37] Wang Y., Hutter K., A constitutive model of multiphase mixtures and its application in shearing flows of saturated solid-fluid mixtures, Granul. Matter 1 (1999) 163–181.

[38] Hutter K., Laloui L., Vulliet L., Thermodynamically based mixture models of saturated and unsaturated soils, Mech. Cohesive-Frict. Mater., 4 (1999) 295–338.

[39] Hutter K. Jöhnk K., Continuum Methods of Physical Modeling, (2004) Berlin: Springer.

[40] Bedford A., Dumheller D., Theories of immiscible and structured mixtures, Int. J. Eng. Sci., 21 (1983) 863–960.

[41] Vardoulakis I., Sulem J., Bifurcation Analysis in Geomechanics, (1995) Glasgow: Blackie Academic & Professional.

[42] Chapman S., Cowling T., The mathematical theory of non-uniform gases, 3rd edn., (1970) Cambridge: Cambridge University Press.

[43] Jenkins J., Hanes H., Collisional sheet flows of sediment driven by a turbulent fluid, J. Fluid Mech., 370 (1998) 29–52.

[44] Jenkins J., Savage S., A theory for the rapid flow identical, smooth, nearly elastic, spherical particles, J. Fluid Mech., 130 (1983) 187–202.

[45] Savage S., Marginal ice zone dynamics modelled by computer simulations involving floe collisions, In: Mobile particulate systems (ed. E. Guazelli & L. Oger), pp. 305–330. (1994) Carghese: Kluwer Academic Publishers.

[46] Savage S., The mechanics of rapid granular flows, Adv. Appl. Mech., 24 (1984) 289–366.

[47] Savage S., Flow of granular materials, In Theoretical and Applied Mechanics (ed. P. Germain, J.-M. Piau & D. Caillerie), (1989) 241–266, Amsterdam: Elsevier.

[48] Savage S., Jeffrey D., The stress tensor in a granular flow at high shear stress rates, J. Fluid Mech., 110 (1981) 255–272.

[49] Zimmerer C. C., Strömungs- und Transportvorgänge in Kanälen mit gekreuzten Gitterstrukturen, Dissertation, Universität Stuttgart, 1998.

[50] Becker, C., Analyse der Strömungsvorgänge des Druckverlustes und Mischverhaltens von gekreuzten Gitterstrukturen, Studienarbeit, Universität Stuttgart, Inst. Chem. Verfahrenstechnik, 1993.

[51] Focke W. W., Selecting Optimum Plate Heat Exchanger Surface Pattern, J. Heat Transfer, 108 (1986) 153-160.

[52] Schock G., Miquel A., Mass Transfer and Pressure Loss in Spiral wound Modules, Desalination, 64 (1987) 339-352.

[53] Zimmerer C. C. Kottke V., Effect of spacer geometry on pressure drop, mass transfer, mixing behavior, and residence time distribution, Desalination, 104 (1996) 129-134.

[54] Skelland A. P. H., Non-Newtonian flow and heat transfer, (1967) New York: Wiley.

[55] Joshi S. D., Bergles A. E., Experimental study of laminar heat transfer to in-tube flow of non-Newtonian fluids, J. Heat Transfer, 102 (1980) 397-401.

[56] Joshi S. D., Bergles A. E., Analytical study of heat transfer to laminar in-tube flow of non-Newtonian fluids, AIChE Symp. Ser., 199 (1980) 270-281.

[57] Pickard J. F., PhD thesis, Council for National Academic Awards, 1979.

[58] Delporte J. P., J. Pharm., Belg., 35 (1980) 417-426.

[59] Prater D. H., PhD thesis, University of Bath, 1982.

[60] Philippoff P., Cellulose Chem., 17 (1936) 57-77.

[61] Aulton M. E., Twitchell A. M. and Hogen J. E., Proc. 4th. APGI Int. Conf. on Pharm. Tech., Paris, 1986.

[62] Nijenhuis K., Thermoreversible Networks Viscoelastic Properties and Structure of Gels, (1997) Berlin: Springer.

[63] Inoue T., Osaki K., Rheological properties of poly(vinyl alcohol)/sodium borate aqueous solutions, Rheol. Acta, 32 (1993) 550-555.

[64] Bourgoin D. J., J. Chemie. Phys., 59 (1963) 923.

[65] Savins J. G., Shear Thickening Phenomena in Poly(vinyl)Alcohol-Borate Complexes Rheol. Acta, 7 (1968) 87-93.

[66] Ochiai H., Simizu S., Tadokoro Y., Murakami I., Complex formation between poly (vinyl alcohol) and borate ion, Polymer, 22 (1981) 1456-1458.

[67] Leibler L., Pezron E., Pincus P. A., Viscosity behavior of polymer solutions in the presence of complex ions, Polymer, 29 (1988) 1105-1109.

[68] Ochiai H., Fujino Y., Tadokoro Y., Murakami I., Polyelectrolyte Behavior of Poly(vinyl alcohol) in Aqueous Borax Solutions, Polymer J., 14 (1982) 423-426.

[69] Ochiai H., Kurita Y., Murakami I., Makromol. Chem., 185 (1984) 167.

[70] Ochiai H., Kurita Y., Murakami I., Intrinsic viscosity of intramolecularly crosslinked polyelectrolyte: Poly(vinyl alcohol)/borax systems, Makromol. Chem., 189 (1988) 351-360.

[71] Witten T. A., et al., Crosslinking in shear-thickening ionomers, Macromolecules, 18 (1985) 1915-1918.

[72] Ballard M. J., et al., The theory of shear thickening polymer solutions, Polymer, 29 (1988) 1287-1293.

[73] Blenke H., Kottke V., Schmidt, K. G., Eine remissionsfotometrische Messmethode zur Bestimmung örtlicher Stoffübergangskoeffizienten in Luft, Wärme- und Stoffübertragung 10 (1977) 9-21.

[74] Kottke V., Blenke H., Meßmethoden konvektiver Stoffübertragung, Chem.-Ing.-Tech., 50 (1978), 81-90.

[75] Kottke V., Blenke H., Verfahren zur Bestimmung örtlicher Stoff- und Wärmeübertragung an beliebig geformten Oberflächen, Verfahrenstechnik, 16 (1982) 504-509.

[76] Gaiser G., Strömungs- und Transportvorgänge in gewellten Strukturen, Dissertation, Universität Stuttgart, 1990.

[77] Zimmerer C., Strömungs- und Transportvorgänge in Kanälen mit gekreuzten Gitterstrukturen, Dissertation, Universität Stuttgart, 1998.

[78] Gschwind P., Stömungs- und Transportvorgänge in gewellten Kanälen mit ineinanderliegender Anordnung der Wände, Dissertation, Universität Stuttgart, 2000.

[79] Gschwind P., Regele A., Kottke, V., Sinusoidal wavy channels with Taylor-Goertler vortices, Experimental Thermal and Fluid Science, 11 (1995) 270-275.

[80] Kühnel W., Kottke V., Visualization and determination of mass transfer at solid walls in fluid flow, FLUCOME Proceedings, 1994.

[81] Kühnel W., Kottke V., An experimental method for visualization and determination of mass transfer at solid walls in liquid flow, EUROTHERM Seminar 1995, Pisa, Proceedings, 61-67.

[82] Zimmerer C.C., Kottke V., Effects of spacer geometry on pressure drop, mass transfer, mixing behavior, and residence time distribution, Desalination, 104 (1996) 129-134.

[83] Zimmerer C. C., Gschwind P., Gaiser G., Kottke V., Comparison of heat and mass transfer in different heat exchanger geometries with corrugated walls, Experimental Heat Transfer, Fluid Mechanics and Thermodynamics (2001) 731-735.

[84] Kühnel W., Experimentelle Methoden zur Sichtbarmachung und Messung des lokalen Stoffübergangs an festen Wänden, Dissertation, Universität Stuttgart, 1998.

[85] Griffiths P. C., Stilbs P., Yu G. E., Booth C. Role of Molecular Architecture in Polymer Diffusion: A PGSE-NMR Study of Linear and Cyclic Poly(ethy1ene oxide), J., Phys. Chem., 99 (1995) 16752-16756.

[86] Einstein A., Über die von der molekularkinetischen Theorie der Wärme geforderte Bewegung von in ruhenden Flüssigkeiten suspendierten Teilchen, Ann. Phys., 17 (1905) 549.

[87] Lafitte G. et al., PFG-NMR Diffusometry: A tool for investigating the structure and dynamics of noncommercial purified pig gastric mucin in a wide range of concentrations, Biopolymers 86 (2007) 165-175.

[88] Stejskal E. O., Tanner J. E., Spin Diffusion Measurements: Spin echoes in the presence of a time-dependent field gradient, The Journal of Chemical Physics, 42 (1965) 288-292.

[89] Tanner J. E., J. Phys. Chem., 52 (1970) 2523.

[90] Legrand J. et al., Diffusion coefficients of ferricyanide ions in polymeric solutions – comparison of different experimental methods, Electrochimica Acta, 45 (2000) 1791-1803.

[91] Churchill S. W., Ozoe H., Correlations for laminar forced convection in flow over an isothermal flat plate and in developing and fully developed flow in an isothermal tube, J. Heat Transfer, 95 (1973) 416-419.

[92] Chandrupatla A. R., Sastri V. M. K., Laminar Forced Convection Heat Transfer of a non-Newtonian fluid in a Square Duct, Int. J. Heat Transfer, 20 (1977) 1315-1324.

[93] Tiu C. et al., Geometric parameters for some flow channels, The Canadian Journal of Chemical Engineering, 46 (1968) 389-393.

[94] Kozicki W. et al., Non-Newtonian flow in ducts of arbitrary cross-sectional shape, Chemical Engineering Science, 21 (1966) 665-679.

[95] Bereiziat D., Thesis, INPL-Nancy, 1993.

[96] Arvia A. J., Bazan J. C., Carrozza J. S. W., The diffusion of ferro- and ferricyanide ions in aqueous potassium chloride solutions and in solutions containing carboxy-methylcellulose sodium salt, Electrochim. Acta, 13 (1968) 81-90.

[97] Legrand J. et al., Diffusion coefficients of ferricyanide ions in polymeric solutions – comparison of different experimental methods, Electrochimica Acta., 45 (2000) 1791-1803.

[98] Bird R. B., Armstrong R. C., Hassanger O., Dynamics of polymeric liquids, 1 (1977) 242-245, New York: Wiley.

[99] Grigull U., Wärmeübergang an Nicht-Newtonsche Flüssigkeiten bei laminarer Rohrströmung, Chem.-Ing.-Tech., 28 (1956) 553-556.

[100] Yau J., Tien C., Simultaneous development of velocity and temperature profiles for laminar flow of a non-Newtonian fluid in the entrance region of flat ducts, Can. J. Chem. Eng., 41 (1963) 139-145.

[101] Chandrupatla A. R., Sastri V. M. K., Laminar forced convection heat transfer of a non-Newtonian fluid in a square duct, Int. J. Heat Mass Transfer, 20 (1977) 1315-1324.

[102] Irvine T. F. Jr., Non-circular duct heat transfer, Modern Developments in Heat Transfer, W. Ibele, ed. Academic, New York, (1963) 1-17.

[103] Shah R. K., London A. L., Laminar flow forced convection in ducts, Supplement 1 to Advances in Heat Transfer, Academic, (1978) New York.

[104] Cheng J. A., Laminar forced convection heat transfer of power law fluids in isosceles triangular ducts with peripheral wall conduction, Dissertation, Mech. Eng. Dept., State Univ. of New York, (1984) Stony Brook.

[105] Notter R. H., Sleicher C. A., The eddy diffusivity in the turbulent boundary layer near a wall, Chem. Eng. Sci., 26 (1971) 161.

[106] Hanna O. T. and Sandall O. C., Developed turbulent transport in ducts for large Prandtl or Schmidt numbers, AIChE J., 18 (1972) 527.

[107] Stewart W. E., Forced convection: IV. Asymptotic forms for laminar and turbulent transfer rates, AIChE. J., 12 (1987) 2008-2016.

[108] Santos J. L. C. et al., Investigation of flow patterns and mass transfer in membrane module channels filled with flow-aligned spacers using computational fluid dynamics (CFD), Journal of Membrane Science, 305 (2007) 103-117.

[109] Zimmerer C.C., Kottke V., Flow visualization and mass transfer in spacer-filled flat channels, FLUCOME Proceedings, (1994) 793-798.

[110] Kurakawa H. et al., Phase behaviour and sol-gel transition of poly(vinyl alcohol)-borate complex in aqueous solution, Polymer, 33 (1992) 2182-2188.

[111] Wu W. et al., Macromolecular, 23 (1990) 2246.

[112] Pezron E. et al., Macromolecular, 22 (1989) 1169.

[113] Leibler L. et al., Viscosity behavior of polymer solutions in the presence of complex ions, Polymer, 29 (1988) 1105-1109.

[114] Ochiai H. et al., Makromol. chem., 185 (1984) 167.

[115] Keita G. et al., The poly(vinyl alcohol)-borate system: influence of polyelectrolyte effects on phase diagrams, Polymer, 36 (1995) 49-54.

[116] Harrison G., Franks G. V., Tirtaatmaja V., Boger D. V., Suspensions and polymers – common links in rheology, Korea Aust. Rheol. J., 11 (1999) 197-218.

[117] Witten T. A., Cohen M. H., Crosslinking in shear-thickening ionomers, Macromolecules, 18 (1985) 1915-1918.

[118] Ballard M. J., Buscall R., Waite F. A., The theory of shear thickening polymer solutions, Polymer, 29 (1988) 1287-1293.

[119] Rabinowitsch B., Z. Phys. Chem. (Leipzig), 145A (1929) 1.

[120] Rao Y. V. C., Heat transfer, Universities Press (2001).

[121] Dunleavy, J. E., Middleman, S., Trans. Soc. Rheol. 10 (1966) 151-168.

10 Appendix

10.1 Screening test on PVA/borax/NaCl shear thickening system

Many studies have been carried out on PVA/borate aqueous solution systems to interpret their thickening and gelification phenomena [110]-[115].

Based on the knowledge of PVA/borax aqueous solutions in the literature, an initial investigation on the rheological property of PVA/borate aqueous solutions in different concentrations was conducted. The flow curves of PVA/borax solutions based on a product of PVA (M_W = 145000, d.h. >= 98%) from MERCK® were investigated (**Fig. 10-1**).

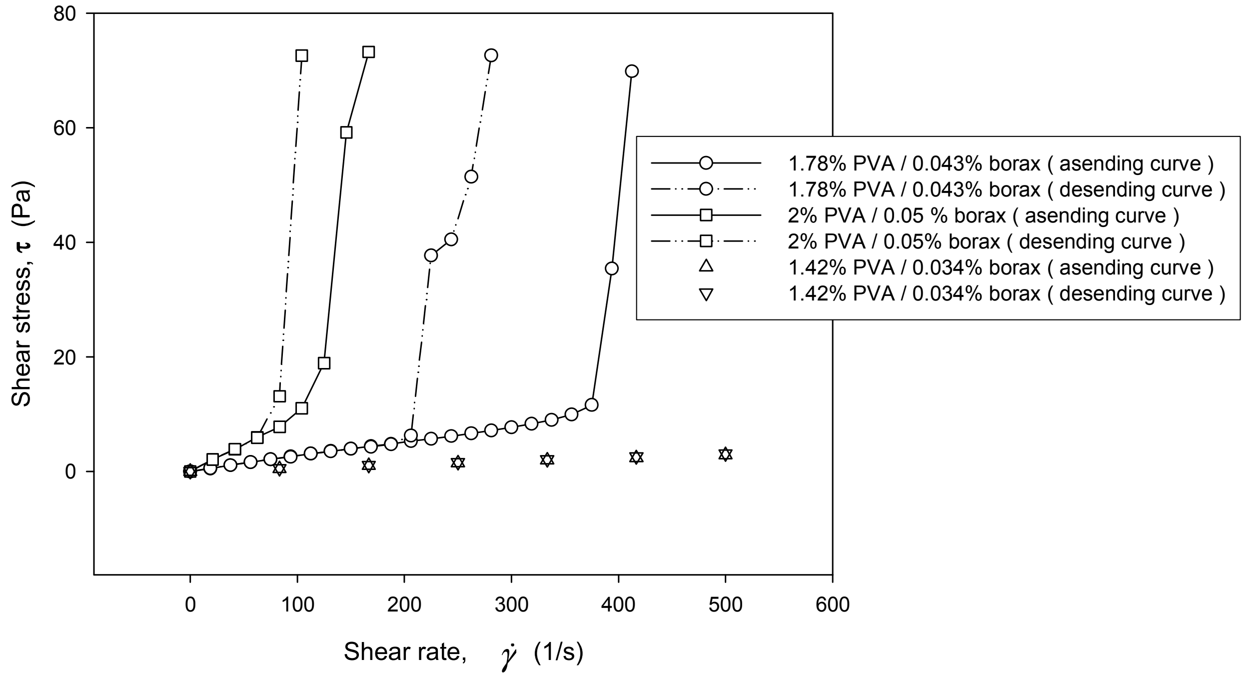

Fig. 10-1 Complex rheological property of PVA/borax aqueous solutions

Fig. 10-1 shows that the rheological property of PVA-borax system is highly affected by the concentration, respectively, the combination of concentration of different components. For a combination of 1.42% PVA and 0.034 % borax, a Newtonian behavior was determined. A little increase in amount of PVA (or borax) strongly affects the rheologic characteristics of the complex, and leads to an abrupt shear thickening after a critical shear rate and to a time-dependent behavior. For the cases of the other two concentrations combinations, a strong dilatantly characterized rheopectic behavior appeared after critical shear strain rates. The critical points depend on the composition of the concentrations.

The dependency of viscosity on shear rate, showing dilatant phenomenon, is desirable for a study on shear thickening. However the time-dependent behavior, the abrupt change (thickening) in a relative narrow range of shear rate - highly sensitive to concentration and of combinations of concentrations- is difficult for practical application.

This strongly shear-induced increasing viscosity combined with rheopectic phenomenon is caused by the gelification. The appropriate region for this study should be before the start of gelation.

There are so many variables to consider for such a complex and sensitive rheological behavior that it is extremely difficult to produce any general results, which can be applied to a variety of problems, before more comprehensive knowledge is extracted from the system and its components.

9 varieties of PVA with different degree of polymerization, molecular weight and degree of hydrolysis (**Tab. 3-4**) were used to screen out an appropriate PVA, which can bind with borax to form a complex having a shear thickening behavior. Further detailed studies were carried out on PVA with different chemical configurations, on the dependency of rheological properties on the concentrations of PVA and borax and their combination, on the effect of ionic strength on rheology as well as on the storage stability of the system.

10.1.1 Basic rheological characteristics of PVA aqueous solutions

A shear-induced viscosity increase of many times over a narrow shear rate range was found in the complexes.

PVA solutions exhibit a linear increase in viscosity with increasing molecular weight (**Fig. 10-2** and **Fig. 10-3**). For a PVA with a given molecular weight, the solution viscosity also increases monotone with concentration (**Fig. 10-4**). A PVA with lower molecular weight and lower degree of hydrolysis demonstrates a higher flow index n value in an aqueous solution.

The viscosity of a PVA solution will decrease with shear rate, a consequence, in part, of disrupting of overlapping chains faster than their ability to associate at higher deformation rates. The shear rate at which non-Newtonian behavior occurs increases with decreasing molecular weight, reflecting a shorter relaxation time of lower molecular weights. Shear thinning is usually explained to arise from chain inclination or alignment of microstructures with the flow direction, thus reducing the local drag [116]. Shear thickening occurring in polymer solutions has been attributed to either intramolecular hydrodynamic interactions due to nonuniform changes of molecular distances during coil deformation of large chains, particularly in viscous solvents, or the transition of intra- to greater intermolecular association of entanglement junctions [117][118].

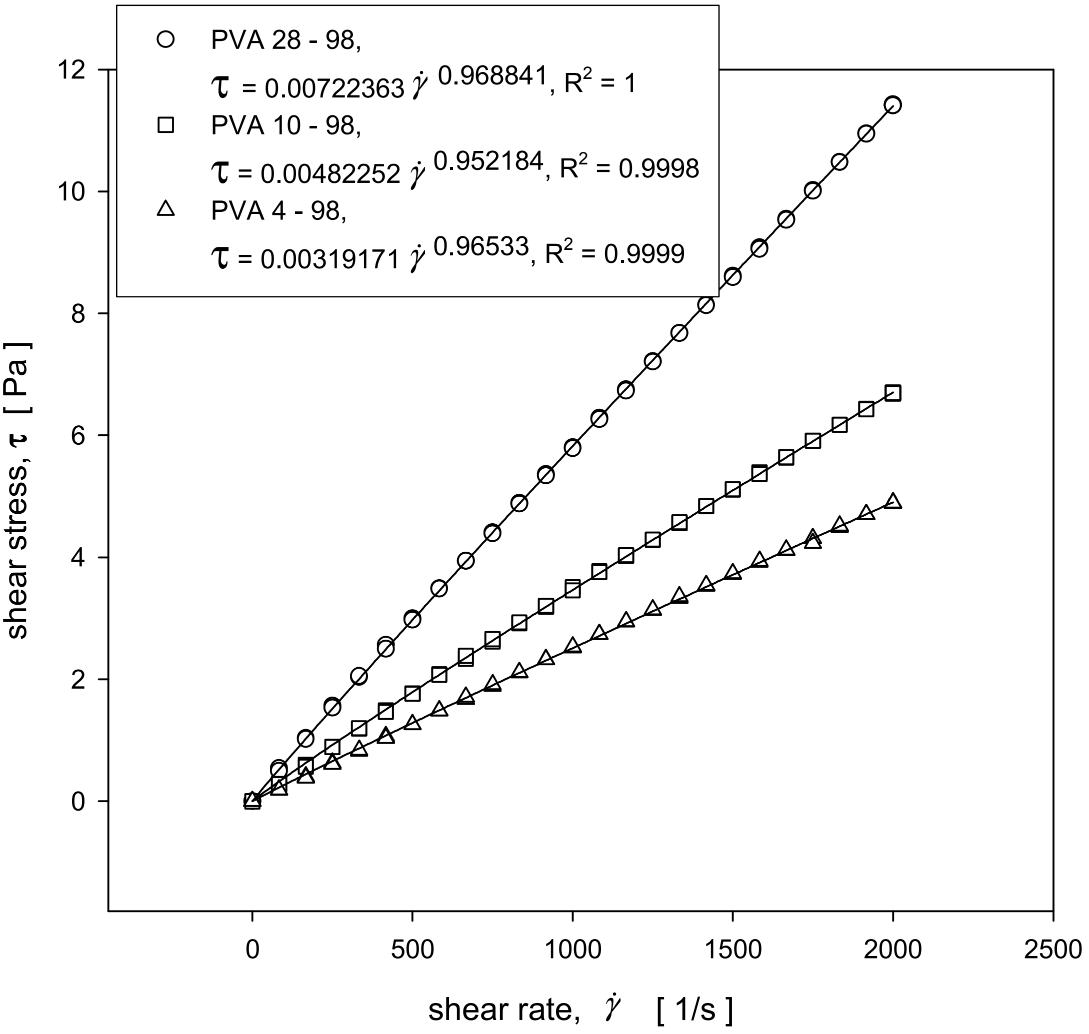

Fig. 10-2 Rheological dependency of PVA on molecular weights with constant degree of hydrolysis, d. h. = 98 %, T = 20 °C, C = 2 %, shear rate = 0 - 2000 [1/s]

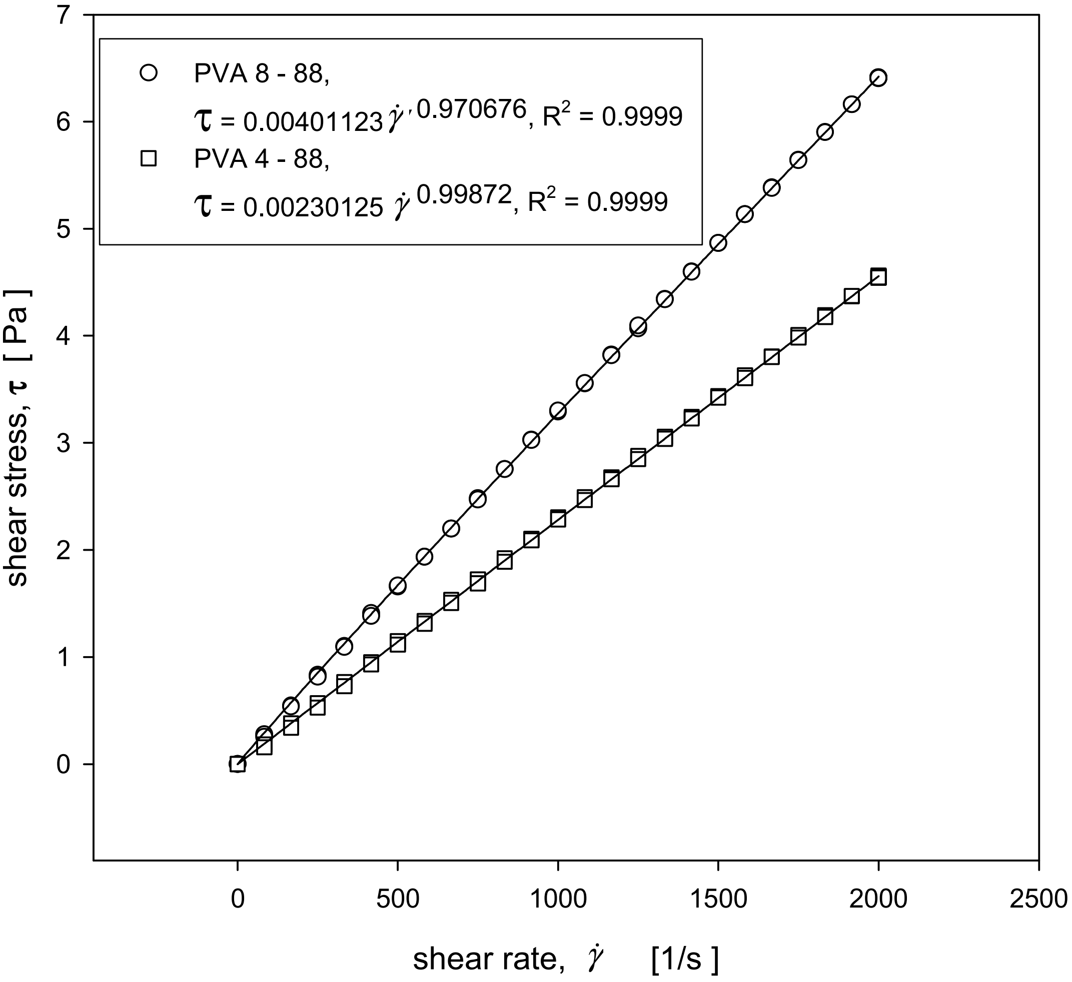

Fig. 10-3 Rheological dependency of PVA on molecular weights with constant degree of hydrolysis, d. h. = 88 %, T = 20 °C, C = 2 %, shear rate = 0 - 2000 [1/s]

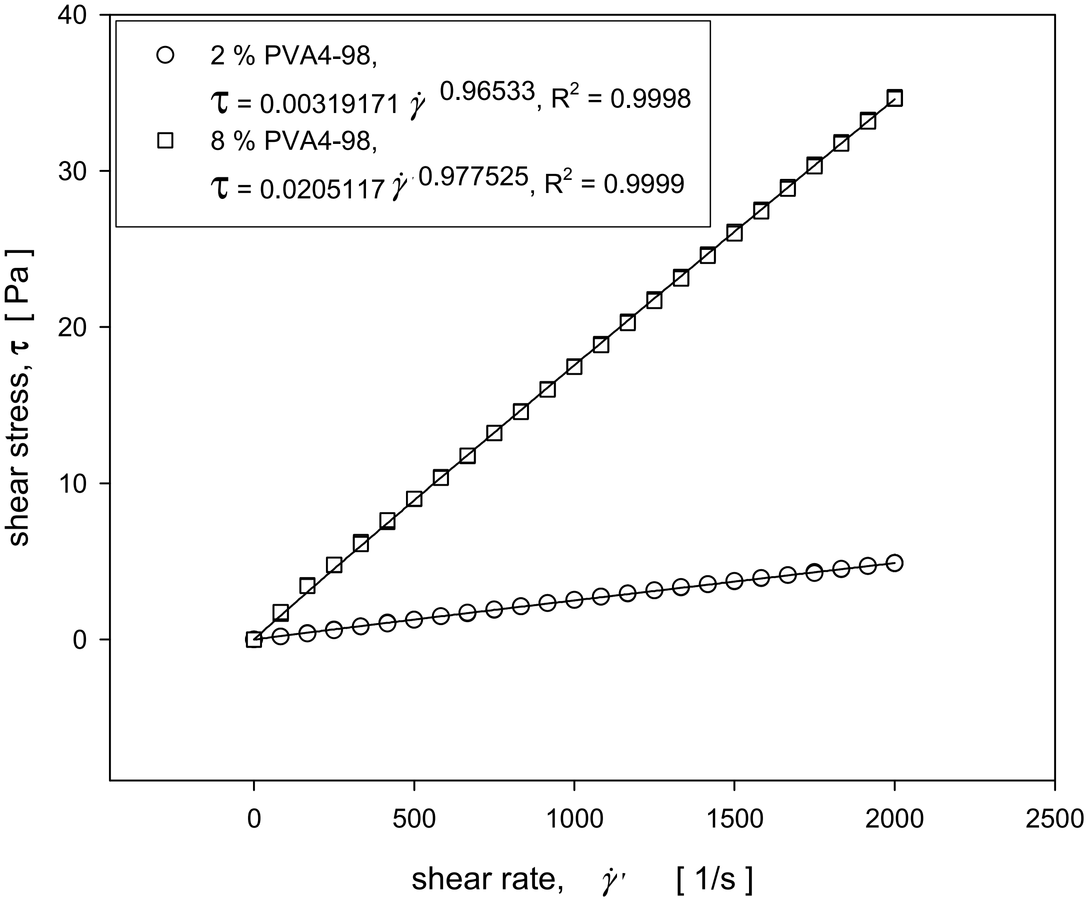

Fig. 10-4 Rheological dependency of a PVA4-98 on concentration and shear rate
T = 20 °C, degree of hydrolysis, d. h. = 98 %, shear rate = 0 - 2000 [1/s]

10.1.2 Rheological characteristics of PVA/borax aqueous solutions

PVA/borax aqueous solution present an increase in viscosity and a higher flow index n value (**Fig. 10-5** to **Fig. 10-7**), except PVA with relative high molecular weight (**Fig. 10-8**), which demonstrates a higher viscosity but a lower flow index n value.

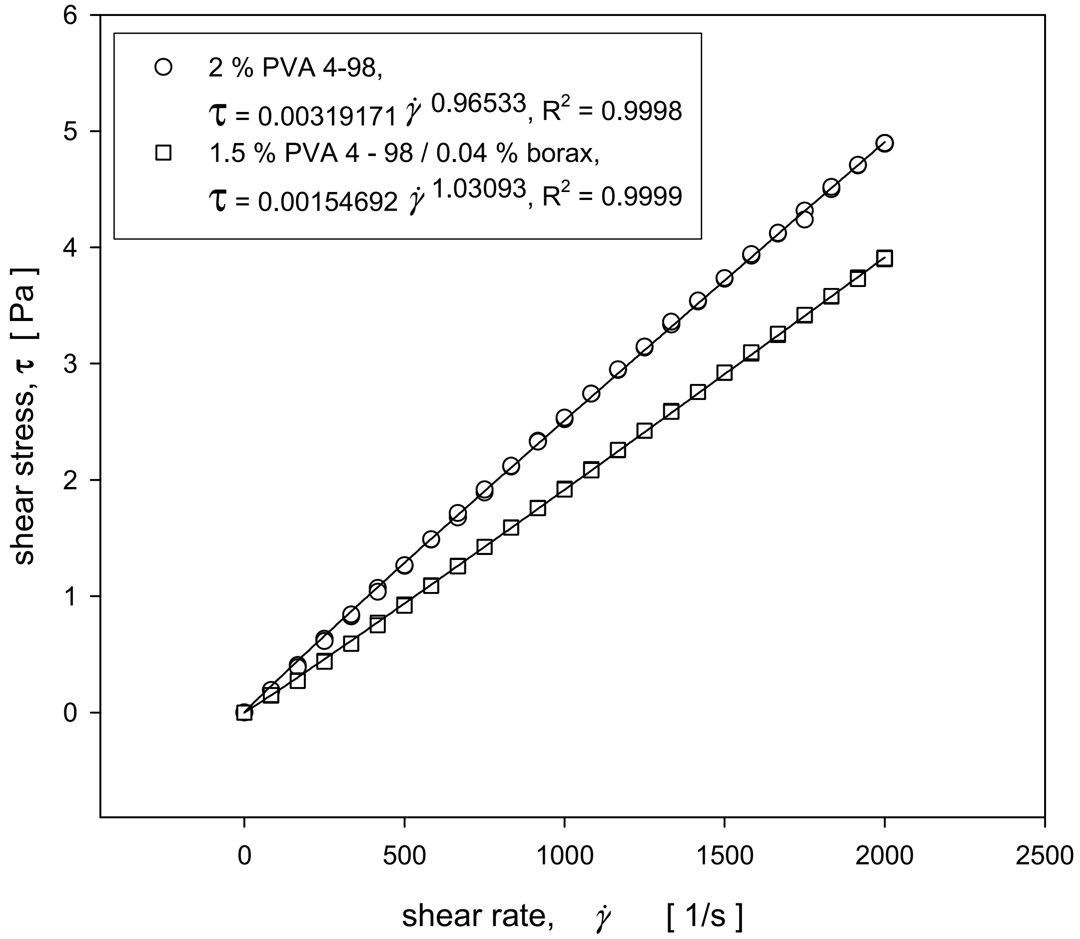

Fig. 10-5 Dependency of the rheological property of a PVA4-98 on addition of borax

T = 20 °C, shear rate = 0 - 2000 [1/s]

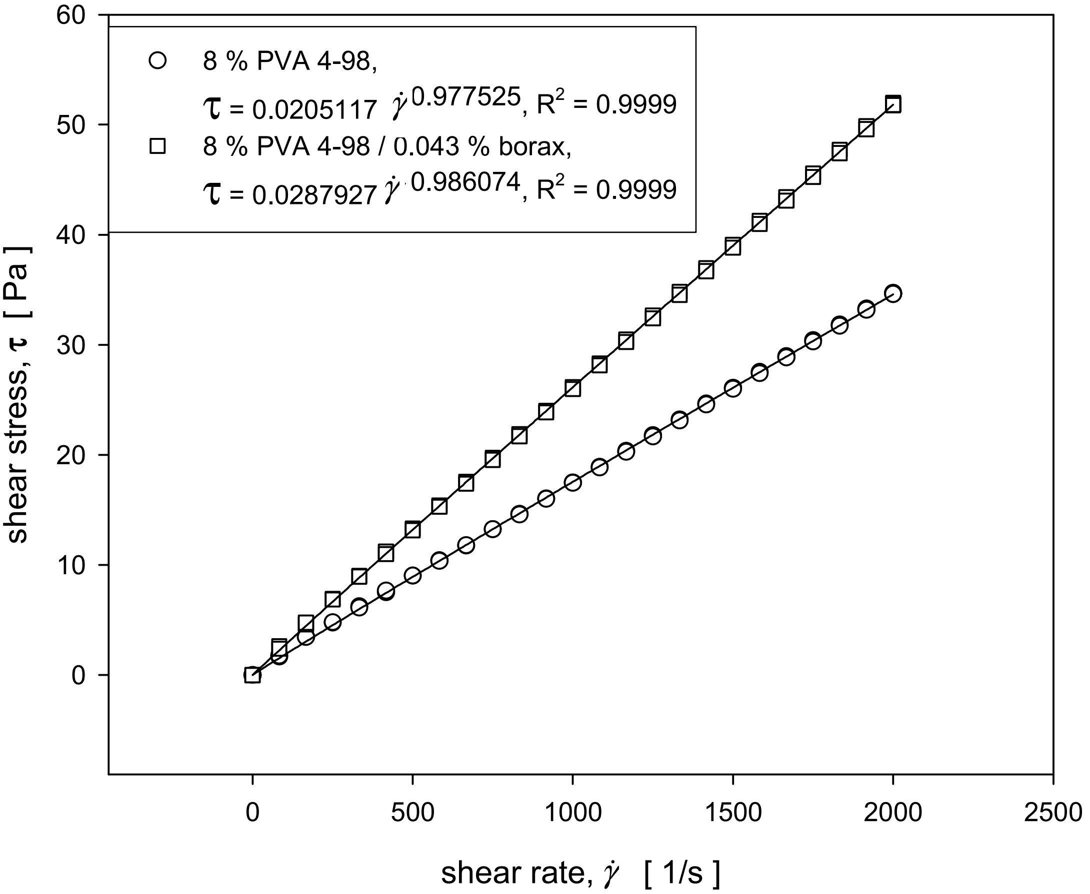

Fig. 10-6 Dependency of the rheological property of a PVA4-98 on addition of borax

T = 20 °C, shear rate = 0 - 2000 [1/s]

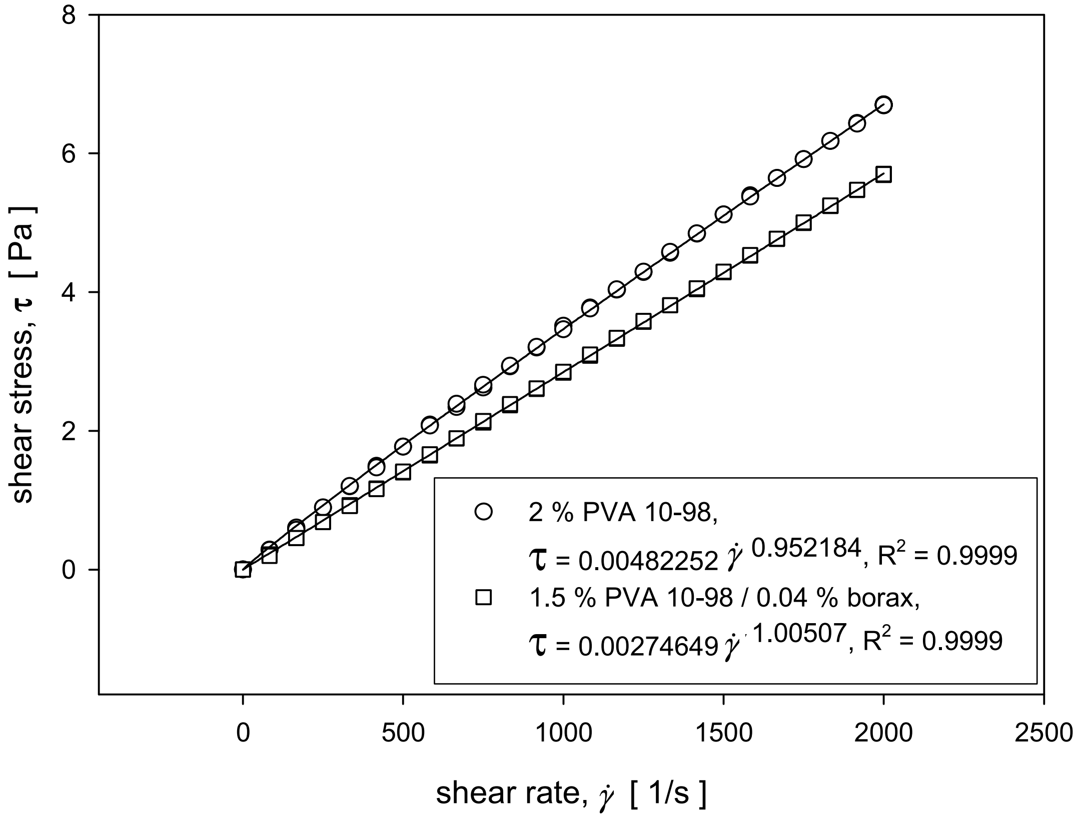

Fig. 10-7 Dependency of the rheological property of a PVA10-98 on addition of borax

T = 20 °C, shear rate = 0 - 2000 [1/s]

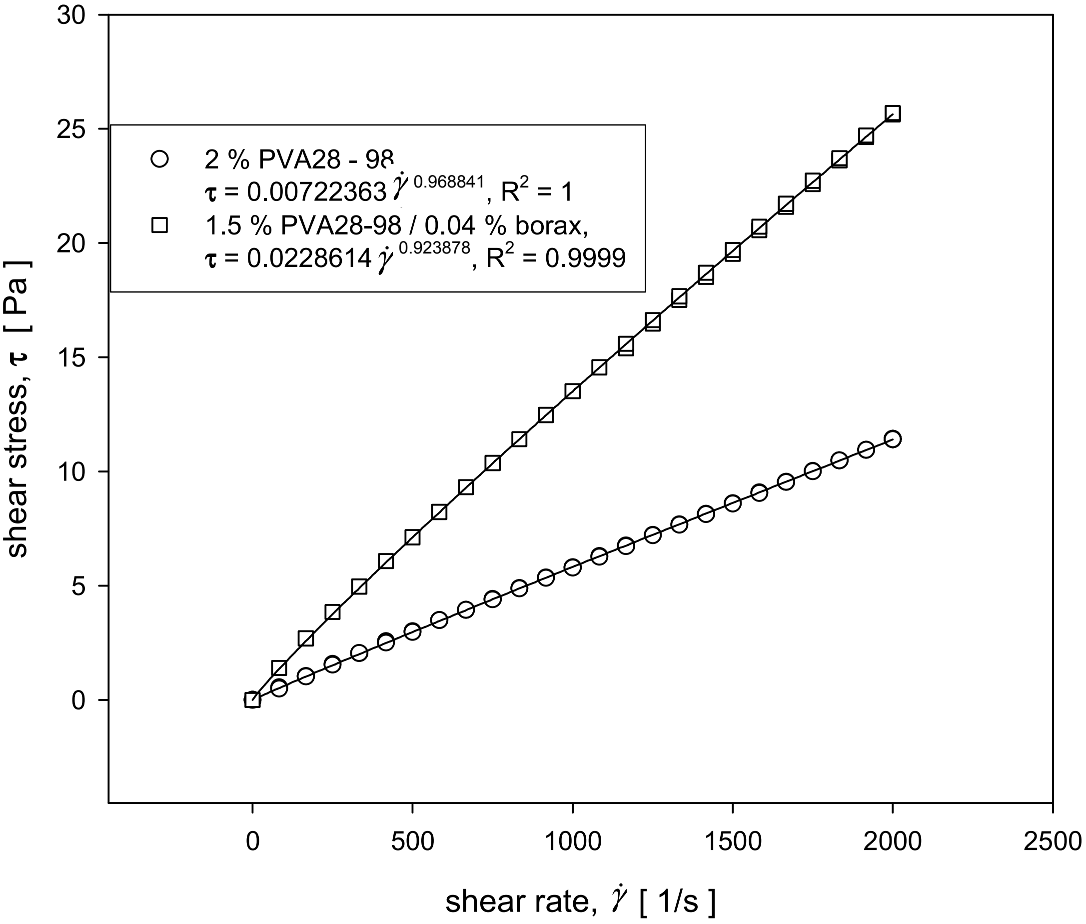

Fig. 10-8 Dependency of the rheological property of a PVA28-98 on addition of borax T = 20 °C, shear rate = 0 - 2000 [1/s]

10.1.3 Effect of the addition of NaCl on the rheological characteristics of PVA/borax/NaCl systems

Based on the rheological characteristics of PVA and PVA/borax aqueous solutions, PVA with relative lower molecular weight and partially hydrolyzed can be more appropriate for building the dilatant system in this study. PVA 4-88 was therefore chosen for the further investigations.

Concentration combination plays an important role in the formation of the PVA/borate complex, the quantity and the type of the complex are the critical factors to determine a thickening or gelation system. Ionic strength in the system becomes important, because a polyelectrolyte behavior can be observed once the PVA/borate complex is formed. The following solutions were prepared as mother solutions for further rheological measurements in order to screen out a suitable dilatant system.

5 % (W/V) PVA 4-88 solution;
0.1 M borax solution ;
0.1 M NaCl solution.

Rheological results are shown in **Tab. 10-1** and **Fig. 10-9**.

Tab. 10-1 Screening test on PVA/borax/NaCl aqueous systems

samples	**PVA 4-88 *** [g]	**borax *** [g]	**NaCl *** [g]	**Water** [g]	C_{PVA} [%, W/V]	C_{borax} [mol/l]	**ratio **** [-]	**η ***** [Pas]
1	29	1	0	0	4.833	0.003	32.304	0.007
2	28	2	0	0	4.667	0.007	15.595	0.079
3	27	3	0	0	4.5	0.01	10.025	1.68
4	26	4	0	0	4.333	0.013	7.241	7.923
5	25	5	0	0	4.167	0.017	5.57	5.507
6	24	6	0	0	4	0.02	4.456	7.985
7	23	7	0	0	3.833	0.023	3.660	8.511
8	22	8	0	0	3.667	0.027	3.063	5.631
9	21	9	0	0	3.5	0.03	2.599	1.28
10	12	18	0	0	2	0.06	0.743	0.001
11	3	27	0	0	0.5	0.09	0.124	0
12	26	4.77	0	0	4.225	0.016	6.072	8.394
13	24	6.815	0	0	3.894	0.022	3.923	10.367
14	25	3	0	2	4.167	0.01	9.283	0.41
15	23	3	0	4	3.833	0.01	8.540	0.139
16	21	3	0	6	3.5	0.01	7.798	0.016
17	21	7	0	2	3.5	0.023	3.342	0.622
18	21	5	0	4	3.5	0.017	4.679	0.161
19	21	3	6	0	3.5	0.01	7.798	-
20	21	4.525	6	0	3.331	0.014	5.17	-
21	21	4	0	5	3.5	0.013	5.848	0.065
22	22	3	0	5	3.667	0.01	8.169	0.049

***: mother solution for PVA 4-88 is 5% (W/V), for borax 0.1 M, for NaCl 0.1 M**

****: ratio = Molar concentration of diol / Molar concentration of boron**

*****: viscosity measured at 20℃, shear rate is 20 [1/s]**

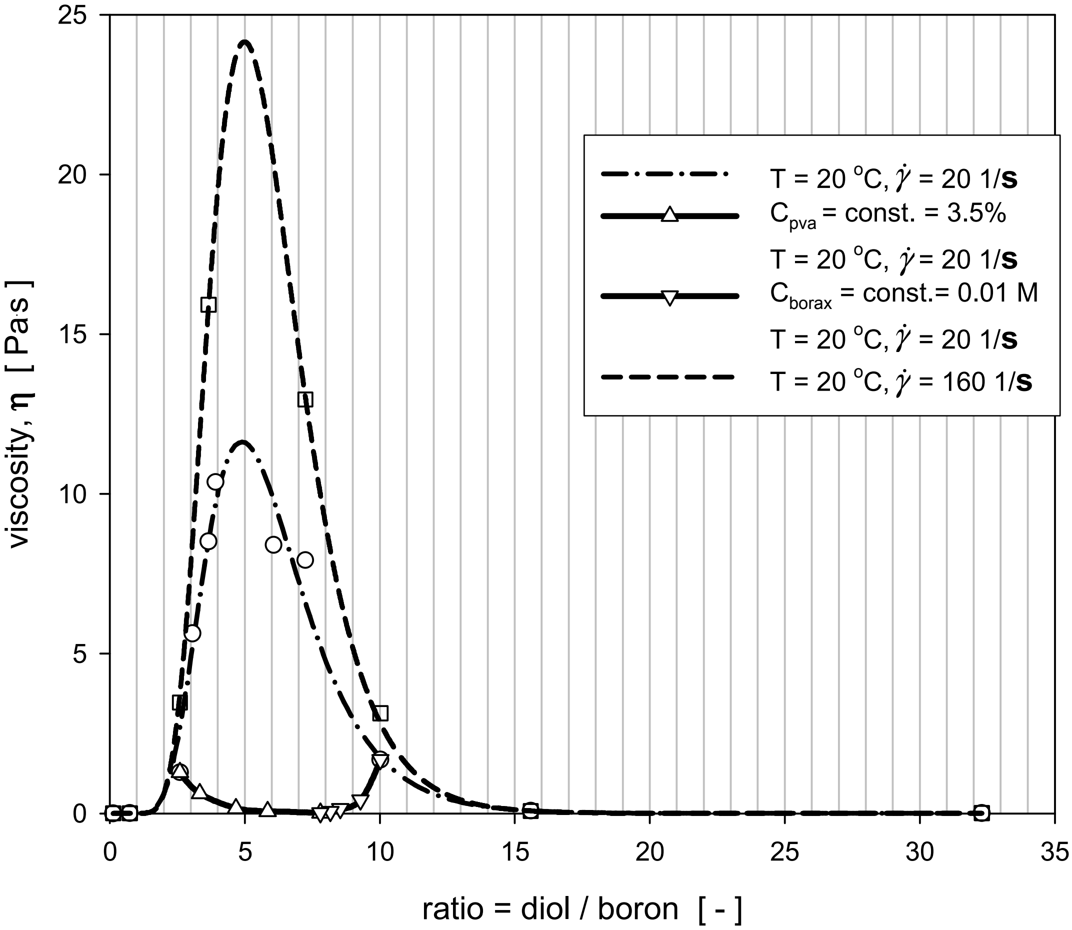

Fig. 10-9 Dependency of viscosity on the ratio of diol to boron in PVA/borax aqueous solutions

A spectrum of apparent viscosity over the ratio of diol to boron in **Fig. 10-9** shows that an increase in viscosity with increasing shear rate in PVA/borax/NaCl system was observed. The maximum peak of viscosity appears at a ratio of diol to boron around 5. The ratio value around 5 is the equilibrium point of the formation of PVA/borate complex. Lower than this value, the concentration of borax is in excess; higher than this value, PVA is then in excess. It is also shown, that viscosity decreases with an increasing ratio of diol to boron when PVA concentration is kept constant at a lower then excess level, and viscosity increases when borax is kept constant at an axcess level. Two important conditions should be taken into account to avoid gelation. One is that the concentration of PVA should be in diluted level; the other is to ensure borax excess to avoid the 1: 2 diol complex formations. That means in order to build an appropriate shear thickening system, a diluted concentration of PVA should be chosen and a ratio of diol to boron lower the equilibrium point value is necessary.

10.2 The density of METHOCEL® K15M aqueous solutions for different concentrations

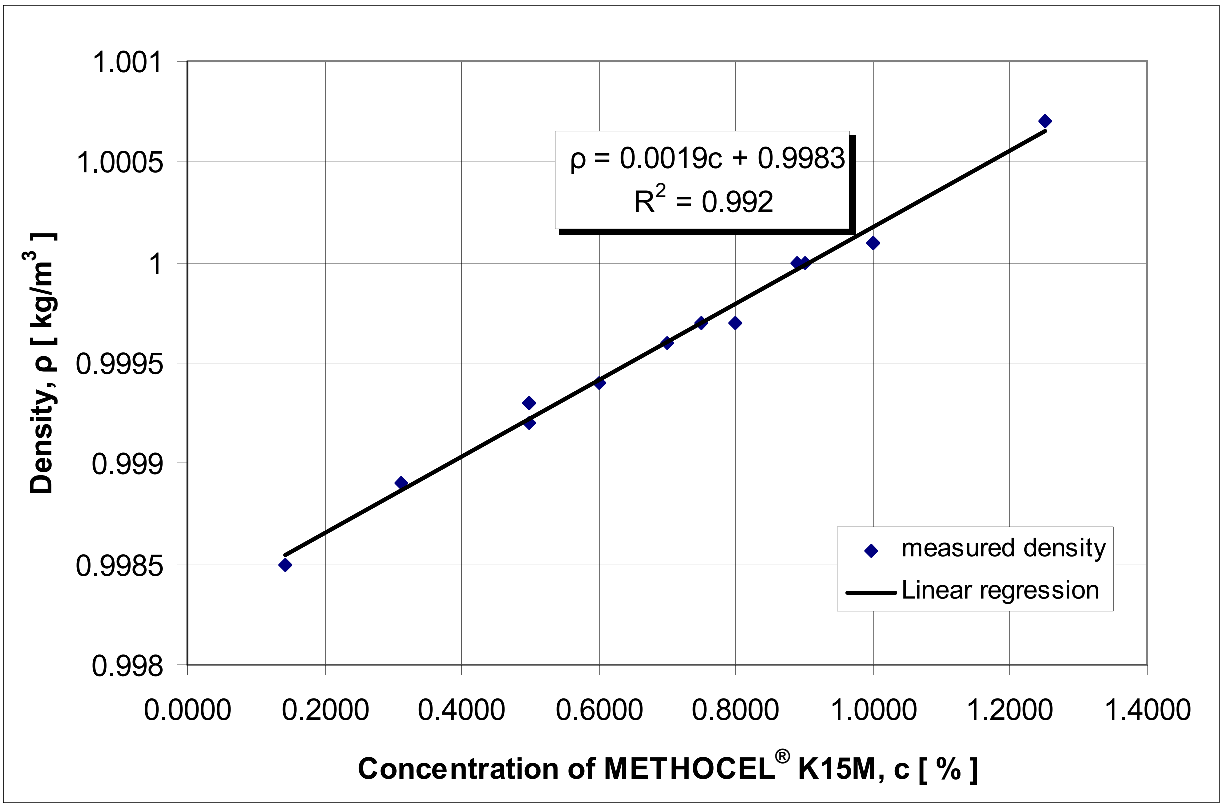

Fig. 10-10 The density $^{/1/}$ of METHOCEL® K15M for different concentrations

$^{/1/}$: measured with Density Meter DMA 48 (Chempro/Paar, Austria)

10.3 Comparison of hydraulic diameters between two definitions

The definition of hydraulic diameter in **Eqn. 2-1** based on the dimension of the whole test section, takes the sides-walls into account. When the width of the test section is infinite large, the value of d_h then becomes $d_{h,d}$. The comparison of hydraulic diameters in **Fig. 10-11** shows that for the test channel with the width B = 150 mm, used in this study, all spacers have an error lower than 5% between the two definitions of hydraulic diameters.

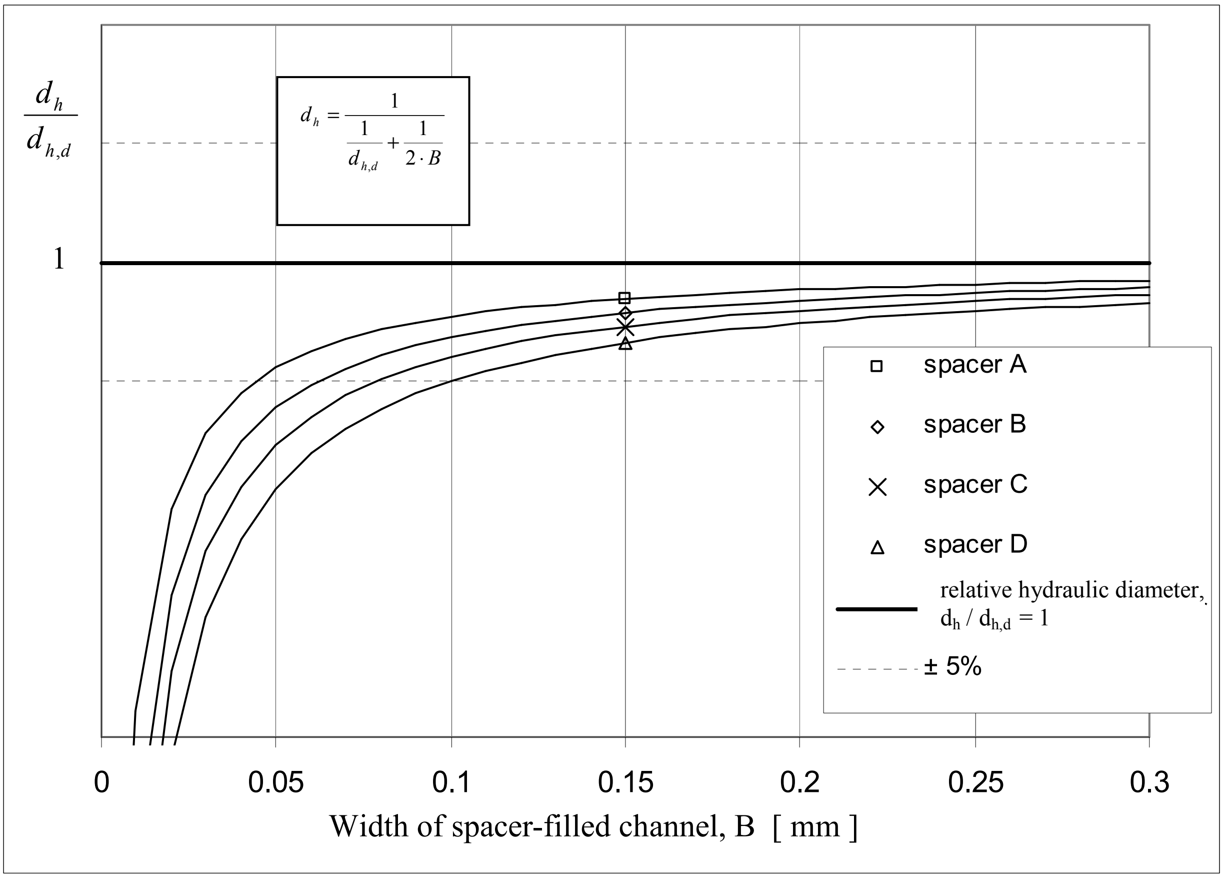

Fig. 10-11 Comparison of hydraulic diameter ratio for two definitions of hydraulic diameter over width of spacer-filled channel

10.4 Visualization of mass transfer distribution for non-Newtonian fluids in spacer-filled channels

The visualization of mass transfer distribution for Acidol-Blue in METHOCEL® K15M in spacer-filled channels is shown from **Fig. 10-12** to **Fig. 10-14**. Flow direction is from the left to the right side. The color density directly corresponds to the local transferred mass. The mass transfer at the onset of the left side of the polyamide membrane is very high, because of an impingement of the flow on the height of the test section. It is clear, that mass transfer decreases over the entrance length with developing concentration boundary layer. The white areas without mass transfer are caused through the bearing or contact lines of the spacer structures. Areas near these contact lines, the mass transfer is distinctly lower, are the so-called extremely low mass transfer area defined in **Tab. 6-1**. Mass transfer in these regions is characterized by diffusion, not convection. For a high Reynolds number, pictures 2 and 4 in **Fig. 10-14**, the mass transfer in the separation zones is also dominantly lower.

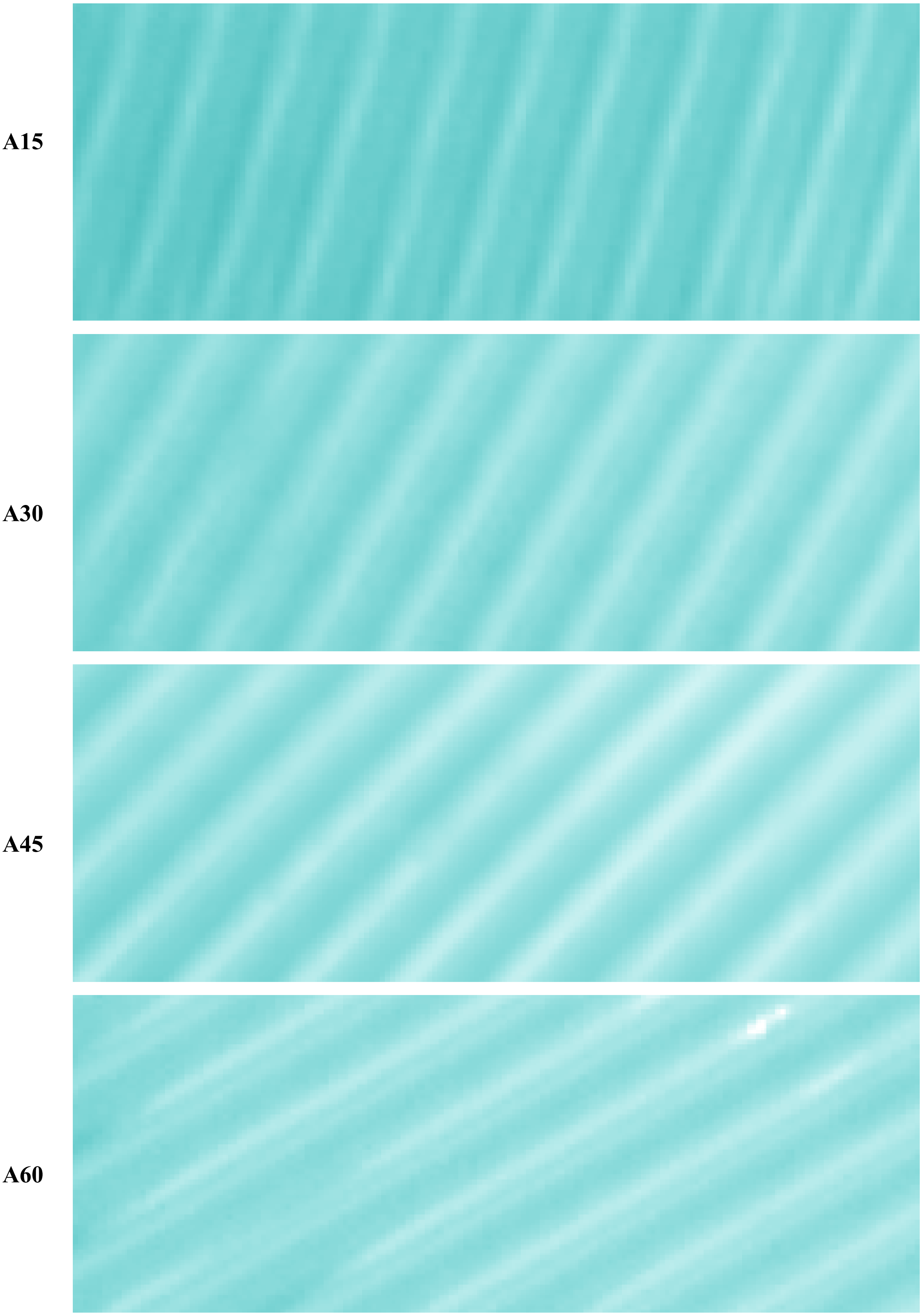

Fig. 10-12 Visualization of mass transfer distribution for spacers with a constant wavelength, $\lambda/a = 4$, $\varphi = 15\text{-}60^{\circ}$, 0. 5% METHOCEL® K15M, $Re_M = 10$.

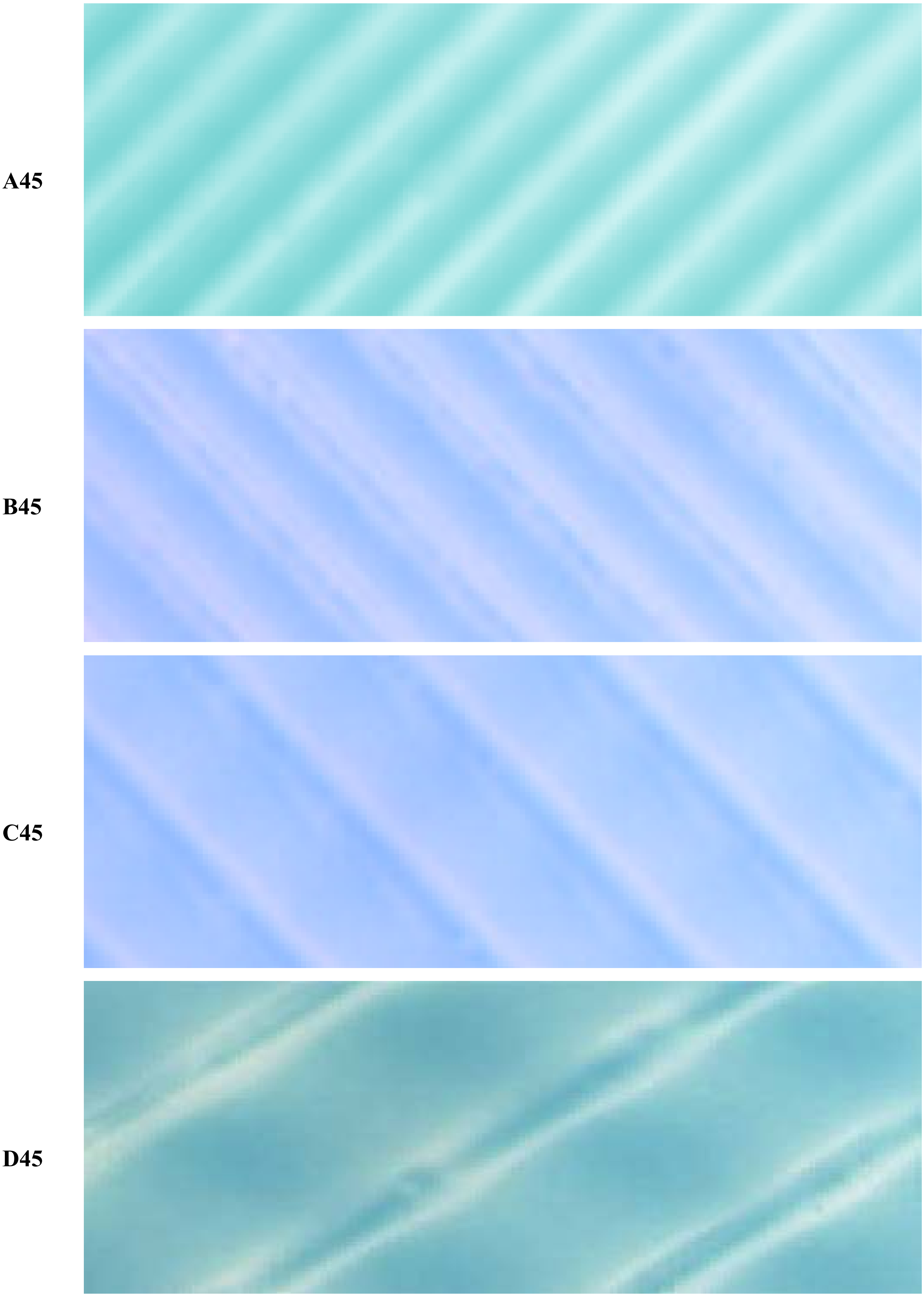

Fig. 10-13 Visualization of mass transfer distribution for spacers with a constant inclination angle φ, $\varphi = 45^{o}$, $\lambda = 4\text{-}11$, 0.5% METHOCEL® K15M, $Re_M = 10$.

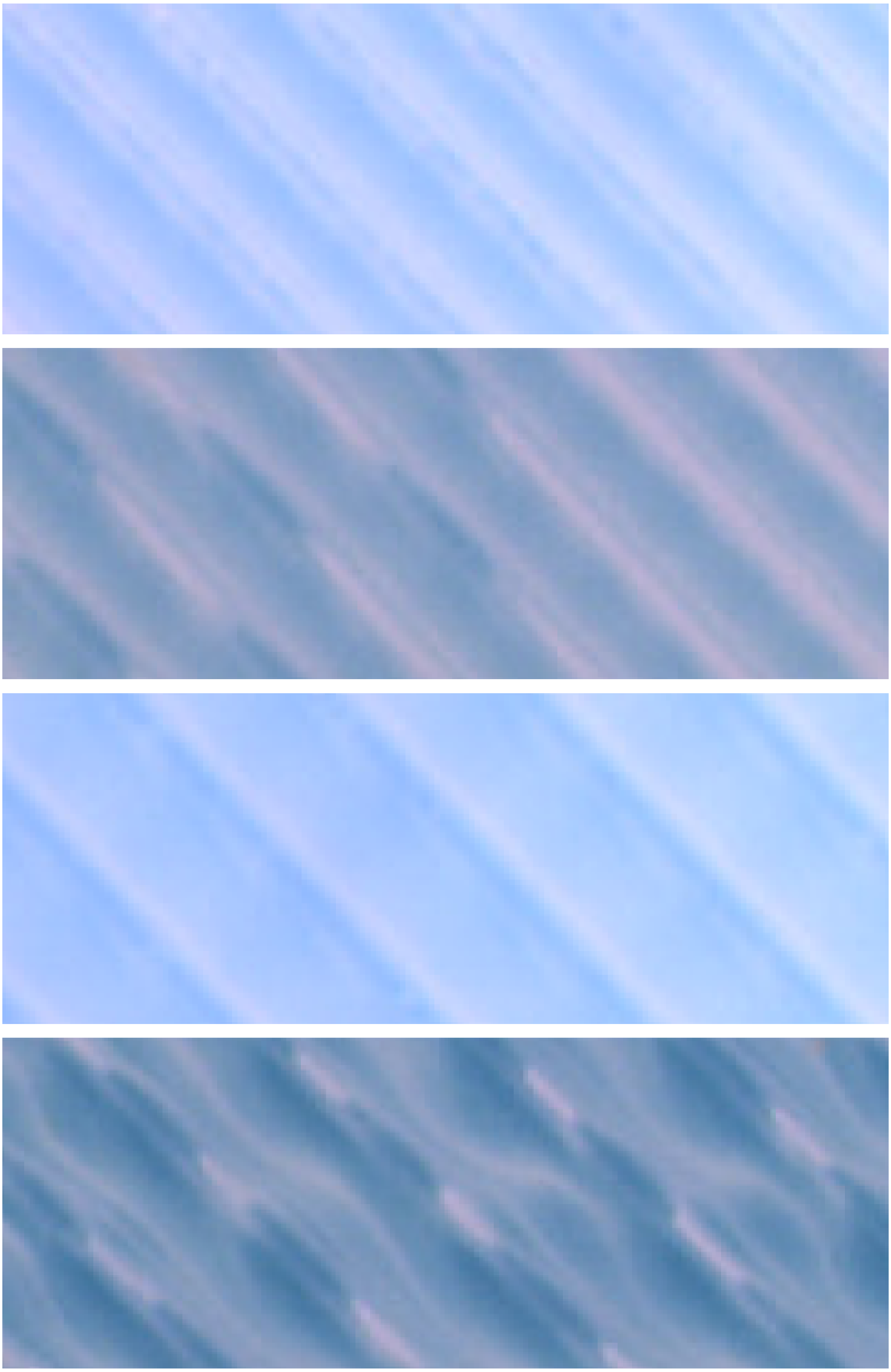

Fig. 10-14 Visualization of mass transfer distribution in dependence of the Reynolds number Re_M, 0.5% METHOCEL® K15M, $\varphi = 45^{\circ}$, $\lambda = 5.5\text{-}7.45$, $Re_M = 10$ (pic. 1 and 3), $Re_M = 50$ (pic. 2 and 4).

10.5 Visualization of mass transfer distribution through numerical method

The visualization of mass transfer distribution, for a specific additional variable in a non-Newtonian fluid flow in spacer-filled channels, was simulated with program ANSYS CFX®. The non-Newtonian fluid is characterized by its shear thinning rheological behavior and modeled by the modified power law equation with a flow index $n = 0.3$. The mass transfer distribution results in their characteristic single diamonds are shown in **Fig. 10-15**. Here, the Sherwood number in a relative scale is used to compare the mass transfer distribution for the spacers with different geometric parameters. The relative Sherwood number, presented by different colors, directly corresponds to the local transferred mass. The high relative Sherwood number, in red color, indicates high amount of transferred mass and that in blue color indicates a low amount transferred mass. The characteristics of the mass transfer distribution for the shear thinning non-Newtonian fluid flow with fully developed concentration boundary layer were won.

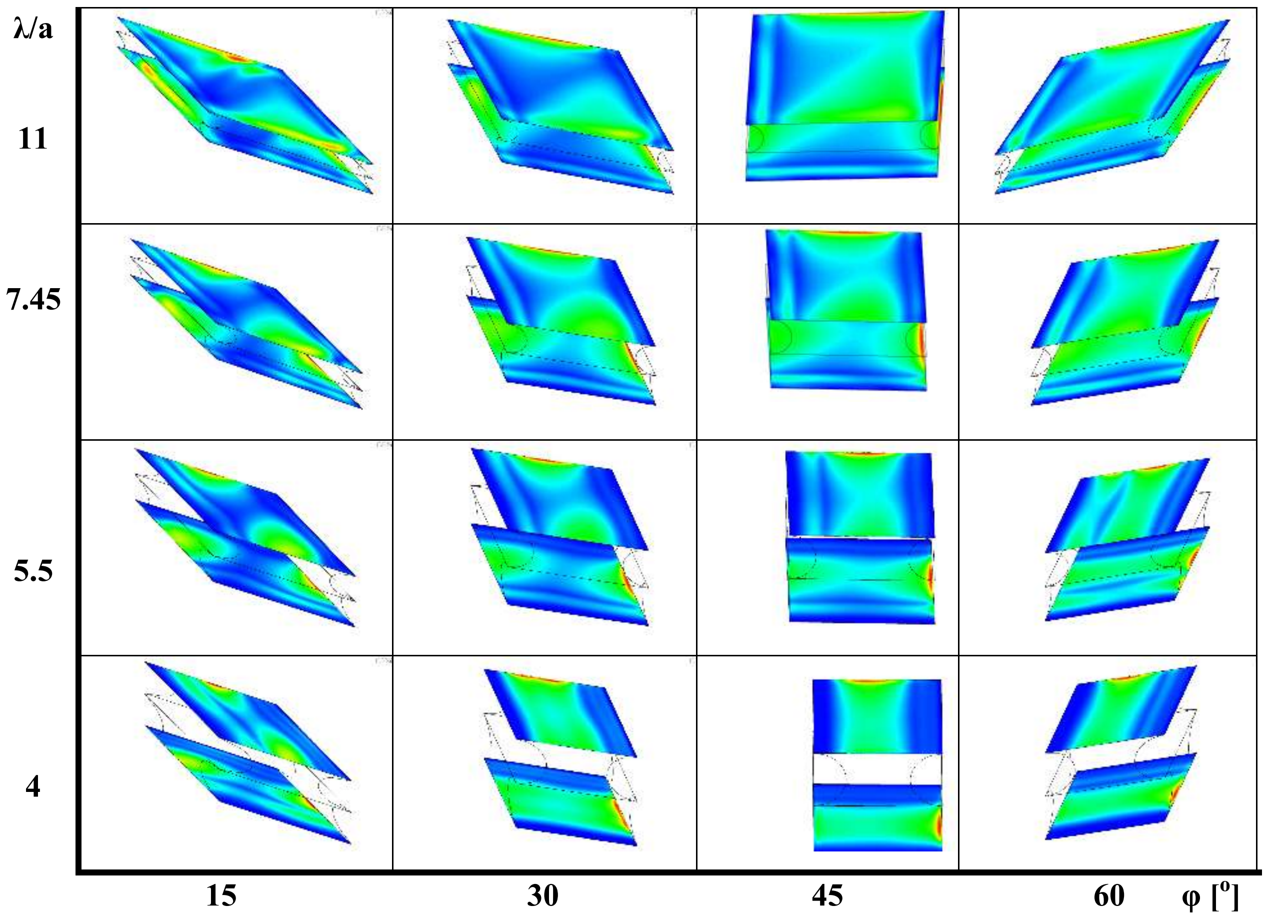

Fig. 10-15 Visualization of mass transfer distribution through numerical method for a non-Newtonian fluid in spacer-filled channels, $\lambda/a = 4\text{-}11$, $\varphi = 15\text{-}60^\circ$, $\eta_0 = 0.08$ [kg/(m s)], $K = 1.08$ [kg/(m s$^{1.7}$)], $n = 0.3$, $Re_M = 2\text{-}20$.